Institute of Experimental Pharmacology and Toxicology

Center for Experimental Medicine

University Medical Center Hamburg-Eppendorf

Investigation of the autophagy-lysosomal pathway in human inherited cardiomyopathies

Dissertation

Submitted to the Department of Chemistry

Faculty of Mathematics, Informatics, and Natural Sciences

University of Hamburg

for the degree of

Doctor of Natural Sciences

(Dr. rer. nat.)

by

Antonia Theresa Luisa Zech

Hamburg, 2019

1st Referee: Prof. Dr. Lucie Carrier

2nd Referee: Prof. Dr. Elke Oetjen

Date of disputation: 05.05.2020

This thesis was carried out from October 2015 until December 2019 (including maternity and parental leave from October 2018 until and including August 2019) at the Institute of Experimental Pharmacology and Toxicology (Director: Prof. Dr. Thomas Eschenhagen) under the supervision of Prof. Dr. Lucie Carrier.

Table of contents

1. Introduction

1.1. Autophagy-lysosomal pathway

Autophagy (greek auto: self; phagein: eating) is one of the two major protein degradation pathways within a cell that degrades long-lived proteins and organelles within lysosomes (Deter and De Duve 1967). Terminally misfolded and short-lived proteins are degraded via the ubiquitin-proteasome system (UPS). Under basal conditions, autophagy is constantly active but can be upregulated as a response to various stimuli of stress, for instance starvation or pathogen infection, to protect against toxic protein aggregates. Furthermore, autophagy is highly conserved within eukaryotes and is keeping cellular homeostasis whilst acting as an energy supplier. Hence, autophagy is of particular importance for post-mitotic cell types. However, defective autophagy can be fatal for every cell type since a low activity may lead to proteotoxicity whilst a high activity may lead to cell death (Maejima et al. 2017). The most prominent form of autophagy is macroautophagy (hereafter called autophagy-lysosomal pathway, short ALP) that involves the formation of an autophagosome enclosing cellular debris and fusing with a lysosome for degradation of its content. ALP is one of three major forms of autophagy, next to chaperone-mediated autophagy (CMA) and microautophagy. CMA requires the translocation of proteins via the chaperone complex into the lysosome whereas microautophagy stimulates the degradation of cellular components/debris by direct engulfment. In the human heart, solely the ALP and CMA but not microautophagy have been described so far. Moreover, both have been shown to either be a selective or non-selective process that degrades big bulks of cellular waste. To date, a few selective forms of autophagy that degrade whole organelles have been described in the human heart (e.g. mitophagy, glycophagy and lysophagy; Figure 1). Further, it has been assumed that ferritinophagy might play a role in the human heart (Bravo-San Pedro et al. 2017; Delbridge et al. 2017; Zech et al. 2019).

1.1.1. The ALP with its single steps

To date, about 30 autophagy-related genes (ATG) are known in mammalian cells, that are involved in the single steps of the quite complex ALP process (Figure 1). In brief, the ALP process comprises phagophore nucleation and elongation, maturation into an autophagosome and subsequent autophagosome-lysosome fusion for cargo degradation.

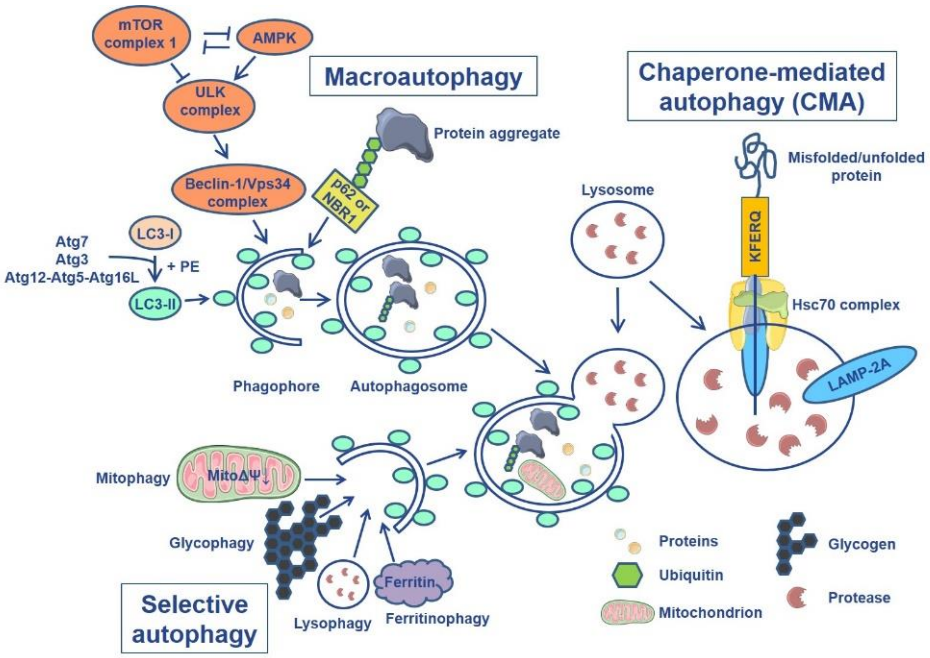

Figure 1: Forms of autophagy found in the human heart. The two most prominent forms of autophagy found in the human heart are the non-selective macroautophagy and chaperone-mediated autophagy. Selective forms of autophagy described in the heart are mitophagy, glycophagy and lysophagy. Further, ferritinophagy has been proposed to play a role in the human heart (Adapted from Zech et al. 2019).

In greater detail, a stress signal induces the formation of the phagophore (also called isolation membrane). For this purpose, a piece of membrane found within the cell is recycled (e.g. plasma membrane, the endoplasmic reticulum (ER) or mitochondria (Hayashi-Nishino et al. 2009; Hailey et al. 2010; Ravikumar et al. 2010)). This step is mainly guided by the ULK complex that consists of ATG13, Unc-51-like autophagy activating kinase 1/2 (ULK1/2), focal adhesion kinase family interacting protein of 200 kDa (FIP200) and ATG101. Further, the mammalian/mechanistic target of rapamycin (mTOR) negatively regulates the ALP by phosphorylating ATG13 and ULK1/2, thus preventing phagophore initiation. However, if mTOR is inhibited, ULK1/2 autophosphorylates itself and subsequently FIP200 and ATG13 and thus initiates phagophore formation. This step is followed by the recruitment of membrane pieces to the phagophore assembly site by ATG9 to initiate autophagosome nucleation. The subsequent autophagosome formation is initiated by the activation of the Beclin-1/Class III PI3K (Phosphatidylinositol-3-phosphate kinase III) that comprises Beclin-1, ATG14L, vacuolar protein sorting 15 and 34 (VPS15 and VPS34). In particular, ULK1/2 phosphorylates Beclin-1 that activates VPS15 and VPS34 which in turn phosphorylates phosphoinositide to produce phosphatidylinositol-3-phosphate (PIP3). PIP3 then triggers membrane elongation that develops into autophagosome formation (Russell et al. 2013; Park et al. 2016, 2018; Maejima et al. 2017).

The actual autophagosome formation, composed of elongation and maturation, is guided by two ubiquitin-like conjugation systems, ATG7-ATG3 or ATG7-ATG10 and ATG12-ATG5-ATG16L. More precisely, ATG7, an E1-like activating enzyme, and ATG10, an E2-like conjugating enzyme, first activate and then conjugate ATG12 to ATG5 via a lysine residue. In conjunction with ATG16L, the E3-like ligase complex is formed (ATG12-ATG5-ATG16L) that associates to the phagophore membrane as a dimer. Concurrently, the cysteine protease ATG4 cleaves microtubule-associated protein 1 light chain 3 (LC3), γ-aminobutyric acid receptor-associated protein (GABARAP) and Golgi-associated ATPase enhancer of 16 kDa (GATE-16) to reveal the C-terminal glycine. ATG7 then activates the cleaved LC3 (LC3-I), which in turn is first conjugated with a phosphatidylethanolamine (PE) group, then transferred to ATG3, before being incorporated into the autophagosomal membrane as LC3-II. Autophagosomes are double-membraned vesicles, and LC3-II is incorporated into the outer and inner autophagosomal membrane. Solely the exterior LC3-II can be recycled by ATG4 that cleaves off PE. LC3-II located inside of the autophagosome is degraded along with the cargo. Due to its presence within the whole ALP process, LC3-II is the main marker of the ALP. Further, LC3-II can be used to evaluate the autophagic activity/flux of the ALP. For this purpose, autophagy modulators such as Bafilomycin A_1 (Bafilo) can be applied to block proper autophagosome-lysosome fusion and thus autophagolysosomal degradation. By determining the levels of LC3-II with and without modulator treatment, the activity of the ALP can be determined. Moreover, LC3-II has also been described to play an important role in cargo recognition (via p62 and neighbour of BRAC1 (NBR1)), autophagosome biogenesis (elongation and membrane closure) and autophagosome-lysosome fusion. However, further research is needed to elucidate the precise mode of action (Feng et al. 2014; Ghosh and Pattison 2018; Zech et al. 2019).

For cargo degradation, the fusion of the autophagosome with a lysosome must take place. Therefore, autophagosomes and lysosomes are transported along microtubules to the perinuclear region. Autophagosomes that form all-over the cytoplasm are transported by dynein, whereas the transport of lysosomes is pH-dependent (Korolchuk et al. 2011). The fusion itself can either be a complete fusion, resulting in an autolysosome, or a kiss-and-run fusion. In this case, solely from the autophagosome content is unidirectionally transferred to the lysosomes in multiple ‘kissing’ events (Jahreiss et al. 2008). Key players of the fusion are Rab GTPases (e.g. Rab7), membrane-tethering complexes and soluble N-ethylmaleimide-sensitive-factor attachment receptors (SNAREs; for commentary, see Nakamura and Yoshimori 2017). The lysosome-associated membrane protein-2 (LAMP-2) that is part of the lysosomal membrane where it is involved in the lysosomal biogenesis, maturation and function (Eskelinen 2006) seems to play a special role in the autophagosome-lysosome fusion. In patients suffering from Danon disease, a LAMP-2 deficiency as well as an accumulation of

autophagic vacuoles have been shown (Nishino et al. 2000; Hashem et al. 2015). Further, in non-cardiomyocytes, LAMP-2 appears to facilitate the proper incorporation of syntaxin-17 (STX17; Qs-SNARE) into the autophagosomal membrane and thus enables an interaction with vesicle-associated membrane protein 8 (VAMP8; R-SNARE) that is located on lysosomes. For cardiomyocytes, a direct interaction of the isoform LAMP-2B with ATG14 and VAMP8 through its cytosolic C-terminal coiled-coil domain has been shown to promote the fusion (Chi et al. 2019).

Within the autolysosome, all former cytoplasmic material is degraded by lysosomal hydrolases (e.g. proteases, phosphatases, lipases). It is assumed that the autolysosome is then recycled and becomes again a single-membraned lysosome, whereby the 'former' cellular waste has been converted from macromolecules to its building blocks that can be used by the cell (e.g. adenosine triphosphate (ATP), amino acids, fatty acids). To ensure proper degradation, an acidic pH of ~4.5 must be maintained by ion channels and the vacuolar H^+-ATPase (V-ATPase). In case of incomplete degradation of the auto-lysosomal content, residual bodies form (Eskelinen and Saftig 2009; Lawrence and Zoncu 2019).

1.1.2. Regulation of the ALP in human heart

The ALP is constantly active at a low basal level in human heart but multiple stimuli (e.g. starvation) can induce its activation. To keep cellular homeostasis, a precise and accurate regulation of the ALP is needed. The serine/threonine kinases mTOR and AMP-activated protein kinase (AMPK) are the two most studied regulators of ALP in the heart (Figure 2). mTOR is the master negative regulator of ALP and crucial for proliferation and protein synthesis. Thus, it is activated under nutrient-rich conditions or by growth factors and inhibited during starvation. To regulate the ALP in the heart, mTOR forms the mTORC1 complex together with the regulatory-associated protein of mTOR (RAPTOR), mammalian lethal with SEC13 protein 8 (mLST8), proline-rich AKT substrate of 40k Da (PRAS40) and DEP domain-containing mTOR-interacting protein (DEPTOR). Under nutrient-rich conditions, growth factors or insulin activate the phosphatidylinositol-3-kinase (PI3K) pathway that in turn activates protein kinase B (PKB)/AKT. PKB/AKT in turn phosphorylates and thus inactivates tuberous sclerosis protein 1 or 2 (TSC1/2), that normally inhibits mTOR. Thus, mTOR is active and the ALP is inactivated. Autophagy modulators can inhibit mTOR, such as the ALP activator rapamycin (Rapa). Rapa inhibits the mTOR kinase activity by forming a complex with FK506-binding protein of 12 kDa (FKBP12) which in turn binds and stabilizes the RAPTOR-mTOR complex. However, mTOR can also be inhibited by AMPK under low levels of nutrients. Therefore, AMPK either phosphorylates RAPTOR directly or indirectly activates TSC1/2. Further, AMPK also inhibits c-jun N-terminal kinase (JNK) and thus prevents the interaction of

Beclin-1 and B-cell lymphoma 2 (Bcl-2) and activates the ALP. AMPK in turn can be inhibited by energy suppliers.

mTORC1 can also be inhibited by glycogen synthase kinase 3 beta (GSK3β) that activates TSC1/2 during energy stress, by the hexokinase-II (HK-II) under glucose deprivation or by oxidation at Cys1483 during oxidative stress. In addition, microRNAs (miRNAs) have been shown to regulate the ALP (e.g. miRNA-212 or miR-99a; Delbridge et al. 2017; Ghosh and Pattison 2018; Sciarretta et al. 2018).

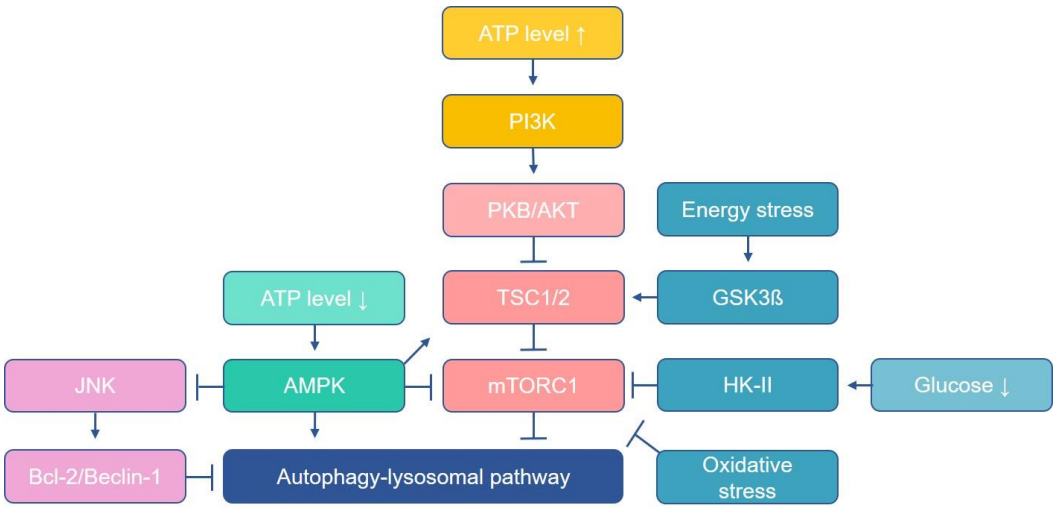

Figure 2: Regulation of the ALP by signalling pathways in the heart. mTORC1 and AMPK mainly regulate ALP activity. mTORC1 can either be activated under nutrient-rich conditions by PI3K signalling or inactivated in case of starvation (via AMPK), glucose depletion (via HK-II), energy stress (via GSK3ß) or oxidative stress (Cys1483 oxidation). During starvation, AMPK is activated and activates the ALP by directly inhibiting mTORC1 or indirectly by binding to TSC1/2. Further, AMPK inhibits JNK that normally promotes Bcl-2/Beclin-1 and thus blocks the ALP.

Another major part of the ALP regulation is performed by post-translational modifications (PTMs), for instance phosphorylation, ubiquitination (‘the’ degradation marker) or acetylation. Modification of proteins by phosphorylation is central in the overall ALP. An example is the phosphorylation of LC3-II at Ser12 preventing its recruitment to the autophagosome. Ubiquitination is important for the recognition of cellular waste. Ubiquitinated proteins are recognized by p62 and NBR1 and subsequently shuttled to the autophagosomes for its degradation. An example for acetylation as part of the ALP is acetylated tubulin that has been shown to interact with histone deacetylase 6 (HDAC6). Subsequently, HDAC6 mediates the transport of protein aggregates towards autophagosomes (McEwan and Dikic 2011).

In non-cardiomyocytes, a strong, reciprocal interplay of mTORC1 and lysosomes has been shown (Figure 3), which can be assumed to also be of importance in cardiomyocytes.

mTORC1 actively regulates the transcription of ATG and lysosomal genes by phosphorylating and thus inhibiting the transcription factor EB (TFEB). Further, active mTORC1 is located on peripheral lysosomes. Here it binds and inhibits the ATP-sensitive Na^+-channel that is part of the lysosomal membrane. However, once mTORC1 is inactivated, it disembarks from the lysosomes, inducing the opening of the ATP-sensitive Na^+-channel. This process is modulated by lysosomes that can sense the level of amino acids within its lumen through the interaction of the V-ATPase with Ragulator. Ragulator anchors Rag guanosine triphosphatases (GTPases) to the lysosomal membrane that in turn translocate active mTORC1 towards the lysosomal membrane. If starvation persists for a longer period, mTORC1 can be re-activated to enable autophagic-lysosomal reformation (Puertollano 2014; Lawrence and Zoncu 2019).

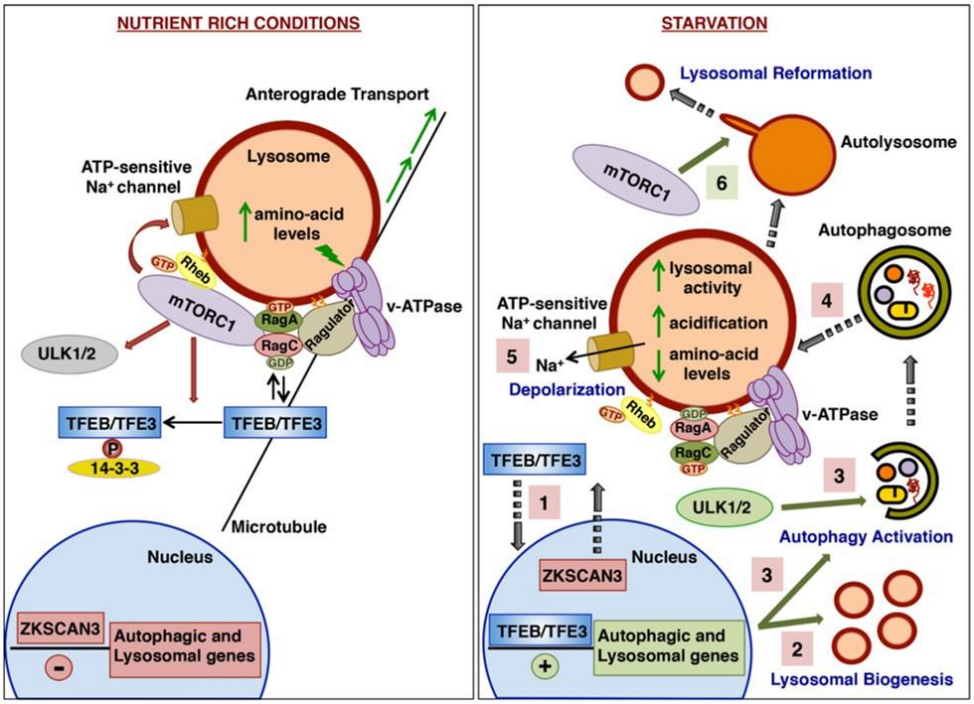

Figure 3: A strong, reciprocal interconnection between mTORC1 and lysosomes as part of the ALP regulation. Active mTORC1 inhibits ALP activation under nutrient-rich conditions (see left part). Therefore, mTORC1 inhibits ULK1/2, TFEB and the Na^+-channel. Concurrently, lysosomes are transported towards cell periphery. In contrast, during starvation, mTORC1 is inactivated and thus TFEB translocates into the nucleus (1), autophagic and lysosomal genes are transcribed (2), the ALP is activated (3) and the Na^+-channel opens (5; see right part). Prolonged starvation periods induce mTORC1 re-activation to induce autophagic-lysosomal reformation (6; Puertollano 2014). RHEB = Ras homolog enriched in brain; TFE3 = Transcription factor binding to IGHM enhancer 3; ZKSCAN3 = Zinc finger with KRAB and SCAN domains 3. Figure was taken from Puertollano 2014.

1.1.3. The role of the ALP in cardiac disease

The heart represents an organ with high energy demand but low regenerative potential. Thus, the heart is highly depending on autophagy as part of the protein quality control machinery, especially during disease. Here, it prevents the accumulation of toxic protein aggregates (Tannous et al. 2008; Sandri and Robbins 2014). Nonetheless, only a few human inherited cardiomyopathies have been shown to be associated with defective autophagy so far. The reported cases always show a mutation in a protein that plays a crucial role within the ALP/autophagy. The first example is Danon disease, an X-linked disorder that is clinically characterized by a mild retardation, skeletal myopathy and cardiac hypertrophy. On a molecular basis, characteristics are LAMP-2 deficiency and accumulation of autophagosomes due to an impaired autophagosome-lysosome fusion (Nishino et al. 2000; Hashem et al. 2015). Another example is the rare, multi-systemic disorder Vici syndrome, which is also associated with defective autophagy and cardiomyopathy. In this case, recessive mutations have been identified in the ectopic P-granules autophagy protein 5 (*EPG5*), which in turn plays a crucial role in autophagosome maturation and autophagosome-lysosome fusion (Cullup et al. 2013; Balasubramaniam et al. 2017). The last example is a patient with left ventricular non-compaction (LVNC) and recessive dilated cardiomyopathy (DCM), who carries a mutation in pleckstrin homology domain containing, family M member 2 (*PLEKHM2*), a protein that is important for endosome localization. Not surprisingly, an impaired autophagic flux was detected in the primary fibroblasts of the patient (Muhammad et al. 2015). The role of the ALP in the pathogenesis of hypertrophic cardiomyopathy (HCM) is still not fully understood, although it represents the most common inherited cardiomyopathy. In septal myectomies of HCM patients carrying either a cardiac myosin-binding protein C (*MYBPC3*) or beta-myosin heavy chain (*MYH7*) mutation, an increased number of autophagosomes and higher protein levels of LC3-II and Beclin-1 were detected (Song et al. 2014). Our group showed higher protein levels of LC3-II but unchanged protein levels of Beclin-1 and p62 in septal myectomies of HCM patients carrying *MYBPC3* in comparison to non-failing samples (Singh et al. 2017). Furthermore, we showed impaired autophagic flux in an HCM mouse model carrying a homozygous *Mybpc3* mutation that was ameliorated by autophagy activation (Singh et al. 2017). These findings indicate a crucial role of the ALP in the pathogenesis of HCM, but to conclude whether the ALP is activated or impaired in the human heart, the evaluation of the autophagic flux in hiPSC-CMs is needed. This should be performed in combination with gene and protein expression analysis for the correct interpretation of the role of the ALP in the human heart (Dorsch et al. 2019; Zech et al. 2019).

1.2. Human inherited cardiomyopathies

Human inherited cardiomyopathies represent quite a heterogenous group of diseases of the myocardium that are associated with mechanical and/or electrical dysfunction of the heart. Further characteristics are either a ventricular hypertrophy or dilatation. Symptoms vary from none to fatigue or chest pain to heart failure (Maron et al. 2006). The two most common forms of human inherited cardiomyopathies are HCM and DCM. HCM is mainly characterized by a thickened left ventricle and septum due to increased cardiomyocyte size (Figure 4, middle; Maron et al. 2006).

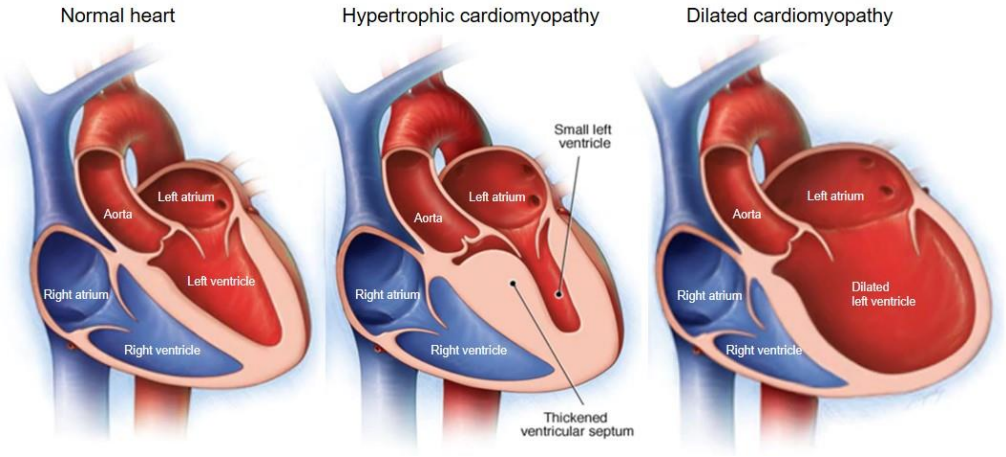

Figure 4: Representation of a hypertrophic and a dilated heart in comparison to a normal heart. Shown is a normal heart (left), an HCM heart (middle) and a DCM heart (right) with the different regions of the heart indicated. The thickening of the left ventricle and septum found in a HCM heart is depicted in the middle. An enlarged left ventricle, a hallmark of a DCM heart, is represented on the right. Adapted figure taken from the Mayo clinic website.

Further characteristics of HCM are myocardial disarray, increased interstitial fibrosis and diastolic dysfunction. Although HCM is rather common with an estimated prevalence of 1:200 to 1:500 in the general population, independent of sex, ethnicity or geographic origin, a substantial portion of mutation carriers do not show any symptoms (Maron et al. 2014; Semsarian et al. 2015). However, women suffering from HCM have an overall worse survival (Geske et al. 2017). HCM can be clinically present at any age and is the most common cause of sudden cardiac death in young athletes. Moreover, HCM accounts for 36% of cases of sudden cardiac death of cardiac etiology (Goff and Calkins 2019). Effective treatments, such as implantable cardioverter-defibrillators (ICDs), surgical septal myectomies or heart transplantation, are available and have lowered the HCM-related mortality rate to <1%/year (Maron et al. 2014). HCM is an autosomal-dominant inherited disease and is caused by mutations in mainly 11 genes encoding sarcomeric proteins, whereby *MYBPC3* and *MYH7* account over 50% of all mutations (Marian and Braunwald 2017). Most mutations are

heterozygous and thus, disease onset appears to depend on the amount of mutant protein. HCM is considered as a sarcomeropathy since more than 1400 mutations in genes encoding sarcomeric proteins were identified (van der Velden and Stienen 2019). Although, solely ~50% of HCM cases are associated with a likely pathogenic or pathogenic mutation and thus inherited (Goff and Calkins 2019). Nonetheless, the vast number of identified mutations and the diverse clinical manifestation indicate that HCM is a very unpredictable, heterogenous and complex disease (van der Velden and Stienen 2019).

DCM is mainly characterized by systolic dysfunction and an enlarged heart with thinned walls, due to hyperplasia of the left ventricle (Figure 4, right part). Patients suffering from DCM commonly progress to heart failure, either due to pump failure (~70%) or sudden cardiac death (~30%; Schultheiss et al. 2019). Hence, it is not surprising that DCM is the most common cause of heart transplantation (Maron et al. 2006). The estimated prevalence of DCM in the general population is still under investigation. Estimations vary from 1:250 to 1:2700, whereby, similar to HCM, a vast discrepancy is found between the frequencies of variants that are supposed to be disease-causing or mutations associated with DCM and incidence/clinical data of DCM. Furthermore, some studies indicated that the prevalence of DCM seems to vary according to sex or ethnicity (McNally and Mestroni 2017; Halliday et al. 2018) but large, multi-ethnic studies with patients varying in age and sex are needed to conclude on this. Interestingly, black people have an almost 3-fold higher risk for developing DCM and an 1.5 to 2-fold higher risk for dying of DCM (Bozkurt et al. 2016). Furthermore, women suffering from DCM seem to have an overall better survival (Halliday et al. 2018) in contrast to women suffering from HCM (see above; Geske et al. 2017). Nonetheless, DCM can occur at all ages but is mostly present in individuals aged 20 to 50 years (Schultheiss et al. 2019). The current therapeutic options for DCM comprise angiotensin-converting enzymes (ACE) inhibitors, ß-blockers, cardiac resynchronization therapy (CRT) alone in form of a pacemaker or in combination with an ICD, and heart transplantation (Bozkurt et al. 2016; Schultheiss et al. 2019). DCM can either be acquired, inherited or idiopathic, whereby acquired forms result from different causes, such as (viral) infections, toxins or allergens, pregnancy, systemic endocrine or autoimmune disease (Maron et al. 2006; Bozkurt et al. 2016; McNally and Mestroni 2017; Schultheiss et al. 2019). In case of idiopathic DCM, the underlying cause has not been identified yet. About 20 to 35% of DCM cases are reported as inherited, whereby mutations were identified in several sarcomeric genes as well as in genes encoding Z-disk proteins, calcium- or potassium channels, the nuclear envelope, heat-shock chaperones and mitochondrial proteins (Bozkurt et al. 2016; McNally and Mestroni 2017; Schultheiss et al. 2019). To date, mutations in >50 different genes have been associated with DCM. Most of these mutations are inherited in an autosomal-dominant pattern with variable expression and penetrance (Braunwald 2017). However, also autosomal-recessive and X-linked inheritance

has been described. The most common mutations are truncating mutations of titin (*TTN*) that account for ~25% of inherited DCM (Herman et al. 2012). Other mutations have been identified in lamin A/C (*LMNA*), *MYH7* and phospholamban (*PLN*; McNally and Mestroni 2017). Altogether, DCM is less well studied than HCM but seems to be even more complex. Not only is the clinical manifestation very heterogenous but also a genetically heterogeneity is established in DCM. Furthermore, most DCM-associated mutations are very rare and the disease progression of DCM varies a lot (Braunwald 2017; Schultheiss et al. 2019).

1.3. Cardiac myosin-binding protein C

The cardiac myosin-binding protein C (cMyBP-C) is encoded by the *MYBPC3* gene, which is the most commonly mutated genes in HCM (see above; Braunwald 2017). *MYBPC3* is composed of 35 exons that build up to a 21 kbp gene (see Figure 5). Further, *MYBPC3* encodes a 150 kDa protein, which in turn consists of eight immunoglobulin-like and three fibronectin-like domains (Carrier et al. 1997).

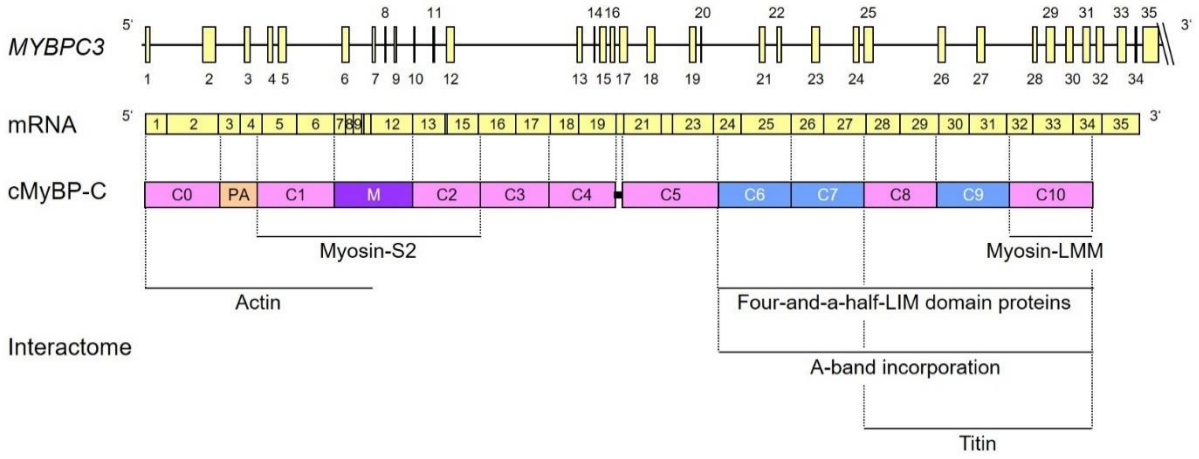

Figure 5: Schematic depiction of the *MYBPC3* gene, its mRNA and protein structure. A total of 35 exons (yellow boxes) are stretched along the 21 kbp genomic sequence. The gene is transcribed into a 3824 bp mRNA-transcript, which in turn is translated into a 1274-amino-acid protein consisting of eight immunoglobulin-like (C0, C1, C2, C3, C4, C5, C8 and C10; in pink) and three fibronectin-type III (C6, C7 and C9; in blue) domains. A proline-alanine rich domain (PA) is located between C0 and C1. A linker region is found between C4 and C5. A cardiac specific region is the M-motif (purple), next to the C0 domain and a 28-amino-acid insertion in the C5 domain. Incorporation of cMyBP-C within the A-band is mediated by the C6-10 domains. Below the interactome of cMyBP-C is visualized. The C0-M region interacts with F-actin, C1-M-C2 with the myosin-S2 domain. The C-terminus of cMyBP-C mediates the interaction with four-and-a-half-LIM domain proteins (C6-10), titin (C8-10) and Myosin-LMM (light meromyosin; C10). Based on Carrier et al. 2015 and UniProt website (Q14896).

In mammals, *MYBPC3* is exclusively expressed in the heart, whereas two other two isoforms, *MYBPC1* and *MYBPC2*, are expressed in the skeletal muscle (Fougerousse et al. 1998). Three unique features distinguish cMyBP-C from the slow (*MYBPC1)* and fast skeletal (*MYBPC2)* isoforms: the N-terminal C0 domain, the MyBP-C motif (M-motif) with four additional phosphorylation sites and 28 additional amino acids (AAs) within the C5 domain (Gautel et al. 1995; Carrier et al. 1997, 2015).

1.3.1. cMyBP-C as part of the sarcomere

cMyBP-C is an important structural protein of the sarcomere, the smallest contractile unit of a cardiomyocyte. The sarcomere is composed of a variety of proteins, and its main task is to facilitate contraction and relaxation. Repeated units of sarcomeres build up to myofilaments that are either thin or thick, which in turn bundle to myofibrils. The border between two sarcomeres is called Z-disc or Z-line and is between 1.6 µm (i.e. contraction) and 2.4 µm (i.e. relaxation; Sadayappan and de Tombe 2014). Thin myofilaments are mainly composed of actin (α-cardiac actin), next to α-tropomyosin and a cardiac troponin complex that in turn consists of cardiac troponin T (cTnT), cardiac troponin I (cTnI) and cardiac troponin C (cTnC). Thick filaments comprise myosin (α and β myosin heavy chain, essential myosin light chain and regulatory myosin light chain), cMyBP-C and titin, whereby titin anchors the thick filament to the Z-disk/line. cMyBP-C forms transverse stripes within the sarcomere that are 43 nm apart and located within the cross-bridge bearing region of actin and myosin (Figure 6; Schlossarek et al. 2011).

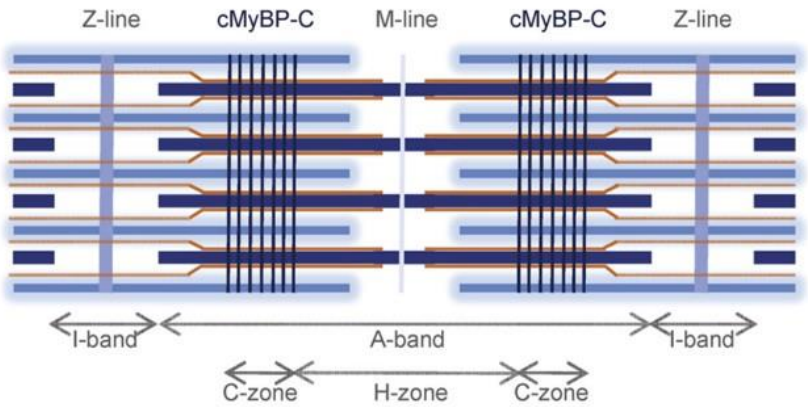

Figure 6: Schematic image of the localization of cMyBP-C within the sarcomere. cMyBP-C is transversally positioned within the C-zones of the A-bands. Two sarcomeres are connected at the M-line that is located in the H-zone of the A-band. The Z-line is found in the I-band and marks the border of two sarcomeres. Thin myofilaments (light blue) are the major component of the I-band, whereas thick myofilaments (middle blue) are found in the A-band and extend to the I-band. Titin is visualized in orange. Adapted from Carrier et al. 2015.

However, the exact organization of cMyBP-C within the sarcomere and its interaction with myosin is still under discussion. At present, there are two structural models: the trimeric collar model (Flashman et al. 2004, 2008) and the strut model (Squire et al. 2003; Schlossarek et al. 2011). The trimeric collar model proposes that three cMyBP-C molecules form a collar-like structure by interacting at the C5-C10 domains and then wrap around a myosin filament (Flashman et al. 2008). In contrast, the strut model suggests the interaction of the C-terminus of cMyBP-C that is bound to a thick filament, with the N-terminus of cMyBP-C that is bound to a thin filament (Squire et al. 2003). cMyBP-C is thought to interact with myosin via its rod region (Lange et al. 2013). Further, cMyBP-C interacts with several sarcomeric proteins as visualized in Figure 5, for instance actin or titin. Due to its location and interaction within the sarcomere, cMyBP-C plays a crucial role in sarcomere organization (Schlossarek et al. 2011).

1.3.2. Regulation of cardiac function by cMyBP-C

To enable cardiac muscle contraction, actin and myosin interact by forming a cross-bridge within the sarcomere that in turn leads to sarcomere shortening and thus force development. This force or electrical excitation of a single cardiomyocyte is then ‘transferred’ to the whole myocardium to enable contraction of the whole heart (Bers 2002; Eschenhagen 2010). Hereby, Ca^{2+} plays a crucial role. During the cardiac action potential (AP), the cell membrane of a cardiomyocyte is depolarized and subsequently Ca^{2+} enters the cell via L-type Ca^{2+} channels (i.e. inward Ca^{2+} current (ICa)), which in turn triggers the Ca^{2+} release from the sarcoplasmic reticulum (SR) via the ryanodine receptors (RyRs) and thus raises the amount of free intracellular Ca^{2+} further (see Figure 7).

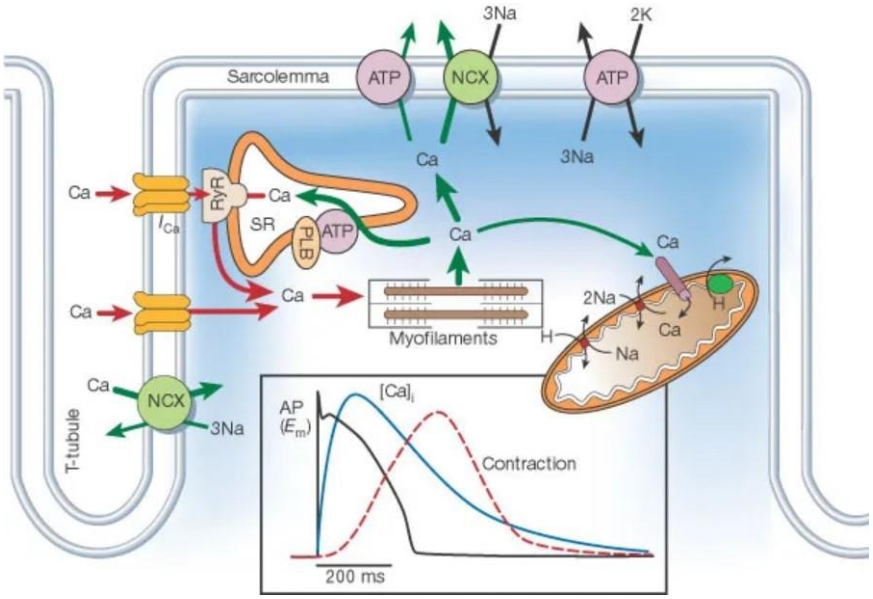

Figure 7: Ca^{2+} influx and outflux in ventricular cardiomyocytes as part of excitation-contraction coupling. Ca^{2+} influx is indicated by red arrows and initiates the contraction. Ca^{2+}

outflux into the cytosol or influx into the mitochondria is indicated by green arrows resulting in relaxation due to decreasing Ca^{2+} -levels. A time course of a typical action-potential (black line) is shown at the bottom, whereby the Ca^{2+} transient (blue line) and the contraction (dotted red line) itself were measured in a rabbit ventricular myocyte. ATP = ATPase; E_m = Membrane potential of sarcolemma; PLB = Phospholamban (Bers 2002).

The free intracellular Ca^{2+} then binds to cTnC, which in turn binds to cTnI. This allows cTnT and tropomyosin to move to the cleft of actin and myosin is thus able to form a cross-bridge with actin, a process that is ATP-driven. In the two heads of each myosin, ATPases are localized that hydrolyse ATP and thus facilitate the interaction with actin. For relaxation of the cardiomyocyte, the intracellular Ca^{2+} concentration has to decrease. Therefore, Ca^{2+} is actively transported into the SR via the SR Ca^{2+} ATPase (SERCA) and out of the cell via the sodium-calcium exchanger (NCX). In addition, intracellular Ca^{2+} can be transported out of the cytosol via the mitochondrial Ca^{2+}-uniport or the sarcolemma Ca^{2+}-ATPase. Due to the lower intracellular Ca^{2+} levels, cTnT and tropomyosin move back to the cTnI and thus actin and myosin cannot form cross-bridges any longer. The cross-bridge formation can be modulated by proteins of the thin and the thick myofilaments, such as cMyBP-C. Due to its localization within the cross-bridge bearing region, cMyBP-C determines the force and speed of the contraction via phosphorylation (Schlossarek et al. 2011) and is required for complete relaxation of the sarcomere (Bers 2002; Pohlmann et al. 2007; Eschenhagen 2010). Thus, cMyBP-C is crucial for normal cardiac function and its alteration can have detrimental effects on the heart, as observed in the pathogenesis of HCM.

1.3.3. cMyBP-C in HCM

To date, about 350 individual *MYBPC3* mutations have been identified in HCM (Carrier et al. 2015), accounting for ~35% of all HCM mutations. In several populations, *MYBPC3* founder mutations have been identified, such as the c.772G>A mutation found in Tuscany, Italy (Olivotto et al. 2008; Vignier et al. 2009). In general, *MYBPC3* mutations are associated with a delayed onset, a lower penetrance, a lower degree of hypertrophy, and an overall better survival. However, a few *MYBPC3* mutations have been associated with progressive heart failure, stroke and sudden cardiac death (Schlossarek et al. 2011). The majority of the *MYBPC3* mutations introduce a frameshift that leads to a premature termination codon (PTC) and subsequently, a truncated form of cMyBP-C. Hereby, the C-terminus of cMyBP-C is affected and thus the major myosin and/or titin-binding sites are missing (Behrens-Gawlik et al. 2014). Normally, you would expect that the truncated protein is incorporated into the sarcomere where it alters the function and thus acts as a ‘poison peptide’. However, this does not seem to be the case for HCM patients carrying a *MYBPC3* mutation. To date, truncated forms of cMyBP-C were not detected by immunoblotting in myocardial samples, implying the

degradation of the truncated protein (Marston et al. 2009; van Dijk et al. 2009). Since most of the *MYBPC3* mutations in HCM are heterozygous, the absence of truncated cMyBP-C should result in an 'disease-causing' haploinsufficiency (Marston et al. 2009; van Dijk et al. 2009). Despite this knowledge, it is still not fully understood how mutations in the *MYBPC3* gene cause HCM on a molecular level.

1.4. Human induced pluripotent stem cells

To better understand the pathogenesis and pathophysiology of inherited cardiac diseases, human *in vitro* disease models are needed. Human myocardial tissue samples are an important and precious tool within cardiac research field that provide fundamental knowledge, but they are very limited in availability, in quantity and in applicability. To date, animal models are widely used in cardiac research, such as mice and rats (for instance Singh et al. 2017; Krause et al. 2018) that contributed enormously to our understanding of the pathogenesis and pathophysiology of human inherited cardiac disease. However, there is a considerable discrepancy between the murine and human cardiac system and thus *in vivo* findings are not directly transferable. Already in 1998, a human embryonic stem cell (hESC) cell line was generated from human blastocysts, laying the groundwork of human *in vitro* stem cell research (Thomson et al. 1998). HESCs have the capacity for unlimited self-renewal and are pluripotent cells that are able to differentiate into every cell type of the three germ layers (Figure 8).

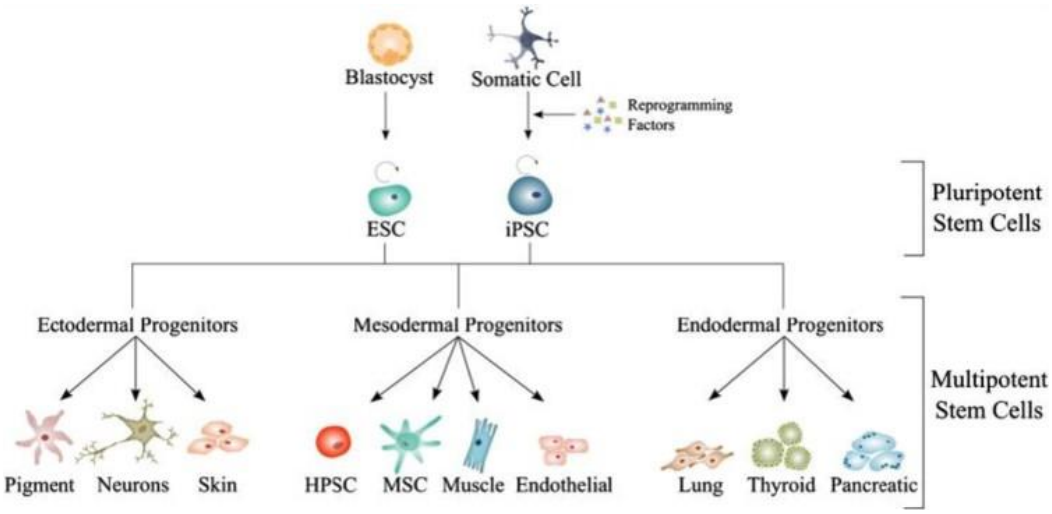

Figure 8: Differentiation potential of ESCs and iPSCs. ESCs and iPSCs are both pluripotent but they differ in their origin. ESCs are part of the inner cell mass of a blastocyst, whereas iPSCs are gained via reprogramming of somatic cells. However, both are able to differentiate into all cell types of the three germ layers (ectoderm, mesoderm and endoderm). Adapted from Kaebisch et al. 2015.

Therefore, hESCs represent an enormous potential for research and medicine but international regulations for hESC experiments are very strict due to the ethically questionable extraction

method of hESCs out of the inner cell mass of human embryos that are ‘left-overs’ from fertility treatments. The ‘real’ breakthrough of stem cell research occurred in 2006 with the generation of mouse induced-pluripotent stem cells (iPSC) from embryonic and adult mouse fibroblasts. The fibroblasts were reprogrammed solely by adding four transcription factors Klf4, c-myc, Oct4 and Sox2 (Takahashi and Yamanaka 2006). The obtained mouse iPSCs possessed the same self-renewal and pluripotency capacity as hESCs and thus were able to differentiate into all cell types of the three germ layers (see Figure 8). Only one year later, a protocol for the generation of human induced-pluripotent stem cells (hiPSCs) from human dermal fibroblasts was published (Takahashi et al. 2007). In the last decade, hiPSC research rapidly grew and the overall procedure was substantially improved. Today, the generation of hiPSCs of all kind of human cell types is established, for instance from peripheral blood cells (Kim et al. 2016; Okumura et al. 2019). Moreover, the reprogramming was further evolved, by stepping away from retroviral transduction with the disadvantage of integration and constitutive expression of the reprogramming factors, towards a non-integrative reprogramming with Sendai-virus (Schlaeger et al. 2015). HiPSCs enable *in vitro* research on post-mitotic cell types such as cardiomyocytes or neurons, since efficient differentiation protocols have been established (Karumbayaram et al. 2009; Breckwoldt et al. 2017). In spite of representing this powerful human *in vitro* tool, researchers encounter problems, such as clone-to-clone variations or batch-to-batch differences (Musunuru et al. 2018). Further, it has been shown that one hiPSC clone that possesses a growth advantage, is able to overgrow the whole culture within a few weeks (Brenière-Letuffe et al. 2018). This is particularly problematic in the context of karyotypic abnormalities that hiPSCs are prone to acquire with increasing passage number (Taapken et al. 2011), or somatic mutations that hiPSCs are known to acquire during and after reprogramming in culture (Gore et al. 2011). Although hiPSC generation and cultivation are still vulnerable and require thorough optimization, hiPSCs are a powerful and versatile human *in vitro* tool.

1.5. Human induced-pluripotent stem cell-derived cardiomyocytes

Due to the unlimited self-renewal, pluripotency and the absence of ethical concerns, hiPSCs are the eligible tool to access cell types with a low regenerative potential, such as cardiomyocytes. Since the discovery of hiPSCs in 2007, a lot of effort was made to develop cardiac differentiation protocols. Hereby, the underlying molecular mechanisms of the participating signalling pathways during mammalian embryological heart development are mimicked. Therefore, hiPSCs are either cultured as a monolayer or within a suspension by forming cell aggregates, so-called embryoid bodies (EB; Breckwoldt et al. 2017; Palpant et al. 2017). Either way, stage-specific application of growth factors in defined media is used to first induce mesodermal lineage and subsequently the cardiac specification to generate hiPSC-

derived cardiomyocytes (hiPSC-CMs; Mummery et al. 2012). The application possibilities are versatile since hiPSC-CMs can be generated indefinitely, functionally characterized *in vitro* and possess the genome of the donor. Furthermore, hiPSCs can be generated from every human being, healthy or diseased, and subsequently differentiated into cardiomyocytes. Thus, it is feasible to study human inherited cardiac diseases *in vitro*, termed disease modelling. This can be combined with the targeted genetic modification of a gene locus of interest to either introduce or remove a mutation on hiPSC level (Hinson et al. 2015; Mosqueira et al. 2018). Although effective disease modelling with (gene-edited) hiPSC-CMs has been shown, the data differs strongly. For instance, the parameter cell size differs greatly, as in the actually size as also the extend of the increase between studies and HCM or DCM hiPSC-CMs. Thus, there is a great need for quantitative comparisons and robust, high content assay (Eschenhagen and Carrier 2018). Nonetheless, disease modelling with (gene-edited) hiPSC-CMs seems to be the tool of choice to ultimately develop novel therapeutic approaches (Figure 9; Eschenhagen et al. 2015; Musunuru et al. 2018; Prondzynski et al. 2019).

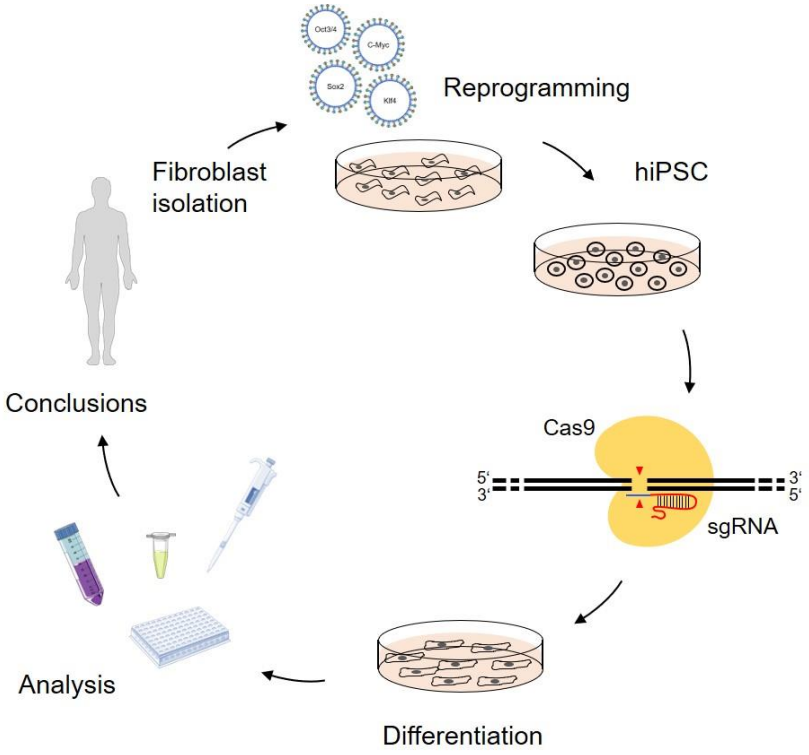

Figure 9: Applications of hiPSCs in biomedical research. By taking a skin biopsy of a patient, fibroblasts can be isolated and subsequently reprogrammed into patient-specific hiPSCs with four transcription factors (Takahashi et al. 2007). Either these patient-specific hiPSCs are directly differentiated into the cell type of interest, in our case cardiomyocytes, or are gene-edited, e.g. by CRISPR/Cas9, to either repair a disease-causing mutation in diseased hiPSCs or to introduce a disease-causing mutation in hiPSCs of a healthy individual. The whole

procedure aims to study the disease in a human *in vitro* model to develop therapeutic approaches on the long run.

1.6. CRISPR/Cas9-based genome editing

Genome editing is an important and versatile tool in basic, biomedical and biotechnological research that enables the precise and targeted alteration of the gene locus of interest. In the last 15 years, a number of genome editing technologies have emerged, such as zinc finger nucleases (ZFNs; Urnov et al. 2005; Miller et al. 2007) and transcription activator-like effector nucleases (TALENs; Hockemeyer et al. 2011). Either way, an endonuclease catalytic domain is tethered to a DNA-binding protein to introduce a targeted DNA double-strand break (DSB) at the investigated genomic loci. Subsequently, the cell's DNA repair-machinery is used for site-specific alteration (Ran et al. 2013). ZFNs are a combination of the cleavage domain of *Fok1* and a designed zinc-finger protein. It was shown that ZFNs can be used to precisely edit site-specific sequences or to integrate whole genes (Urnov et al. 2005; Miller et al. 2007; Moehle et al. 2007). The DNA binding domain of TALENs consists of multiple units of ~34 AAs (TALE repeats) that are nearly identical (only two AAs difference) and are arranged in tandems. For each gene editing approach, the DNA binding domain is specific and tethered to a nuclease, enabling site-specific alteration with TALENs (Hockemeyer et al. 2011). However, the 'real' breakthrough in genome editing was the discovery of the clustered regularly interspaced short palindromic repeats (CRISPR)/CRISPR-associated (Cas) system as part of the adaptive immune system in bacteria and archaea. In short, the host specifically incorporates short sequences (20 bp 'protospacer') from the invader (virus or plasmid) into the CRISPR gene locus. Upon transcription and processing, small crRNAs (CRISPR RNAs) are formed that guide a multifunctional Cas-protein complex, containing the Cas9 nuclease, to the anew incoming foreign genetic elements, which subsequently performs cleavage. The Cas9 nuclease expression cassette as well as the trans-activating crRNA (tracrRNA) are part of the CRISPR gene locus. A DSB is solely introduced by the Cas9 nuclease if a protospacer-adjacent motif (PAM) is present at the 3'-end of the 20 bp protospacer. Hereby, the self-targeting of the CRISPR locus by the Cas-protein complex is prevented. To further clarify, the CRISPR/Cas system in *Streptococcus thermophilus*, which is relatively simple and well-studied, is displayed in Figure 10 (Bhaya et al. 2011).

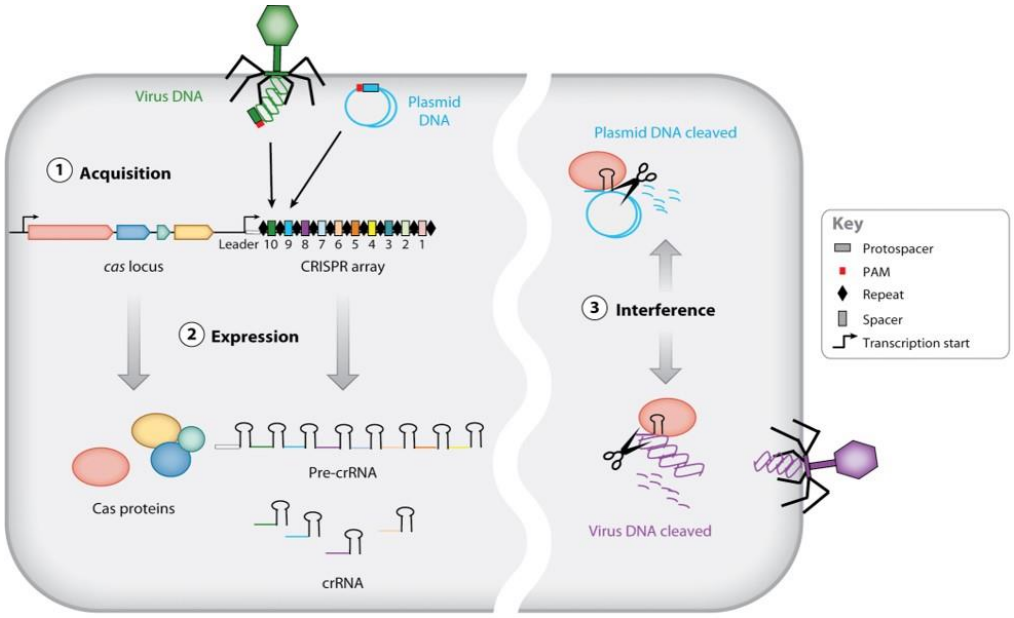

Figure 10: CRISPR/Cas as part of the bacterial adaptive immune system. The CRISPR/Cas system found in *Streptococcus thermophilus* is shown exemplarily to illustrate the overall mechanism. First, the CRISPR spacer acquisition takes places whereby double-stranded DNA fragments or protospacer containing a PAM from a virus or plasmid are introduced into the leader end of a CRISPR array within the host DNA (1). The Cas locus encodes Cas1 and Cas2 and is located close to the CRISPR array that contains the unique spacers (coloured boxes) that in turn are interspaced by repeats (Black diamond). Next, pre-CRISPR RNA (pre-crRNA) and Cas proteins are produced (2). After transcription, the pre-crRNA is subsequently cleaved into crRNA by the Cas proteins. The crRNA solely contains a single spacer (coloured spacer) and a partial repeat (hairpin). The actual CRISPR interference can take place immediately or later on (3). Hence, foreign nucleic acid of great resemblance with a spacer of a crRNA is cleaved by Cas proteins, preventing virus replication or plasmid activity. Adapted from Bhaya et al. 2011.

Scientists all over the world apply the CRISPR/Cas system to specifically alter sequences in the human genome. Hereby, the most widely used CRISPR/Cas9 system is from *Streptococcus pyogenes* that introduces a DSB 3 bps upstream of a 5'-NGG-3' PAM sequence. However, the CRISPR/Cas9 system of *Streptococcus pyogenes* had to be adapted for efficient editing of the human genome. Therefore, the crRNA and tracrRNA were combined into a single-guide RNA (sgRNA) and encoded by a plasmid that already contained a human codon-optimized Cas9, as well as a selection marker, e.g. GFP. This plasmid is then introduced into the target cells either by transfection, nucleofection or viral transfer (Ran et al. 2013). In the cells, the Cas9 and sgRNA are expressed and a DSB is introduced at the target site, which is fixed by the cell's DNA repair machinery. Consequently, a random or specific mutation is introduced at the targeted genomic locus. The DNA repair machinery consists of

two major pathways: the non-homologous end joining (NHEJ) and homology-directed repair (HDR; Figure 11). Hereby, the NHEJ leads to a random alteration of the target site due to its mode of action. In NHEJ the two ends of the DSB are just re-joined which often results in the random addition or removal of a few bases, so-called insertion-deletion (indel) mutations. This approach is used by scientists that want to introduce a frameshift and subsequent PTC, resulting in a KO of the gene of interest. However, if a precise and defined genome editing is intended, HDR is needed. Hereby, a 'repair'/'mutation' template is introduced into the cells, either in form of double-stranded DNA (dsDNA) or as single-stranded oligonucleotides (ssODNs) with homology arms flanking the targeted sequence. When designing a CRIPSR/Cas9 genome editing approach, it has to be kept in mind that the HDR is only active in dividing cells. Furthermore, the efficiency of HDR varies a lot with the cell type, cell state, the genomic locus and the repair template (Ran et al. 2013).

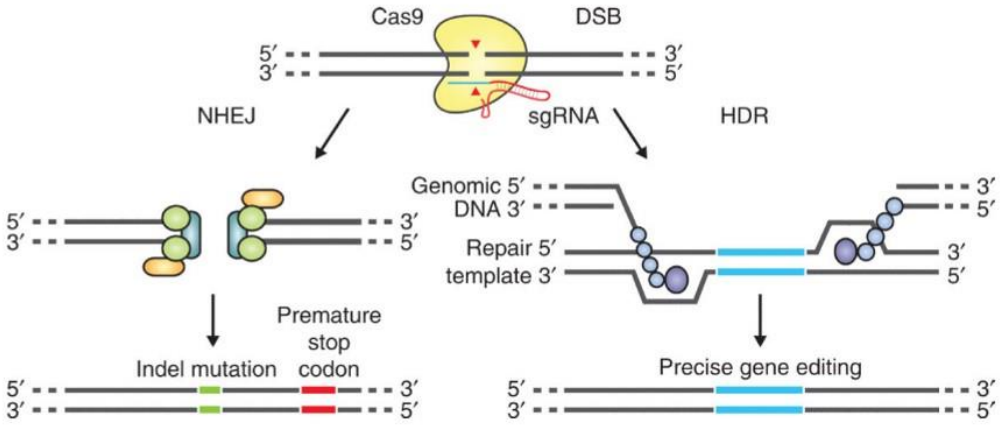

Figure 11: CRISPR/Cas9 gene editing introduces a DSB and thus repair either via NHEJ or HDR. The Cas9 (yellow) introduces a DSB and thus activates the endogenous DNA repair either via NHEJ or HDR. NHEJ performs a random repair by processing and re-joining the site of DSB, thereby introducing indel mutations and consequently a frameshift and a subsequent PTC in gene coding regions. A more precise DNA repair is feasible with HDR that uses a repair template in form of a plasmid or ssODN to accurately gene edit the site of junction (Ran et al. 2013).

Unsurprisingly, CRISPR/Cas9 quickly replaced ZFNs and TALENs after its discovery as the genome editing technique of choice. The overall approach of ZFNs, TALENs and CRISPR/Cas9 is quite similar, since all three approaches introduce a targeted DSB which is then repaired by the cell's DNA repair machinery. However, CRISPR/Cas9 is very easy to design, easily executed, has a high target efficiency and can easily be adapted to new targets by just ordering new oligos encoding the 20-nucleotide guide sequence. Further, CRISPR/Cas9 is also suited for high-throughput and multiplexed gene editing. Nonetheless, the CRISPR/Cas9 system also has a few limitations, such as the requirement of the NGG-

PAM at the targeted locus or dreaded off-target events. However, the NGG-PAM sequence is found on average every 8 – 12 bp in the human genome and thus it is quite likely to find a suitable sgRNA. An off-target event represents an introduction of a DSB and thus an indel mutation at an unwanted site within the genome that possesses a high sequence-similarity to the designed sgRNA. To minimize the probability of off-target events and also to simplify the overall design, several online prediction tools for CRISPR/Cas9 are available (e.g. http://crispr.mit.edu/). These websites give a list of all suitable sgRNAs for the region of interest that are scored according to similarity to other genomic loci within the human genome and the number of putative off-target sites. Furthermore, a list of the putative off-target sites sorted by likelihood is provided. Even though the CRISPR/Cas9 system has only been used for a couple of years in labs all over the world, many papers have been published and also the system itself has been refined (e.g. high fidelity Cas9; Kleinstiver et al. 2016).

In the cardiac research field, several studies have been published showing the functional characterisation and *in vitro* analysis of gene-edited hiPSC-CMs (Hinson et al. 2015; Mosqueira et al. 2018). In one case, even the translation to affected patients was possible and has led to the adjustment of their treatment (Prondzynski et al. 2019). Hence, (gene-edited) hiPSC-CMs are a suitable tool to not only study human inherited cardiomyopathies *in vitro* but also to ultimately develop novel therapeutic approaches (Eschenhagen and Carrier 2018).

2. Aim of study

The ALP is one of the two major proteolytic systems within cells that is crucial for cellular homeostasis and of special importance for cardiomyocytes as they represent a post-mitotic cell type. HCM and DCM are the two most common inherited cardiomyopathies and *MYBPC3* is the most frequently mutated gene in HCM. However, it is still unknown how (defective) autophagy and/or mutations in *MYBPC3* contribute to the pathogenesis of HCM and DCM. Thus, this thesis aimed to decipher the putative interplay of the ALP and cMyBP-C on disease progression of human inherited cardiomyopathies to finally unravel novel therapeutic options.

Therefore, the first aim of this thesis was to evaluate the putative alteration of the ALP in cardiac tissue samples of HCM and DCM patients on protein and gene expression level and further evaluate the biological activity of autophagy (=autophagic flux) on protein level in hiPSC-CMs derived from an HCM and a DCM patient.

The second aim of this study was to generate a human cellular model of HCM that is deficient in cMyBP-C. Therefore, hiPSCs from a healthy individual were gene-edited via CRISPR/Cas9 and subsequently, the genetic modification validated, the hiPSCs differentiated into beating CMs and characterized in 2D culture to validate their suitability as an *in vitro* model of HCM.

3. Material & Methods

The here used materials, chemicals, reagents and devices are described in detail in the appendix (Chapter 9).

3.1. Cell Culture

3.1.1. Cell culture media

All used cell culture media are listed in Table 1.

Table 1: Listing and composition of cell culture media.

Media	**Composition**
2D culture medium	DMEM 1% (v/v) Penicillin/streptomycin 10% (v/v) Horse serum 10 µg/mL Human recombinant insulin 33 µg/mL Aprotinin
CoM	DMEM/F-12 without glutamine 1% (v/v) Non-essential amino acids 1% (v/v) L-glutamine 0.5% (v/v) Penicillin/streptomycin 3.5 µL/500 mL ß-Mercaptoethanol 20% (v/v) Knockout serum replacement 10 ng/mL bFGF After incubation on mitotically inactivated mouse embryonic fibroblasts (strain CF-1) for 24 h, the medium was collected and sterile filtered (0.1 µm). 30 ng/mL bFGF (added shortly before usage)
FTDA	DMEM/F-12 without glutamine 2 mM L-glutamine Lipid mix (1:1000) 5 mg/L Transferrin 5 µg/L Sodium selenite 0.1% (v/v) Human serum albumin 5 µg/mL Human recombinant insulin 2.5 ng/mL Activin-A 30 ng/mL bFGF (added shortly before usage)

	50 nM Dorsomorphin dihydrochloride 0.5 ng/mL TGFß 1
mTESR 1	400 mL mTESR 1 Basal medium 100 mL mTESR 1 5x Supplement mTESR 1 is a commercially available complete, serum-free, defined and feeder-free hiPSC-medium. It contains recombinant human bFGF and recombinant human TGFß. The exact composition is not freely available.
Stage 0-medium	FTDA (without bFGF) 4 mg/mL Polyvinyl alcohol 10 µM Y-27632 30 ng/mL bFGF (added shortly before usage)
Stage 1-medium	RPMI 1640 4 mg/mL Polyvinyl alcohol 10 mM HEPES (pH 7.4) 0.05% (v/v) Human serum albumin 250 µM Phosphoascorbate 5 mg/L Transferrin 5 µg/L Sodium selenite Lipid mix (1:1000) 10 µM Y-27632 3 ng/mL Activin-A 10 ng/mL BMP-4 5 ng/mL bFGF All growth factors were added shortly before usage.
Stage 1-wash medium	RPMI 1640 10 mM HEPES (pH 7.4) 4 mg/mL Polyvinyl alcohol
Stage 2.1-medium	RPMI 1640 10 mM HEPES 0.5% (v/v) Penicillin/streptomycin 0.05% (v/v) Human serum albumin 250 µM Phosphoascorbate

	5 mg/L Transferrin 5 µg/L Sodium selenite Lipid mix (1:1000) 1 µM Y-27632 1 µM XAV 939 All growth factors were added shortly before usage.
Stage 2.1-wash medium	RPMI 1640 10 mM HEPES (pH 7.4) 0.5% (v/v) Penicillin/streptomycin
Stage 2.2-medium	RPMI 1640 2% (v/v) B27 plus insulin 10 mM HEPES 0.5% (v/v) Penicillin/streptomycin 500 µM 1-Thioglycerol 1 µM Y-27632 1 µM XAV 939 All growth factors and B27 plus insulin were added shortly before usage.
Stage 2.3-medium	RPMI 1640 2% (v/v) B27 plus insulin 10 mM HEPES 0.5% (v/v) Penicillin/streptomycin 500 µM 1-Thioglycerol 1 µM Y-27632 B27 plus insulin and Y-27632 were added shortly before usage.

3.1.2. HiPSC culture

The culture and expansion of hiPSC is based on the publication by Breckwoldt et al. (2017) with one difference that passaging was performed with Accutase (Sigma Aldrich). HiPSC culture was either performed by me (for CRISPR approach) or Thomas Schulze and Birgit Klampe (for cardiac differentiation; Institute of Experimental Pharmacology and Toxicology (IEPT), UKE, Hamburg). The used hiPSC line ERC018 was kindly provided by Prof. Thomas Eschenhagen and was generated as part of the IndivuHeart-study and declared as healthy control according to the study guidelines. Dr. Aya Domke-Shibamiya and Dr. Sandra Laufer

(UKE Stem Cell Core Facility) isolated fibroblasts from skin biopsies and subsequently reprogrammed the fibroblasts using a Sendai virus-based Kit (CytoTune™-iPS 1.0 Sendai Reprogramming Kit; Life Technologies). Cultivation and expansion of hiPSC was performed in FTDA medium in hypoxia (5% O_2) on Geltrex-coated (1:200; Thermo Fisher Scientific) cell culture plates and flasks. Before cardiac differentiation, the pluripotency of the hiPSC was evaluated by flow cytometry (FC) using the stage-specific Embryonic Antigen 3 (SSEA3) marker. Testing for a mycoplasma contamination was regularly performed by June Uebeler (IEPT, UKE, Hamburg, Germany).

The HCM hiPSC lines (HCMrepair, HCM, HCMmut) were kindly provided by Prof. Lucie Carrier and Dr. Maksymilian Prondzynski. The DCM hiPSC lines (DCMrepair, DCM) were kindly provided by Prof. Arne Hansen and Dr. Anika E. Knaust.

This thesis conforms to the ethical guidelines outlined by the Declaration of Helsinki and the Medical Association of Hamburg. Furthermore, the donors gave informed consent and all methods used to generate and analyse the hiPSCs were approved by the local ethics committee of Hamburg (approval numbers PV3501 and PV4798).

3.2. CRISPR/Cas9-mediated knockout of *MYBPC3*

This CRISPR/Cas9 gene editing approach was performed in parallel to the experiments of Dr. Anika E. Knaust (Knaust 2017), Dr. Maksymilian Prondzynski (Prondzynski 2017) and Dr. Alexandra Madsen (Löser 2018). Further, Dr. Sandra Laufer and Dr. Christiane Neuber from the UKE Stem Cell Core Facility supported all experiments by offering their help and expertise.

3.2.1. Validation of targeted genomic locus in ERC018 hiPSC

The here selected CRISPR/Cas9 gene editing approach is based on a publication from Ran et al. (2013) and the chosen cell line ERC018 was kindly provided by Prof. Thomas Eschenhagen. To validate the targeted genomic sequence, DNA of ERC018 hiPSC was first isolated with the DNeasy Blood & Tissue Kit (QIAGEN; according to manufacturer's instructions) and subsequently exon 6 was amplified by Touchdown PCR (see Table 2 and Table 3). The size of the PCR product was verified on a 1% agarose gel (not shown).

Table 2: Touchdown PCR approach for exon 6 of *MYBPC3* using PrimeSTAR polymerase. The used primers target exon 6 of *MYBPC3* (see Table S5).

Substance	Quantity
5xPrimeSTAR buffer	10 µL
2.5 mM dNTPs	4 µL
Fwd primer (10 µM)	0.5 µL
Rev primer (10 µM)	0.5 µL
DMSO	1 µL
PrimeSTAR	0.5 µL
Genomic DNA (50 – 100 ng)	1 µL
ddH_2O	Fill up to 50 µL

Table 3: Program of Touchdown PCR of PrimeSTAR polymerase. Expected size of PCR product is 515 bp. * = - 0.5 °C per cycle. ** = Elongation time is dependent on the size of PCR product (1 kb/min). ∞ = Hold.

Temperature	Time	Cycles
98 °C	10 sec	11 x
65 °C*	30 sec	
72 °C	52 sec**	
98 °C	10 sec	24 x
60 °C	30 sec	
72 °C	52 sec**	
72 °C	7 min	
4 °C	∞	

After purification with the QIAquick PCR Purification Kit (QIAGEN) according to the manufacturer's instructions, the purified PCR product was ligated with the CloneJET PCR Cloning Kit (Thermo Fisher Scientific). Shortly, all the components were pipetted together (Table 4), briefly vortexed, spun down and incubated for 5 min at room temperature (RT).

Table 4: Ligation mix using the CloneJET PCR cloning kit. A 1:3 ratio of PCR product and vector was used. Vector backbone includes an ampicillin resistance.

Substance	Quantity
2x reaction buffer	10 µL
Purified PCR product (25 ng)	2.7 µL
pJET 1.2/blunt cloning vector	1 µL
ddH_2O	5.3 µL
T4 DNA ligase	1 µL

Subsequently, the ligation approach was heat shock transformed into TOP10 competent E.coli. In brief, the competent cells were thawed on ice (5 – 15 min), 3 µL ligation mix was added and the mixture again incubated on ice for 30 min. Then, a 45 sec heat shock (42 °C) was performed, followed by a 5 min incubation on ice and the addition of 200 µL S.O.C. medium. Next, the samples were incubated for 1 h at 37 °C, gently shaking, and subsequently plated on ampicillin containing agar plates. The next day, five clones were inoculated in 3 mL LB-medium containing ampicillin and incubated overnight (ON) at 37 °C, gently shaking. Plasmid DNA was isolated according to manufacturer's instructions (NucleoSpin Plasmid Miniprep kit, Macherey-Nagel) and 50 - 100 ng/µL were sent for Sanger sequencing at MWG/Eurofins (for analysis see 4.2.1).

3.2.2. CRISPR/Cas9 gene editing approach and cloning

To introduce a DSB at the end of exon 6 of *MYBPC3* and subsequently a frameshift, a CRISPR/Cas9 approach using the wild-type pSpCas9(BB)-2A–GFP plasmid (Addgene PX-458; Figure S1) was designed (Figure 12; Ran et al. 2013; http://crispr.mit.edu/). Out of the list provided by http://crispr.mit.edu/, Guide#12 (quality score of 62) was picked since it targets a PAM sequence at the end of exon 6 with a high score and little predicted off-targets.

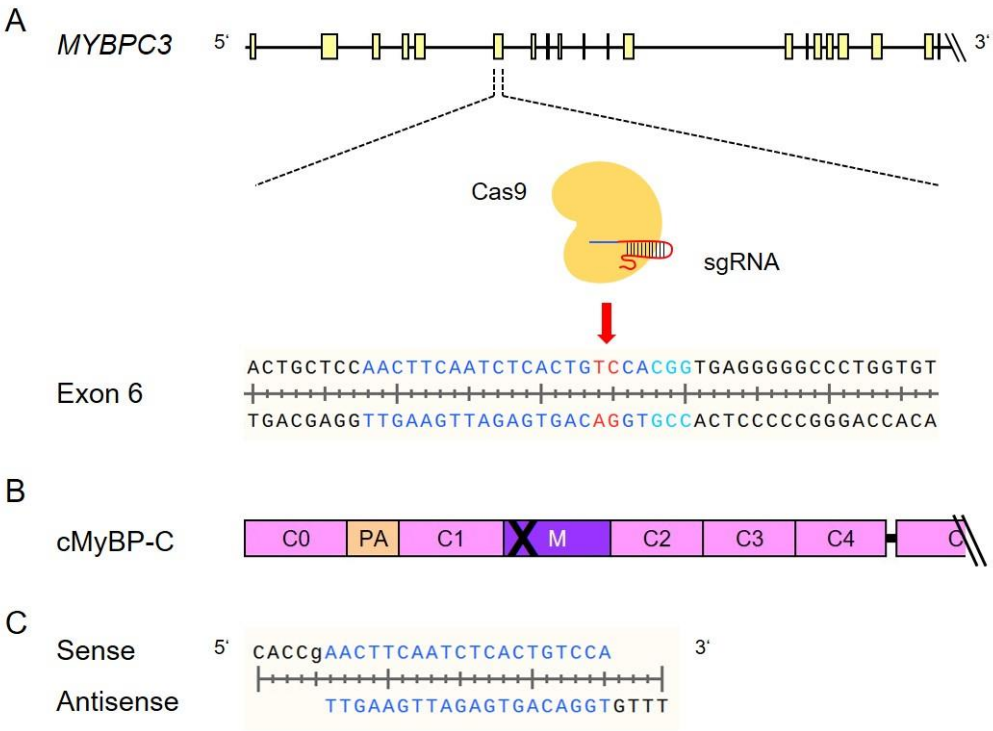

Figure 12: CRISPR/Cas9 design for *MYBPC3* knockout in ERC018 hiPSC. A schematic image shows the Cas9 (yellow) that is guided by the sgRNA with its scaffold (red) to the targeted region in exon 6 of *MYBPC3* (A). The sgRNA guide sequence perfectly pairs with the targeted sequence in the genomic DNA (dark blue). Light blue nucleotides = PAM. Red nucleotides indicate the putative cutting site where Cas9 mediates a DSB. Furthermore, a schematic image of cMyBP-C with its IG-like C domains, the proline-alanine rich domain (PA) and the MyBP-C motif (M) is shown (B). Black cross indicates the putative premature termination codon (PTC) in exon 9 induced by a frameshift mutation at the end of exon 6. The sgRNA sense and antisense oligonucleotide sequences (C; dark blue) with the 5' overhang (black) that is required for successful cloning are shown.

The concordant sgRNA oligonucleotides were ordered (sense and antisense, see Figure 12; MWG/Eurofins) with a 5'-overhang for successful cloning and annealed for 5 min at 95 °C (Table 5), followed by a 1 h cool-down at RT.

Table 5: Approach for sgRNA annealing.

Substance	**Quantity**
Oligo Fwd (200 µM)	4 µL
Oligo Rev (200 µM)	4 µL
10x annealing buffer	2 µL
ddH_2O	10 µL

To insert the annealed sgRNA into the pSpCas9(BB)-2A-GFP, the vector was digested with *Bbs*I and extracted out of an agarose gel with the QIAquick gel extraction kit (QIAGEN). Next, the annealed sgRNA was ligated into the linearized vector. Therefore, the ligation mix was pipetted (Table 6) and incubated for 90 min at 22 °C.

Table 6: Ligation mix using T4 ligase. A 1:3 ratio of vector to annealed sgRNA was chosen and calculated with a publicly available ligation calculator (http://www.insilico.uni-duesseldorf.de/Lig_Input.html).

Substance	**Quantity**
pSpCas9(BB)-2A-GFP (50 ng)	1 µL
Annealed sgRNA (0.4 ng)	1.1 µL
T4 Ligase (5 U/µL)	1 µL
10x T4 Ligase buffer	2 µL
ddH_2O	Fill up to 20 µL

Subsequently, the ligated product was amplified in Top10 competent E.coli and sent for sequencing (see above). Sequencing revealed the correct insertion of the sgRNA into the pSpCas9(BB)-2A-GFP vector (not shown) using the U6 Fwd primer (Table S5). To gain a higher concentrated pSpCas9–*MYBPC3*-sgRNA-2A-GFP plasmid, a maxiprep according to manufacturer's instructions was performed (NucleoBond Xtra Maxi Kit, Macherey-Nagel).

3.2.3. Nucleofection optimization for ERC018

To determine the best conditions for nucleofection of ERC018, the Primary Cell Optimization 4D-NucleofectorTM X Kit (Lonza) was tested with the 4D-Nucleofector X Unit (Lonza). The P3 and P4 nucleofection buffer are the most suitable buffers for nucleofection of hiPSCs. Thus, ERC018 hiPSCs were incubated with the apoptosis inhibitor Y-27632 (Y; 10 µM; Biobyrt) for 1 h before being washed twice with PBS and dissociated into single cells with Accutase (Sigma Aldrich) for 5 min at 37 °C, 5% CO_2. Two hundred thousand cells for each well of the 16-well nucleovette test strip were needed, thus 1.7 million (Mio.) hiPSCs per nucleofection buffer were taken (half an approach extra for pipetting error), spun down for 5 min at 200 g and resuspended in 170 µL P3/P4 nucleofection buffer (139.4 µL Nucleofector solution + 30.6 µL supplement). Then, 0.5 µg of the pMax GFP vector was added before pipetting 20 µL into each well of the 16-well nucleovette strip. Seven different nucleofection programs (CA-137, CB-150, CD-118, CE-118, CM-113, DC-100, DN-100) were tested together with a negative control program. After nucleofection, the cells were incubated for 5 min at 37 °C and 5% CO_2 before being plated into a Matrigel-coated (1:60; Corning) 24-well plate in CoM with bFGF (30 ng/mL; PeproTech) and Y, each approach in one well. Twenty-four hours after nucleofection, the

morphology was investigated by microscopy (not shown) and GFP expression quantified by FC. Therefore, the cells were dissociated with Accutase for 5 min at 37 °C and 5% CO_2 and measured at the UKE FACS Core Facility with the FACS Canto II flow cytometer (BD) to determine cell survival (cell number) and nucleofection efficiency (GFP+ cells).

3.2.4. CRISPR/Cas9 gene editing of *MYBPC3* via nucleofection in ERC018

ERC018 hiPSCs passage (p) 37 were incubated for 1 h with Y and washed twice with PBS. For cells cultured in FTDA (homemade), dissociation was performed using Accutase (+Y) for 5 min at 37 °C (5% CO_2) and subsequently single cells were mixed 1:1 with FTDA. Cells cultured in mTESR (STEMCELL) were singularized with Gentle Cell Dissociation Reagent (+Y; STEMCELL) for 8 min at 37 °C (5% CO_2). After centrifugation (5 min at 200 g), the cells were resuspended in the according medium. For each condition, one well with 400 000 cells was seeded as negative control (12-well plate). For nucleofection, 800 000 cells for each approach were spun down (5 min at 200 g), resuspended in the nucleofection mix (Table 7) and subsequently pipetted into electroporation cuvettes (Lonza).

Table 7: Nucleofection mix for *MYBPC3*-KO in ERC018.

Substance	**Quantity**
P3 Nucleofector solution	82 µL
Supplement	18 µL
pSpCas9-*MYBPC3*-sgRNA-2A-GFP (2000 ng)	1.25 µL

After nucleofection with program CA-137 and CB-150, electroporation cuvettes containing the mixes were incubated for 5 min at 37 °C (5% CO_2). Then, 500 µL pre-warmed CoM (+Y, +bFGF; for FTDA cells) or mTESR (+Y, +bFGF) were pipetted into the electroporation cuvettes before transferring the whole approach into one well of a 12-well plate already containing 500 µL CoM/mTESR (+Y, +bFGF). Twenty-four hours after nucleofection, GFP+ cells were visualized by microscopy and 1 mL medium was added on top. Forty-eight hours after nucleofection, the GFP+ cells were washed once with PBS and singularized either with Accutase or Gentle Cell Dissociation Reagent (see above) and filtered (30 µM). GFP+ cells were sorted with the FACSAria IIIu cell sorter (BD; UKE FACS Core Facility) into a 1.5-mL tube with CoM medium (+Y, +bFGF), centrifuged for 3 min at 150 g and subsequently seeded into a Matrigel-coated 6-well plate for single colony formation. CA-137-nucleofected cells that were cultivated in mTESR were split into two 6-wells, all other approaches were seeded in one 6-well. Forming colonies and their morphology was observed every day using a microscope. Until the picking of colonies, medium was changed daily, for the first seven days containing the apoptosis inhibitor Y. Solely the mTESR cells nucleofected with CA-137 survived single

colony formation and were therefore picked. Before picking, Y was added to the medium. Picking refers to scraping of a single colony with a 100-µL pipette tip under microscopic visualization (EVOS FL Cell Imaging System) and transfer into a Matrigel-coated 48-well. The next day, medium was solely added on top but in the following days a normal complete medium change took place. Almost confluent clones were split with EDTA (5 min at RT) and transferred into a 24-well plate. This was repeated twice (by splitting in a 1:2 ratio) to generate enough cellular mass for cryopreservation and DNA isolation (DNeasy Blood & Tissue Kit, QIAGEN). Sequencing of exon 6 of *MYBPC3* was performed to reveal an alteration of the genomic sequence. Only the modified clones were kept in culture and transferred to FTDA medium for expansion to generate several cryovials of the CRISPR clones.

3.2.5. Subcloning and off-target analysis of CRISPR clones

In order to distinguish the genotype of the two alleles individually, PCR fragments of *MYBPC3* exon 6 (see Table 2 and Table 3) from each CRISPR clone were subcloned as described above (see 3.2.1). For each CRISPR clone six to eight single colonies were picked, DNA was isolated and analysed by sequencing (*MYBPC3* exon 6 Fwd primer; see 4.2.3).

Furthermore, for each of the 10 most likely off-target sites, primer pairs specific for that genomic region were designed (Table S5). DNA was extracted with the DNeasy Blood & Tissue Kit (QIAGEN; according to manufacturer's instructions) from the three CRISPR clones and amplified by PCR (see Table 8 and Table 9). The correct size of each PCR product was verified on an agarose gel (not shown) before purification with the QIAquick PCR Purification Kit (QIAGEN) and sent for sequencing and compared to the NCBI database (see 4.2.4).

Table 8: Touchdown PCR mix for off-target analysis using AmpliTaqGold polymerase. The used fwd and rev primer are listed in Table S5.

Substance	**Quantity**
10x PCR buffer	2 µL
25 mM $MgCl_2$	1.2 µL
10 mM dNTPs	0.4 µL
Fwd primer (10 µM)	0.5 µL
Rev primer (10 µM)	0.5 µL
AmpliTaq Gold (1kb/min)	0.2 µL
Genomic DNA	20-50 ng/µL
ddH_2O	Fill up to 20 µL

Table 9: Touchdown PCR program for AmpliTaq Gold polymerase. Expected size of PCR products varies from 473 bp to 771 bp (Table S5). * = - 0.5 °C per cycle. ** = Elongation time is dependent on the size of PCR product (1 kb/min). ∞ = Hold.

Temperature	Time	Cycles
94 °C	5 min	
94 °C	30 sec	11 x
65 °C*	30 sec	
68 °C	52 sec**	
94 °C	30 sec	24 x
60 °C	30 sec	
68 °C	52 sec**	
68 °C	7 min	
4 °C	∞	

3.2.6. Karyotype analysis of CRISPR clones

To validate whether successfully CRISPR clones show a correct karyotype hiPSCs were analysed by G-banding and NanoString Technology. For G-banding, hiPSCs of each clone (p47-49) were thawed and cultured for two passages in FTDA. For examination, cells were plated on two Geltrex-coated 6-wells, and when the confluency reached ~80%, the cells were handed over to the Department for Human Genetics at the UKE for cytogenetic analysis. The karyotype was also evaluated in a younger passage of all CRISPR clones with the NanoString Technology. Therefore, the nCounter Human Karyotype Panel was used (NanoString Technologies) according to manufacturer's instructions. 300 ng genomic DNA was fragmented by Alu1 restriction digestion for 1 h at 37 °C. The fragmentation was verified on a 1% agarose gel, before the samples were denatured at 95 °C for 5 min to obtain single-stranded DNA and subsequently put on ice until hybridization reaction was ready (at least 2 min). The hybridization mix was pipetted (Table 10) and incubated for 16 h at 65 °C before being loaded onto the nCounter Cartridge and run on the nCounter SPRINT Profiler.

Table 10: Hybridization mix for karyotyping with NanoString Technology.

Substance	Quantity
Reporter CodeSet	3 µL
Hybridization buffer	5 µL
Denatured DNA	10 µL
Capture ProbeSet	2 µL

The NanoString karyotype experiment was performed by Elisabeth Krämer and analysed by Dr. Giulia Mearini (IEPT, UKE, Hamburg, Germany).

3.2.7. Genotyping of CRISPR clones

Similar to standardized genotyping of mice strains, generated CRISPR clones were subjected to genotyping on a regular basis to validate the identity and prevent mix-ups. Thus, DNA was isolated of either hiPSCs (before differentiation) or CMs (after differentiation or thawing) with the DNeasy Blood & Tissue Kit (QIAGEN) and amplified by PCR (see Table 2 and Table 3). The resulting PCR product was purified (QIAquick PCR Purification Kit; QIAGEN), sent for sequencing and subsequently compared to the wild-type genomic sequence and the original CRISPR clone genomic sequences (see 4.2.7).

3.3. Generation, cultivation and treatment of hiPSC-CMs

3.3.1. Cardiac differentiation of hiPSC

ERC018 hiPSCs and the CRISPR hiPSC lines were differentiated into CMs with the established in-house differentiation protocol published by Breckwoldt et al. in 2017. This is a growth factor, EB-based differentiation protocol with three-stages that has been frequently described (Lemme et al. 2018; Schulze et al. 2019) and mainly produces ventricular hiPSC-CMs. The used media are described in detail in 3.1.1. Differentiation of all hiPSC lines were performed by me or in collaboration with Maksymilian Prondzynski, Anika E. Knaust or Marta Lemme.

Stage-0 consisted of dissociating hiPSCs that were grown in a monolayer in Geltrex-coated T80 cell culture flasks under hypoxia by first adding the apoptosis inhibitor Y (1 h before the dissociation) and then EDTA. Then, 30 Mio. cells per 100 mL Stage-0 medium were incubated in 500 mL spinner flasks on magnetic stirrer plates ON under hypoxia to induce EB formation. Stage-1 was performed on the next day and consisted of first washing and then estimating the EB volume. About 180-250 µL EBs were cultured in suspension in Pluronic F-127 (Sigma-Aldrich)-coated T175 flasks under hypoxia in Stage-1 medium and thereby mesodermal differentiation was induced. The following growth factors were used for the mesodermal induction: BMP4 (10 ng/mL), Activin A (3 ng/mL) and bFGF (5 ng/mL). For the next two days, half medium changes were performed. Then, EBs were again washed and their volume estimated before transferring 180-250 µL EBs into Stage-2 medium to induce cardiac differentiation. Again, half medium changes were performed for the next two days before performing a complete medium change by transferring the EBs into Stage-2.1 medium. This medium contains insulin and XAV 939, a WNT-signalling inhibitor. For the next three days, half

medium changes were performed and subsequently, the cells were transferred into Stage-2.2 medium (without XAV 939) and cultured for five more days. On average, nicely shaped EBs started spontaneous beating between day 8 and 12 of cardiac differentiation. After 17 days of cardiac differentiation, the EBs were enzymatically dissociated for up to 3.5 h at 37 °C with Collagenase II (200 U/mL, Worthington) into single cells. HiPSC-CMs were either directly plated in 2D (24-well plate) or frozen in cryovials in freezing solution. Therefore, the cryopreservation system Asymptote EF600M (Grant Instruments) device was used for a controlled, gentle freezing down to -80 °C. Subsequently, the frozen cells were transferred to -150 °C for long-term storage. The percentage of hiPSC-CMs positive for cTnT was determined by FC.

3.3.2. Thawing, cultivation and treatment of hiPSC-CMs

HiPSC-CMs were thawed with a gentle protocol to enable high recovery rates of CMs. Therefore, the cryovial was taken from the -150 °C storage and cells were immediately thawed in a water bath (37 °C) before being gently transferred into a 50-mL falcon tube using a 2 mL serological pipette. The empty cryovial was rinsed with 1 mL of pre-warmed 2D culture medium. Subsequently, this 1 mL was added dropwise (one drop every 4-5 sec) to the cell suspension in the 50-mL falcon whereby the falcon was gently swirled. Then, 1 mL of pre-warmed 2D culture medium was added dropwise with one drop every 2-3 sec while the falcon was gently swirled. Next, 7 mL of pre-warmed 2D culture medium was added with one drop every sec while the falcon was gently swirled. The whole cell-medium-mixture was then inverted 2-3x, and the number of cells determined (Neubauer chamber).

For 2D culture of hiPSC-CMs of ERC018 and the CRISPR clones, 12-well and 96-well plates were coated with Geltrex (1:100) and for one 12-well 440 000 cells and for one 96-well 2500-5000 cells seeded. The hiPSC-CMs were cultured for up to 30 days (37 °C, 5% CO_2, normoxia) with being fed three times a week. HiPSC-CMs were monitored carefully by microscopic evaluation and every week, images and videos were taken. At day 7 and day 30, hiPSC-CMs cultured in 96-well plates were treated for 3 h at 37 °C with either DMSO (0.05%), Rapa (2.5 µM; Sigma-Aldrich) or Bafilo (50 nM; Sigma-Aldrich). After two washing steps with PBS, the cells were fixed with Roti-Histofix (Roth) for 20 min at 4 °C. After three more washing steps, the 96-plate was sealed and stored at 4 °C until immunofluorescence analysis (see 3.5.11). To detect putative truncated forms of cMyBP-C, hiPSC-CMs were treated at day 29 for 24 h at 37 °C with either 0.01% or 0.1% DMSO or 1 µM or 10 µM MG-132 (proteasome inhibitor; Merck Biosciences). To evaluate the autophagic flux, hiPSC-CMs were treated at day 30 for 3 h at 37 °C with 0.05% DMSO, 2.5 µM Rapa or 50 nM Bafilo. In both cases, the cells were washed once with PBS and subsequently harvested with Accutase solution (5 min at 37 °C). The cell pellets were first washed with PBS and then snap-frozen in liquid nitrogen. All cell pellets were

stored at -80 °C. HiPSC-CMs samples were prepared for molecular analysis (Western Blot (WB), RNA, mass spectrometry). Treatment of all hiPSC lines was performed by me or with the help of Maksymilian Prondzynski, Mirja Schulze or Marta Lemme, since drug application was not possible during pregnancy.

3.4. Human tissue samples

Human tissue samples were provided by Prof. Thomas Eschenhagen in case of DCM and non-failing (NF) samples, as being donor hearts not suitable for transplantation. Prof. Lucie Carrier provided septal myectomies of HCM patients. The human heart samples were chopped into small pieces and snap-frozen in liquid nitrogen. Subsequently, the human heart samples were either stored as a piece or powder at -80 °C until further use. Protein and RNA were isolated by Elisabeth Krämer and Jutta Starbatty or in collaboration with me. This thesis conforms to the ethical guidelines outlined by the Declaration of Helsinki and the Medical Association of Hamburg. The donors gave informed consent.

3.5. Molecular analysis

3.5.1. Isolation of proteins for WB

To isolate proteins from human cardiac tissue, 30 mg tissue powder were combined with 6.25 volumes of H_2O with protease inhibitors (Roche Complete mini EDTA free Protease Inhibitor; 1 tablet in 10 mL) and homogenized using the TissueLyser (QIAGEN), two times 30 sec at 20 Hz. Then, the mixture was centrifuged for 30 min at 16 000 g at 4 °C. Subsequently, the supernatant (cytosolic fraction) was collected and stored at -20 °C until utilization. After two washing steps with H_2O with protease inhibitors with centrifugation steps for 5 min at 16 000 g at 4 °C, the pellet was homogenized in 6.25 volumes of Kranias buffer (with 0.1% DTT) using the TissueLyser two times for 30 sec at 20 Hz to yield the membrane-enriched fraction. To evaluate protein levels in hiPSC-CMs, the cells were dissolved in 100 µL Kranias buffer (0.1% DTT) by vigorous pipetting and short vortexing. The concentration of proteins was evaluated by Qubit measurement (Qubit Protein Assay Kit; Thermo Fisher Scientific).

3.5.2. Evaluation of protein level by WB

For hiPSC-CMs 7.5 µg protein and for human cardiac tissue samples 10 µg protein was mixed with 6x Laemmli buffer and ddH_2O (21 µL in total). The mixture was incubated either for 10 min at 55 °C for autophagic flux analysis or 5 min at 95 °C for all other proteins. Subsequently, the mixture was loaded onto an agarose gel (10% for ubiquitin analysis; 12% for autophagic flux and other proteins). SDS-PAGE was performed for 10 min at 80 V, then for ~ 70 min at 150 V. Subsequently, transfer of proteins onto a nitrocellulose or PVDF membrane (0.45 µm)

took place. After the successful transfer, the membranes were washed with TBS-T and stained with Ponceau solution (Sigma-Aldrich) to visualize all proteins attached to the membrane. After an image was taken at the ChemiDoc Touch Imaging System (Bio-Rad), membranes were blocked either in 5% skim milk or 5% BSA for 1 h at RT to prevent unspecific binding events. To visualize proteins of interest, primary antibody incubation was performed at 4 °C ON in TBS-T and secondary antibody incubation for 1 h at RT in 5% skim milk/TBS-T under gentle rotation. Either the Clarity Western ECL Substrate (Bio-Rad) or the SuperSignal West Dura ECL (Thermo Fisher) were used for visualization at the ChemiDoc Touch Imaging System. Analysis and quantification of protein bands was performed with the ImageLab software (Bio-Rad). The quantified protein bands were either normalized to cTnT or to the ponceau staining. Silke Düsener-Reischmann and Dr. Saskia Schlossarek (IEPT, UKE, Hamburg) helped with the conduction of WBs in this thesis.

3.5.3. Isolation of proteins for mass spectrometry analysis

Mass spectrometry preparation, measurement and analysis was performed by Dr. Elke Hammer and Maren Depke at the Interfaculty Institute of Genetics and Functional Genomics (University Medicine Greifswald).

Protein was extracted from 2D-cultured hiPSC-CMs by five cycles of freezing (liquid nitrogen) and thawing (30 °C, 1 400 rpm) in 8 M urea/ 2 M thiourea. Cell debris and insoluble material was separated by centrifugation (20 000 × g, 1 h at 4 °C). After determination of protein content with the Coomassie Plus (Bradford) Assay Kit according to manufacturer's instructions (Thermo Fisher Scientific), equal protein amounts from 2-4 wells of each batch were pooled and subjected to proteolytic digestion.

3.5.4. Sample preparation for mass spectrometry analysis

Four µg of total protein from each sample were reduced for 15 min at 37 °C with 2.5 mM UltraPure DTT (Invitrogen) and alkylated for 30 min at 37 °C with 10 mM Iodacetamide (Sigma Aldrich). Protein were lysed for 3 h at 37 °C using LysC (1:100; Promega) and subsequently digested with Trypsin Gold ON at 37 °C (Promega). The tryptic digestion was stopped by adding acetic acid (final concentration 1%) followed by desalting using ZipTip-µC18 tips (Merck Millipore). Eluted peptides were concentrated by evaporation under vacuum and subsequently resolved in 0.1% acetic acid, 2% acetonitrile (ACN) containing Hyper Reaction Monitoring/indexed Retention Time (HRM/iRT) peptides (Biognosys AG) according to manufacturer's instructions.

3.5.5. Mass spectrometry measurements

Before mass spectromic (MS) data acquisition, tryptic peptides were separated on an µPACTM micro-Chip (Pharmafluidics) using an Ultimate 3000 nano-LC system (Thermo Fisher Scientific). Peptides were eluted at a constant temperature of 50 °C and a flow rate of 600 nL/min. MS data was recorded on a QExactive HFx mass spectrometer (Thermo Electron). To design a spectral library, MS/MS peptides were separated by 2 h-linear gradients with increasing acetonitrile concentration from 5 to 25 % in 0.1 % acetic acid and data were recorded in data dependent mode (DDA). The MS scans were carried out in a m/z range of 350 to 1650 m/z. Data was acquired with a resolution of 60 000 and an automatic gain control (AGC) target of 3×10^6 at maximal injection times of 45 ms. The top 12 most abundant isotope patterns with charge ≥2 from the survey scan were then selected for fragmentation by high energy collisional dissociation (HCD) with a maximal injection time of 22 ms, an isolation window of 1.3 m/z, and a normalized collision energy of 27.5 eV. Dynamic exclusion was set to 45 s. The MS/MS scans had a resolution of 15 000 and an AGC target of 1×10^5. The acquisition of MS data for relative quantitation was performed in data independent mode (DIA) after peptide pre-fractionation using a 100 min-linear gradient from 5% to 25% acetonitrile in 0.1% acetic acid. Briefly, the data was acquired in the m/z range from 350 to 1200 m/z, the resolution for MS was 120 000 and for MS/MS 30 000. The AGC target was 3×10^6 for MS and MS/MS. The number of DIA isolation windows was 70 of 11 m/z with 1 m/z overlap.

3.5.6. Analysis of mass spectrometry data

Proteins were identified using SpectronautTM Pulsar 13.4 software (Biognosys AG) against a spectral library generated from DDA measurements of all 34 different samples of the study. The spectral library construction by Spectronaut was based on a database search using a human protein database (Uniprot vs 03_2019, 20404 entries) extended by sequences of bovine fibrinogen subunits A, B, and C. Because of the use of horse serum as medium supplement, sequences of 10 proteins reproducibly identified by proteotypic peptides were added to the database. The target-decoy search was performed with a parent mass error of ±20 ppm, fragment mass error of 0.01 Da, and allowing full-tryptic peptides (trypsin/P cleavage rule) with a minimal peptide length of six amino acids and up to two internal cleavage sites. The search included carbamidomethylation at cysteine as fixed modification and oxidation at methionine and acetylation at protein N-termini as variable modifications. The generation of the ion library in SpectronautTM v13.4.190802.43655 resulted in a constructed library consisting of 335 310 fragments, 30 756 peptides and 3 376 protein groups. The Spectronaut DIA-MS analysis was carried out as described previously (Palma Medina et al. 2019) with project specific modifications. Briefly, the following parameter settings were applied: dynamic MS1 and MS2 mass tolerance, dynamic XIC RT extraction window, automatic calibration,

dynamic decoy strategy (library size factor = 0.1, minimum limit = 5000), protein Q-value cutoff of 0.01, precursor Q-value cutoff of 0.001. The search included variable and static modifications as described above for spectral library construction. A local cross run normalization was performed using complete profiles with a Q-value <0.001. The MS2 peak area was quantified and reported. Missing values were parsed using an iRT profiling strategy with carry-over of exact peak boundaries (minimum Q-value row selection = 0.001). Only non-identified precursors were parsed with a Q-value > 0.0001. Ion values were parsed when at least 20% of the samples contained high quality measured values. Peptides were assigned to protein groups and protein inference was resolved by the automatic workflow implemented in Spectronaut. Only proteins with at least two identified peptides were considered for further analyses. Data has been median normalized on ion level before statistical analysis was carried out on peptide level after exclusion of peptides with oxidized methionine using the algorithm ROPECA (Suomi and Elo 2017). Binary differences have been identified by application of a moderate t-test (Phipson et al. 2016). Multiple test correction was performed according to Benjamini-Hochberg. Variance within the data set was visualized by principal component analyses (PCA). For representation of protein intensities Hi3Peptides were used.

3.5.7. Isolation of RNA from human cardiac tissue and hiPSC-CMs

For human cardiac tissue samples, total RNA was isolated with the SV Total RNA Isolation System from Promega according to the manufacturer's instructions. For hiPSC-CMs, RNA of all clones and ERC018 was isolated with the RNeasy Mini Kit (QIAGEN) according to manufacturer's instructions.

3.5.8. Validation of *MYBPC3*-KO on mRNA level

To validate the gene editing of *MYBPC3* by CRISPR/Cas9, 200 ng RNA was transcribed into cDNA with the Superscript III First Strand cDNA synthesis Kit (Thermo Fisher Scientific). The component mix was pipetted (Table 11), incubated for 5 min at 65 °C and subsequently for 5 min on ice.

Table 11: Component mix.

Substance	**Quantity**
50 µM oligo-dT primer	1 µL
10 mM dNTP mix	1 µL
RNA	200 ng
DEPC-water	Fill up to 10 µL

At the same time, the cDNA synthesis mix (Table 12) was pipetted and mixed gently with the already prepared component mix.

Table 12: cDNA synthesis mix.

Substance	Quantity
10x RT buffer	2 µL
25 mM $MgCl_2$	4 µL
0.1 M DTT	2 µL
RNaseOut (40 U/µL)	1 µL
SuperScript III Reverse Transcriptase	1 µL

The mix was incubated for 50 min at 50 °C before being terminated for 5 min at 85 °C. After a 5 min incubation at 4 °C, 1 µL RNase H was added and the whole mix was again incubated at 37 °C for 20 min. The cDNA was amplified by PCR using the PrimeSTAR polymerase (see Table 2 and Table 3) with a primer pair targeting exon 4 to exon 9 of *MYBPC3* (Table S5). PCR products were visualized on a 1% agarose gel before being subcloned (see 3.2.1). For each CRISPR clone 16 single colonies were picked, DNA extracted and sent for sequencing (*MYBPC3* exon 4 Fwd primer).

3.5.9. Evaluation of mRNA levels by NanoString Technology

To evaluate the gene expression in human cardiac tissue, the nCounter XT CodeSet Gene Expression Assay comprising of a customized human basic TagSet and a customized autophagy extension TagSet was used according to the manufacturer's instructions (NanoString Technologies; Table S6). Thus, a hybridization mix was pipetted (Table 13) and incubated at 67 °C for 16 h.

Table 13: Hybridization mix for gene expression analysis of human cardiac tissue.

Substance	Quantity
Hybridization buffer	5 µL
TagSet (Human basic)	2 µL
Extension TagSet (Autophagy extension)	2 µL
30x Working Probe A Pool (Human basic)	0.5 µL
30x Working Probe B Pool (Human basic)	0.5 µL
30x Working Extension Probe A Pool (Autophagy extension)	0.5 µL
30x Working Extension Probe B Pool (Autophagy extension)	0.5 µL
RNA (40 ng)	Up to 4 µL

Subsequently, the samples were mixed 1:1 with RNase-free H_2O by flicking, shortly spun down and pipetted into the cartridge. The analysis of the runs was performed with the nSolver Analysis Software 4.0 (NanoString Technologies). The runs themselves and the analysis of the runs were performed by me with the help of Dr. Maksymilian Prondzynski and Elisabeth Krämer.

3.5.10. Evaluation of mRNA level by RT-qPCR

Further, the expression of *MYBPC3* in the hiPSC-CMs of the three CRISPR clones and ERC018 was validated by RT-qPCR. Therefore, SYBR-Green (Thermo Fisher Scientific) was used according to manufacturer's instructions (Table 14) and the samples were amplified during 45 cycles with the ABI PRISM 7900HT Sequence Detection System (Applied Biosystems). All target sequences were analysed in triplicates and the transcript levels were normalized to *GAPDH* (glyceraldehyde 3-phosphate dehydrogenase; exon 5 to exon 6). The target sequences for *MYBPC3* were exon 1 to exon 2 and *MYBPC3* exon 26 (Table S5). To validate the trisomy, exon 4 of *LMNA* was validated (Table S5). The relative differences between ERC018 and the CRISPR clones were calculated with the $2^{-\Delta\Delta Ct}$ method for relative quantifications. Dr. Saskia Schlossarek (IEPT, UKE, Hamburg) assisted with RT-qPCR analysis.

Table 14: RT-qPCR master mix.

Substance	**Quantity**
Maxima SYBR Green/ROX qPCR Master Mix (2x)	5 µL
Fwd primer (10 µM)	0.9 µL
Rev primer (10 µM)	0.9 µL
cDNA (1:5 dilution; add to individual PCR tubes)	1 µL
DEPC-water	2.2 µL

3.5.11. Immunofluorescence and cell size analysis of hiPSC-CMs

To perform immunofluorescence staining, hiPSC-CMs cultured in 96-well plates were incubated with primary antibody (Table S3) that was diluted in permeabilization buffer (50 µL/96-well; Table S2). The incubation was performed ON at 4 °C under gentle agitation and protected from light. On the next day, the hiPSC-CMs were washed twice with PBS and incubated with the secondary antibody (Table S4), also diluted in permeabilization buffer (50 µL/96-well), for 1 h at RT in the dark under gentle agitation. During the last 20 min of this 1 h incubation, Hoechst 33342 (1:2500 in PBS, 50 µL/well; Thermo Fisher Scientific) was added to stain the nuclei. After two washing steps with PBS, fresh PBS was added and the wells were analysed by confocal microscopy (LSM 800, Zeiss) either for protein expression or cell size.

For the analysis of the cell size of hiPSC-CMs, images of three wells per cell line were taken of every single cell showing a nice striation and overall shape. The quantification was performed using Fiji software (ImageJ). The approach was based on the publication of Prondzynski et al. (2017).

3.6. Statistical analysis

GraphPad Prism software 8.3.0 was used to perform statistics. Data was presented as mean±SEM either as bar graphs, stacked bar graphs or scatterplots. Either the unpaired Student's *t*-test or one-way ANOVA (plus Tukey or Bonferroni's post-test) was used to determine whether the difference between groups was statistically significant, whereby a p-value lower than 0.05 was considered to be statistically significant. The number of replicates, batches and wells was expressed as n=replicate number/batch number/well number.

4. Results

4.1. Evaluation of a putative common ALP alteration in human inherited cardiomyopathies

Previously, our group showed impaired protein quality control (UPS and ALP; Schlossarek et al. 2012; Singh et al. 2017) in a HCM mouse model carrying a *Mybpc3* knock-in mutation that resembles a human founder mutation found in Tuscany, Italy (c.772G>A; Olivotto et al. 2008; Vignier et al. 2009). Upon activation of autophagy (caloric restriction or Rapa treatment), a (partial) amelioration of the cardiomyopathic phenotype was observed (Singh et al. 2017). However, the role of the ALP and its biological activity within human inherited cardiomyopathies needed to be further elucidated.

4.1.1. Common autophagy alteration in cardiac tissue samples of HCM and DCM patients

Thus, the putative alteration of the ALP was investigated in septal myectomies of HCM patients carrying *MYBPC3* mutations, explanted hearts of DCM patients and NF individuals as controls. The main markers of autophagy were evaluated by immunoblotting (Figure 13A). LC3-II is found in the inner and outer membrane of the autophagosome and is degraded within the autolysosomes. LC3-II protein levels were >2.5-fold higher in HCM and DCM patients than in NF samples (Figure 13B), implying either an increased formation or accumulation of autophagosomes. p62 is a shuttle protein that guides poly-ubiquitinated aggregates to the ALP. In DCM, p62 protein levels were 2.5-fold higher than in NF samples, indicating either an increase or accumulation of poly-ubiquitinated proteins (Figure 13C). In contrast, p62 levels did not differ between HCM and NF samples. To validate the activity of the main negative regulator of autophagy, mTORC1, the protein levels of one downstream target of mTORC1, phosphorylated S6 (pS6) were determined (Figure 13D). Markedly lower levels of pS6 were detected in HCM and DCM than in NF samples. Furthermore, the protein levels of LAMP-2, one of the main markers of lysosomes, were determined. LAMP-2 protein levels were dramatically lower in HCM samples, whereas they were 3-fold higher in DCM than in NF samples (Figure 13E).

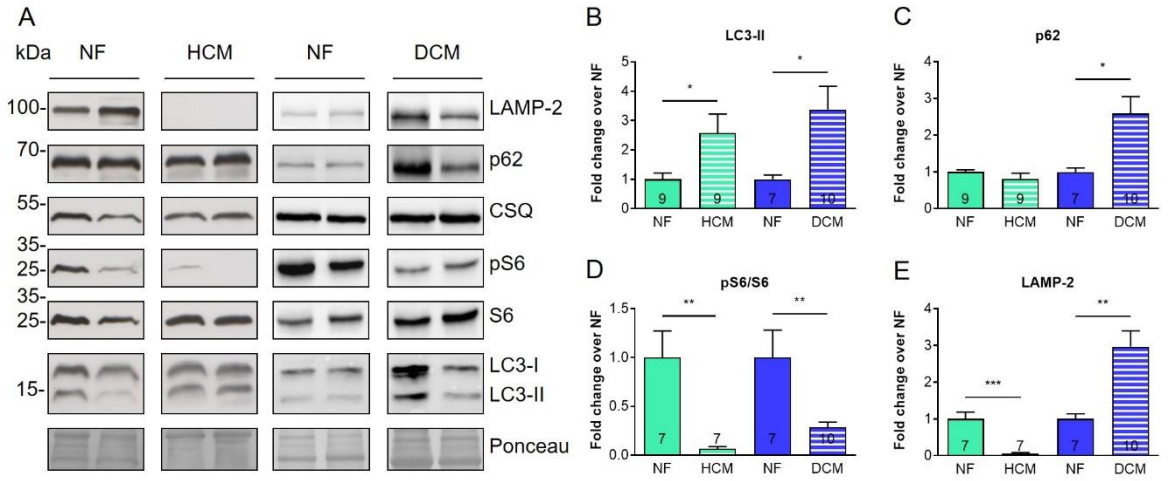

Figure 13: Protein levels of autophagy markers in ventricular tissues of HCM and DCM patients. A representative WB of the main marker of the ALP determined in HCM carrying a mutation in *MYBPC3* and DCM patients in relation to NF samples (A) and its quantifications are shown (B - E). Calsequestrin (CSQ), S6 and ponceau were used as loading controls and for normalization. Data are expressed as mean±SEM (*p<0.05, **p<0.01, ***p<0.001 vs NF, unpaired Student's *t*-test). N-numbers are indicated (see bars).

Then, gene expression analysis of NF, HCM and DCM patient samples was performed with the NanoString technology (Figure 14). Hereby, the group of HCM patients carrying a *MYBPC3* mutation and HCM patients with non-*MYBPC3* mutations were merged since statistical analysis did not show any significant differences between those two groups.

Higher levels of natriuretic peptide A (*NPPA*) and periostin (*POSTN*) and lower levels of cardiac alpha-myosin heavy chain (*MYH6*) and signal transducer and activator of transcription 3 (*STAT3*) were detected. This data confirmed the diseased state of the HCM and DCM patients. Furthermore, alterations in the expression of genes contributing to Ca^{2+} handling (e.g. lower levels of ATPase sarcoplasmic/endoplasmic reticulum Ca^{2+} transporting 2 (*ATP2A2*) or protein phosphatase 1 regulatory inhibitor subunit 1A (*PPP1R1A*)) or fibrosis (e.g. higher levels of collagen type I alpha 1 chain (*COL1A1*)) were detected in HCM and DCM patients when compared to NF individuals. The gene expression analysis of the main marker of autophagy in HCM and DCM patient samples, revealed a diverse, inconclusive pattern. For instance, lower levels of microtubule associated protein 1 light chain 3 beta (*MAP1LC3B*) encoding LC3B and higher levels of mechanistic target of rapamycin kinase (*MTOR*) were detected in both HCM and DCM, whereas the levels of lysosomal-associated membrane protein 2 (*LAMP2*) and sequestome 1 (*SQSTM1)* mRNA did not differ between HCM, DCM and NF samples.

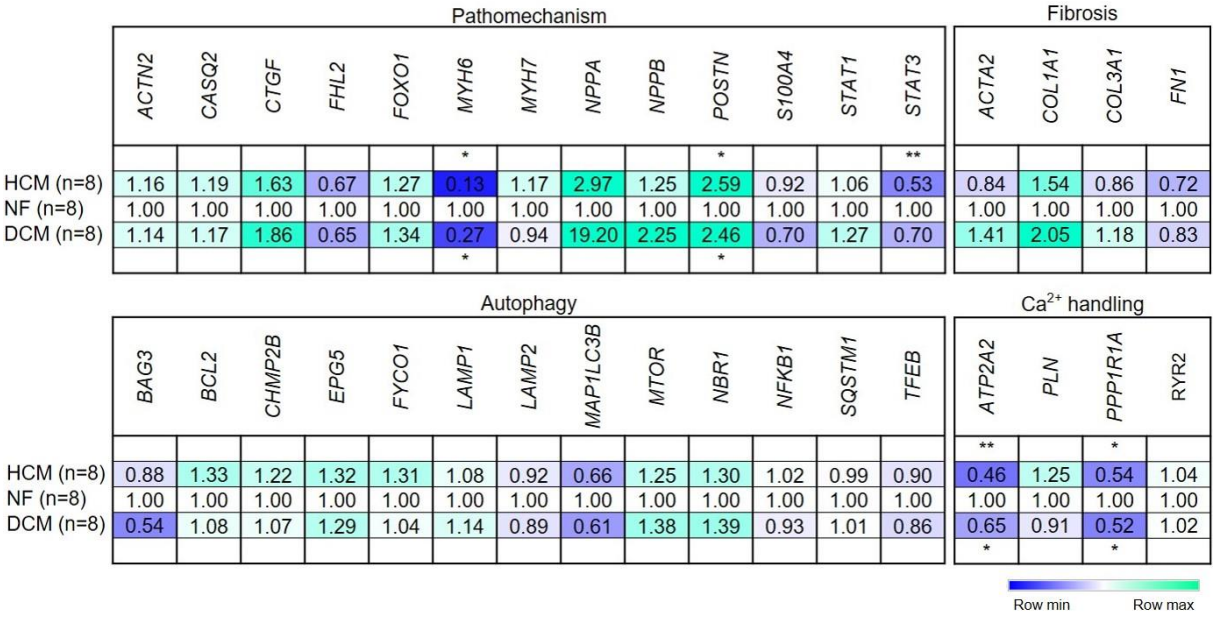

Figure 14: Determination of mRNA levels in ventricular tissue of HCM and DCM patients. Gene expression analysis was performed to analyse the main marker of the ALP, as well as the pathomechanism, fibrosis and Ca^{2+} handling in HCM and DCM tissue samples and compared to NF individuals. n = number of individuals. mRNA levels were determined in single samples that were pooled for data analysis. Data were normalized to six housekeeping genes (*ABCF1*, *ACTB*, *CLTC*, *GAPDH*, *PGK1*, *TUBB*) and related to NF. A cut-off of <0.8 or >1.2-fold change to NF was set for the heatmap construction. Exemptions were made for several genes (e.g. *LAMP1* and *LAMP2*) as they represent important markers, in this case for the ALP. Data are expressed as mean±SEM (*p<0.05, **p<0.01 vs NF, unpaired Student's *t*-test).

4.1.2. Evaluation of the autophagic flux in hiPSC-derived cardiomyocytes

It is not sufficient to determine basal levels of the main marker of the ALP to validate whether the ALP is actually activated or impaired in human inherited cardiomyopathies. Therefore, the autophagic flux/biological activity has to be evaluated. Unfortunately, it was not feasible to assess the autophagic flux in human myocardial samples since an ALP modulator treatment is needed. However, hiPSC-CMs represent a suitable *in vitro* tool since an ALP treatment can be performed. Evaluation of the autophagic flux is estimated with the difference in LC3-II protein between treated and untreated samples, as LC3-II is part of the autophagosome membrane and is degraded within autolysosomes.

First, the feasibility of the autophagic flux evaluation in hiPSC-CMs had to be tested. Therefore, hiPSCs from a healthy individual were first differentiated into beating CMs (Breckwoldt et al. 2017), cultured in 2D and on day 30 a 3 h treatment was performed. HiPSC-CMs were treated either with 50 nM Bafilomycin A_1 (Bafilo), a vascular type H(+)-ATPase that acts as an autophagosome-lysosome fusion inhibitor, alone or in combination with 2.5 µM Rapa, an

inhibitor of the main negative regulator of autophagy, mTORC1, and thus activates the ALP. Subsequently, the hiPSC-CMs were harvested, snap-frozen and analysed by immunoblotting (Figure 15). Treatment with Bafilo, alone or in combination with Rapa, induced a marked accumulation in LC3-II protein, due to the block of autophagosome-lysosome fusion. Similarly, higher level of p62 protein, but to a lower extent than LC3-II, were present in the Bafilo-treated hiPSC-CMs. As expected, Rapa treatment, alone or in combination with Bafilo, induced a marked reduction of pS6 levels, a downstream target of mTORC1. ALP modulator treatment revealed that the evaluation of the autophagic flux is feasible in hiPSC-CMs and thus in human inherited cardiomyopathies.

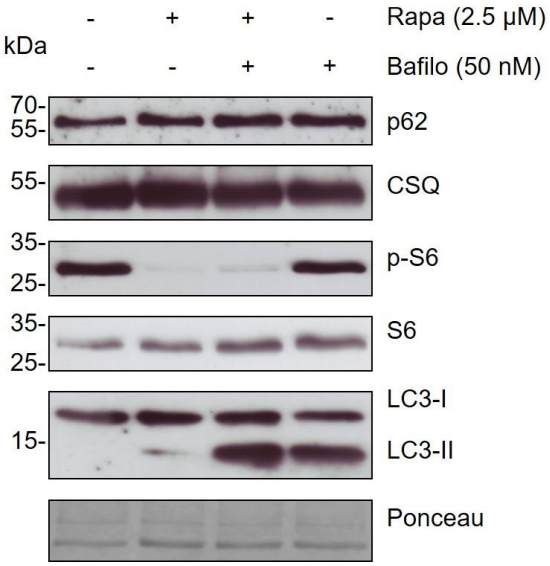

Figure 15: Establishment of autophagic flux evaluation in hiPSC-CMs. HiPSC-CMs of a healthy individual were cultured for 30 days *in vitro* before treatment with 2.5 µM Rapa, alone or in combination with 50 nM Bafilo. Immunoblotting results of LC3-II, p62 and pS6 are shown. CSQ, S6 and ponceau were used as loading controls.

4.1.3. Evaluation of the autophagy-lysosomal pathway in hiPSC-derived cardiomyocytes from patients with inherited cardiomyopathies

Next, hiPSC-CMs derived from an HCM patient (c.740C>T, p.T247M missense mutation in α-actinin 2 (*ACTN2*); heterozygous (HCMhet) and homozygous (HCMhom)) and a DCM patient (c.40_42delAGA, pArg14del mutation in *PLN*; heterozygous (DCM)), their corresponding isogenic CRISPR controls (HCMrepair and DCMrepair) and a healthy control (healthy ctrl) were systematically evaluated for a putative common alteration of autophagy in inherited cardiomyopathies. Therefore, all hiPSC-CM lines were cultured for 30 days while being constantly monitored by light microscopy (representative Figure 16 and Figure S2).

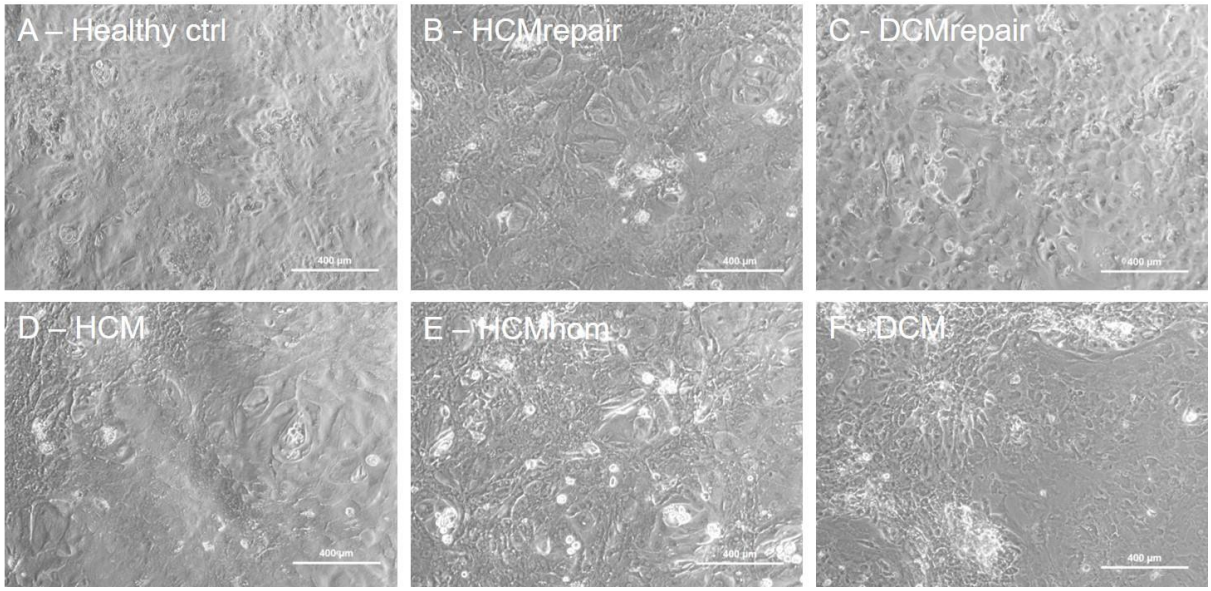

Figure 16: Phenotypic evaluation of the hiPSC-CMs of all investigated lines at day 28 of culture. To monitor the phenotype during the 30-day culture, all hiPSC-CM lines were subjected to microscopic evaluation (A – F). Scale bar = 400 µm. 10x magnification.

Next, basal levels of the main marker of the ALP were evaluated in 30-day old hiPSC-CMs of a healthy ctrl, HCMrepair, HCMhet and HCMhom that were treated with DMSO for 3 h by immunoblotting (Figure 17A). A marked increase in LC3-II protein was detected in healthy ctrl in comparison to HCMrepair (Figure 17B), whereas the protein levels of p62 and LAMP-2 did not differ between healthy ctrl and HCMrepair hiPSC-CMs (Figure 17C). The levels of LC3-II, p62 and LAMP-2 were unchanged in HCMhet and HCMhom in comparison to the HCMrepair (Figure 17B, C, D).

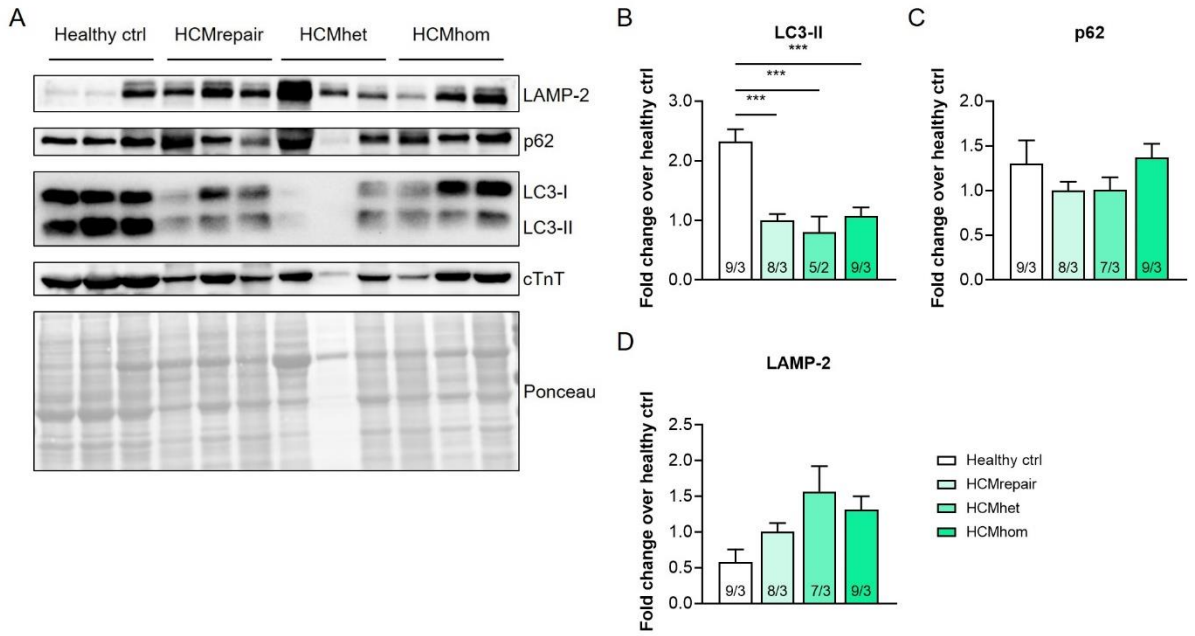

Figure 17: Evaluation of basal levels of the main ALP marker by immunoblotting in healthy ctrl, HCMrepair, HCMhet and HCM hom hiPSC-CMs. DMSO (0.05%; 3 h)-treated, 30-day old hiPSC-CMs of a healthy control (ctrl), HCMrepair, HCMhet and HCMhom were analysed for the main ALP marker (B – D). An exemplary, corresponding immunoblot is shown in A. Ponceau and cardiac troponin T (cTnT) were used as loading controls, whereby ponceau was used for normalization. n = number of analysed wells/number of differentiation batches. Data are expressed as mean±SEM (***p<0.001 vs HCMrepair, one-way ANOVA, Tukey's post-test).

The basal protein levels of the main marker of the ALP were also investigated by immunoblotting in hiPSC-CMs of a healthy ctrl, DCMrepair and DCM (Figure 18A). Markedly higher levels of LC3-II protein, but unchanged levels of p62 and LAMP-2 protein were detected in healthy ctrl hiPSC-CMs when compared to DCMrepair hiPSC-CMs (Figure 18B, C, D). The levels of LC3-II, p62 and LAMP-2 did not differ between DCMrepair and DCM hiPSC-CMs, although a tendency towards higher levels of LAMP-2 in DCM hiPSC-CMs was detected (p = 0.0842; Figure 18D).

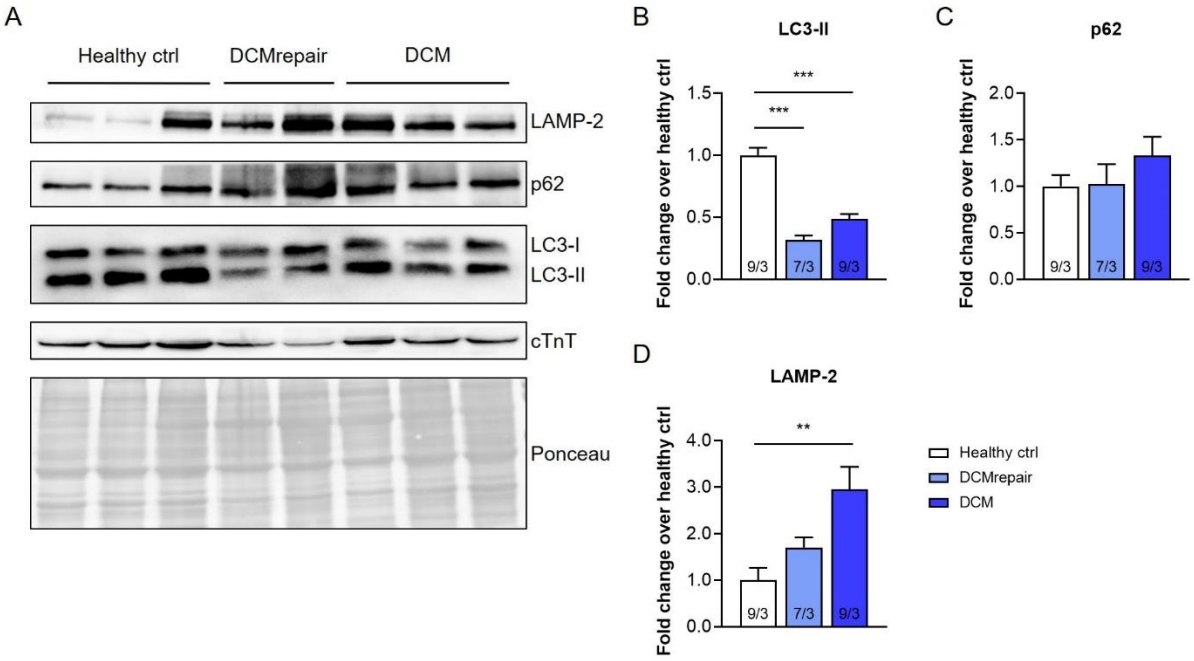

Figure 18: Investigation of the basal levels of the main ALP marker by immunoblotting in healthy ctrl, DCMrepair and DCM hiPSC-CMs. Thirty-day-old hiPSC-CMs were treated for 3 h with 0.1% DMSO (0.05%; 3 h). Subsequently, the main marker of the ALP was analysed by immunoblotting (B – D) whereby an exemplary, corresponding immunoblot is shown in A. Ponceau and cTnT were used as loading controls, whereby ponceau was used for normalization. n = number of analysed wells/number of differentiation batches. Data are expressed as mean±SEM (**p<0.01, ***p<0.001 vs DCMrepair, one-way ANOVA, Tukey's post-test).

On day 30 of culture, the hiPSC-CMs were treated either with DMSO (0.05%) or Bafilo (50 nM) and subsequently the protein levels of LC3-II and p62 were investigated (Figure 19A - F). Bafilo treatment induced a marked, significant increase in LC3-II protein levels in all investigated hiPSC-CM lines (Figure 19G). The increase in LC3-II protein was similar in HCMrepair and DCMrepair hiPSC-CMs, whereas healthy ctrl hiPSC-CMs showed an increase of LC3-II to a higher extent. Of interest, the levels of LC3-II protein increased to a higher extent in HCMhet and HCMhom than in HCMrepair, indicating an increased autophagic flux in the mutated HCM hiPSC-CMs. In contrast, LC3-II protein levels were increased to a lower extent in DCM than DCMrepair, implying a reduced autophagic flux in the diseased DCM hiPSC-CMs. In case of p62, higher protein levels were solely determined in healthy ctrl and HCMhet hiPSC-CMs after Bafilo treatment (Figure 19H), suggesting that the autophagic flux was overall not well detected on p62 level. However, p62 might have formed aggregates after Bafilo treatment, which could not have been detected with the here applied protein lysis buffer.

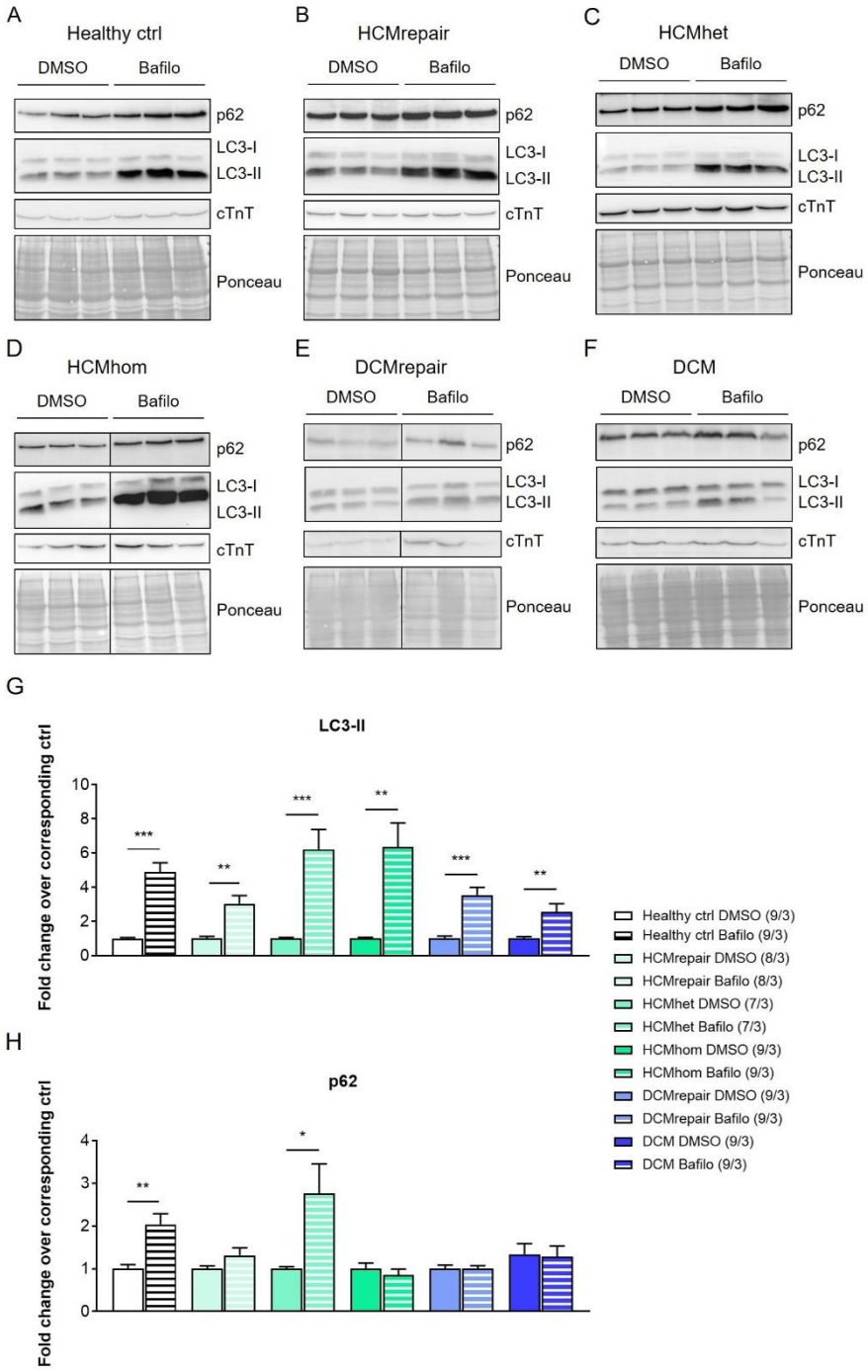

Figure 19: Analysis of the autophagic flux by immunoblotting in hiPSC-CMs. Thirty-day-old hiPSC-CMs of a healthy ctrl, HCMrepair, HCMhet, HCMhom, DCMrepair and DCM were treated either with 0.05% DMSO or 50 nM Bafilo for 3 h. The corresponding quantifications of LC3-II and p62 are shown (G + H), as well as exemplary immunoblots for all investigated cell lines (A - F). Ponceau and cTnT were used as a loading controls. However, solely ponceau was used for normalization. n = number of analysed wells/number of differentiation batches. Data are expressed as mean±SEM (*p<0.05, **p<0.01, ***p<0.001 vs corresponding DMSO control, unpaired Student's *t*-test).

Concurrently, samples of all six hiPSC-CM lines were treated on day 30 of culture either with DMSO (0.05%) or Bafilo (50 nM) and sent as frozen pellets to our collaborators at the University Medicine Greifswald (Dr. Elke Hammer and Maren Depke, Interfaculty Institute of Genetics and Functional Genomics) for mass spectrometry analysis. They processed and analysed the samples with the LC-MS/MS. Unfortunately, due to technical issues one batch of HCMhet was lost. Furthermore, to validate the Bafilo treatment, the protein levels of p62 were evaluated by LC-MS/MS of DMSO and Bafilo treated hiPSC-CMs (Figure 20). The protein levels of LC3-II were not used to validate the Bafilo treatment since an additional enrichment step for post-translational modifications would have been needed to detect the lipidated form of LC3 with the LC-MS/MS. For all investigated hiPSC-CM lines, an increase in p62 protein level was detected after Bafilo treatment, suggesting that the autophagic flux worked, but it was significant only in the healthy ctrl, HCMhet, HCMhom and DCMrepair hiPSC-CMs. Of note, the autophagic flux increase for each individual hiPSC-CM line is quite similar to the increase detected in LC3-II after Bafilo treatment by immunoblotting (see Figure 19).

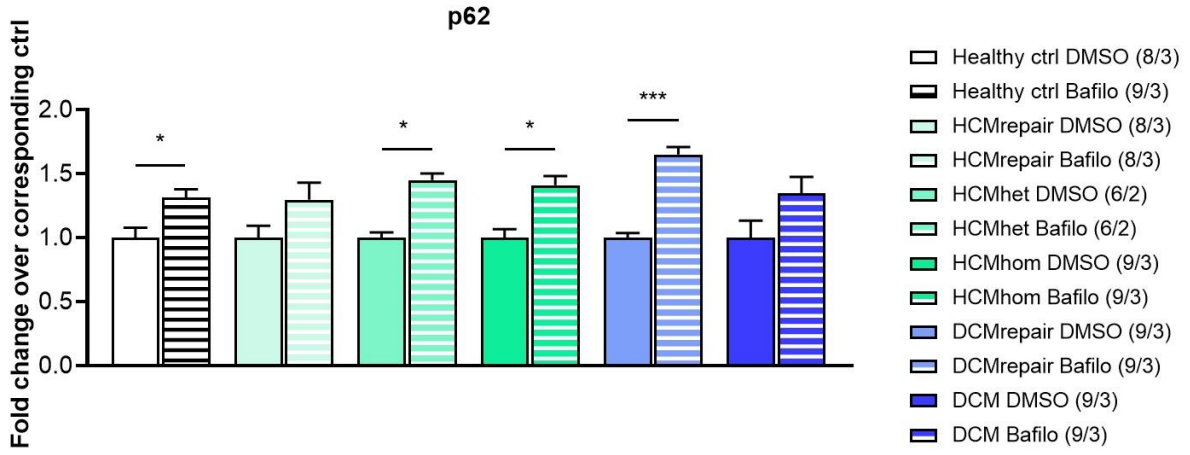

Figure 20: Autophagic flux evaluation with p62 protein level in all investigated hiPSC-CMs determined by mass spectrometry analysis. Thirty-day-old hiPSC-CMs were either treated with DMSO (0.05%) or Bafilo (50 nM) for 3 h and subsequently analysed by LC-MS/MS. Normalized Hi3 protein intensities are shown. n = number of wells/number of differentiation batches. Data are expressed as mean±SEM (p*<0.05, p***<0.001 vs corresponding control; unpaired Student's *t*-test).

The principal component analysis (PCA) of the data set is shown with its five dimensions (Figure 21). The most prominent finding was a vast difference between DCM and DCMrepair hiPSC-CMs in comparison to the remaining hiPSC-CM lines as displayed in the1st Dimension. The 2nd dimension of the PCA pointed out the big difference between the DCM, HCM (each with its isogenic controls) and healthy control hiPSC-CMs. Unfortunately, the 3rd dimension of the PCA showed that the effect of the Bafilo treatment was lower than the batch-to-batch

variability. This was quite unexpected, since the Bafilo treatment effect detected by immunoblotting was quite obvious (see Figure 19), as well as the effect on p62 detected by mass spectrometry (see Figure 20).

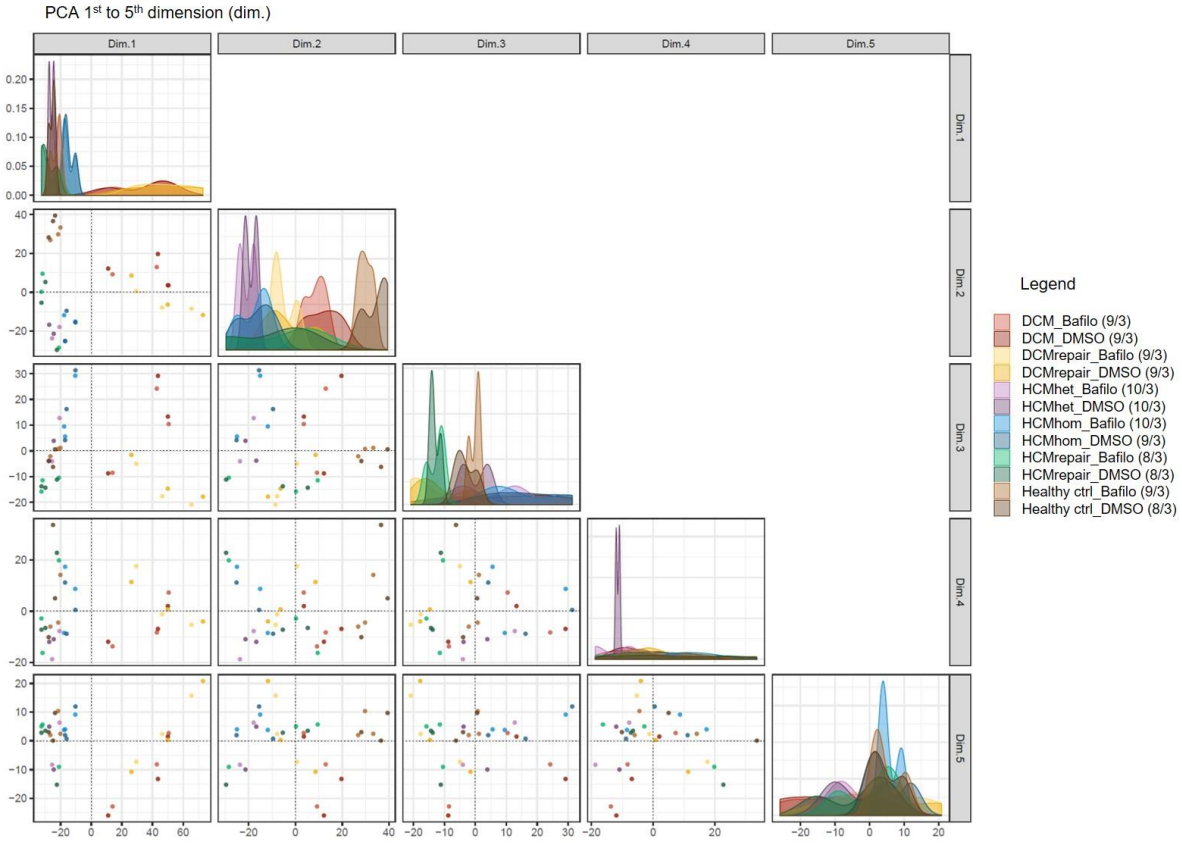

Figure 21: PCA analysis of treated hiPSC-CMs. The 1st dimension highlighted the vast difference between DCM and DCM repair to the other investigated cell lines. The 2nd dimension showed the big difference between DCM, HCM (each with its isogenic control) and healthy control. The 3rd dimension demonstrated that the effect of the Bafilo treatment is lower than the batch-to-batch variability. The 4th and 5th dimensions did not show a clear picture and were difficult to interpret. n = number of analysed wells/number of differentiation batches.

For better illustration, a 3D PCA plot was created that visualizes the more prominent effect of the marked difference between different cell lines and batches (Figure 22A; 1st and 2nd dimension of the 'regular' PCA) in contrast to the effect of the Bafilo treatment (Figure 22E; 3rd dimension of the 'regular' PCA). Moreover, the dramatic difference between batches (Figure 22B), between the different hiPSC-CM lines (Figure 22C) and the genetic background (Figure 22D) was also visualized in a 3D PCA plot.

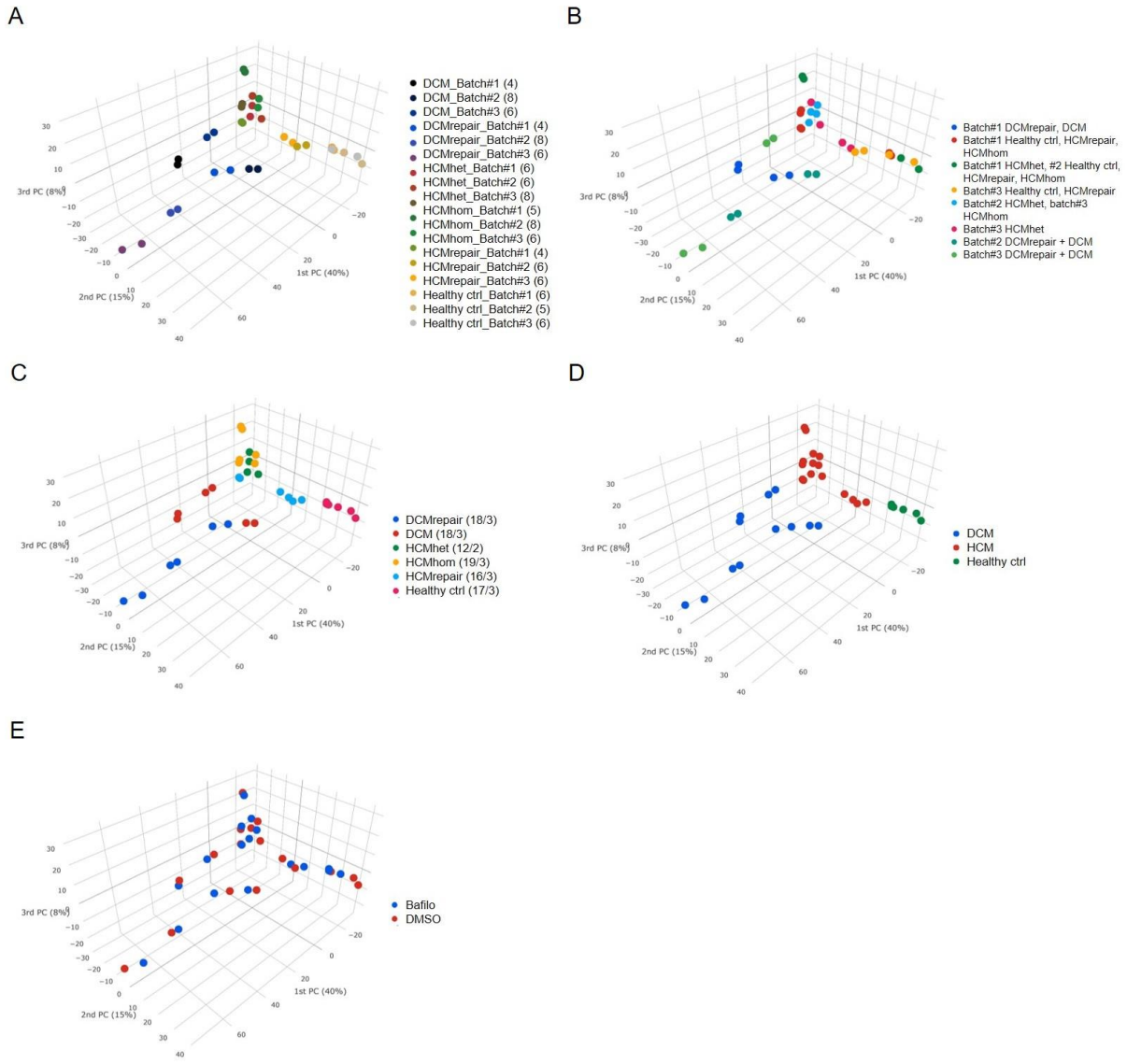

Figure 22: 3D PCA plots of the investigated hiPSC-CM lines. 3D PCA plot of all treated hiPSC-CMs revealed a vast difference between cell lines and batches (A). The dramatic difference between the batches (B), the marked difference between the different hiPSC-CMs lines (C) and the genetic background (D) is shown. The difference between cell lines and batches was stronger than the effect of the actual Bafilo treatment (E). n = number of analysed wells within one batch/number of batches (if not otherwise indicated in the legend).

However, the marked difference between the different genetic backgrounds was also detected by immunoblotting. A representative immunoblot is shown in Figure S3, whereas the quantification is shown in Figure 23. Here, the protein levels of LC3-II and p62 were analysed in hiPSC-CMs of healthy ctrl, HCMrepair and DCMrepair. This analysis revealed a significant difference between healthy ctrl and HCMrepair and DCMrepair for LC3-II and a significant difference for p62 between HCMrepair and DCMrepair. Of note, the significantly lower levels of LC3-II in HCMrepair and DCMrepair hiPSC-CMs were already detected in the evaluation of

the basal levels of the main ALP marker, whereas the tendency towards higher levels of p62 in HCMrepair hiPSC-CMs in comparison to healthy ctrl was not observed (see Figure 17 and Figure 18).

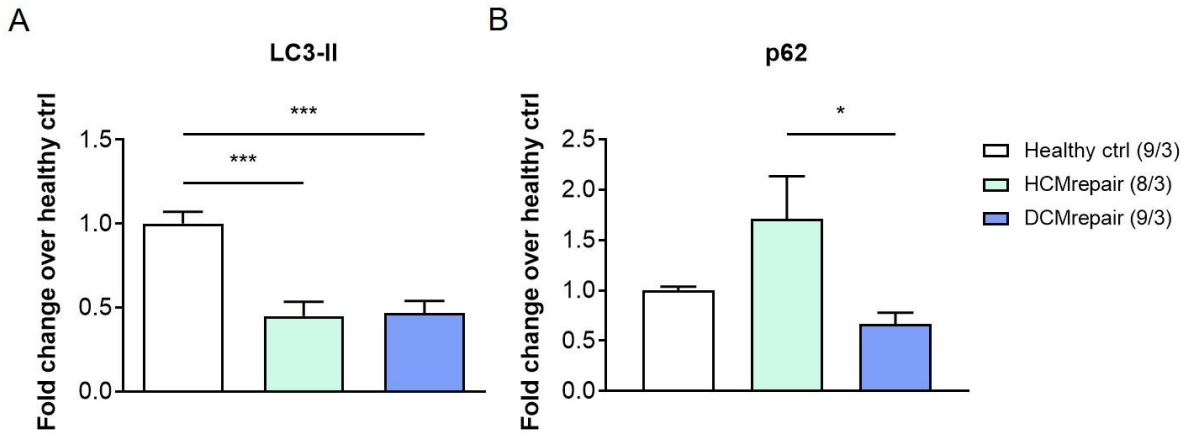

Figure 23: Evaluation of the impact of different genetic backgrounds on the ALP. HiPSC-CMs were cultured for 30 days and treated with 0.05% DMSO. Subsequently, the levels of LC3-II and p62 were investigated by immunoblotting (A + B). Ponceau and cTnT were used as loading controls. Ponceau was used for normalisation. n = number of analysed wells/number of differentiation batches. Data are expressed as mean±SEM (*p<0.5, ***p<0.001, one-way ANOVA, Tukey's post-test).

Although, a batch-to-batch variability was visible in the immunoblots, this effect was not stronger than the Bafilo treatment effect (Figure 24). The protein levels of LC3-II and p62 were analysed in three independent differentiation batches in healthy ctrl hiPSC-CMs. This analysis revealed a variation between the three batches for the protein level of LC3-II and p62 (Figure 24B,C) although this was not significant. Interestingly, the 1st and 2nd batch of healthy control hiPSC-CMs showed a lower variability than the 3rd batch which could be explained by culture conditions. The 1st and 2nd batch were cultured in closer proximity than the 3rd batch.

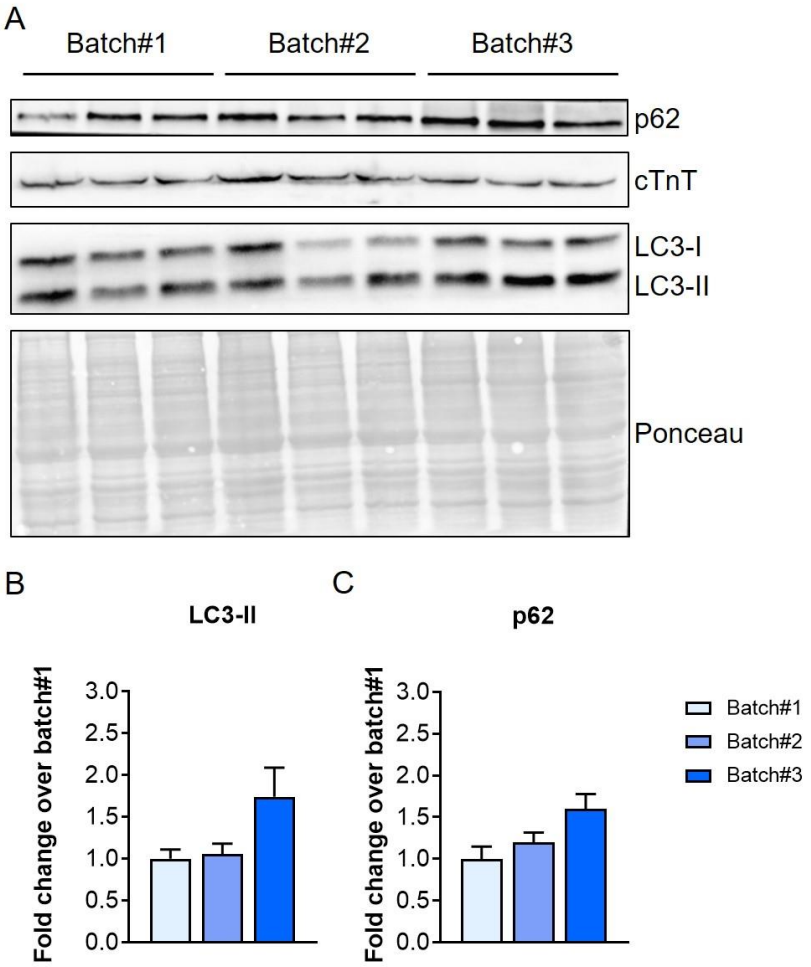

Figure 24: Batch-to-batch variability in healthy ctrl hiPSC-CMs. Three independent differentiation batches of healthy ctrl hiPSC-CMs were treated with 0.05% DMSO and subsequently analysed for the basal levels of LC3-II (B) and p62 protein (C) by immunoblotting (A). HiPSC-CMs were cultured for 30 days. Ponceau and cTnT were used as loading controls, Ponceau was used for normalisation. n = 3 wells/batch. Data are expressed as mean±SEM (one-way ANOVA, Tukey's post-test).

Further, a batch-to-batch variability was also displayed in DCMrepair hiPSC-CMs (Figure 25). Here, a significant difference between the three batches for the levels of p62 were detected (Figure 25C). For LC3-II, there is only a tendency towards lower LC3-II levels in the 3rd batch (Figure 25B). Noteworthy, the 2nd and 3rd batches were cultured in closer proximity than the 1st batch.

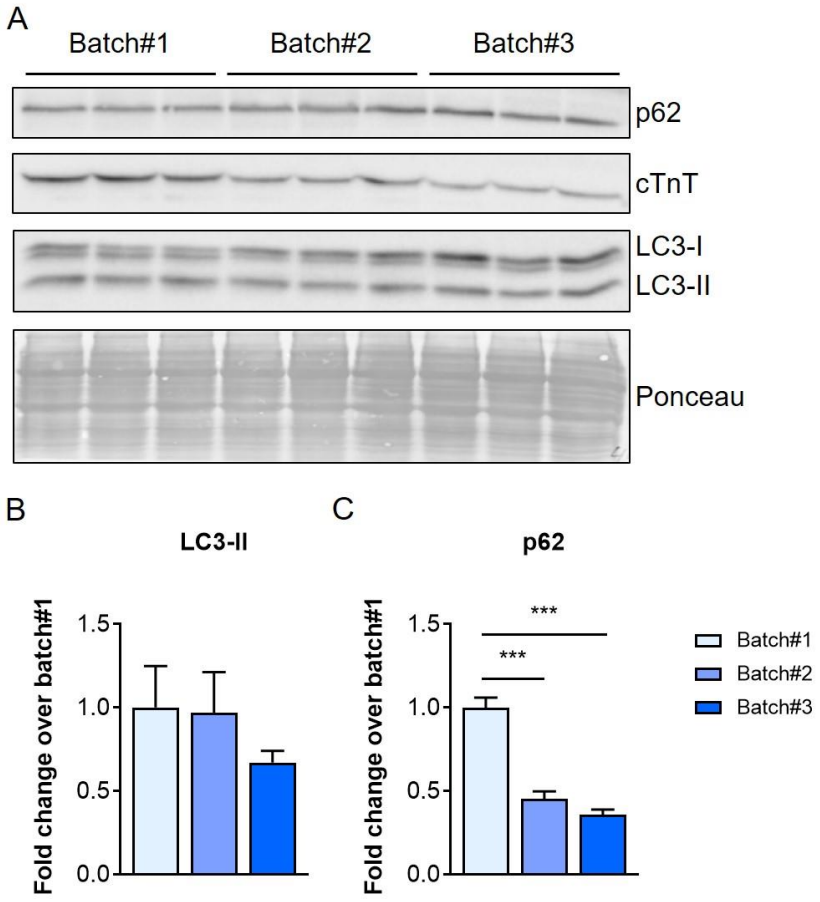

Figure 25: Batch-to-batch variability in DCMrepair hiPSC-CMs. Protein levels of LC3-II (A) and p62 protein (B) were analysed by immunoblotting (A) in hiPSC-CMs that were cultured for 30 days and treated with 0.05% DMSO. Ponceau and cTnT were used as loading controls, whereas ponceau was used normalization. n = 3 wells/batch. Data are expressed as mean±SEM (***p<0.001, one-way ANOVA, Tukey's post-test).

The batch-to-batch variability was much more prominent, when cTnT instead of ponceau was used as a cardiac loading control (Figure 26), demonstrated by a significant difference in LC3-II (Figure 26B) and p62 (Figure 26C) protein levels between the three independent batches of DCMrepair hiPSC-CMs.

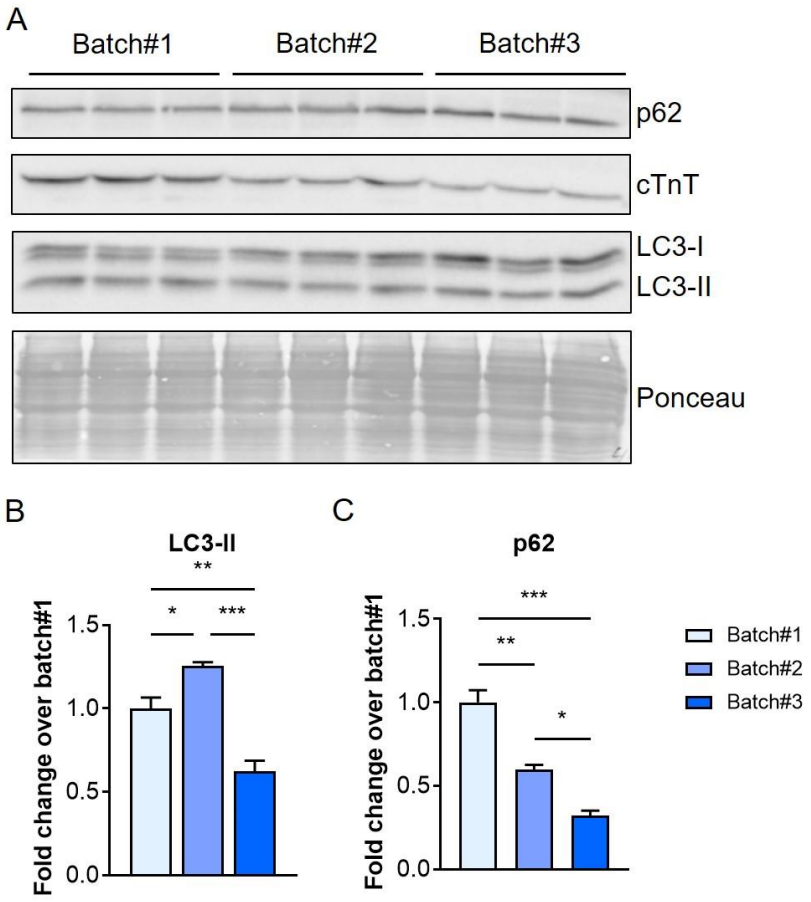

Figure 26: Batch-to-batch variability in DCMrepair hiPSC-CMs when normalization to a cardiac marker. HiPSC-CMs were cultured for 30 days and treated with 0.05% DMSO. The levels of LC3-II (B) and p62 (C) were determined in a subsequent immunoblot (A). Ponceau and cTnT were used as loading controls. cTnT was used for normalisation. n = 3 wells/batch. Data are expressed as mean±SEM (*p<0.5, **p<0.01, ***p<0.001, one-way ANOVA, Tukey's post-test).

Next, the main markers of the ALP were visualized by immunofluorescence staining. Unfortunately, the here used LC3 antibody gave only very weak signals that did not meet our quality standards as any other that we tested. A mTagRFP_mWasabi_hLC3 tandem construct should be used in the future to visualize LC3 and the autophagic flux in hiPSC-CMs.

Nonetheless, p62 and LAMP-2 were investigated by immunofluorescence staining in all investigated 30-day old hiPSC-CMs lines. First, the combination of p62, cTnT and Hoechst was stained in DMSO- and Bafilo-treated healthy control hiPSC-CMs (Figure 27). As expected, an increase in p62 signal after Bafilo treatment was detectible in healthy control hiPSC-CMs. Noteworthy, a prominent staining of p62 was detectible in the nuclear region. cTnT was used as a marker to visualize sarcomeres.

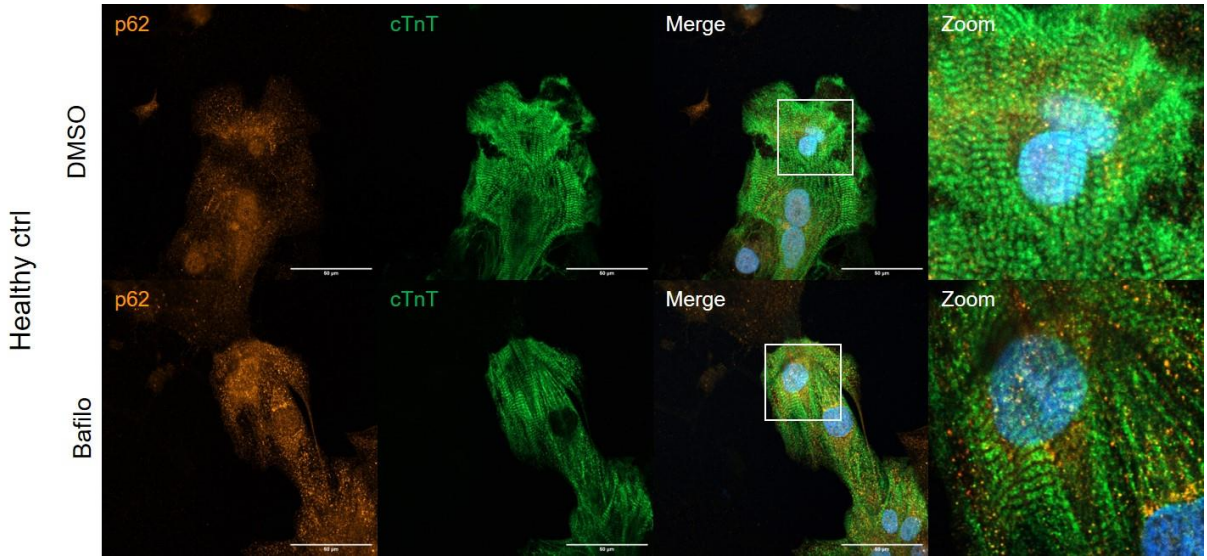

Figure 27: p62 evaluation in 30-day-old hiPSC-CMs healthy ctrl by immunofluorescence staining. Thirty-day-old hiPSC-CMs were treated either with 0.05% DMSO or 50 nM Bafilo for 3 h and stained for p62 (orange), cTnT (green) and Hoechst (blue). The merged images, a zoom of the merged images and the single channels of p62 and cTnT are shown. White box highlights the magnified area (zoom). Scale bar = 50 µm. 40x magnification.

Next, p62 in combination with cTnT and Hoechst was stained in treated hiPSC-CMs of HCMrepair, HCMhet and HCMhom (Figure 28). Overall, the Bafilo treatment did increase the p62 signal intensity in all three HCM hiPSC-CM lines. Of note, the p62 signal intensity seemed stronger in HCMhom hiPSC-CMs than in HCMrepair and HCMhet at baseline and after Bafilo treatment.

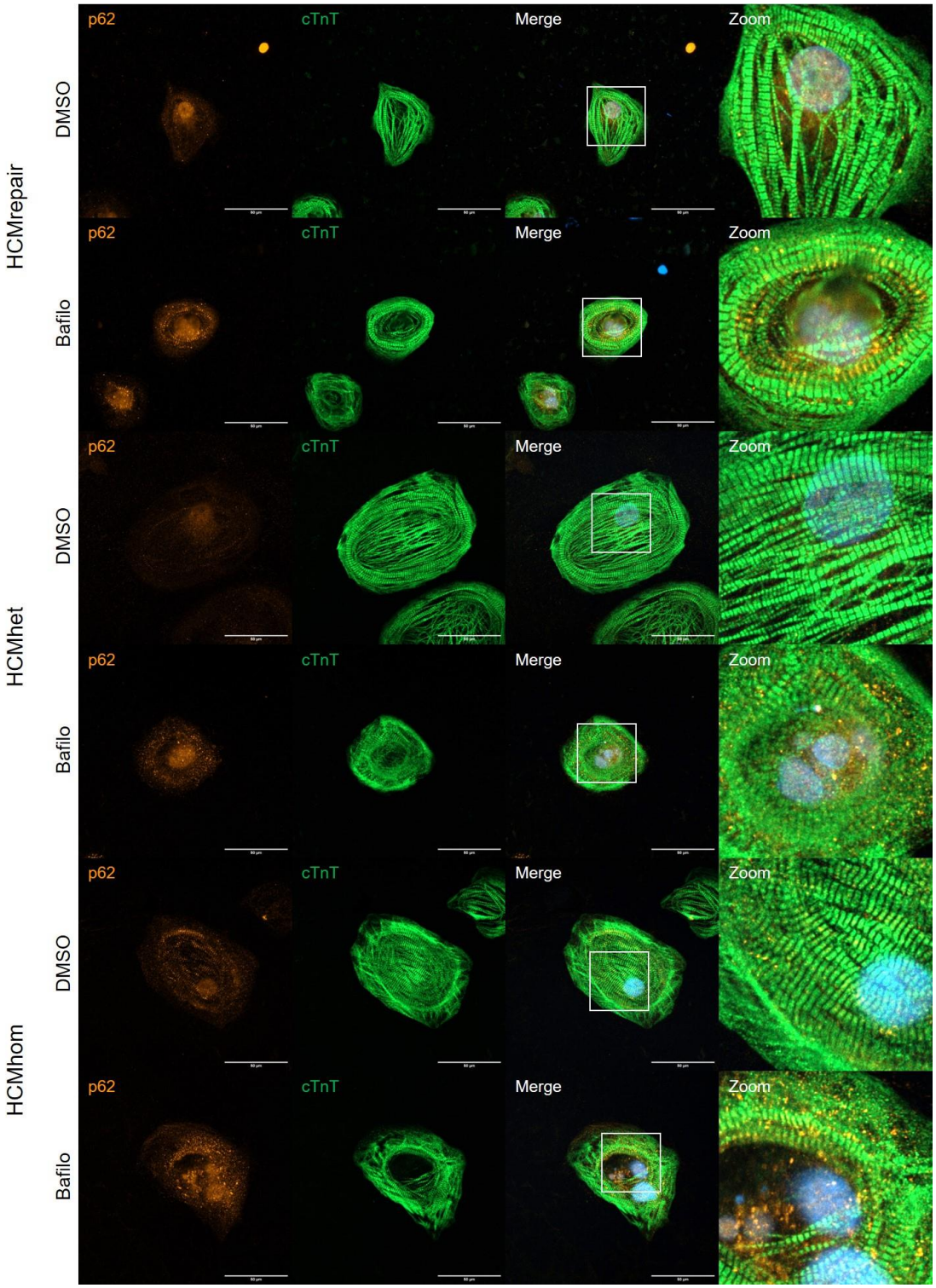

Figure 28: p62 evaluation in HCMrepair, HCMhet and HCMhom by immunofluorescence staining in 30-day-old hiPSC-CMs. Treatment with either 0.05% DMSO or 50 nM Bafilo of HCMrepair, HCMhet and HCMhom hiPSC-CMs and subsequent staining for p62 (orange), cTnT (green) and Hoechst (blue) was performed. Merged images, zoom of merged images and p62 and cTnT single channels are shown. White box highlights the magnified area (zoom). Scale bar = 50 µm. 40x magnification.

Quite striking was the detection of striated structures with p62 after bafilo treatment that was the most visible in all HCM hiPSC-CM lines but most prominent in HCMhom hiPSC-CMs (Figure 29), which also showed a marked decrease in the levels of many components of the sarcomere in the mass spectrometry analysis (data not shown). The detection of striated structures with p62 suggests a higher ALP activity along sarcomeres, although a counter-staining for a sarcomeric protein is missing.

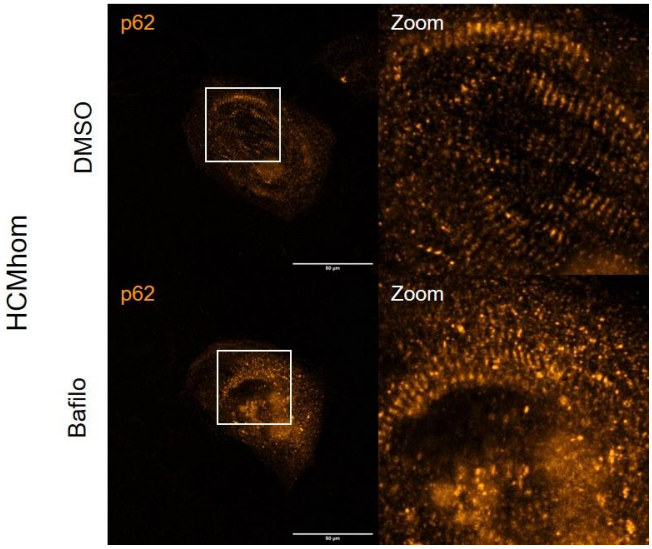

Figure 29: p62 immunofluorescence staining in HCMhom hiPSC-CMs. Thirty-day old hiPSC-CMs of HCMhom were either treated with DMSO (0.05%) or Bafilo (50 nM) and stained for p62 (orange). The single image as well as a zoom of it is shown. Noteworthy is the nice striation of the sarcomere visualized with p62 staining. White box highlights the magnified area (zoom). Scale bar = 50 µm. 40x magnification.

Furthermore, DCMrepair and DCM hiPSC-CMs treated with either DMSO or Bafilo were stained for p62, cTnT and Hoechst (Figure 30). Again, the Bafilo treatment induced an increase in p62 signal in both hiPSC-CM lines. Overall, p62 seemed to be quite strong but it is noteworthy that overall morphology was not as ‘beautiful’ as in the other investigated hiPSC-CM lines since fibroblasts were visualized in these images.

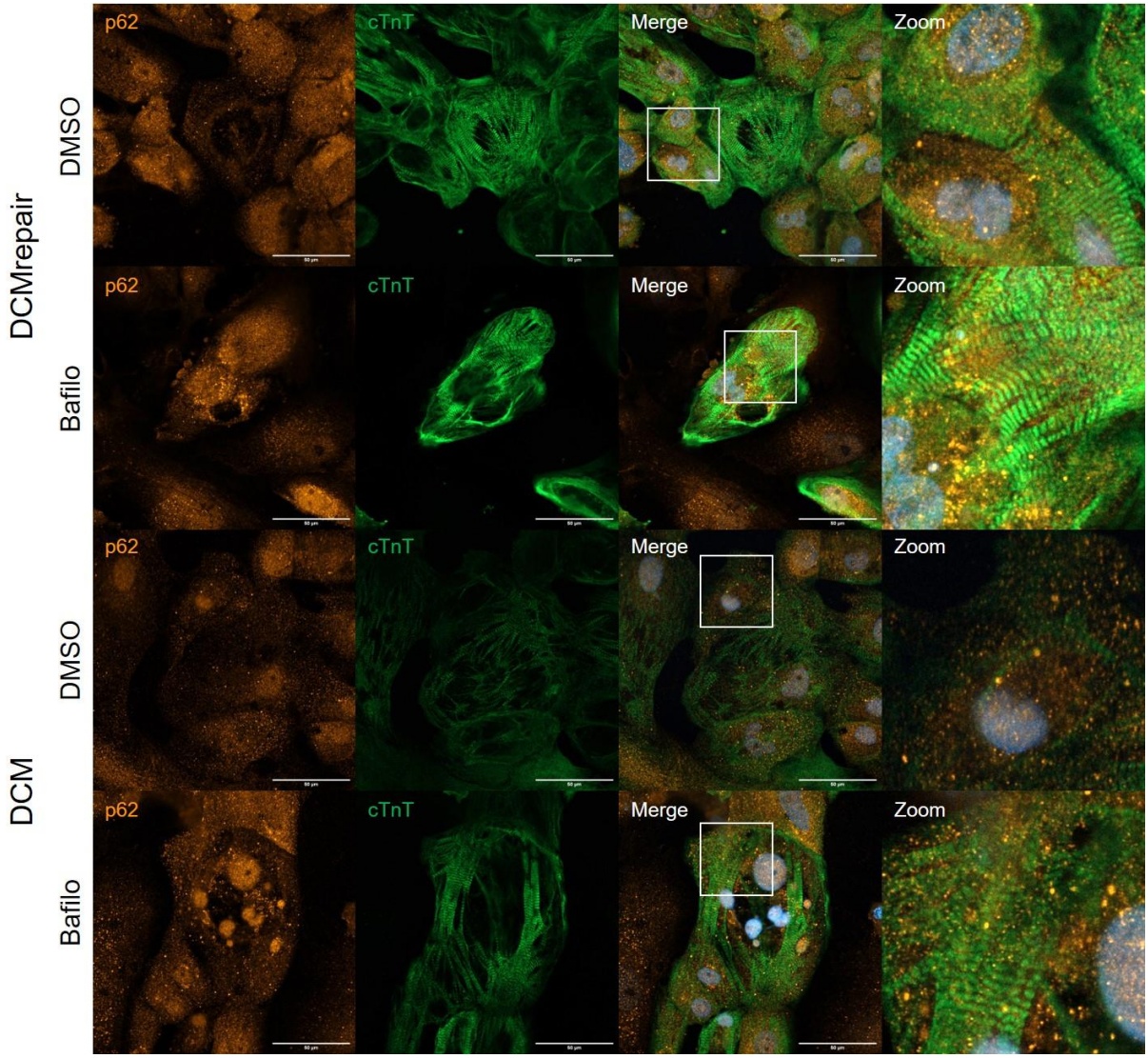

Figure 30: p62 evaluation in DCMrepair and DCM by immunofluorescence staining in 30-day-old hiPSC-CMs. Treatment with either 0.05% DMSO or 50 nM Bafilo of DCMrepair and DCM hiPSC-CMs and subsequent staining for p62 (orange), cTnT (green) and Hoechst (blue) was performed. Merged images, a zoom of the merged images and p62 and cTnT single channels are shown. White box highlights the magnified area (zoom). Scale bar = 50 µm. 40x magnification.

To visualize LAMP-2 protein in all investigated hiPSC-CM lines, immunofluorescence staining in combination with titin and Hoechst was performed in untreated 30-day old hiPSC-CMs (Figure 31). The perinuclear localization of LAMP-2 was clearly visible in all hiPSC-CM lines, as well as an even distribution all over the cell. By eye, there was no dramatic difference between the here evaluated hiPSC-CM lines. Titin was used to visualize the striated sarcomere.

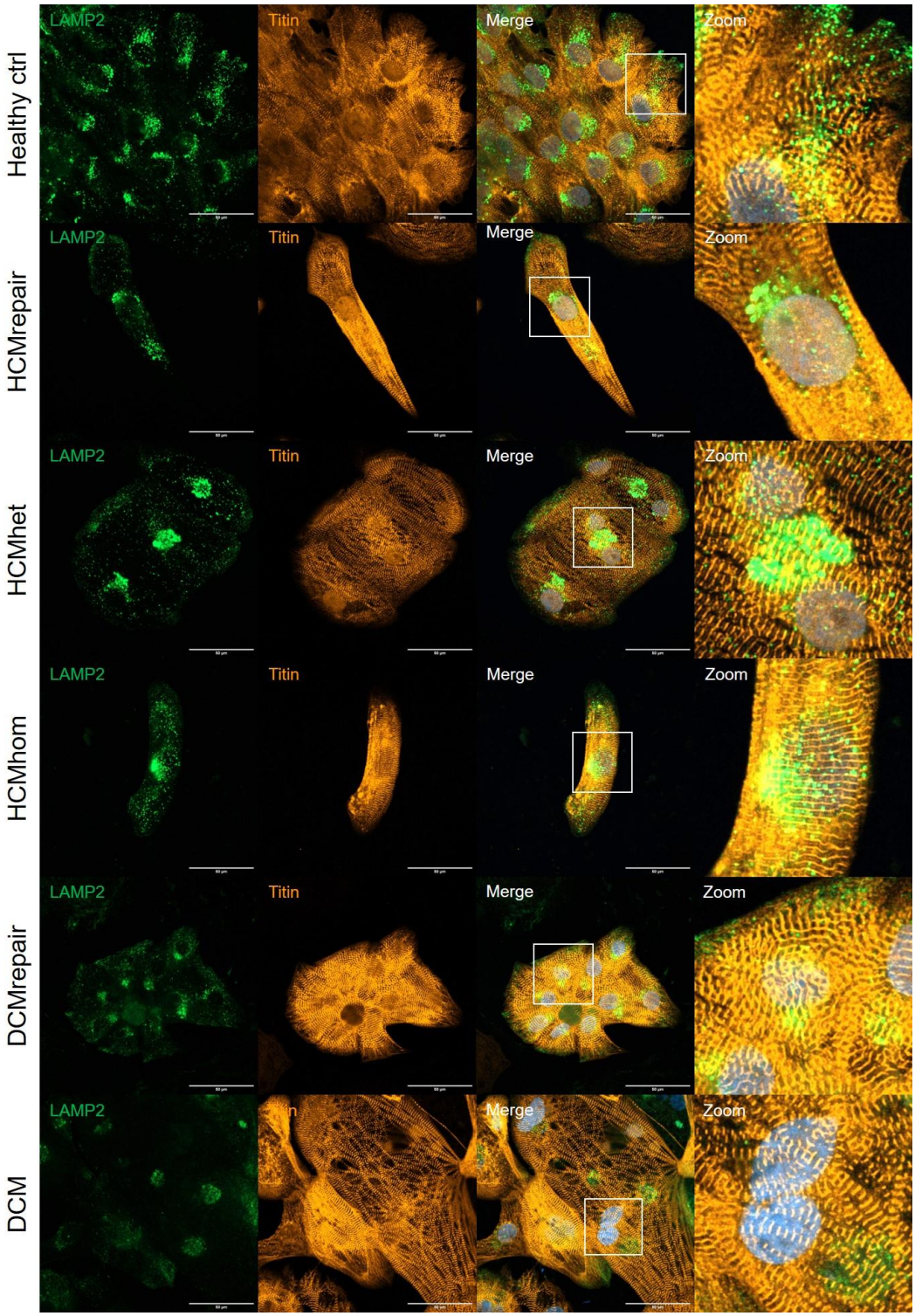

Figure 31: LAMP-2 immunofluorescence staining in all investigated hiPSC-CMs. Untreated healthy ctrl, HCMrepair, HCMhet, HCMhom, DCMrepair and DCM were stained for LAMP-2 (green), titin (orange) and hoechst (Blue). The merged images, a zoom of the merged images and the single channels of LAMP-2 and titin are shown. White box highlights the magnified area (zoom). Scale bar = 50 µm. 40x magnification.

4.2. Generation and validation of *MYBPC3*-deficient hiPSC-derived cardiomyocytes as a human *in vitro* model of HCM

In order to investigate the role of cMyBP-C in hiPSC-CMs and HCM, a stable *MYBPC3*-knockout (KO) hiPSC-line had to be generated. Therefore, the cutting-edge genome editing technology CRISPR/Cas9 was used to mimic a founder mutation from Tuscany, Italy (c.772G>A; Olivotto et al. 2008), aiming to introduce a frameshift mutation that results in the absence of cMyBP-C. In HCM patients carrying this founder mutation, a nonsense mRNA was detected, leading to a PTC in exon 9 due to skipping of exon 6 and thus this would result in a truncated protein (Helms et al. 2014). Further, in an HCM mouse model carrying a *Mybpc3*-targeted knock-in mutation that resembles this founder mutation, three different forms of mRNA were detected. A missense mRNA, which results in a E264K 150 kDa cMyBP-C, a nonsense mRNA, where skipping of exon 6 leads to a PTC in exon 9 and a putative truncated protein, and a deletion/insertion mRNA. Here, the skipping of exon 6 is accompanied by the partial retention of intron that restores the reading frame, resulting in a 147 kDa cMyBP-C (Vignier et al. 2009).

4.2.1. Selection of *MYBPC3* target sequence

The overall CRISPR/Cas9-mediated KO approach for *MYBPC3* was based on a publication from Ran and colleagues (Ran et al. 2013) and was designed with an online tool from MIT (http://crispr.mit.edu/). To validate whether the targeted genomic loci within the here used healthy control hiPSC line ERC018 does not carry any SNPs or mutations, it was amplified by PCR and sent for sequencing (for primers see Table S5; for protocol see 3.2.1). Neither a SNP, nor a mutation was detected (Figure 32) and thus, the MIT tool-based designed sgRNA was suitable to target *MYBPC3* in ERC018. Subsequently the designed sgRNA was subcloned into the plasmid encoding the Cas9 nuclease and GFP (see 3.2.2).

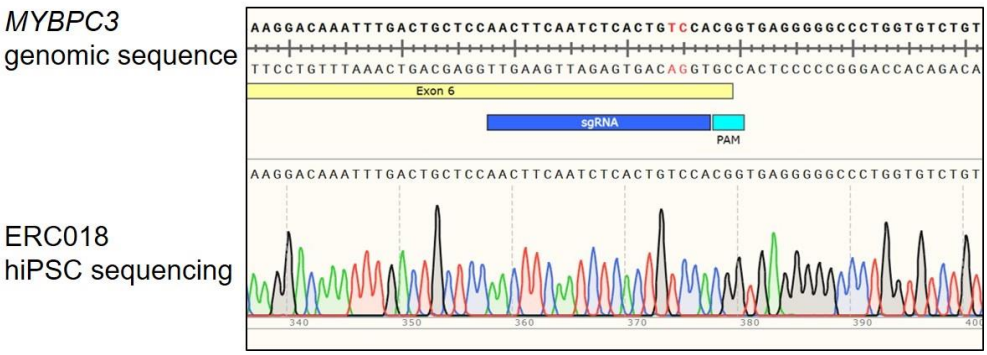

Figure 32: Validation of the genomic loci targeted by the designed sgRNA in ERC018. The database sequence of the targeted genomic loci extracted from the human genome assembly GRCh38/hg38 and the sequencing results of the targeted genomic loci in ERC018 hiPSCs are shown. Sequencing alignment has been created with SnapGene. Red nucleotides

indicate the putative cutting site. Yellow feature = exon 6. Dark blue feature = sgRNA. Light blue feature = PAM.

4.2.2. Nucleofection optimization for ERC018

Nucleofection is the best-known transfection method for hiPSCs and was therefore chosen to genetically modify ERC018. Since, hiPSCs lines differ a lot regarding their nucleofection efficiency and susceptibility an optimization run was performed. Therefore, 200,000 cells were nucleofected with the pmaxGFP vector (0.5 µg) and subsequently analysed by flow cytometry to determine the best combination of nucleofection buffer (P3 or P4) and program (Table 15; for further details see 3.2.3).

Table 15: Overview of the nucleofection optimization of ERC018. Results for each tested condition are shown as number of cells 24 h after nucleofection (5 min measurement at low flow rate), GFP+ cell number and percentage determined by flow cytometry.

Buffer	Program	Cell number	GFP+ cells	Nucleofection efficiency
P3	CA-137	844	100	11.8%
	CB-150	978	73	7.5%
	CD-118	1391	83	6.0%
	CE-118	1209	70	5.8%
	CM-113	885	55	6.2%
	DC-100	814	39	4.8%
	DN-100	1097	57	5.2%
P4	CA-137	422	96	22.7%
	CB-150	918	112	12.2%
	CD-118	1288	72	5.6%
	CE-118	1147	96	8.4%
	CM-113	1158	66	5.7%
	DC-100	960	42	4.4%
	DN-100	1169	47	4.0%

However, due to low survival and many apoptotic cells, the optimization run was repeated in collaboration with Dr. Alexandra Madsen (see Table 16; Löser 2018). The repetition of the optimization revealed that the combination of buffer P3 and program CA-137 or CB-150 was the best combination in terms of high cell survival and nucleofection efficiency and thus subsequently both combinations were used in parallel for experiments.

Table 16: Repetition of nucleofection optimization of ERC018. Again, the table shows for each tested condition the number of cells 24 h after nucleofection (5 min measurement at low flow rate), GFP+ cell number and percentage determined by flow cytometry. Program CA-137 and CB-150 combined with buffer P3 appeared to be the best choices (indicated by red box).

Buffer	Program	Cell number	GFP+ cells	Nucleofection efficiency
P3	CA-137	2450	1186	48.4%
	CB-150	4285	1885	44.0%
	CD-118	3923	1278	32.6%
	CE-118	3421	1171	34.2%
	CM-113	3637	1326	36.5%
	DC-100	2426	900	37.1%
	DN-100	1086	439	40.4%
P4	CA-137	1533	647	42.2%
	CB-150	2419	899	37.2%
	CD-118	3329	1138	34.2%
	CE-118	3197	1076	33.7%
	CM-113	4536	1607	35.4%
	DC-100	2309	622	26.9%
	DN-100	1426	518	36.3%

4.2.3. Nucleofection and single clone expansion

ERC018 hiPSC (p37) cultivated in mTESR or FTDA were nucleofected with 2000 ng pSpCas9-*MYBPC3*-GFP and program CA-137 or CB-150 and visualized 24 h after nucleofection. Figure 33 depicts ERC018 hiPSCs that were cultured in mTESR and either not nucleofected or nucleofected with program CA-137 or CB-150. Many cells nucleofected with program CA-137 showed a strong GFP signal within their nucleus (Figure 33). In contrast, cells nucleofected with program CB-150 resulted in a weaker GFP signal within their nucleus (Figure 33). For both conditions, dead cells were floating in the supernatant but overall CA-137-nucleofected cells showed better morphology. Cells nucleofected in FTDA and subsequently plated in CoM showed a very weak GFP signal and abnormal morphology regardless of the program (not shown), similar to mTESR CB-150-nucleofected cells. As expected, the non-nucleofected control cells only show an autofluorescent GFP signal (Figure 33).

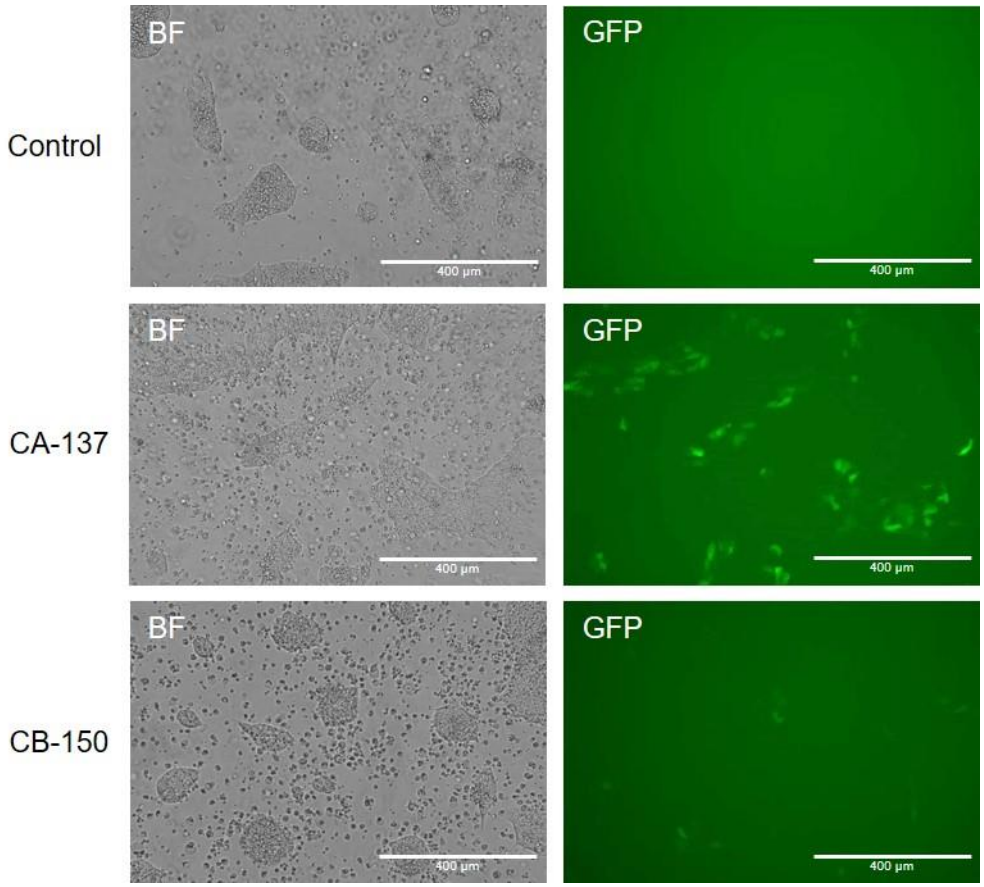

Figure 33: Expression of GFP in ERC018. The level of GFP expression was determined 24 h after nucleofection. Shown is a non-nucleofected control and nucleofected ERC018 cells either with program CA-137 or CB-150 in mTESR. BF = Brightfield; GFP = Green Fluorescent Protein. Scale bar = 400 µm. 10x magnification.

For all conditions, two parallel approaches were performed and combined for fluorescence-activated cell sorting (FACS) 48 h after nucleofection to separate GFP-positive and -negative cells. Figure 34 exemplarily shows the FACS gating strategy for ERC018 nucleofected with CA-137 in mTESR. GFP-negative cells were discarded, whereas single, GFP-positive cells were kept. Additionally, GFP-positive doublets were discarded to prevent contamination of non-fluorescent cells.

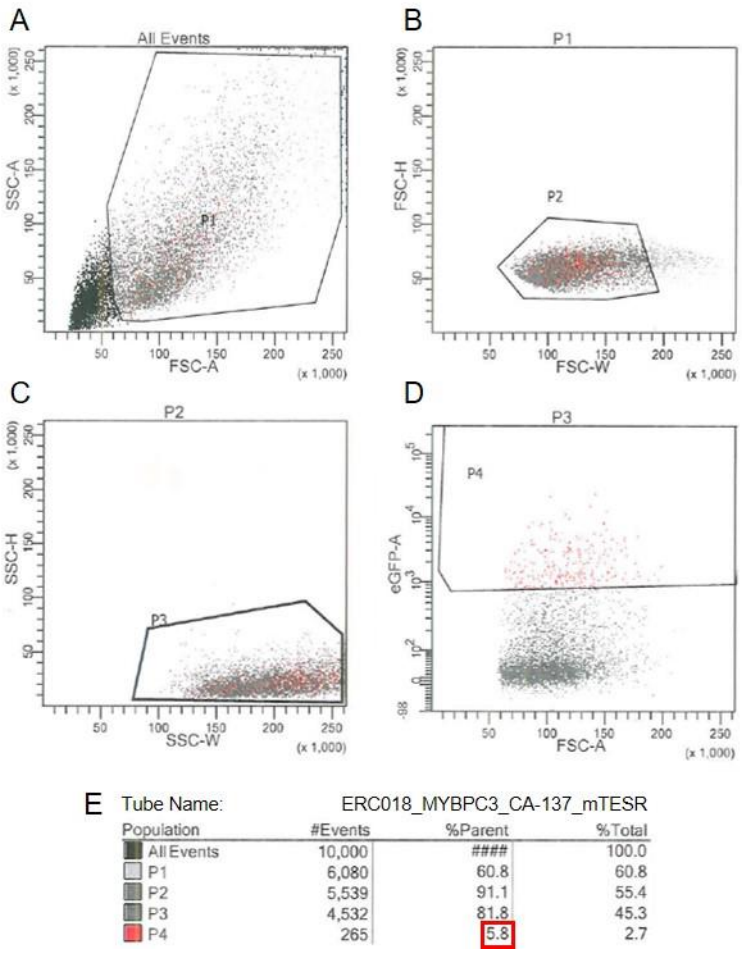

Figure 34: FACS gating strategy for *MYBPC3*-KO in ERC018. Performed by the FACS Sorting Core Unit at the UKE. To exclude dead cells and small debris, cells were distinguished by their size with the forward scatter (FSC) and granularity with the sideward scatter (SSC) (P1; A). Aggregates or doublets were excluded by P2 (B) and P3 (C). P4 represents single, GFP-positive cells (D). E: Population statistics. Red square highlights nucleofection efficiency. A = Area. H = Height. W = Width

Table 17 lists the number of GFP-positive cells and the nucleofection efficiency for all tested approaches. The best result was obtained for ERC018 nucleofected with CA-137 in mTESR with a nucleofection efficiency of 5.8% and 4403 GFP-positive cells. Sorted cells were plated in a 6-well plate for single colony formation.

Table 17: Overview of the CRISPR run.

Approach	GFP + cells	Nucleofection efficiency
CA-137 + mTESR	4403	5.8%
CB-150 + mTESR	908	0.6%
CA-137 + CoM	244	6.5%
CB-150 + CoM	153	0.6%

Cells nucleofected with CA-137 and cultivated in mTESR were split between two wells. Unfortunately, the nucleofected cells cultivated in CoM (both programs) and the CB-150 nucleofected cells in mTESR did not survive the single colony formation and were discarded. For the CA-137-nucleofected cells in mTESR, 35 single colonies were picked and expanded, whereof 26 survived and 9 clones were discarded due to spontaneously differentiation, growth stop or poor morphology. The DNA of 26 surviving clones was extracted and the targeted genomic locus amplified by PCR and analysed by sequencing. This revealed 10 wild-type (WT), three homozygous (hom.), 10 heterozygous (het.) and three compound heterozygous clones (c.het.; Table 18).

Table 18: Overview of CRISPR clones. The number of WT, hom., c.het. and het. clones were determined.

Clones	Number
Total	35
Surviving clones	26
WT clones	10
Hom. clones	3
C.het. clones	3
Het. clones	10

Figure 35 exemplarily shows the sequencing results for clone#11, clone#14 and clone#15. Clone#11 turned out to carry a homozygous deletion of 10 bp at the Cas9 cutting site on both alleles. Clone#14 showed a shifted alignment with double peaks and clone#15 showed double peaks within the electropherogram. Both indicate either a heterozygous or a compound heterozygous alteration. Therefore, the clones were subcloned to analyse the single alleles which revealed for clone#14 a T insertion on one allele and a 7-bp deletion on the other allele. Clone#15 showed a 7-bp deletion on one allele and one WT allele. However, the 7-bp deletions of clone#14 and clone#15 were not identical. They were slightly shifted within the sequence.

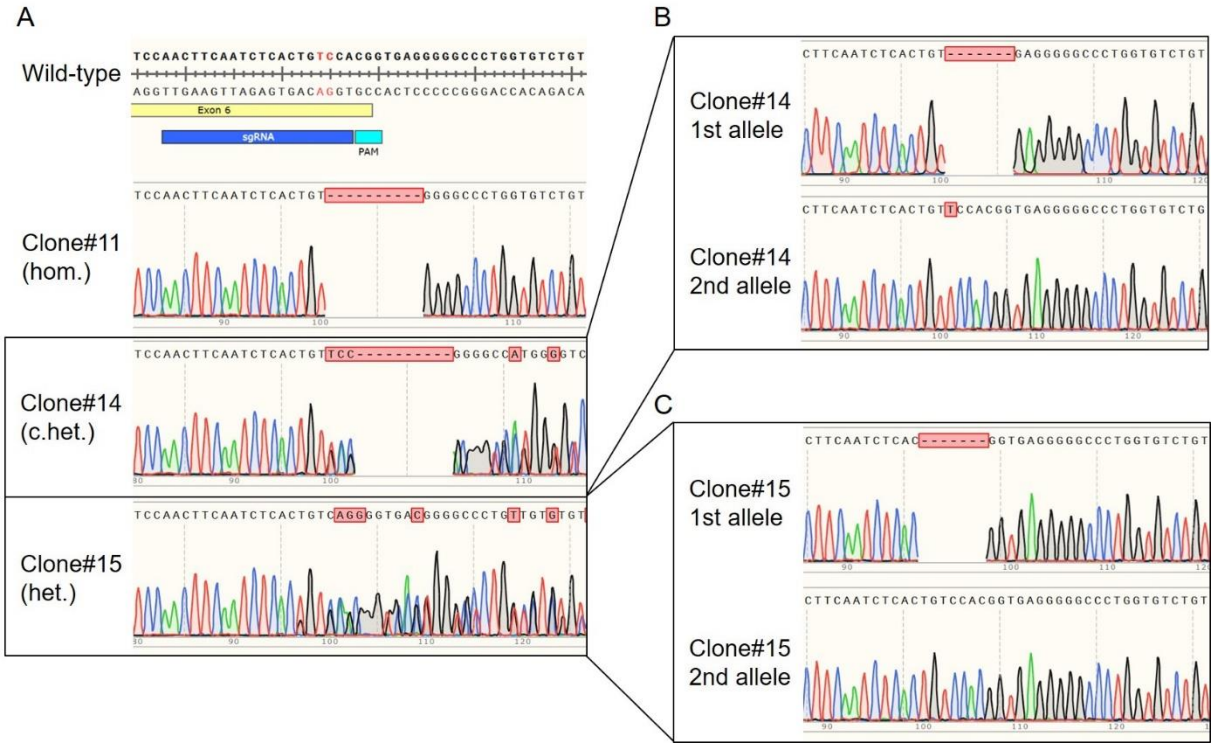

Figure 35: Sequencing results of CRISPR clones. Alignment of hom. clone#11, c.het. clone#14 and het. clone#15 to wild-type sequence is shown (A). Due to initial indistinctive sequence results, allele specific sequencing of clone#14 (B) and clone#15 (C) was performed. Mismatches compared to the database sequence (upper, bold sequence) are highlighted in red within the sequencing results.

To evaluate the genotype of the two alleles individually, subcloning of PCR fragments of exon 6 of *MYBPC3* and the subsequent sequencing of 6 to 7 single colonies per CRISPR clone took place (Figure 36). Sequencing revealed a pure hom. clone#11 whereby 6/6 colonies showed the 10-bp deletion. The c.het. clone#14 showed the T insertion in 4/7 colonies and the 7-bp deletion in 3/7 colonies. For the het. clone#15, 4/7 colonies exhibited the 7-bp deletion and 3/7 colonies the WT sequence. It was not aimed to reproduce the human mutation but to create a KO by mimicking the consequence of the human G>A transition on the last nucleotide of exon 6, leading to the skipping of exon 6, a frameshift and subsequent PTC in exon 9. These data showed that indeed a frameshift and PTC in exon 9 was induced.

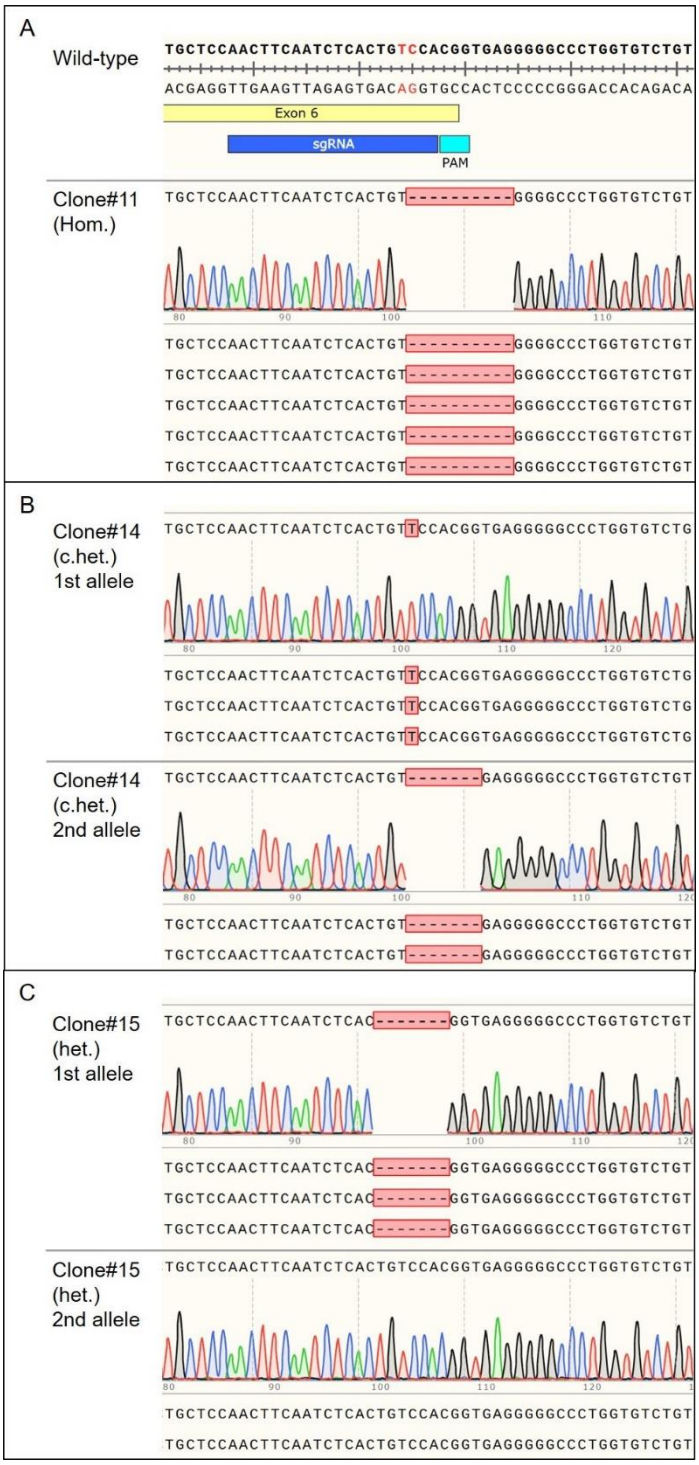

Figure 36: Subcloning of CRISPR clones to evaluate allelic distribution of the introduced indels. The alignment of hom. clone#11 (A), c.het. clone#14 (B) and het. clone#15 (C) to the wild-type sequence is shown.

4.2.4. Off-target analysis

Our CRISPR/Cas9 gene editing approach employed a single sgRNA to guide the Cas9 enzyme to the sequence of interest. This sgRNA consisted of 20 nucleotides and with its relatively short length, it gave rise to putative unintended binding to ‘untargeted’ sequences

within the genome that show high similarity. Unintended DSB at untargeted sequences are called off-target events. The online tool (http://crispr.mit.edu/), which was used to design the overall CRISPR approach, listed putative off-target sites including an off-target probability score. This value reflects the probability of an off-target event based on the number of mismatches between the sgRNA and the targeted genomic sequence. For this approach 254 off-target sites were defined, including 25 within genes. The hom. (clone#11), the c. het. (clone#14) and the het. (clone#15) clones were tested for the Top 10 most likely off-target events (see Table 19; primer sequences (see Table S5).

Table 19: Listing of the Top 10 off-targets for the used sgRNA with their name, position, score, location and mismatch number. The score represents the chance of the sgRNA to bind to the respective putative off-target sequence. Off-target 6 is located within a gene. Thus, the respective gene accession number is shown.

Target	Chromosome	Strand	Position	Score	Gene	Mismatches
OT_#1	7	-1	155492910	6.51	None	2
OT_#2	12	-1	88323889	4.33	None	2
OT_#3	18	-1	40057293	1.46	None	3
OT_#4	15	-1	70268202	1.35	None	4
OT_#5	17	1	37313010	1.29	None	4
OT_#6	1	-1	159827878	1.26	NM_001013661	4
OT_#7	2	-1	193584573	1.04	None	3
OT_#8	15	-1	41867364	0.95	None	3
OT_#9	7	1	147681890	0.84	None	3
OT_#10	19	-1	13493402	0.84	None	4

Sequencing revealed no alteration of genomic loci of the Top 10 putative off-targets, exemplarily shown for off-target #1 (OT_#1) in Figure 37.

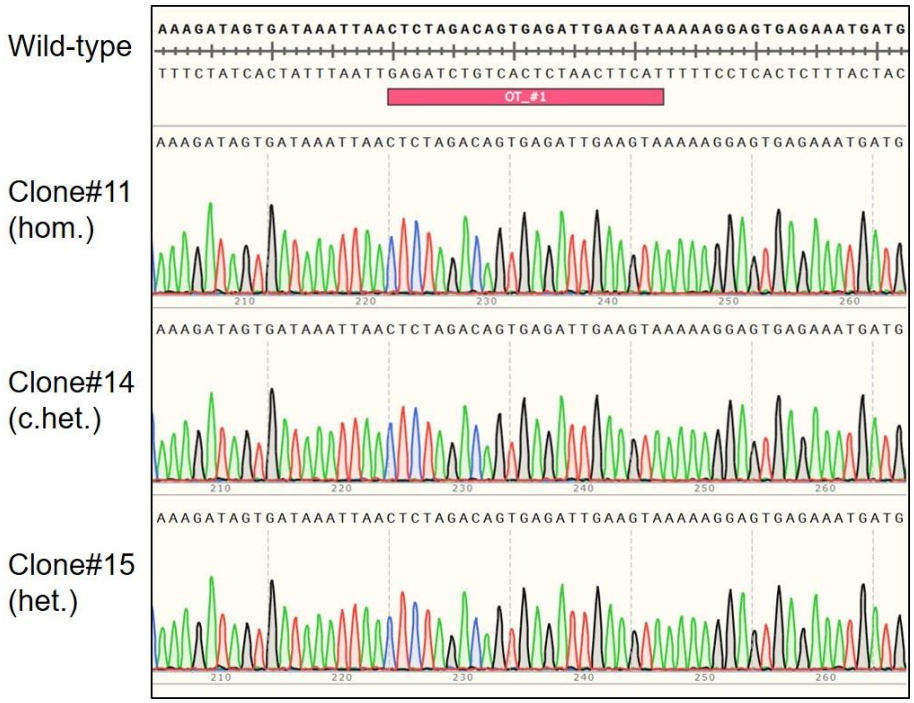

Figure 37: Sequencing results of off-target #1. The alignment of off-target sequence #1 to the sequencing results of all three investigated clones is shown.

4.2.5. Karyotype analysis

It is known that hiPSCs are prone to acquire karyotypic abnormalities that accumulate with prolonged culture time (Taapken et al. 2011). To validate whether culture conditions or gene editing by CRISPR/Cas9 altered the karyotype, the hom. (clone#11; p49), the c.het. (clone#14; p47) and the het. (clone#15; p47) clones were analysed by G-banding. Unfortunately, this revealed a karyotypic abnormality (47, XX+1), showing a trisomy in chromosome 1 (Figure 38). Since all CRISPR clones showed a trisomy in chromosome 1, rather the culture conditions before gene editing and not the gene editing by CRISPR/Cas itself seem to be causative.

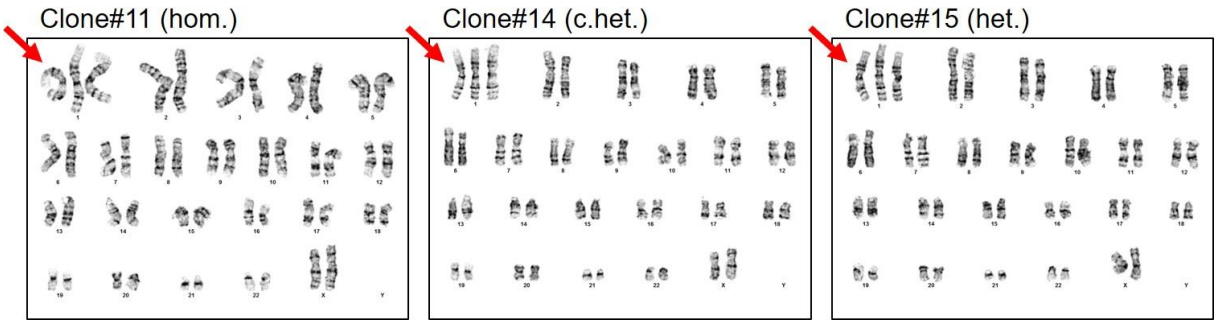

Figure 38: Karyotype analysis of CRISPR clones by G-banding. This analysis was performed by the Department of Human Genetics at the UKE.

To ensure that the high passage number of the tested clones did not cause the karyotypic abnormality, the youngest passage of each clone and wild-type ERC018 (p26) were evaluated

by NanoString Technology (Figure 39). This analysis confirmed the trisomy in chromosome 1 in all three CRISPR clones, whereas ERC018 showed a normal karyotype.

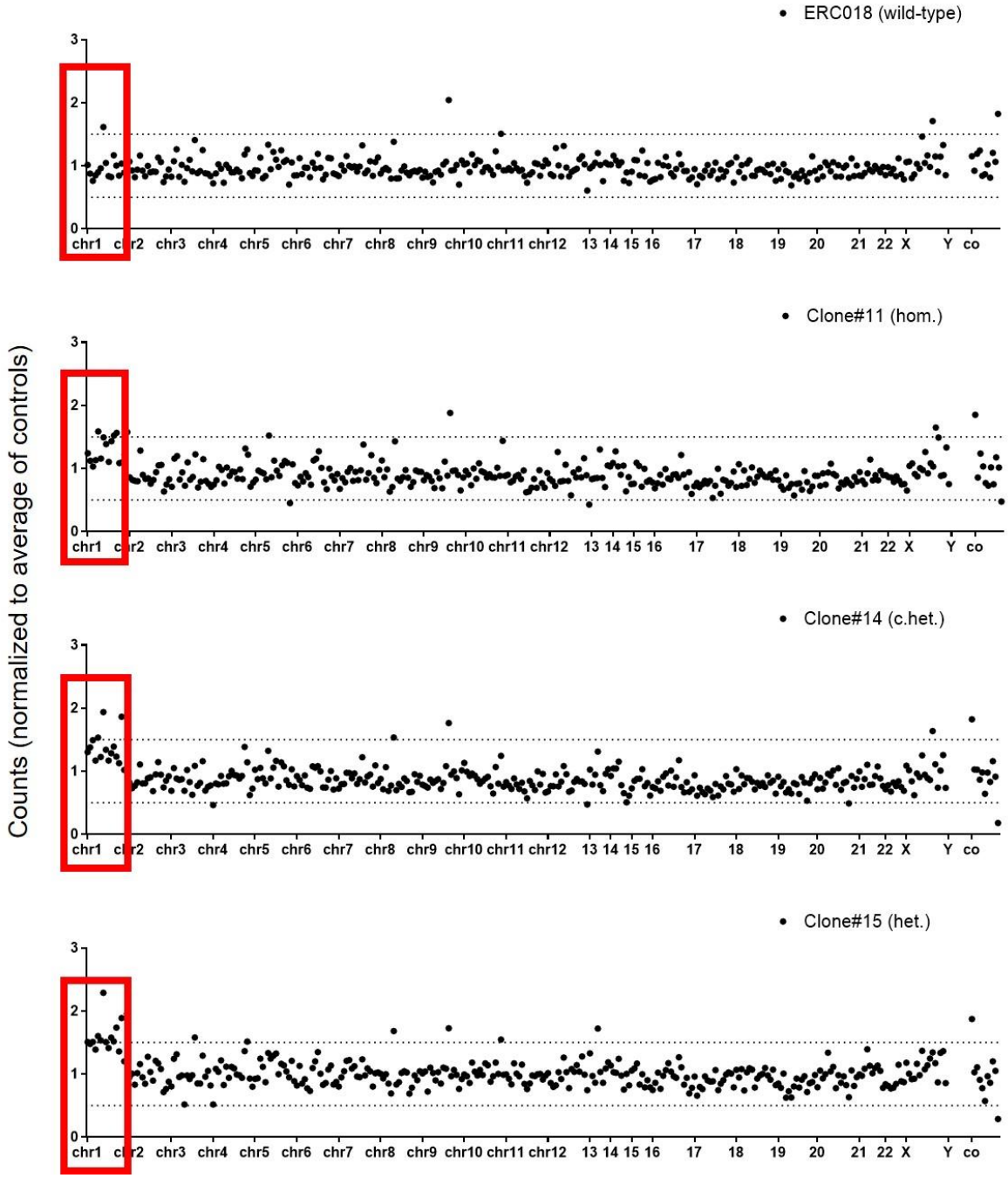

Figure 39: Karyotype analysis of CRISPR clones by NanoString Technology. Evaluation of the karyotype of ERC018 and the three CRISPR clones with the NanoString. Red box highlights chromosome 1.

All generated and used cell lines in this study are shown in Table 20.

Table 20: Cell lines generated and used in this study.

Cell line	Clone	Genetic modification	Karyotype
ERC018	Sv1634	None (WT)	46, XX
Hom.	Clone#11	10 bp deletion (CCACGGTGAG) on both alleles	47, XX + 1
C.het.	Clone#14	1 bp insertion (T) on one allele + 7 bp deletion (CCACGGT) on one allele	47, XX + 1
Het.	Clone#15	7 bp deletion (TGTCCAC) + WT	47, XX + 1

4.2.6. Cardiac differentiation

In order to validate whether the CRISPR hiPSC clones were able to differentiate into beating cardiomyocytes, a protocol developed in our institute was used (Breckwoldt et al. 2017). As Figure 40 visualises, all three CIRSPR clones and wild-type ERC018 hiPSCs were able to form stable and clear shaped EBs that started beating between day 8 to 12 of cardiac differentiation.

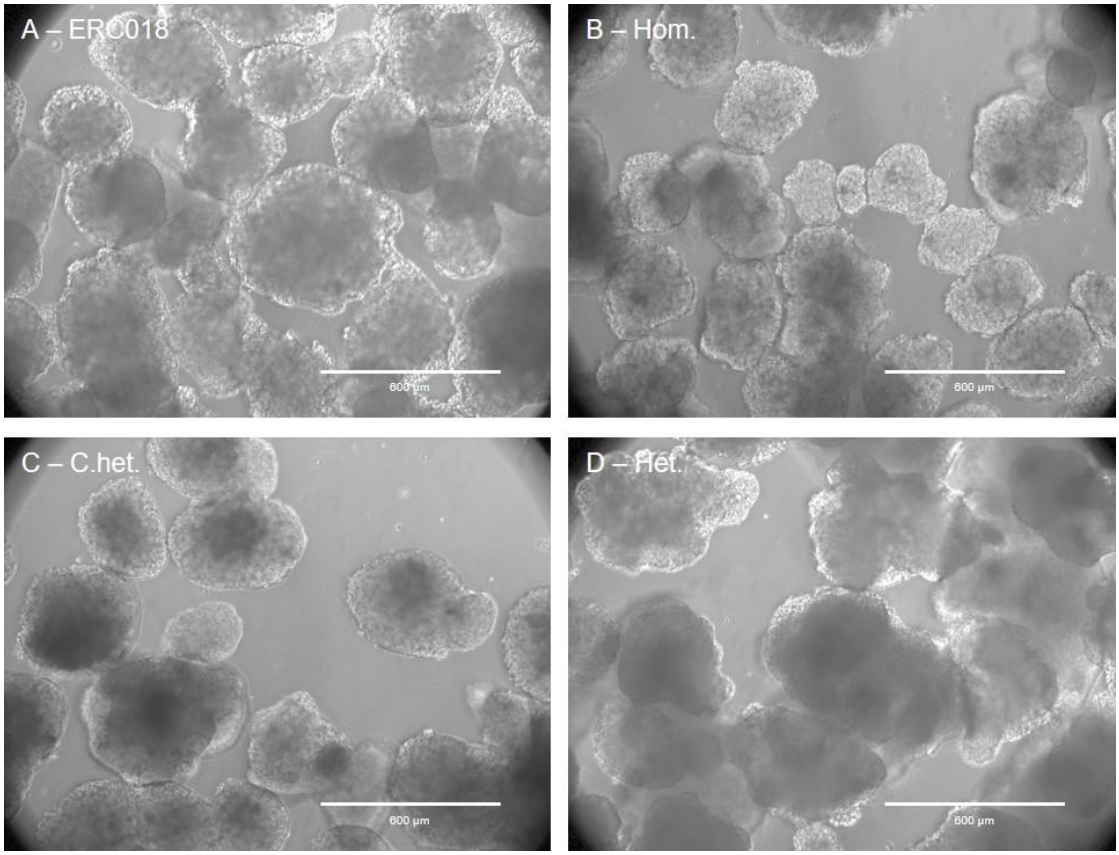

Figure 40: Cardiac differentiation of the investigated cell lines by EB-formation. EBs are shown on day 16 of cardiac differentiation. A = ERC018; B = Hom. clone#11; C = C.het. clone#14; D = Het. clone #15. Scale bar = 600 µm. 10x magnification.

On day 17 of cardiac differentiation, the EBs were dissociated and the proportion of cardiomyocytes was determined by FC, whereby cTnT served as a cardiac marker. Figure 41 exemplarily shows the FC gating strategy with ERC018 hiPSC-CMs. Hereby, 96.2% of the ERC018 were cTnT+. The FC settings were set with the FITC-isotype control that showed a minor cTnT+ cell population (0.31%).

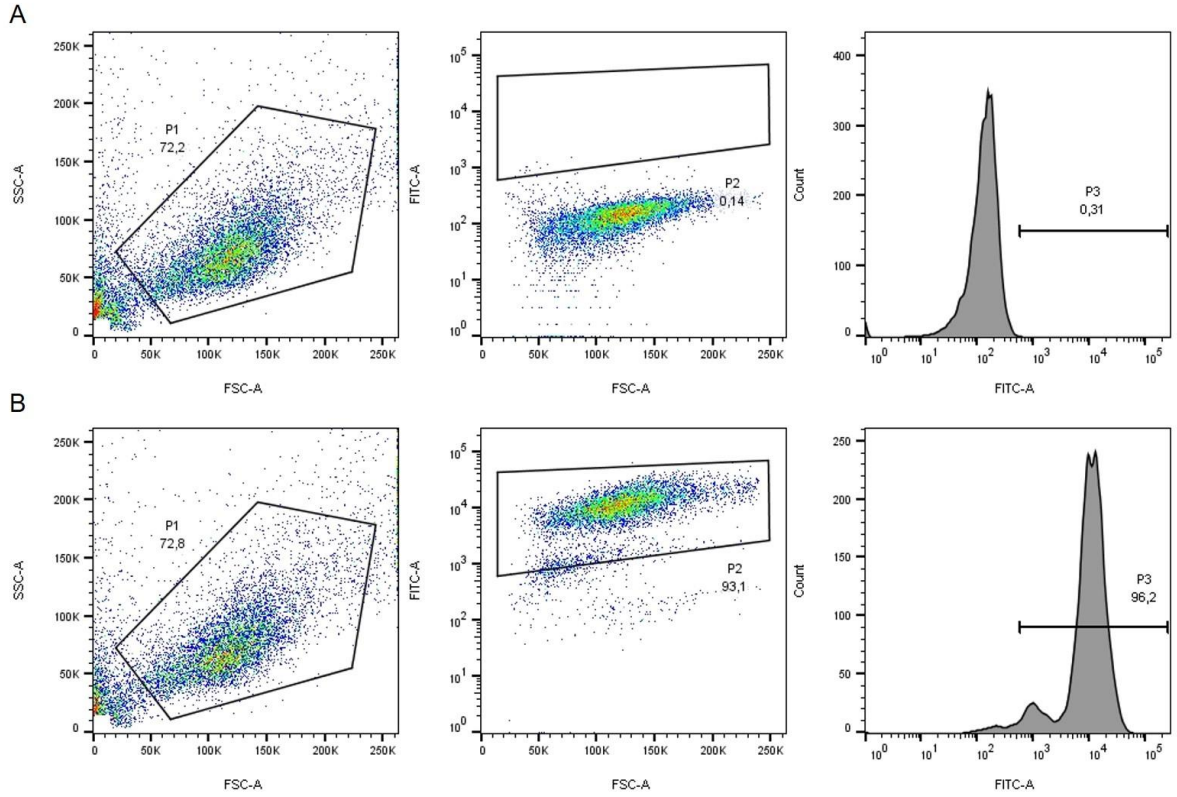

Figure 41: Flow cytometry analysis of hiPSC-CMs after cardiac differentiation. ERC018 hiPSC-CMs were either stained with FITC-Isotype control (A) or FITC-cTnT (B). Cellular debris was excluded from the analysis (P1). Aggregates and doublets were excluded (P2) and the percentage of single cTnT+ hiPSC-CMs (P3) illustrated in a histogram. Analysed with FlowJo (BD Biosciences). A = Area.

To evaluate cardiac differentiation efficiency, the number of output cells (CMs) was divided by the number of input cells (hiPSCs; Figure 42B). Compared to ERC018, all CRISPR clones did not show a significant difference regarding the cardiomyocytes yield after differentiation (Figure 42A), as values ranged from 73.2% to 98% (mean 80.53±2.85% to 93.58±2.29%). The same held true for the differentiation efficiency as this ranged from 0.5 to 0.9 (mean 0.57±0.14 to 1.09±0.36) in all hiPSC lines except for one outlier differentiation for c.het. clone#14 with 1.78. Thus, neither the alteration of *MYBPC3* by CRISPR/Cas9 gene editing nor the trisomy seemed to affect cardiac differentiation.

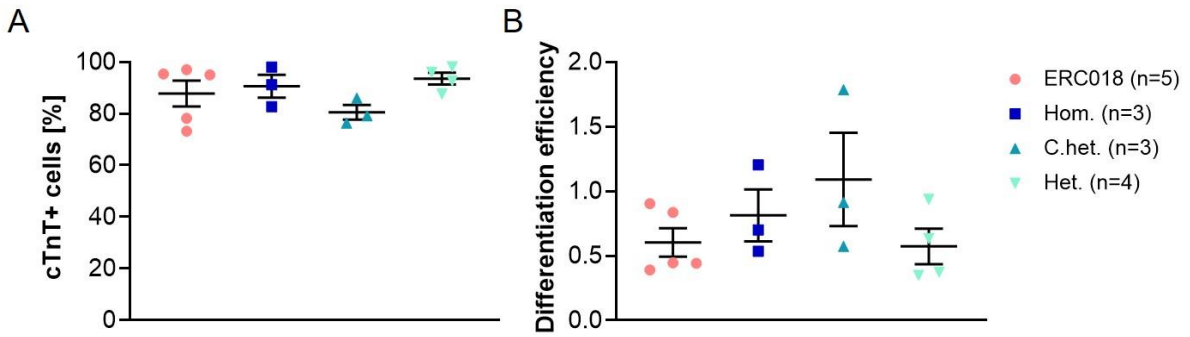

Figure 42: Output of cardiac differentiation. To validate the quality of cardiac differentiation, the percentage of cTnT-positive (cTnT+) cells after differentiation was quantified by FC (A) and the number of output cells was divided by the number of input cells to obtain the differentiation efficiency (B). n = number of differentiations.

Furthermore, CM yield of all performed differentiation runs with all hiPSC lines was determined (Figure 43). The overall differentiation output varied between 33 Mio. to 170 Mio. with one outlier for c.het. clone#14 with 304 Mio. cells. Of course, this parameter is highly dependent on the number of input hiPSCs, in contrast to the differentiation efficiency, but still suited to illustrate the CM yield of all differentiated hiPSC lines. Further, this representation emphasizes the strong variation within the CM yield in the differentiation runs performed for all hiPSC lines.

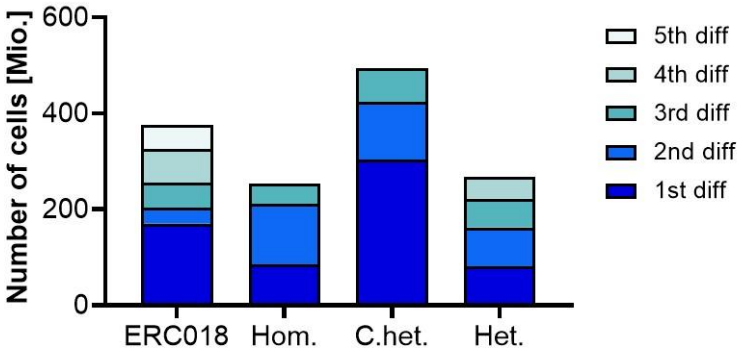

Figure 43: Overview of cardiomyocyte yield of all combined differentiation runs. Five single differentiation runs were performed, whereby ERC018 was differentiated five times, het. clone#15 four times and hom. clone#11 and c.het. clone#14 three times.

4.2.7. Validation of genotype on hiPSC and hiPSC-derived cardiomyocyte level

Genotyping of the generated CRISPR clones after differentiation and thawing verified the genetically modified locus. Figure 44 exemplarily outlines the genotyping approach by analysing hiPSCs and CMs after differentiation and thawing of hom. clone#11.

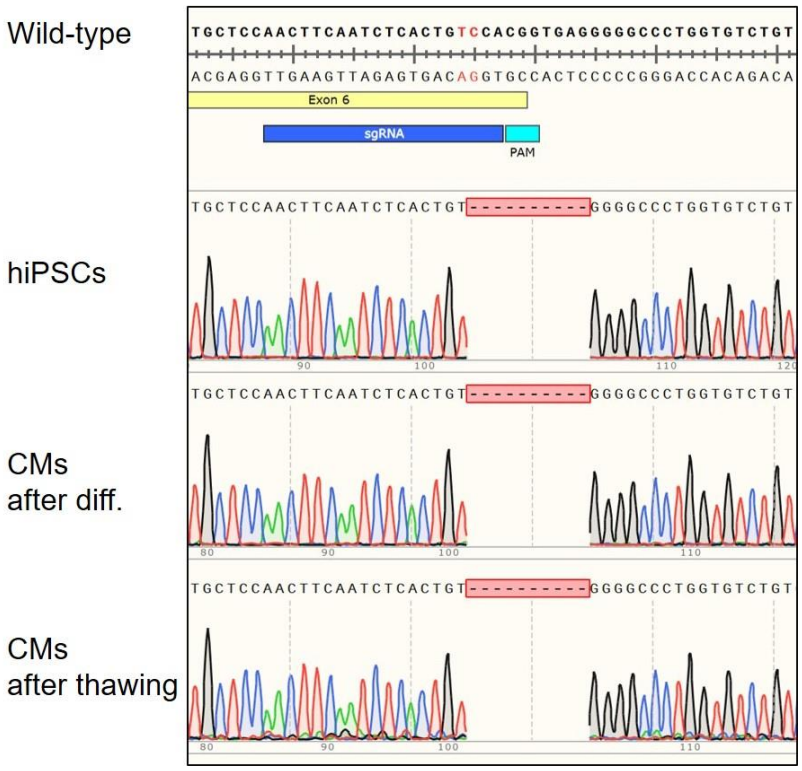

Figure 44: Validation of the genotype of Clone#11 (Hom.). Sanger sequencing of hom. clone#11 on hiPSC and CM level after differentiation (diff.) and after thawing is shown.

4.2.8. Molecular validation of the functional *MYBPC3* knockout

Since the successful alteration of *MYBPC3* by CRISPR/Cas9 putatively introduced a frameshift and subsequently a PTC, it is expected that the nonsense-mediated mRNA decay pathway (NMD) would label the mRNA containing the PTC for degradation to prevent translation of truncated protein. This was expected since HCM patients, as well as a *Mybpc3*-target knock-in HCM mouse model revealed a nonsense mRNA, which results in skipping of exon 6 and a PTC in exon 9 (Vignier et al. 2009; Helms et al. 2014). Therefore, the gene editing of *MYBPC3* on genomic DNA (gDNA) level was validated on mRNA level by RT-PCR and RT-qPCR, and for protein levels by WB on respective extracts from hiPSC-CMs.

To validate the mRNA of *MYBPC3* by RT-PCR, RNA of all hiPSC-CM lines was isolated, transcribed into cDNA and exon 4 – 9 was amplified by PCR and analysed on a 1% agarose gel (Figure 45). The expected band of 473 bp was solely detected for ERC018 and het. clone##15, whereas the c.het. clone#14 showed a slightly smaller band with a smear above. A considerable smaller band of roughly 350 bp was detected for the hom. clone#11, accompanied with a smear in the lane.

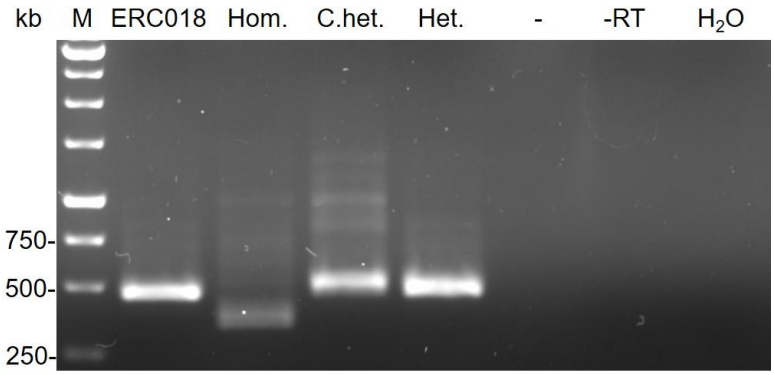

Figure 45: Analysis of *MYBPC3* gene editing on mRNA level. RNA of untreated ERC018, hom. clone#11, c.het. clone#14 and het. clone#15 hiPSC was transcribed into cDNA and exon 4-9 was amplified by PCR. - = empty lane. -RT = cDNA approach without transcriptase. H_2O = Water control. M = 1kb DNA ladder (GeneRuler).

To evaluate the putative forms of mRNA, subcloning according to 3.2.1 was performed. For each CRISPR clone, 16 single colonies were picked, the DNA extracted and sent for sequencing (*MYBPC3* exon 4 fwd primer). Figure 46 visualizes the forms of mRNA that were detected for the CRISPR clones. Sequencing of hom. clone#11 revealed either skipping of exon 6 with a consequential PTC in exon 9 or the retention of intron 6 leading to a PTC in intron 6. Both was expected, since this clone showed a 10-bp deletion that was supposed to introduce a frameshift. Sequencing of c.het. clone#14, revealed either a PTC in exon 9 or the retention of intron 6 with a subsequent PTC in intron 6 for both, the T insertion and the 7-bp deletion. As expected, the het. clone#15 showed the WT mRNA sequence and a frameshift induced by the 7-bp deletion, leading to a PTC in exon 9. Exemplarily sequencing results of all CRISPR clones are shown in Figure S4, Figure S5 and Figure S6, respectively.

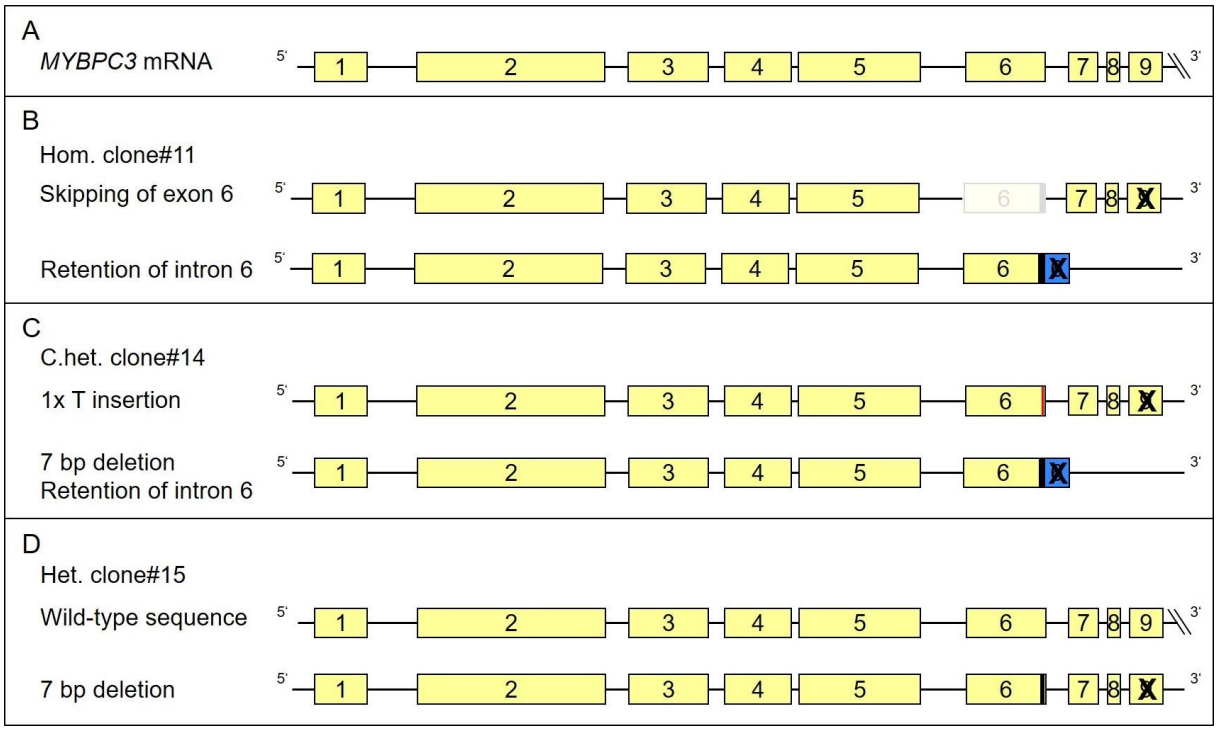

Figure 46: Overview of the mRNA formed for each CRISPR clone. The wild-type mRNA of *MYBPC3* is shown (A). The detected forms of mRNA for the hom. clone#11 (B), the c.het. clone#14 (C) and the het. clone#15 (D) are shown. Yellow = Exons. Blue = Intron. X = PTC. Black block = deletion. Red line = 1x T insertion.

However, additional forms of mRNA were detected due to alternative splicing, resulting either in complete or partial retention of intron 8 or the formation of a new splice site (Figure 47). The partial and complete retention of intron 8 was detected for the hom. clone#11, in both cases resulting in a frameshift and a PTC in exon 9. For c.het. clone#14, the partial retention of intron 8 was solely detected for the allele with the T insertion. Unfortunately, this led to the restoration of the reading frame and a 3864 bp mRNA and a protein of roughly the WT size of 1287 AAs. The 7-bp deletion in c.het. clone#14 caused the formation of a new donor splice site (GTGAG), the subsequent deletion of 2 bp and ‘regular’ splicing of intron 6. Nevertheless, a frameshift was induced with a PTC in exon 9. For het. clone#15, complete retention of intron 8 was only detected for the WT allele, inducing a frameshift and a PTC in exon 9. It is possible that the WT allele shows a partial retention of intron 8 but this was not detected in the present study. This would lead to a 936-bp mRNA, which results in a truncated protein of a length of 311 AAs. Exemplarily sequencing results of all CRISPR clones with their additional isoforms of mRNA due to alternative splicing are shown in the supplement (Figure S7), as well as the sequencing of c.het. clone#14 showing the new splice site (Figure S8).

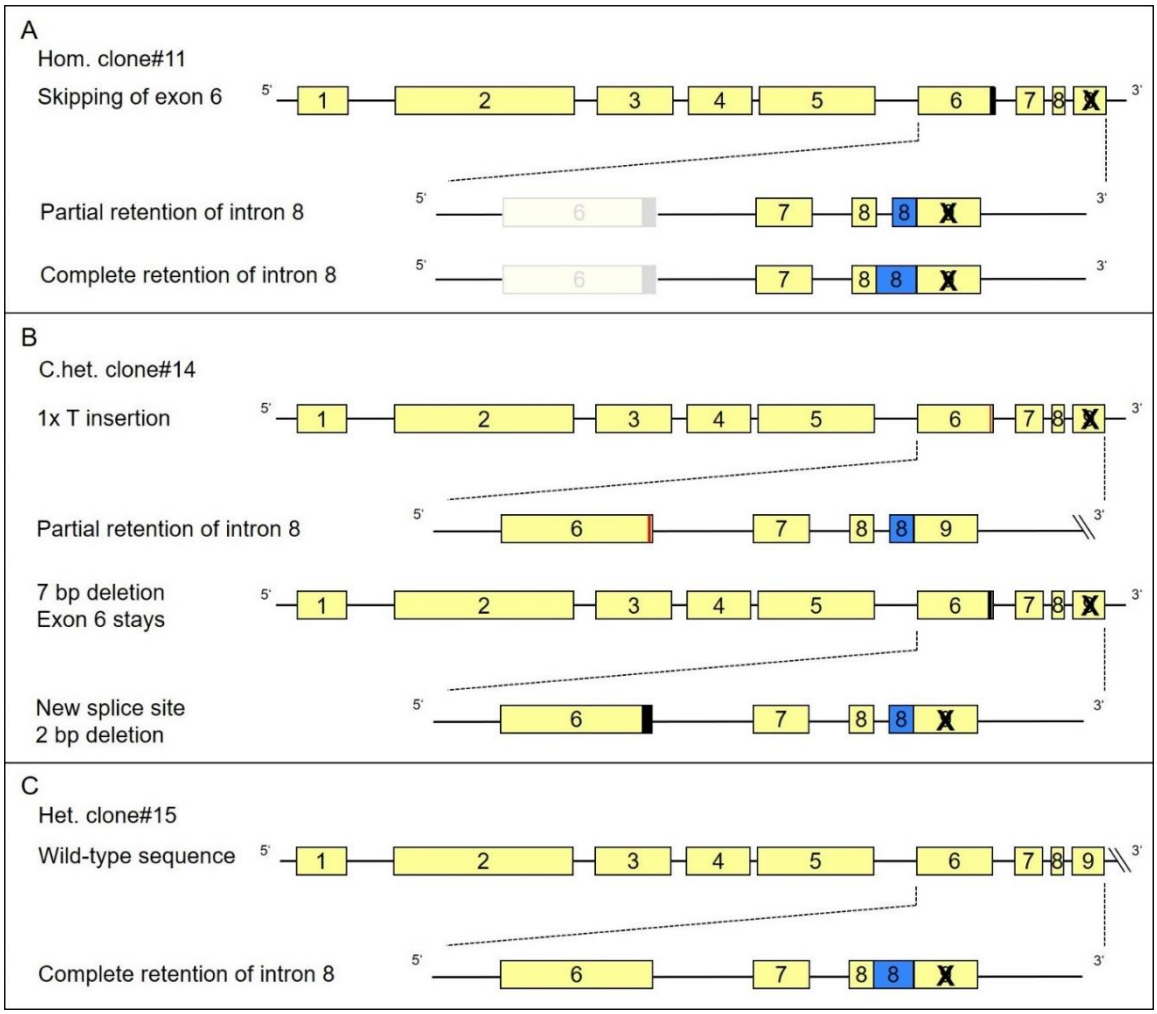

Figure 47: Additional forms of mRNA of all CRISPR clones due to alternative splicing. The additional forms of mRNA of hom. clone#11 (A), c.het. clone#14 (B) and het. clone#15 (C) is shown. Yellow = Exons. Blue = Intron. X = PTC. Black box = Deletion. Red line = 1x T insertion.

Furthermore, for hom. clone#11 the creation of a cryptic splice site would be possible, which would enable proper splicing of intron 6 that would still lead to PTC in exon 9 (Figure S9). A summary of the CRISPR clones with their alteration on gDNA, their forms of mRNA including alternative splicing and putative forms of protein are listed in Table 21. In all cases, except for the T insertion of the c.het. clone#14, the genetic modification of *MYBPC3* has led to a PTC resulting in shorter mRNA and a putative truncated protein.

Table 21: Overview of CRISPR clones in regard to gDNA, mRNA and (expected) protein of cMyBP-C. For gDNA and mRNA analysis subcloning was performed. For gDNA analysis six to seven colonies were picked per clone and for mRNA analysis 15 colonies for each clone as indicated in the brackets. The length of the emerging mRNA, the number of changed/additional amino acids (AAs) with the resulting length of the protein and the expected molecular weight in kDa is listed.

Alteration / Clone	gDNA	mRNA		Protein	
Hom. clone#11	10 bp deletion (6/6)	Retention of intron 6 (2/15)	840 bp	+23 AAs	279 AAs, ~29.5 kDa
		Skipping of exon 6 (9/15)	780 bp	+41 AAs	259 AAs, ~27 kDa
		Skipping of exon 6 + partial retention of intron 8 (3/15)	771 bp	+38 AAs	256 AAs, ~26.5 kDa
		Skipping of exon 6 + complete retention of intron 8 (1/15)	786 bp	+42 AAs	261 AAs, ~27 kDa
		Cryptic splice site (0/15)	891 bp	+41 AAs	296 AAs, ~31 kDa
C.het. clone#14	1xT insertion (4/7)	1xT insertion (5/15)	855 bp	+28 AAs	284 AAs, ~30 kDa
		1xT insertion + partial retention of intron 8 (3/15)	3864 bp	+40 AAs	1287 AAs, ~142 kDa
	7 bp deletion (3/7)	Retention of intron 6 (5/15)	843 bp	+24 AAs	280 AAs, ~29.5 kDa
		+ deletion of 2 bp (new splice site; 2/15)	891 bp	+41 AAs	296 AAs, ~31 kDa
Het. clone#15	Wild-type (3/7)	Wild-type (11/15)	4217 bp	Wild-type	1274 AAs, 140.5 kDa
		Wild-type + complete retention of intron 8 (1/15)	930 bp	+26 AAs	309 AAs, ~33 kDa
	7 bp deletion (4/7)	7 bp deletion (3/15)	891 bp	+41 AAs	296 AAs, ~31 kDa

Additionally, expression of *MYBPC3* was analysed by RT-qPCR, aiming to validate whether stable transcripts were produced. Therefore, the transcript levels of *MYBPC3* were evaluated in hiPSC-CMs of all three CRISPR clones and ERC018 with primers that specifically bind upstream (exon 1 to exon 2; Figure 48A) or downstream (exon 26; Figure 48B) of the genetically modified region. For both primer pairs a significant reduction of ~55% of *MYBPC3* transcript was detected for the hom. clone#11 in comparison to ERC018, whereas the c.het. clone#14 and the het. clone#15 solely showed a reduction of ~30%. Thus, one can assume that the nonsense mRNA is not fully degraded in hiPSC-CMs. Implication of the NMD should be validated by a cycloheximide treatment in the near future.

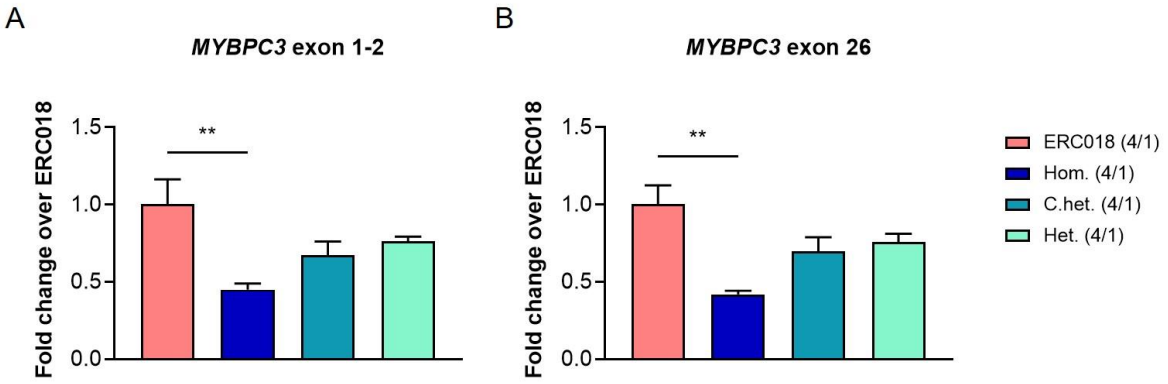

Figure 48: Validation of the *MYBPC3* expression in hiPSC-CMs of ERC018 and the three CRISPR clones. The transcript levels of *MYBPC3* on exon 1 to exon 2 (A) and exon 26 (B) were evaluated by RT-qPCR in hiPSC-CMs of ERC018, hom. clone#11, c.het. clone#14 and het. clone#15. The transcript levels were normalized to *GAPDH* and related to ERC018. n = number of analysed wells/number of differentiation batches. Data are expressed as mean±SEM (**p<0.01, one-way ANOVA, Tukey's post-test).

To validate putative effects of the chromosome 1 trisomy found in all CRISPR clones, the expression of *LMNA* (located on chromosome 1) was exemplarily investigated by RT-qPCR in hiPSC-CMs of ERC018, hom. clone#11, c.het. clone#14 and het. clone#15 (Figure 49). Only c.het. clone#14 showed a ~30% higher *LMNA* transcript levels than in ERC018. Hom. clone#11, het. clone#15 and ERC018 showed similar expression levels of *LMNA*. An increase in *LMNA* should have been found in all three CRISPR clones. Thus, it is assumed that there is not a strong effect of the trisomy of chromosome 1 for *LMNA*, given that only c.het. clone#14 showed a slight increase of ~30%. However, no general statement regarding the trisomy of chromosome 1 can be made since only a single gene on chromosome 1 was investigated here.

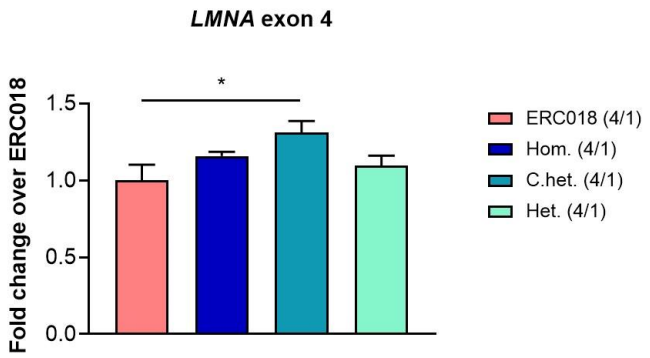

Figure 49: Evaluation of *LMNA* expression in hiPSC-CMS of ERC018, hom. clone#11, c.het. clone#14 and het. clone#15. Exon 4 of *LMNA* was evaluated by RT-qPCR in hiPSC-CMs of ERC018 and the three CRISPR clones to validate the effect of the trisomy on mRNA level. The transcript levels were normalized to *GAPDH* and related to ERC018. n = number of analysed wells/number of differentiation batches. Data are expressed as mean±SEM (*p<0.05, one-way ANOVA, Tukey's post-test).

However, there was a difference in the CT values of the housekeeping gene *GAPDH* between hiPSC-CMs of ERC018 and the CRISPR clones that was significant for the c.het. clone#14 Figure 50). This could explain the higher transcript levels of LMNA mRNA detected for c.het. clone#14.

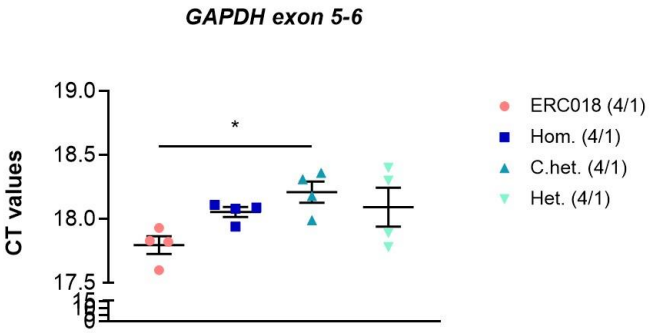

Figure 50: *GAPDH* mRNA levels in the CRISPR clones and ERC018. Exon 5 to exon 6 of *GAPDH* was investigated by RT-qPCR in hiPSC-CMs of ERC018, hom. clone#11, c.het. clone#14 and het. clone#15. n = number of analysed wells/number of differentiation batches. Data are expressed as mean±SEM (*p<0.05, one-way ANOVA, Tukey's post-test).

Next, the level of cMyBP-C protein was determined in all three CRISPR clones and ERC018 by immunoblotting. Therefore, cells were treated either with DMSO (DM; 0.01% or 0.1%) or the proteasome inhibitor MG-132 (MG; 1 µM or 10 µM) to detect putative truncated cMyBP-C. Subsequently the samples were analysed by immunoblotting with an antibody targeting the N-terminal region of cMyBP-C (Figure 51). As expected, ERC018 showed a strong signal for cMyBP-C which was comparable to the signal of the het. clone. This is similar to results obtained in a *Mybpc3*-targeted knock-in mice used as a mouse model of HCM, are known to

have ~80% of WT cMyBP-C protein (Vignier et al. 2009). Truncated cMyBP-C was not detected for the hom. clone. There was a weak signal of cMyBP-C for the c.het. clone#14 that could be explained by the partial retention of intron 8 due to alternative splicing of *MYBPC3* mRNA on the allele with the T insertion. Unfortunately, this led to the restoration of the reading frame and a 3864-bp mRNA and a protein of roughly the WT size of 1287 AAs. The MG-132 treatment did not reveal any form of truncated cMyBP-C. This was expected since truncated cMyBP-C has not been detected yet in (untreated) septal myectomy samples of HCM patients carrying a mutation in *MYBPC3* (Marston et al. 2009; van Dijk et al. 2009). However, treatment with epoxomicin that blocks the chymotrypsin-like proteasome irreversibly, would be suggested to detect putative truncated protein. In the *Mybpc3*-targeted knock-in mice truncated protein was detected in the urea fraction with a custom build cMyBP-C peptide antibody, which was directed against the novel AAs caused by the frameshift. This antibody did not detect wild-type cMyBP-C (Vignier et al. 2009). Since the present study used the crude protein fraction to investigate the putative truncated forms of cMyBP-C, a repetition with epoxomicin and the isolation of the urea fraction would be recommended. Although truncated protein was not detected with MG-132 treatment, a signal of around 30 kDa was detected in the DMSO-treated ERC018 samples that we cannot yet explain. The quantification of the immunoblot is shown in supplemental Figure S10.

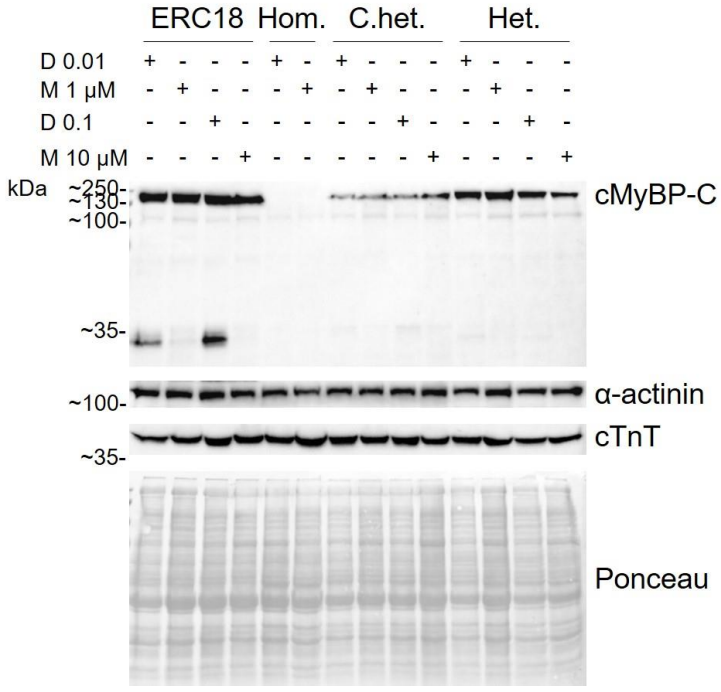

Figure 51: Validation of cMyBP-C KO by immunoblot. All four cell lines were treated either with 0.01% or 0.1% DMSO (DM) or 1 µM or 10 µM MG-132 for 24 h and subsequently analysed by immunoblotting for the protein level of cMyBP-C with an N-terminal antibody (1-120 AAs). α-Actinin 2, cTnT and ponceau were used as loading controls. Ponceau was used for normalization.

To validate whether the MG-132 treatment indeed worked, ubiquitinated proteins were evaluated by immunoblotting (Figure 52). MG-132 is an inhibitor for proteasome degradation and thus treatment should have led to an increase in ubiquitinated protein. The immunoblot was exemplarily performed for ERC018 hiPSC-CMs, which was either treated with DMSO (0.01% or 0.1%) or MG-132 (1 µM or 10 µM). In fact, MG-132 treatment did induce an increase in ubiquitinated proteins, proving its effectiveness. Again, the band that was previously detected with the cMyBP-C antibody at roughly 30 kDa (see above) was detectible solely in the DMSO treated samples and remains unexplainable.

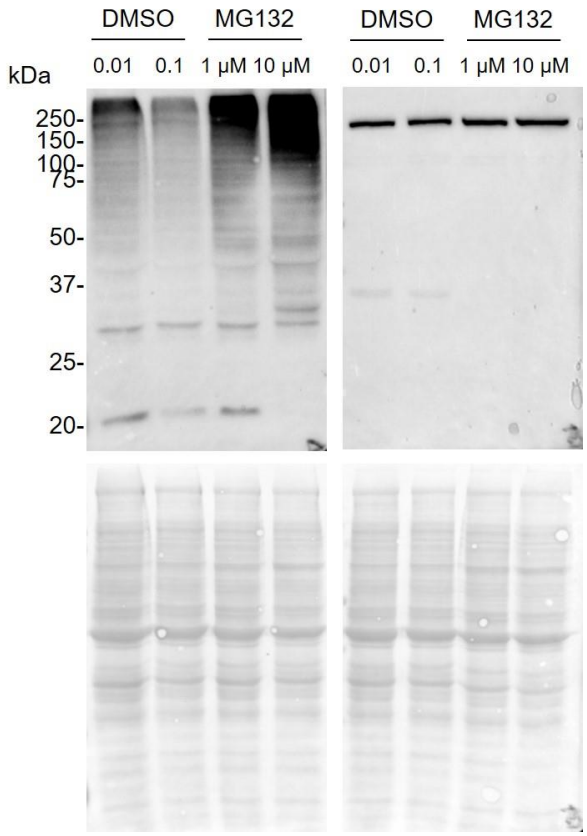

Figure 52: Validation of MG-132 treatment in ERC018 hiPSC-CMs. 30-day old hiPSC-CMs were treated either with 0.01% or 0.1% DMSO or 1 µM or 10 µM MG-132 for 24 h and analysed by immunoblotting for ubiquitinated proteins (upper left) and cMyBP-C (upper right). Ponceau was used to evaluate equal loading (lower part).

4.2.9. Morphological analysis of *MYBPC3*-KO in 2D-cultured hiPSC-CMs

To validate putative effects of the *MYBPC3* knockout on the phenotype, all investigated hiPSC-CM lines were cultured for 30 days in 12-well plates (2D) and morphology was evaluated by light microscopy (every 7 days) and immunofluorescence (7 d and 30 d).

The morphological analysis by light microscopy did not reveal striking differences between the cell lines (Figure 53), although there was an overall tendency towards bigger and faster beating cells in the three CRISPR lines, which would need further follow-up.

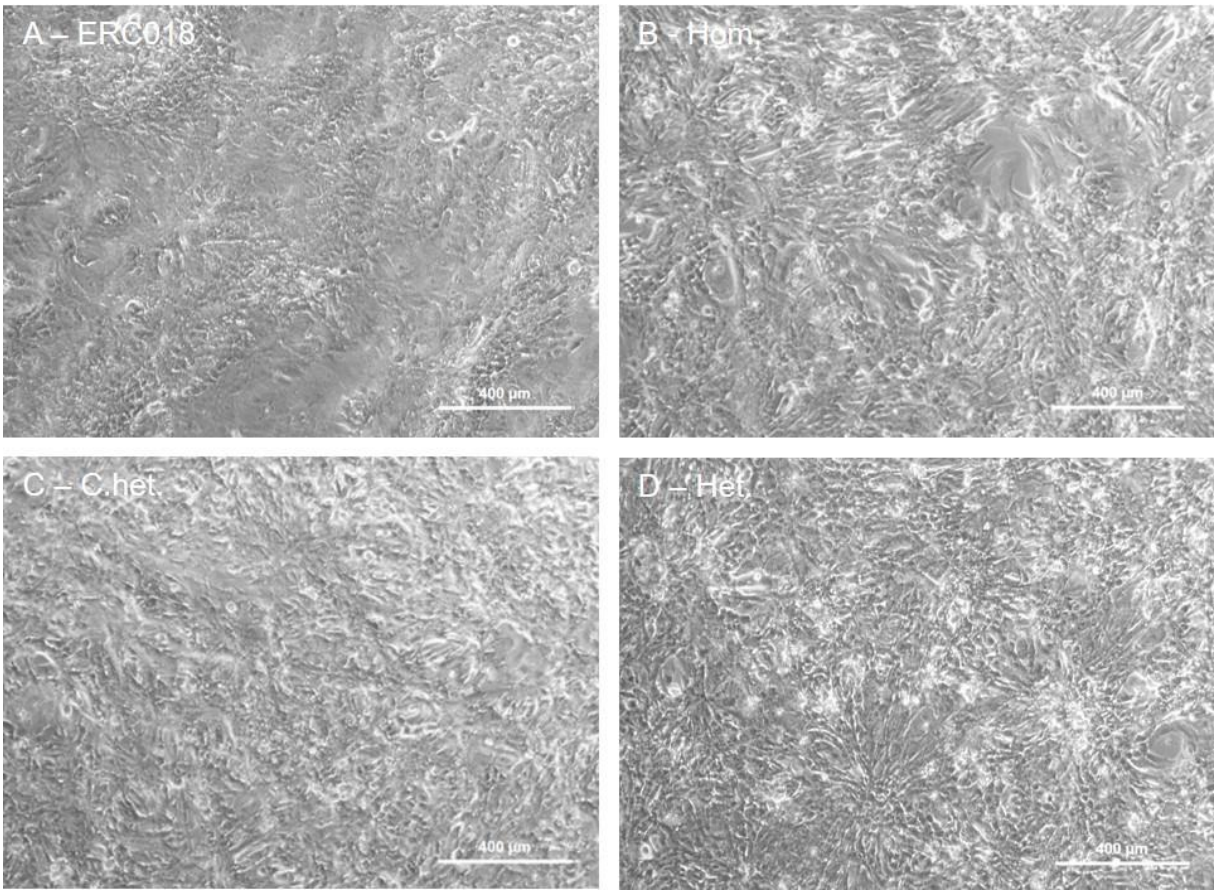

Figure 53: Morphological analysis of 30-day old hiPSC-CMs. ERC018 (A), hom. clone#11 (B), c.het. clone#14 (C) and het. clone#15 (D) were cultured for 30 days and their morphology evaluated every seven days by light microscopy. Scale bar = 400 µm. 10x magnification.

To visualize the KO of *MYBPC3*, hiPSC-CMs of all three clones and ERC018 were fixed at day 7 and stained with titin, cMyBP-C and Hoechst (Figure 54). As expected, ERC018 and the het. clone#15 showed a striated pattern with titin and cMyBP-C (n-terminal antibody from Santa Cruz) in alternation. The hom. clone#11 showed no signal for cMyBP-C, whereas the c.het. clone#14 showed a relative prominent staining for cMyBP-C. Both clones showed a striated sarcomere with titin. The rather prominent cMyBP-C signal found in the c.het. clone#14 could be explained by the alternative splicing of *MYBPC3* on the allele with the T insertion, which restores the reading frame resulting an almost full-length cMyBP-C.

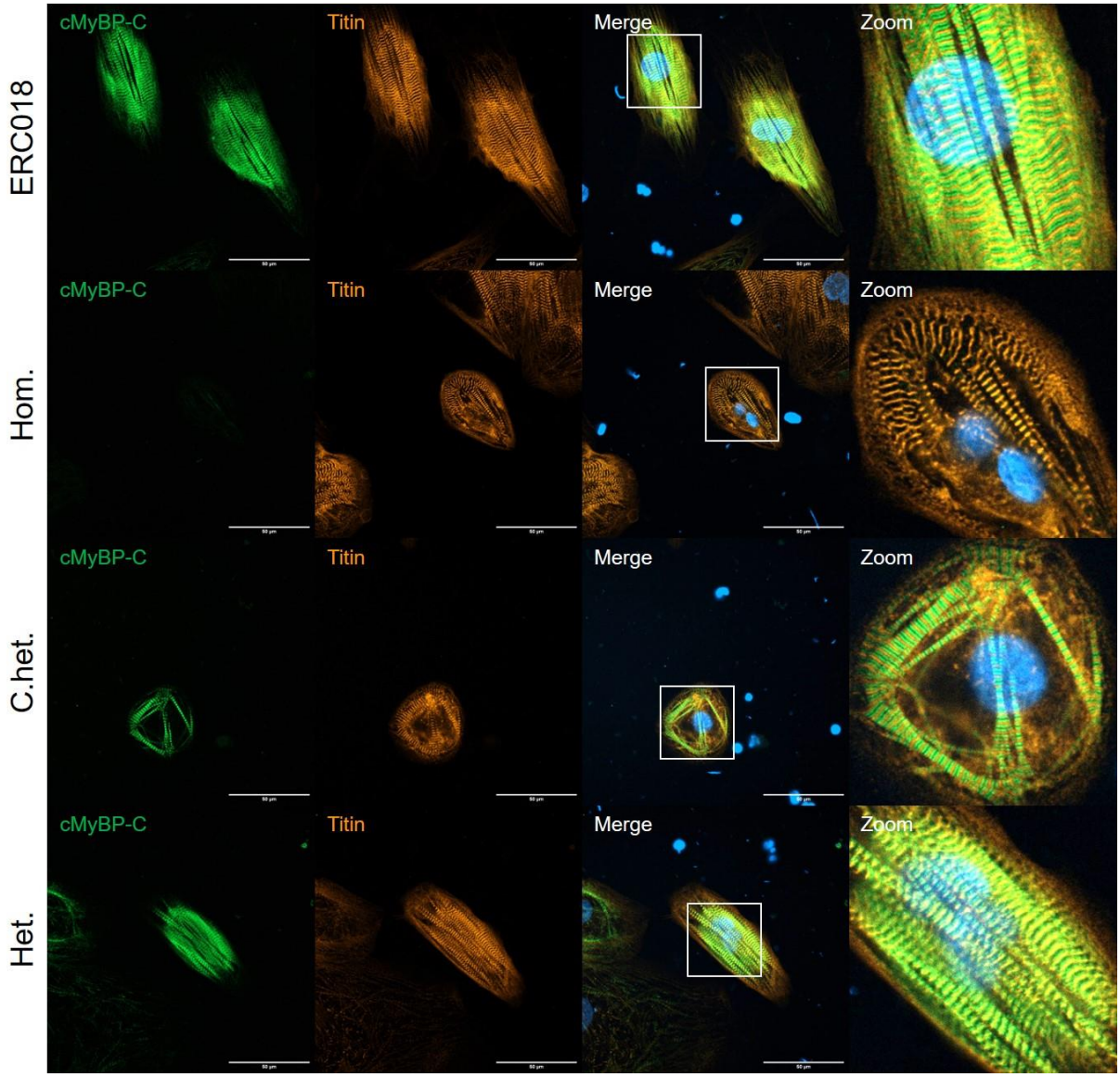

Figure 54: Validation of KO in hiPSC-CMs by immunofluorescence. All three CRISPR cell lines and ERC018 were stained for cMyBP-C (green), titin (orange) and Hoechst (blue). The single channels of cMyBP-C and titin, a merged image and a zoom of the merged image are shown. An N-terminal cMyBP-C antibody (1-120AAs) was used. White box highlights the magnified area (zoom). Scale bar = 50 µm. 40x magnification.

Immunofluorescence staining of cMyBP-C (C0-C1 antibody) in combination with α-actinin 2 was also performed in 7-day-old (Figure 55) and 30-day old hiPSC-CMs (Figure S11). Striation for all hiPSC-CM lines was visible with α-actinin 2. A signal for cMyBP-C was detected for the c.het. clone#14 and the het. clone#15 that was weaker than the one for ERC018. Unfortunately, a faint signal for cMyBP-C that was detected for the hom. clone#11. This was not expected (see above), might be due to antibody un-specificity. This was observed in both, 7-day-old and 30-day-old hiPSC-CMs.

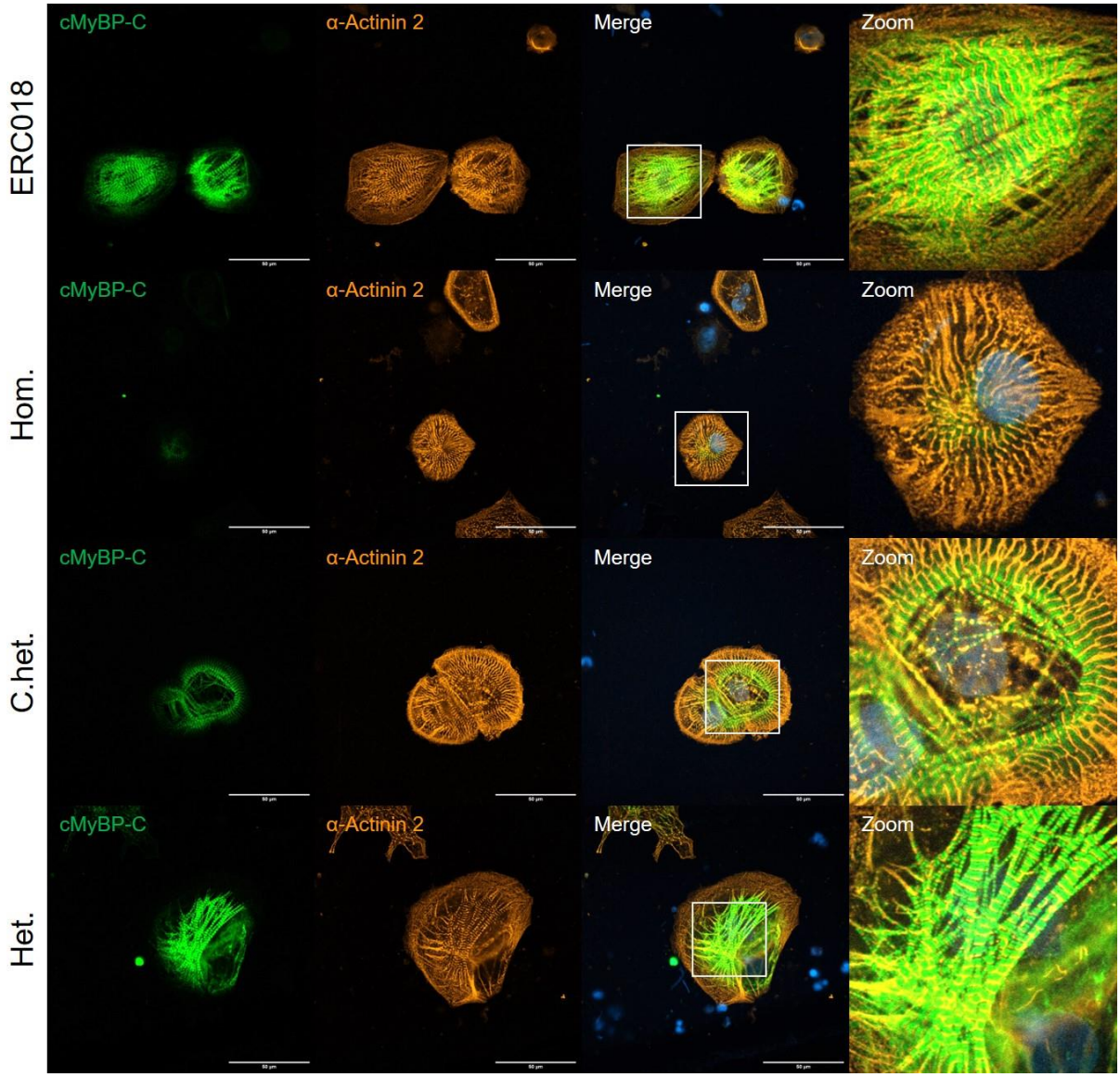

Figure 55: Evaluation of cMyBP-C with C0-C1 antibody in combination with α-actinin 2 in 7-day old hiPSC-CMs. ERC018 and the three CRISPR clones were stained for cMyBP-C (green), α-actinin 2 (orange) and Hoechst (blue). The merged image, a zoom of the merged image, as well as the single channel images for cMyBP-C and α-actinin 2 are shown. White box highlights the magnified area (zoom). Scale bar = 50 µm. 40x magnification.

The sequence of *MYBPC3* was altered by CRISPR/Cas9 gene editing to obtain an HCM *in vitro* model. To assess a putative hypertrophy of this HCM *in vitro* model, morphology was evaluated in 7-day and 30-day old hiPSC-CMs by α-actinin 2 staining. Images were taken in low magnification and subsequently the cell area was analysed with ImageJ (Figure 56). At 7 d *in vitro*, all CRISPR clones showed a significantly smaller cell area than ERC018 (~1800 µm^2 vs. ~3600 µm^2). After 30 days *in vitro* ERC018 showed a smaller cell area of 2804±381 µm^2. In contrast, cell area of all CRISPR clones increased with days in culture, showing significantly higher cell area for both c.het. and het clones than ERC018, whereas the hom. clone did not

significantly differ to ERC018 (hom. clone#11 with 5331±840.3 µm^2, the c.het. clone#14 with 5770±865.3 µm^2 and the het. clone#15 with 7785±1749 µm^2). Morphological analysis indicated myofibrillar disarray (data not shown) that will be analysed in more detail in the near future.

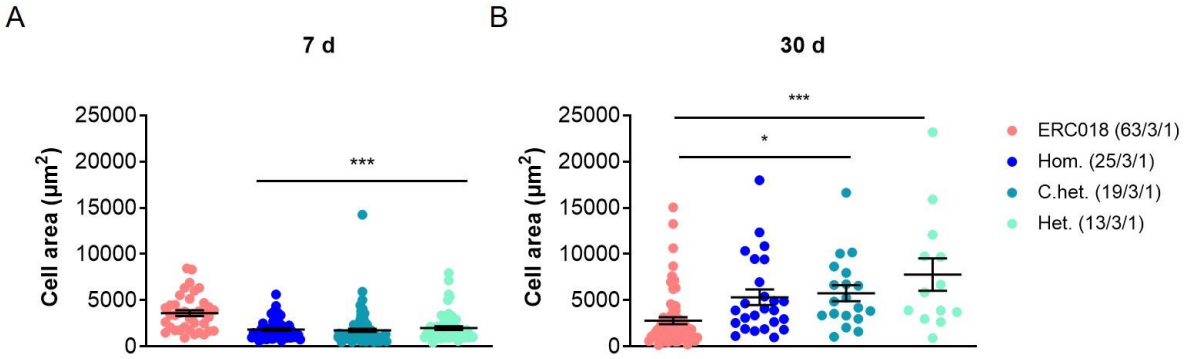

Figure 56: Evaluation of cell area in 7-day- and 30-day-old hiPSC-CMs. ERC018, hom. clone#11, c.het. clone#14 and het. clone#15 were seeded in 96-well plates at a density of 2500 cells per well and cultured for 7 d (A) and 30 d (B). Cell area was determined by α-actinin 2 staining and by confocal microscopy and analysed with Fiji software (ImageJ). n = number of analysed cells/number of analysed wells/ number of differentiation batches. Data are expressed as mean±SEM (*p<0.05, ***p<0.001, one-way ANOVA, Tukey's post-test).

5. Discussion

The overall objective of the present study was to decipher the putative interplay of the (defective) ALP and cMyBP-C on the pathogenesis of human inherited cardiomyopathies. To date, it has only been shown that the ALP keeps cellular homeostasis by degrading long-lived proteins and organelles, as well as (toxic) aggregates, which is of particular importance in post-mitotic CMs. Further, it is known that HCM and DCM are the two most common human inherited cardiomyopathies and *MYBPC3*, encoding cMyBP-C, is the most frequently mutated gene in HCM. However, it is still unknown how the ALP and mutations in *MYBPC3* affect HCM and DCM and if there is an (presumed) interplay. Thus, there is a great need for research that ultimately unravels novel therapeutic options for human inherited cardiomyopathies. The major findings of this study were: i) autophagy is altered in human HCM and DCM tissue samples, ii) autophagic flux is higher in HCM but lower in DCM hiPSC-CMs; iii) *MYBPC3*-deficient hiPSC-CM lined showed reduced levels of mutant mRNA and protein, as well as an increased cell area over culture time.

5.1. Alteration of the ALP in human hypertrophic and dilated cardiomyopathies

The first aim of the presented study was to evaluate a putative ALP alteration in human inherited cardiomyopathies, as defects can be fatal. A low activity may lead to proteotoxicity whilst a high activity may lead to cell death (Maejima et al. 2017). Furthermore, the heart is especially depending on a well function protein quality control, as it represents an organ with low regenerative potential. Here, the ALP prevents the accumulation of toxic protein aggregates (Tannous et al. 2008; Sandri and Robbins 2014). Thus, it is quite surprising that only a few human inherited cardiomyopathies have been linked to a defect in the ALP, such as Danon disease (Nishino et al. 2000; Hashem et al. 2015), Vici syndrome (Cullup et al. 2013; Balasubramaniam et al. 2017), LVNC and a recessive form of DCM (Muhammad et al. 2015). However, it has been stressed by others to investigate the impact of autophagy in disease pathogenesis for HCM and DCM on altering protein and gene expression levels (Dorsch et al. 2019; Mosqueira et al. 2019b). Therefore, the ALP was investigated in human myocardial tissue samples of NF individuals, HCM and DCM patients, as well as HCM and DCM hiPSC-CMs. Further, the autophagic flux was evaluated on protein level in hiPSC-CMs from a healthy ctrl, an HCM (heterozygous and CRISPR homozygous) and DCM patient (heterozygous), and their corresponding CRISPR isogenic controls.

5.1.1. Markers of the ALP are dysregulated in human tissue and hiPSC-CMs of HCM and DCM patients

To evaluate the role of autophagy in human inherited cardiomyopathies, the main markers of the ALP were investigated by immunoblotting and gene expression analysis in cardiac tissue samples of HCM and DCM patients and compared to NF individuals. Higher levels of LC3-II protein were detected, which implies either increased formation or accumulation of autophagosomes, accompanied by a potential ALP activation due to mTORC1 down regulation (pS6↓) for HCM and DCM (see Figure 13). In HCM patients, markedly lower levels of LAMP-2 were detected, caused either by an increased autophagic activity due to enhanced autolysosome turnover or a lysosomal defect and thus impaired autophagosomes-lysosome fusion. In DCM patients, markedly higher levels of LAMP-2 and p62 were detected. Higher levels of p62 suggest either an increased amount or accumulation of ubiquitinated proteins, whereas higher levels of LAMP-2 might indicate an increased autophagic activity due to higher amounts of cargo material or impaired autophagosome-lysosome fusion but proper formed lysosomes. Similar results were obtained by Song et al. (2014) by detecting higher protein levels of LC3-II and Beclin-1 next to an increased number of autophagosomes in septal myectomies of HCM patients carrying either a mutation in *MYBPC3* or *MYH7*. Recent findings of our group showed higher protein levels of LC3-II but unchanged levels of p62 in septal myectomies of HCM patients carrying a mutation in *MYBPC3* (Singh et al. 2017). Of particular interest is the marked difference of LAMP-2 in HCM and DCM patients, especially in the context of Danon disease that is associated with LAMP-2 deficiency and hypertrophic cardiomyopathy. The absence of LAMP-2 results in the accumulation of autophagosomes due to defective autophagosome-lysosome fusion (Nishino et al. 2000; Hashem et al. 2015). Two groups showed that *LAMP-2B*-deficient hiPSC-CMs and Danon-derived hiPSC-CMs have defects in autophagosome-lysosome fusion, as well as mitochondrial and contractile abnormalities. The authors were able to rescue those phenotype by the re-introduction of *LAMP-2B* (Hashem et al. 2017; Chi et al. 2019). Although the regulation of mitophagy differs from the ALP, cargo is taken up into the autophagosome and subsequently degraded within the autolysosome (Zech et al. 2019). Further, this might imply that the reintroduction of the WT *MYBPC3* could be able to rescue the phenotype. A recent study that investigated a putative ALP alteration in DCM patients detected an accumulation of aggregates that were associated with higher levels of p62 in immunohistochemistry staining, and lower levels of LAMP-2 by immunofluorescence staining (Caragnano et al. 2019). This is in contrast to the present study, which detected markedly higher levels of LAMP-2 next to higher levels of p62.

Subsequently, gene expression analysis of cardiac tissue samples of HCM and DCM patients was performed and compared to NF individuals. This revealed a complex and inconclusive pattern for the ALP but confirmed the progressed diseased state (e.g. higher *NPPA* and lower

MYH6 levels). This was supported by altered expression of genes, encoding proteins contributing to fibrosis and Ca^{2+} handling. Recently, our group showed similar gene expression patterns for the ALP in HCM patients carrying *MYBPC3* mutations, such as lower *MAP1LC3B* and higher *MTOR*, but also differences, such as higher levels of *SQSTM1* whereas this study showed that levels of *SQSTM1* did not differ. One reason for this could be that the previous study solely investigated HCM patients carrying a *MYBPC3* mutation, whereas the present study also considered non-*MYBPC3* HCM patients for gene expression analysis, since no significant difference was detected in the gene expression pattern between the two groups. However, with regard to hypertrophy, Ca^{2+} handling and fibrosis, similar results were obtained, such as markedly lower levels of *MYH6*, lower levels of *ATP2A2* and higher levels of *COL1A1* that are hallmarks of HCM (Singh et al. 2017). A recent publication showed lower level of *TFEB* mRNA but higher levels of mTOR protein in cardiac tissues samples of DCM patients. The authors conclude that a suppression of the ALP is present in DCM (Caragnano et al. 2019). All of these studies detected basal states of the ALP in HCM and DCM but it remains elusive whether the ALP is impaired or activated. Thus, the evaluation of the autophagic flux is vital to draw any conclusion about a putative ALP alteration.

Thirty-day-old hiPSC-CMs from a healthy control, an HCM patient (homozygous and heterozygous), a DCM patient (heterozygous) and their corresponding isogenic CRISPR controls were evaluated for a putative common alteration of the ALP (see Figure 17 and Figure 18). HiPSC-CMs of HCMrepair, HCMhet, HCMhom, DCMrepair and DCM showed significantly lower levels of LC3-II in comparison to healthy ctrl hiPSC-CMs. Lower levels of LC3-II indicate either an increased LC3 turnover or lower basal activity of the ALP. Only one publication evaluated the basal levels of LC3-II in hiPSC-CMs. Here, significantly higher levels of LC3-II were detected in comparison to non-isogenic control hiPSC-CMs as well as a markedly higher number of early autophagosomes. However, this study evaluated healthy and Danon disease hiPSC-CMs (Hashem et al. 2015). The present study showed markedly higher protein levels of LC3-II, but unchanged protein levels of p62 and LAMP-2 in healthy ctrl than in HCMrepair and DCMrepair hiPSC-CMs. The absence of difference in the levels of p62 and LAMP-2 might indicate that the isogenic CRISPR controls HCMrepair and DCMrepair are getting closer to a ‘healthy’ phenotype due to the genetic correction. However, a marked difference was detected for LC3-II, as healthy ctrl hiPSC-CM showed markedly higher levels than HCMrepair and DCMrepair hiPSC-CMs, which indicates either a lower basal activity of the ALP or an impaired autophagic flux. Unexpectedly, the levels of LC3-II, p62 and LAMP-2 did not differ between HCMrepair, HCMhet and HCMhom hiPSC-CMs, as well as between DCMrepair and DCM hiPSC-CMs. This was surprising and is in contrast to the findings obtained in human myocardial tissue samples, such was higher LC3-II in HCM and DCM, but lower LAMP-2 in HCM and higher LAMP-2 in DCM (see Figure 13). The absence of the difference in between

the HCM and DCM hiPSC-CM lines indicates a low basal activity of the ALP (LC3-II-), a constant degradation of ubiquitinated cargo (p62-) and proper autophagosome-lysosome fusion (LAMP-2-). However, DCM hiPSC-CMs showed a tendency towards higher level of LAMP-2 in comparison to DCMrepair hiPSC-CMs and thus a trend towards DCM tissue samples, where significantly higher levels of LAMP-2 were detected (see Figure 13). However, the HCM patients carry *MYBPC3* mutations, whereas the HCM hiPSC-CMs carry a mutation in *ACTN2*. On gene expression level, no significant difference between HCM patients carrying a *MYBPC3* mutation and non-*MYBPC3* HCM patients was observed, this analysis includes the here investigated *ACTN2* mutation (see Figure 14). To verify this finding, hiPSC-CMs carrying a *MYBPC3* mutation should be investigated as well as human myocardial tissue samples of non-*MYBPC3* HCM patients in parallel to all here used samples.

All of these studies detected basal states of the ALP in HCM and DCM, it remains elusive whether the ALP is impaired or activated. Thus, the evaluation of the autophagic flux is vital to draw any conclusion about a putative ALP alteration.

5.1.2. Autophagic flux is dysregulated in HCM and DCM hiPSC-CMs

To unravel whether the ALP is activated or impaired in HCM and DCM hiPSC-CMs, the autophagic flux was evaluated in 30-day-old hiPSC-CMs of all investigated lines by detecting protein levels of LC3-II and p62 in the absence and presence of Bafilo by immunoblot, mass spectrometry and immunofluorescence analysis. The immunoblot of all hiPSC-CM lines revealed that the Bafilo treatment induced a marked increase in LC3-II protein, whereas p62 was only higher in healthy ctrl and HCMhet hiPSC-CMs (see Figure 19). The increase in LC3-II after Bafilo treatment verified that the evaluation of the autophagic flux worked in all of the investigated hiPSC-CMs lines, also in the diseased hiPSC-CMs, which is in line with a recent study (Chi et al. 2019). Of interest, the increase in LC3-II after Bafilo treatment was higher in HCM hiPSC-CMs and lower in DCM hiPSC-CMs than in the corresponding isogenic controls. Only one other study modulated the autophagic flux by Bafilo treatment in healthy and diseased hiPSC-CMs. The authors showed a similar extent of increase in LC3-II protein levels after Bafilo treatment in both healthy isogenic and non-isogenic controls, Danon and LAMP-2B KO hiPSC-CMs (Chi et al. 2019). Another study evaluated the autophagic flux in healthy and diseased Danon hiPSC-CMs after transduction with mRFP-GFP-LC3B and subsequent immunofluorescent analysis. This is a robust method to evaluate the autophagic flux, since the GFP signal is quenched in lysosomes due to the low pH. Thus, early autophagosomes exhibit a signal for RFP and GFP, whereas autolysosomes only show a signal for RFP. The authors detected more early autophagosomes, whereas mature autophagosomes were nearly absent in Danon hiPSC-CMs, indicating impaired autophagic flux as maturation of autophagosomes and subsequent fusion with a lysosome does not seem to take place. Consequently, the

authors did not apply Bafilo but Rapa to modulate the autophagic flux, which led to an increase in LC3-II and more early autophagosomes (Hashem et al. 2015). Another study investigated the autophagic flux in WT and Danon disease hiPSC-CMs obtained from two monozygotic twins carrying a heterozygous LAMP-2 mutation. Of note, not all of the generated hiPSC lines showed a mutation in LAMP-2, thus the authors selected for each twin one with (Danon) and without (WT) LAMP-2 mutation, and evaluated the autophagic flux by transducing with mRFP-GFP-LC3B or by applying pepstatin A, a protease inhibitor found within the lysosome. In Danon hiPSC-CMs, the authors observed more early autophagosomes and a significant increase in LC3-II after pepstatin A treatment (Yoshida et al. 2018). The marked increase in LC3-II after Bafilo treatment is in contrast to findings obtained in *Mybpc3*-targeted knock-in mice that showed a blunted autophagic flux. However, this was only detected in 60-week-old mice, but not in 10-week-old mice (Singh et al. 2017). Thus, the effect on the autophagic flux could be 'masked' in hiPSC-CMs due to their well-known immaturity (Yang et al. 2014). A recent study showed that hiPSC-CMs of enhanced maturity can be obtained by Torin 1 treatment, which is a mTOR inhibitor and thus activates autophagy. Here, it also induced the shift to a quiescent cell state and thus led to the dose-dependent increase in expression of sarcomeric proteins and ion channels and an increase in the relative maximum force of contraction, short a 'more' mature hiPSC-CM phenotype (Garbern et al. 2019). Of course, a higher degree of maturation would be desirable, as human cardiac tissue samples are obtained from patients, who underwent septal myectomy or heart transplantation surgery. Thus, related human cardiac tissue samples represent the late stage of the disease and hiPSC-CMs are rather immature and therefore cannot resemble the disease *in vitro* fully. However, the immaturity also has an advantage, since it enables scientists to study the early pathogenesis of diseases, such as HCM and DCM. This is reasonable since it is still unknown how mutations in (sarcomeric) genes lead to the disease phenotype in HCM and DCM (Eschenhagen and Carrier 2018).

To further improve our understanding of the pathogenesis of HCM and DCM, as well as the role of the autophagic flux, mass spectrometry analysis was performed on all investigated hiPSC-CM lines after DMSO or Bafilo treatment. Unfortunately, this revealed that the effect of the Bafilo treatment was lower than the batch-to-batch variability. This was unexpected since the effect of the Bafilo treatment was detected by immunoblotting (see Figure 20 and Figure 22E) and further, the increase in p62 after Bafilo treatment detected by mass spectrometry resembled the increase in p62 detected by immunoblotting (see Figure 19). It could be argued that the Bafilo concentration was too low, since the only other study that evaluated the autophagic flux in hiPSC-CMs by Bafilo application, used 8-fold more Bafilo than in the present study (400 nM for 4 h vs. 50 nM for 3 h; Chi et al. 2019). Here, the validation of the LC3-II protein levels after Bafilo treatment by mass spectrometry would have been very helpful, unfortunately, an additional enrichment step for post-transcriptional modifications would have

been needed to detect the lipidated form of LC3 with the LC-MS/MS. Hence, the Bafilo treatment effect might have been more prominent, if post-translational modifications, such as LC3-II, were evaluated. Thus, it is recommended to repeat the experiment with an extra enrichment step for post-transcriptional modifications, especially since post-transcriptional modifications are vital for the ALP regulation (McEwan and Dikic 2011; Delbridge et al. 2017). The repetition could be performed either with all samples or with a smaller subset, due to high sample numbers (three independent differentiations, three individual experiments of six hiPSC-CMs lines, with two conditions and at least three replicates per condition). Also, a higher n-number per condition and batch would be desirable, as immunoblot analysis, mass spectrometry and immunofluorescence analysis were performed in parallel, and samples for a follow-up RNA-seq were taken. Nonetheless, a repetition would be highly recommended, as mass spectrometry analysis facilitates to not only investigate the autophagic flux by investigating single proteins but to grasp the overall involved proteins and thus signalling pathways. Thus, mass spectrometry could help to reveal the underlying mechanism of HCM and DCM pathogenesis and to understand the role of the ALP.

Concurrently, the main markers of the ALP were analysed by immunofluorescence staining in all hiPSC-CM lines. Unfortunately, the most important marker of the ALP, LC3, was not included in this analysis, since a suitable antibody did not meet our quality standards. This is (very) unfortunate, since a marked increase in LC3-II after Bafilo treatment was detected in all hiPSC-CM lines by immunoblotting (see Figure 19). Nonetheless, immunofluorescence analysis revealed an increase in p62 signal intensity after Bafilo treatment in all investigated hiPSC-CM lines (see Figure 27, Figure 28 and Figure 30). This was unexpected since immunoblot results only showed an increase in p62 in healthy ctrl and HCMhet hiPSC-CMs. A reason for this could be the analysis of the crude protein lysate by immunoblot, which is in line with the two other publications that investigated the ALP in hiPSC-CMs (Hashem et al. 2015; Chi et al. 2019). However, the protein lysis with Urea buffer could be recommend, since immunofluorescence analysis showed even the formation of p62 aggregates by Bafilo treatment. Although, the increase in healthy ctrl and HCMhet hiPSC-CMs after Bafilo treatment in the immunoblot argues against this, it is noteworthy that HCMhom hiPSC-CMs already showed a stronger signal of p62 at baseline. Furthermore, in the HCM hiPSC-CM lines, p62 seemed to make a striated pattern, which might be sarcomeres or T-tubules or the SR. Nonetheless, this indicates a higher ALP activity along those striated structures. It could be speculated that mutated *ACTN2* is translated directly in close proximity of the sarcomere but subsequently ubiquitinated and shuttled via p62 to the ALP for the degradation. This hypothesis would fit to a recent publication that described sarcomeres as very dynamic structures that are constantly maintained, which is assured by localized translation and degradation (Lewis et al. 2018). Furthermore, the authors suggest two half-lives for sarcomeric

proteins, a longer one for incorporated sarcomeric proteins and a very short one for not incorporated excess proteins. Thus, the marked accumulation of p62 putatively close to the sarcomere might indicate that there is such an excess of mutant ACTN2 that next to the UPS, also the ALP degrades sarcomeric proteins to prevent the accumulation of toxic proteins. Also, LAMP-2 was visualized by immunofluorescence staining, but similar levels were detected in all hiPSC-CM lines (see Figure 31). This was not expected, since the analysis of LAMP-2 in HCM and DCM myocardial tissue samples showed either markedly higher (HCM) or lower level (DCM) of LAMP-2. However, this finding is in line with the analysis of the basal levels of LAMP-2 in all investigated hiPSC-CM lines (see Figure 17 and Figure 18). LAMP-2 was prominently localized around the nucleus, as well as an even distribution throughout the cytoplasm. This localization was expected since lysosomes are found all over the cell ultimately being transported to the perinuclear region for fusion with an autophagosome (Korolchuk et al. 2011), as shown by others (Hashem et al. 2015).

Next to the low effect of the Bafilo treatment, mass spectrometry clearly showed the vast difference between DCMrepair and DCM hiPSC-CMs in comparison to the other hiPSC-CM lines (1st dimension, Figure 21; Figure 22A+C). A difference of the DCM hiPSC-CM lines has been suspected since the behaviour of the cells *in vitro* differed to the remaining lines and also emphasizes that hiPSC-CMs resemble the patient *in vitro*. This fits to the second most prominent finding was the marked difference between the different genetic backgrounds (Healthy ctrl vs. HCMrepair/HCMhet/HCMhom vs. DCMrepair/DCM; 2nd dimension, Figure 21 and Figure 22A+D). This was expected, since it has been shown, that the genetic background has an influence on the severity of the disease (Smith et al. 2018). Although the disease hallmarks were resembled in HCM hiPSC-CMs, the authors detected a considerable variability between hiPSC-CMs that were obtained from the father with an established HCM phenotype and his two sons that were either not carries of the here investigated mutation (E99K1) or did not shown any symptoms yet. Therefore, genetically matching isogenic controls were used in the present study, to exclude effects due to the genetic background, such as the epigenetic status and differentiation capacity (Musunuru et al. 2018). As mentioned before, it was not expected that the effect of Bafilo treatment was lower than the batch-to-batch variability as shown in the 3rd dimension of the PCA. Beforehand, a certain degree of a batch-to-batch variability was expected, but not to this extent. A recent publication reported batch-to-batch variability in two commercially available hiPSC-CM lines (iCells and Cor.4U). While evaluating hiPSC-CMs as a human *in vitro* model, they detected a batch-to-batch variability in a number of parameters, such as the baseline beating rate (Huo et al. 2017). The marked difference between the different genetic backgrounds was also detected by immunoblotting, shown by a significant difference in LC3-II and p62 between hiPSC-CMs of healthy ctrl, HCMrepair and DCMrepair (see Figure 23). Furthermore, immunoblots revealed batch-to-batch variabilities to

a lower extent (see Figure 24 and Figure 25), whereby the Bafilo treatment effect was significant. Interestingly, lower variability was visible between batches that were cultured in closer time frames. Thus, an effect of the culture conditions on the hiPSC-CMs cannot be excluded and was previously described (Dambrot et al. 2014). This study showed that serum-supplemented medium masked the hypertrophy phenotype. Thus, it could be argued that the effect of the cardiac phenotype on the ALP was masked by culture conditions, such as serum-supplementation. Surprisingly, the batch-to-batch variability was more prominent, when the immunoblots were normalized to a cardiac marker (cTnT; see Figure 26). cTnT was used as loading control to solely detect the effect in CMs. However, hiPSC-CMs of high purity were used (on average at least 85% and not lower than 71%) and thus ponceau can be used as loading control. The strong effect of cTnT on the batch-to-batch variability was not expected. However, cTnT is also an important component of the sarcomere and thus hiPSC-CMs that harbour mutations in genes encoding sarcomeric proteins might also disturb the homeostasis/expression of other sarcomeric proteins. Interestingly, mass spectrometry analysis revealed a significant downregulation of cTnT in HCMhom in comparison to HCMrepair and HCMhet hiPSC-CMs (Figure 57). Similarly, many other proteins of the sarcomere are much less present in HCMhom than in HCMrepair (data not shown). These findings suggest that HCMhom hiPSC-CMs exhibit a marked instability of sarcomeric components, which could lead to sarcomere failing.

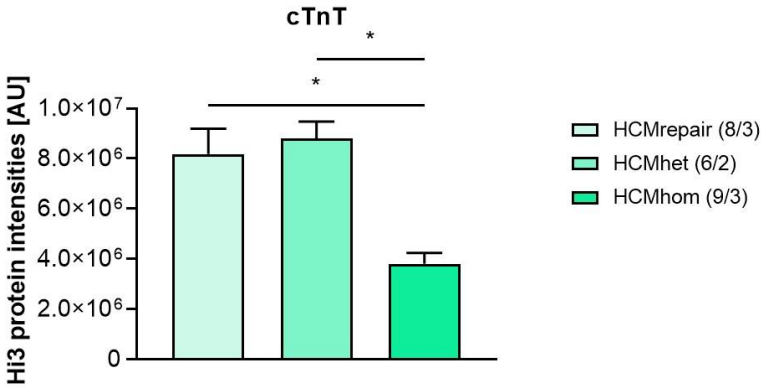

Figure 57: cTnT protein level in all HCM hiPSC-CMs determined by mass spectrometry analysis. Thirty-day-old hiPSC-CMs were treated with DMSO (0.05%) for 3 h and subsequently analysed by LC-MS/MS. n = number of wells/number of differentiation batches. Data are expressed as mean±SEM (*p<0.05; one-way ANOVA, Tukey's post-test).

Moreover, it is not surprising that hiPSC-CMs do express batch-to-batch variations, as well as the difference in the genetic background, as many steps are involved in the generation of hiPSCs, the subsequent differentiation into CMs, the cultivation and treatment of the hiPSC-CMs and analysis. This study aimed to 'prevent' batch-to-batch variabilities while still detecting a valuable effect. Therefore, three independent differentiation runs of every cell line, culture of

the 2D hiPSC-CMs under same conditions in close proximity, subsequent analysis (immunoblot, mass spectrometry, immunofluorescence analysis) with one batch of hiPSC-CMs at the same time, including treatment and culture, were performed. Unfortunately, due to regular culture problems, batch differences, external and technical factors, not always the same sample set could be used. For instance, several wells of HCMhet hiPSC-CMs were lost during culture due to a too strong beating behaviour, but only in two out of three batches. The reasons for this remain elusive, however many factors are involved in the overall procedure and only the variation of the cultivator could have a huge impact. Nonetheless, the same differentiation runs were analysed for every hiPSC-CM line by immunoblotting, mass spectrometry and immunofluorescence analysis.

This study investigated a putative ALP alteration in HCM and DCM and even though, a lot of data was gathered, it remains unclear whether the ALP is activated or impaired. However, it could be that external factors that lead to batch-to-batch variabilities as well as immaturity could 'mask' the effect of the disease on the autophagic flux. Nonetheless, this study showed that the autophagic flux can be evaluated in hiPSC-CMs derived from an HCM and a DCM patient. Also differences between the hiPSC-CM lines were detected, such as a higher increase in LC3-II in HCM but a lower increase in DCM hiPSC-CMs when compared to the corresponding isogenic control. The increase in the autophagic flux in HCM hiPSC-CMs might be a compensatory mechanism to reduce the p62 aggregates. In all investigated hiPSC-CMs, an increase in p62 after Bafilo treatment was detected by mass spectrometry and immunofluorescence. Furthermore, the small number of publications that evaluated the autophagic flux in hiPSC-CMs, indicate a great need for further studies. Especially since pathomechanisms that lead from the mutation to the phenotype are still not fully elucidated for both HCM and DCM (Eschenhagen and Carrier 2018).

5.2. Generation and validation of *MYBPC3*-deficient hiPSC-derived cardiomyocytes as a human *in vitro* model of HCM

The second aim of the presented study was to evaluate the role of cMyBP-C in the pathogenesis of HCM in a human context. Therefore, a cMyBP-C deficient human cellular model of HCM was generated by CRISPR/Cas9 gene editing of hiPSCs from a healthy individual. Hereby, it was aimed to introduce a frameshift mutation that resembles a founder mutation from Tuscany, Italy (c.772G>A; Olivotto et al. 2008; Vignier et al. 2009). Subsequently, the genetically modified hiPSCs were differentiated into beating CMs and characterized *in vitro* to evaluate the eligibility as a human cellular HCM model.

5.2.1. cMyBP-C-deficient hiPSC-CM lines reveal features of human HCM *in vitro*

To evaluate the role of cMyBP-C in the diseased human heart, a functional *MYBPC3*-KO hiPSC line was generated by CRISPR/Cas9 gene editing. Hereby, the applied CRISPR/Cas9 approach had a high efficiency since ~74% of the picked clones survived and 50% were genetically modified. Further, three homozygous clones were obtained, resulting in a ~11.5% KO efficiency. The remaining genetically modified clones were either heterozygous (~38.5%) or compound heterozygous (~11.5%). The applied CRISPR/Cas9 approach was based on one of the first publications that thoroughly explained how to perform CRISPR/Cas9 gene editing in mammalian cells (Ran et al. 2013). The authors emphasized the overall easiness of the design, execution and adaption of the CRISPR/Cas9 system by reaching high CRISPR/Cas9 gene editing efficiencies and performing multiplex editing (65-68% efficiency). However, the authors genetically modified HEK 293FT and HUES9 cells and not hiPSCs. HEK 293FT is one of the most widely used *in vitro* cell line worldwide since it is fast growing, easily maintained and shows high transfection rates. However, the applicability of HEK 293FT cells in research is under discussion since its origin, phenotype, karyotype and tumorigenicity is ambiguous (Stepanenko and Dmitrenko 2015). Therefore, HUES9 cells were CRISPR, which is a hESC cell line and thus closer to the here used *in vitro* model hiPSCs. However, also for the stable HUES9 cell line, CRISPR/Cas9 gene editing via HDR resulted in low efficiencies (2.2%). Furthermore, the authors pointed out that hiPSCs can vary widely in their transfection efficiency, maintenance and tolerance towards single-colony formation (Ran et al. 2013). This was also shown by other groups and many improvements have been undertaken to improve CRISPR/Cas9 gene editing, such as the refinement of the Cas9 nuclease activity to reduce off target events (Kleinstiver et al. 2016), the optimization of ‘repair’/’mutation’ templates for HDR (Okamoto et al. 2019) or the overall modification of CRISPR/Cas9 gene editing in hiPSCs (Paquet et al. 2016; Giacalone et al. 2018).

In the present study, the high gene editing efficiency of 50% in hiPSC clones that survived picking (~37% of all picked clones) was reached by applying CRISPR/Cas9 gene editing via NHEJ. This untargeted KO approach was selected since it was aimed to introduce a frameshift in *MYBPC3* that results in a PTC in exon 9, similar to what was observed in the patients carrying the founder mutation (c.772G>A; Olivotto et al. 2008) or in the corresponding HCM mouse model carrying a *Mybpc3*-targeted knock-in that resembles the very same founder mutation (Vignier et al. 2009). CRISPR/Cas9 gene editing via NHEJ is known to be more efficient than targeted genetically modification via HDR, which is quite limited in its applicability and thus, under constant optimization to yield higher efficiencies (Paquet et al. 2016; Okamoto et al. 2019). Further, by using a CRISPR/Cas9 gene editing approach via NHEJ, only a single plasmid encoding the Cas9 nuclease and the sgRNA needs to be delivered into hiPSCs, without an additional ‘repair’/’mutation’ template that requires successful double transfection

of a single hiPSC. Nonetheless, the here used CRISPR/Cas9 gene editing approach had to be continuously improved to successfully generate a *MYBPC3*-deficient hiPSC line. The first bottleneck was the successful delivery of the plasmid encoding the Cas9 nuclease and the applied sgRNA. In the present study, nucleofection was used but also transfection and regular electroporation has been described. However, nucleofection is the most widely used and supposedly most gentle delivery approach with the highest overall gene targeting efficiencies (Byrne et al. 2014). For nucleofection, a variety of programs and two different buffers were tested (see 3.2.3) and the best combination applied (CA-137 and P3 buffer; see Figure 33). The second bottleneck was the survival of FACS sorting for GFP+ clones and the subsequent single colony formation. Here, mTESR medium turned out to be the game changer. Although ERC018 hiPSCs cultivated in CoM and mTESR medium before nucleofection showed a similar percentage of GFP+ cells (6.5% vs 5.8%) at the FACS, solely the mTESR cultivated cells survived single colony formation.

Nonetheless, *MYBPC3* was successfully modified and thus, one homozygous (hom. clone#11), one compound heterozygous (c.het. clone#14) and one heterozygous clone (het. clone#15) were validated for their purity and putative off-target events. The ten most likely off-target loci did not show any traces of Cas9 nuclease activity. Low off-target activity of Cas9 has been published by others (Smith et al. 2014; Veres et al. 2014) and suggests that an optimized Cas9 nuclease (e.g. high fidelity Cas9; Kleinstiver et al. 2016) might only be required for genes that have a high similarity to their isoforms. Nevertheless, one publication that reported an off-target event in the related isoform did not detect a phenotype that was induce by the off-target event (see Mosqueira et al. 2018). A recent study provided a new versatile and precise tool to perform gene editing, Prime editing, with even lower off-target activity. Prime editing directly writes the new genetic information into a specified DNA site without the introduction of DSBs or donorDNA. Therefore, a catalytically impaired Cas9 nuclease is fused to an engineered reverse transcriptase, which is in turn programmed by a prime editing guide RNA that specifies the target site and encodes the desired edit (Anzalone et al. 2019). Nonetheless, whole-genome sequencing is advisable to fully exclude off-target events in CRISPR clones.

The subsequent evaluation of the karyotype by two independent methods revealed a trisomy of chromosome 1 in all three CRISPR clones. This karyotypic abnormality seemed to be acquired during regular culture before CRISPR/Cas9 gene editing was performed and not caused by the actual CRISPR/Cas9 procedure. The likelihood to acquire the very same karyotypic abnormality coincidentally is rather low (Närvä et al. 2010). Besides, another PhD student detected a trisomy in chromosome 1 in all of her CRISPR clones that originated from the very same ERC018 hiPSCs. Her CRISPR/Cas9 approach was also plasmid-based but

here a targeted KO of DNA methyltransferase 3A (*DNMT3A*) was performed (Löser 2018). Further, it has been published that karyotypic abnormalities do constantly occur in hiPSC culture, independent of reprogramming or culture conditions, at low and high passage numbers. However, the probability to acquire such a karyotypic abnormality seems to increase with higher passage number (Taapken et al. 2011). Thus, the relatively high passage number of p37 of the used ERC018 hiPSCs at nucleofection, seemed to be rather problematic. In general, if the acquired karyotypic abnormality represents a growth advantage, the single hiPSC carrying such an abnormality will overgrow the whole culture within a few weeks as seen by Brenière-Letuffe et al. (2018). The authors performed RGB marking of three different hiPSC lines with LeGo vectors that allow to track sub-clonal distribution over time by FC or immunofluorescence analysis and observed a reduction in sub-clonal diversity with culture time. Therefore, high quality culture should be ensured by stringent and robust standards, such as a master hiPSC bank of low passage number and a correct karyotype, short culture times of a few passages and regular testing for genomic integrity, even though this is time and cost consuming (Brenière-Letuffe et al. 2018). Further, for genetically modified hiPSCs, it is highly advisable to perform regularly genotyping, as it is mandatory in mice and also performed in the present study. In hiPSCs, the most frequently acquired abnormalities are a trisomy in chromosome 8 or chromosome 12 (Taapken et al. 2011) but a trisomy of chromosome 1 has not been published yet. However, chromosomal aberrations have been frequently detected in hESCs (q arm; Taapken et al. 2011). In humans, a trisomy of chromosome 1 has been reported to either result in a miscarriage or in prenatal death of the embryo within the first weeks of pregnancy (Hanna et al. 1997; Dunn et al. 2001; Banzai et al. 2004). Thus, the trisomy in chromosome 1 supposedly (adversely) affects hiPSCs. As a small attempt to validate the putative effect of the trisomy in chromosome 1, by determining the expression of *LMNA* (located on chromosome 1) by RT-qPCR in hiPSC-CMs of ERC018 and the three CRISPR clones (see Figure 49). Only c.het. clone#14 showed a significant increase of ~30% in *LMNA* when compared to ERC018, whereby an increase in *LMNA* mRNA was expected in all three CRISPR clones since all of them carry a trisomy in chromosome 1. Nevertheless, *LMNA* is only one out of ~2000 genes that are located on chromosome 1. Furthermore, significantly higher CT levels of GAPDH, the applied housekeeping gene, were detected in c.het. clone#14, which could explain the increase in *LMNA* mRNA level. Thus, RNAseq would be advised to evaluate the effect of the trisomy on gene expression level. Scientists all over the world handling hiPSCs are struggling with abnormal karyotypes but there is no systematic evaluation of chromosomal aberrations or trisomy in hiPSCs or hiPSC-CMs to date. Thus, the question remains if and how karyotypic abnormalities affect the cell's integrity or phenotype and moreover how its occurrence can be ultimately prevented. The here applied CRISPR/Cas9 approach was repeated by a master student under my supervision and a functional *MYBPC3*-

KO was generated with a normal karyotype. However, this finding is not part of the present study.

Even though, all of the investigated CRISPR clones showed a trisomy in chromosome 1, all three were successfully differentiated into beating CMs, whereby there was no significant difference in the hiPSC-CMs yield or in the differentiation efficiency when compared to ERC018 hiPSC-CMs. Thus, cardiac differentiation appeared not to be affected by the genetic modification of *MYBPC3* or the trisomy in chromosome 1. At least for the genetically modified hiPSCs, a decreased or impaired cardiac differentiation was not expected since many studies showed the successful cardiac differentiation of gene-edited hiPSCs. Hereby, the mutation was either introduced into a healthy genome (Mosqueira et al. 2018) or corrected in a diseased patient hiPSC line by CRISPR/Cas9 (Hinson et al. 2015; Smith et al. 2018; Prondzynski et al. 2019). To date, the effect of a karyotypic abnormality on the cardiac differentiation has not been systematically evaluated and thus remains elusive.

5.2.2. Diseased modelling of *MYBPC3*-deficient hiPSC-CM lines revealed haploinsufficiency and increased cell area with culture time

To validate whether the genetic modification of *MYBPC3* indeed induced a frameshift and thus a PTC and the putative degradation via NMD of its mRNA was evaluated. The NMD degrades nonsense mRNA transcripts to prevent the translation of truncated and thus (putatively) toxic protein. In HCM patients carrying the founder mutation (c.772G>A), a nonsense mRNA was detected, whereby skipping of exon 6 resulted in a PTC in exon 9 putatively and subsequently in a truncated protein (Helms et al. 2014). In *Mybpc3*-target knock-in mice that resemble the founder mutation, three different mutant mRNAs were detected. A missense mRNA, which results in a E264K protein, a nonsense mRNA, that is associated with the skipping of exon 6, a PTC in exon 9 and a truncated protein, and a deletion/insertion mRNA that results in a roughly wild-type sized cMyBP-C (Vignier et al. 2009). The here applied CRISPR design was an untargeted approach that aimed to introduce a frameshift and a subsequent PTC, to resemble a human founder mutation (c.772G>A). However, the formation of similar mRNA forms were expected.

For all CRISPR clones, mRNA forms with an induced frameshift and a PTC was detected (see Figure 46). Unexpectedly, additional forms of mRNA were detected in all three CRISPR clones due to alternative splicing, that either resulted in the partial or complete retention of intron 8 and in one case to the formation of a new splice site (see Figure 47). However, this only seems to be problematic for the c.het. clone#14. Here, the partial retention of intron 8 on the allele with the T insertion led to the restoration of the reading frame and thus a 3864-bp mRNA is transcribed and consequently, a nearly wild-type sized protein of 1287 amino acids is

produced. To verify the here detected alternative forms of mRNA and to assure that no additional alternative mRNA forms were formed, it would be recommended to increase the PCR product size (e.g. exon 4 – 11) for excluding the retention of a proximate intron or to perform RNA-seq. Nonetheless, the present study obtained MYBPC3-deficient hiPSC-CM lines that resemble the human founder mutation as a frameshift and a subsequent PTC was detected.

The validation of the different forms of *MYBPC3* mRNA (see Figure 48), revealed a significant reduction of ~55% of *MYBPC3* transcript only in the hom. clone#11. This reduction is in line with a recent publication of our group that showed a 50% reduction of *MYBPC3* mRNA in HCM hiPSC-CMs than to non-isogenic control hiPSC-CMs. However, these hiPSC-CM were carrying a heterozygous mutation (c.1358-1359insC; Prondzynski et al. 2017), and not a homozygous mutation as in the present study. Though, a recent study showed that the genetic background has an influence on the severity of the cardiac disease phenotype *in vitro* (Smith et al. 2018). This implies that the disease phenotype *in vitro* differs in its severity between hiPSC-CMs in which mutations have been introduced into a healthy background versus the repair of the mutation in diseased background. Nonetheless, for all three CRISPR clones it can be assumed that not all forms of (‘regular’ and alternative) mRNA are degraded via NMD. A repetition of the mRNA evaluation after NMD inhibitor treatment with cycloheximide is recommended. Nevertheless, we were really surprised by the multiple forms of alternatively formed mRNA transcripts since this was not published at the time of design and execution of the experiments.

Since truncated proteins have not been detected yet (Marston et al. 2009; van Dijk et al. 2009) and a potential degradation by the UPS is possible (Sarikas et al. 2005), all three CRISPR clones and ERC018 were treated with the proteasome inhibitor MG-132 and subsequently analysed by immunoblotting with an N-terminal cMyBP-C antibody (see Figure 51). A WT sized band of cMyBP-C was detected in ERC018, c.het. clone#14 and het. clone#15 but not in the hom. clone#11. However, the weak cMyBP-C signal for the c.het. clone#14 could be explained by the alternative splicing detected on the T insertion allele that restored the reading frame. The het. clone#15 showed a signal for cMyBP-C that is comparable to the one of ERC018. This was expected since *Mybpc3*-targeted knock-in mice, which resemble the same founder mutation, are known to have ~80% of WT cMyBP-C protein (Vignier et al. 2009). A truncated form of cMyBP-C with an expected size of roughly ~30 kDa was not detected in all three CRISPR clones or ERC018 hiPSC-CMs that were treated with MG-132, although the treatment proved to be effective (see Figure 52). ERC018 hiPSC-CMs were also expected to show truncated cMyBP-C due the here detected alternative splicing in the wild-type sequence of het. clone#15 (see Figure 47). However, truncated forms of cMyBP-C have not been detected in

HCM patients yet, implying haploinsufficiency as a disease mechanism (Marston et al. 2009; van Dijk et al. 2009). Furthermore, truncated cMyBP-C was also not detected in HCM hiPSC-CMs carrying a heterozygous *MYBPC3* mutation, but reduced full-length cMyBP-C levels (Prondzynski et al. 2017). Nonetheless, the results of the mRNA evaluation indicated that the putative degradation of the mRNA via NMD is only partial. This is of particular of interest, since a recent study showed that a chronic activation of the NMD due to a *MYBPC3* mutation lead to cardiac hypertrophy. Although the investigated *MYBPC3* mutations (p. 943x; p.R1073) differ from the here investigated mutation, these mutations also introduce a frameshift with a subsequent PTC (Seeger et al. 2019): Thus it is highly recommend to make another attempt to detect truncated cMyBP-C. Therefore, hiPSC-CM lines should be treated with a permanent proteasome inhibitor, such as epoxomicin. Maybe this could also help to further clarify the band of ~30 kDa that was detected in ERC018 hiPSC-CMs in the DMSO and not in MG-132 treated samples. In the literature, solely a 40 kDa band of cMyBP-C has been described that seems to play a crucial role in the stressed heart of humans and mice (Govindan et al. 2012; Razzaque et al. 2013).

Our findings emphasize that the verification of genetical modification on gDNA level must not be transferable to mRNA and protein level. In the course of this year, a study was published addressing the rescue of the target activity in CRISPR KOs due to alternative splicing and translation initiation (Smits et al. 2019). The authors investigated 193 genetically modified deletions to be able to make an assessment, hereof a third showed either alternative splicing or translation initiation. Even though this study worked with HAP1 cells that are derived from a patient with chronic myeloid leukaemia, the overall findings should be transferrable.

Next, the three CRISPR clones and ERC018 hiPSC-CMs were morphologically analysed. Light microscopy did not reveal big differences between the cell lines (see Figure 53), just a tendency towards bigger and faster beating cells was observed over a period of 30 days. The putatively altered beating behaviour was not further investigated due to time limitations. However, immunofluorescence staining confirmed striated sarcomeres for all investigated cell lines thus proper formation of sarcomeres. Surprisingly, one cMyBP-C antibody showed a weak signal of cMyBP-C in hom. clone#11 at seven and 30 days (Figure 55 and Figure S11). This was unexpected since a regular-sized or truncated form of cMyBP-C has not been detected by immunoblotting and also not by immunofluorescence with an N-terminal cMyBP-C antibody (see Figure 54). Nonetheless, the presence of a truncated protein or lack of specificity of the antibody cannot be excluded. As expected, the het. clone#15 showed a relatively strong signal for cMyBP-C matching the findings of the immunoblot (see Figure 51). The cMyBP-C signal for the c.het. clone#14 was relatively prominent and can be explained by alternative splicing (see Figure 47).

Evaluation of the cell area was performed, since hypertrophy is a hallmark of HCM (see Figure 56). The three CRISPR hiPSC-CMs exhibited larger cell size than ERC018 at 30 days of culture. This finding is in line with a recent publication of our group that determined a significantly higher cell area of HCM hiPSC-CMs than in non-isogenic and isogenic control hiPSC-CMs (Prondzynski et al. 2019). A nice overview was provided by Eschenhagen and Carrier (2019) that reviewed the hallmarks of HCM and DCM in hiPSC-CMs provided by several studies. In regard to cell size, the authors pointed out that although an increase in cell size was detected in the different HCM hiPSC-CM studies (156±85%, n = 15), there is a vast discrepancy in the actual size of the CMs, as well as in the extent of the increase. Unfortunately, the above-mentioned experiments were only performed once due to time limitations. Further experiments are planned for the future, such as the evaluation of myofibrillar disarray that was indicated by immunofluorescence analysis. Nevertheless, the here performed experiments indicate that the generated cMyBP-C-deficient hiPSC-CMs could be a putative *in vitro* HCM model. However, further experiments are needed and the effect of the trisomy in chromosome 1, which is present in all CRISPR clones, on disease phenotypes needs to be further evaluated.

In the literature, several hiPSC-based disease models of HCM have been described that seem to resemble disease hallmarks, for instance larger cell size, myocardial disarray or higher expression of *NPPA*, *NPPB* and *MYH7*, even the translation to the clinics was shown in one study (Brodehl et al. 2019; Prondzynski et al. 2019). Thus hiPSC-CMs seem to be the appropriate tool to study human inherited cardiomyopathies *in vitro*. Nevertheless, results of disease modelling studies vary significantly and thus there is a great need for systematic and thorough analysis, preferable in high throughput format, that enables quantitative comparisons (Eschenhagen and Carrier 2018). A recent study exactly addresses this by providing a high-throughput phenotyping toolkit to characterized HCM hiPSC-CMs that can be used to minimize technical artefacts and thus allows to solely evaluate the molecular and functional parameters of HCM *in vitro* (Mosqueira et al. 2019a). Moreover, we rather seem to be at the beginning to understand hiPSC-CMs and their associated molecular mechanisms. For instance, it has been shown that age of the patient and genetic background has an influence on the severity of the cardiac disease phenotype *in vitro* (Smith et al. 2018). This is supported by a recent study that performed disease modelling experiments with an HCM hiPSC-CMs line, but also detected a significant difference between a non-isogenic and a isogenic control hiPSC-CM line (Prondzynski et al. 2019). Thus, disease modelling should be performed in hiPSC-CMs with the genetically matching isogenic controls (Musunuru et al. 2018). Further, hiPSC-CMs are known to be rather immature and to exhibit phenotypic heterogeneity and also culture conditions seem to influence the disease phenotype *in vitro* (Eschenhagen and Carrier 2018). Furthermore, patients suffering from inherited cardiomyopathies are generally rather old at the

occurrence of first symptoms. Since hiPSC-CMs are known to be rather immature (Yang et al. 2014), it might be too much to expect of hiPSC-CMs to resemble all disease hallmarks, at least at the present. Nonetheless, disease modelling with hiPSC-CMs seems to be a rather promising *in vitro* tool that shall bring us closer to the ultimate goal to develop novel therapies.

5.3. Conclusion and further perspectives

The present study aimed to investigate the putative participation and interplay of an (defective) ALP and *MYBPC3* mutations on the pathogenesis of human inherited cardiomyopathies (HCM and DCM). A (putative) alteration of the ALP in HCM and DCM is indicated by higher protein levels of LC3-II in both, and lower LAMP-2 in HCM, but higher LAMP-2 in DCM tissue samples. Further, the autophagic flux seems to be dysregulated in diseased hiPSC-CMs, as indicated by a higher increase in LC3-II protein in mutated HCM hiPSC-CMs than in HCMrepair and a smaller increase in LC3-II in DCM than in DCMrepair hiPSC-CMs after Bafilo treatment. Of interest seems to be p62 that showed only higher protein levels in DCM tissue samples and unchanged levels in DCMrepair and DCM hiPSC-CMs, but only showed an increase in its level after Bafilo treatment in healthy ctrl and HCMhet hiPSC-CMs. However, the evaluation of the autophagic flux by mass spectrometry and immunofluorescence revealed an increase of p62 in all investigated hiPSC-CMs after Bafilo treatment. Furthermore, *MYBPC3*-deficient hiPSC-CM lines were generated that resemble hallmarks of HCM, such as haploinsufficiency and hypertrophy. However, the ALP was not investigated in this *in vitro* model. As of today, it remains unclear how the ALP and cMyBP-C (adversely) affect HCM and DCM and if there is an (presumed) interplay.

Therefore, future experiments are planned, such as a repetition of the evaluation of the autophagic flux by mass spectrometry by analysing post-transcriptional modifications is planned to be able to analyse LC3-II. Further, the utilization of a mTagRFP_mWasabi_hLC3 tandem construct to visualize and evaluate the autophagic flux in hiPSC-CMs. Moreover, the HCMhom hiPSC-CMs should be further characterized as a putative *in vitro* model of proteotoxicity, as these cells show an increase autophagic flux that might compensate the marked aggregation of p62 detected by immunofluorescence that was not detected by immunoblotting. Further, mass spectrometry analysis revealed markedly lower levels of several sarcomeric proteins, for instance cTnT. Thus, the HCMhom hiPSC-CM line could help to further clarify the role of the ALP in disease progression of human inherited cardiomyopathies.

6. Summary

The autophagy-lysosomal pathway (ALP) maintains cellular homeostasis by degrading long-lived proteins and organelles. Hypertrophic (HCM) and dilated cardiomyopathy (DCM) are the two most common human inherited cardiomyopathies and *MYBPC3*, encoding the cardiac myosin-binding protein C (cMyBP-C), is the most frequently mutated gene in HCM. However, it remains elusive how an (altered) ALP and *MYBPC3* mutations effectively contribute to the pathogenesis of HCM and DCM. Therefore, myocardial tissue samples of HCM and DCM patients, as well as 2D cultured human induced-pluripotent stem cell-derived cardiomyocytes (hiPSC-CMs) of an HCM patient and a DCM patient were evaluated for a putatively altered ALP. Besides, homozygous, compound heterozygous and heterozygous *MYBPC3*-deficient human cellular models of HCM were generated and characterized as hiPSC and hiPSC-CMs.

The ALP evaluation in cardiac tissues samples showed lower levels of LAMP-2 in HCM, but higher levels of LAMP-2 in DCM that were also present in DCM hiPSC-CMs by tendency. Further, a higher autophagic activity was detected in HCM hiPSC-CMs, whereas DCM hiPSC-CMs showed a lower autophagic activity than the corresponding isogenic controls. Protein expression changes observed in mass spectrometry of samples treated with an ALP inhibitor however seemed to correlate more with batch-to-batch variability and/or genetic background than with the treatment. Although, a batch-to-batch variability was also detected by immunoblotting, the differences were not as prominent as the ALP-inhibition-induced increase in LC3-II. Despite this, an increase of p62 after ALP inhibition was detected in all hiPSC-CMs by mass spectrometry and immunofluorescence. In all HCM hiPSC-CMs a striated pattern of p62 aggregates was detected by immunofluorescence staining, suggesting a higher ALP activity along sarcomeres, t-tubules or the sarcoplasmic reticulum.

Concurrently, the *MYBPC3*-deficient hiPSC clones, generated by CRISPR, were differentiated into hiPSC-CMs of high purity, although a trisomy of chromosome 1 was detected in all of them. mRNA analysis revealed alternative splicing, resulting in multiple forms of mRNA, whereby the reading frame of the compound heterozygous clone was restored on one allele and nearly full-length cMyBP-C was detected. For the homozygous clone, full-length cMyBP-C was not detected. Further, truncated cMyBP-C was not detected in all CRISPR clones, although *MYBPC3* mRNA was still present in lower amounts. Cell area analysis at day 30 of culture indicated hypertrophy in all CRISPR clones. Thus, the generated HCM model might be a suitable *in vitro* tool, but further experiments are needed.

Finally, it remains unclear how the altered ALP and *MYBPC3* mutations affect HCM and DCM. However, the ALP is vital for the heart during disease, as it prevents the accumulation of toxic proteins and a defect of the ALP in human inherited cardiomyopathy has been shown. Also, the role of *MYBPC3* within HCM has been deeply investigated. But it remains unclear how a

mutation in *MYBPC3* and the involvement of the ALP ultimately lead to HCM or DCM pathomechanism. Thus, there is a great need for research that ultimately aims to unravel novel therapeutic options for human inherited cardiomyopathies.

7. Zusammenfassung

Der Autophagie-lysosomale Signalweg (ALP) ist von entscheidender Bedeutung für die zelluläre Homöostase, da er langlebige Proteine und Organellen abbaut. Hypertrophe (HCM) und dilatative Kardiomyopathie (DCM) sind die zwei am häufigsten vorkommenden humanen vererbbaren Kardiomyopathien und *MYBPC3*, welches das kardiale Myosin-bindende Protein-C (cMyBP-C) kodiert, ist das am häufigsten mutierte Gen in HCM. Jedoch ist es bis heute ungeklärt, wie ein (veränderter) ALP und Mutationen in *MYBPC3* effektiv an der Pathogenese von HCM und DCM beteiligt sind. Deswegen wurden myokardiale Gewebsproben von HCM und DCM Patienten, sowie Kardiomyozyten, die aus humanen induzierten pluripotenten Stammzellen von einem HCM Patienten und einem DCM Patienten (hiPSC-CMs) differenziert wurden, auf eine mögliche Veränderung des ALPs untersucht. Zudem wurden homozygote, gemischt heterozygote und heterozygote *MYBPC3*-defiziente, humane zelluläre HCM Modelle generiert und auf Stammzell- und Kardiomyozytenebene näher charakterisiert.

Die Untersuchung des ALPs in humanem kardialem Gewebe zeigte einen niedrigeren Proteinspiegel von LAMP-2 in HCM aber einen höheren Proteinspiegel in DCM, welcher auch tendenziell in DCM hiPSC-CMs präsent war. Zudem wurde eine gesteigerte autophagische Aktivität in HCM, aber eine verringerte autophagische Aktivität in DCM hiPSC-CMs im Vergleich zu den zugehörigen isogenen Kontrollen gezeigt. Die massenspektrometrische Analyse von ALP-Inhibitor-behandelten Proben zeigte, dass die Batch-zu-Batch Variabilität und/oder der genetische Hintergrund stärker mit der Veränderung der Proteinexpression in den behandelten Proben zu korrelieren scheint als mit der Behandlung. Obwohl eine Batch-zu-Batch Variabilität auch im Immunoblot bestand, war diese nicht stärker als der Anstieg in LC3-II nach ALP-Inhibierung. Jedoch zeigten die massenspektrometrische Untersuchung und die Immunfluoreszenzfärbung einen Anstieg der p62 Proteinmenge nach ALP-Inhibierung, unabhängig von der beobachteten Variabilität. Zudem zeigten die Immunfluoreszenzfärbungen aller HCM hiPSC-CMs eine deutliche Akkumulierung von p62 in einem quergestreiften Muster, welches eine höhere ALP-Aktivität an den Sarkomeren, den T-Tubuli oder dem Sarkoplasmatischen Retikulum andeutet.

Zeitgleich wurden mittels CRISPR generierte *MYBPC3*-defiziente hiPSC Klone mit hoher Effizienz zu hiPSC-CMs differenziert, obwohl eine Trisomie von Chromosom 1 in allen geCRISPRten Klonen vorlag. Diese zeigten zahlreiche mRNA Variationen von *MYBPC3*, die unter anderem durch alternatives Spleißen entstanden waren. Dies war nur problematisch für den gemischt heterozygoten Klon, da hier das Leseraster wiederhergestellt wurde und ein cMyBP-C in fast voller Länge detektiert wurde. Für den homozygoten Klon wurde cMyBP-C nicht in voller Länge detektiert. Zudem wurde in keinem der geCRISPRerten Klone trunkiertes cMyBP-C gefunden, obwohl entsprechende *MYBPC3* mRNA in reduzierter Menge vorhanden

war. Messungen der Zellfläche nach 30 Tagen Kultivierung deuteten auf eine Hypertrophie hin, ein Kennzeichen von HCM. Aus den Daten lässt sich schließen, dass das hier generierte humane HCM Modell geeignet scheint, HCM *in vitro* zu untersuchen, wobei jedoch weitere Experimente nötig sind.

Abschließend lässt sich sagen, dass unklar bleibt, wie der veränderte ALP und *MYBPC3* Mutationen HCM und DCM beeinträchtigen. Nichtdestotrotz ist der ALP essentiell für das Herz während einer Erkrankung, da er die Akkumulierung von toxischen Proteinen verhindert und eine Beeinträchtigung des ALPs in humanen vererbbaren Kardiomyopathien gezeigt wurde. Auch die Rolle von *MYBPC3* in HCM wurde schon ausführlich untersucht. Jedoch, bleibt unklar, wie eine Mutation in *MYBPC3* und die Beteiligung des ALPs schließlich zu den Pathomechanismen von HCM und DCM führen. Folglich gibt es einen großen Forschungsbedarf, um neue therapeutische Optionen für humane vererbbare Kardiomyopathien zu entwickeln.

8. Literature

Anzalone A V., Randolph PB, Davis JR, et al (2019) Search-and-replace genome editing without double-strand breaks or donor DNA. Nature 576:149–157. doi: 10.1038/s41586-019-1711-4

Balasubramaniam S, Riley LG, Vasudevan A, et al (2017) EPG5-Related Vici Syndrome: A Primary Defect of Autophagic Regulation with an Emerging Phenotype Overlapping with Mitochondrial Disorders. JIMD Rep 42:19–29. doi: 10.1007/8904_2017_71

Banzai M, Sato S, Matsuda H, Kanasugi H (2004) Trisomy 1 in a case of a missed abortion. J Hum Genet 49:396–397. doi: 10.1007/s10038-004-0164-1

Behrens-Gawlik V, Mearini G, Gedicke-Hornung C, et al (2014) MYBPC3 in hypertrophic cardiomyopathy: from mutation identification to RNA-based correction. Pflugers Arch Eur J Physiol 466:215–223. doi: 10.1007/s00424-013-1409-7

Bers DM (2002) Cardiac excitation–contraction coupling. Nature 415:198–205. doi: 10.1038/415198a

Bhaya D, Davison M, Barrangou R (2011) CRISPR-Cas Systems in Bacteria and Archaea : Versatile Small RNAs for Adaptive Defense and Regulation. Annu Rev Genet 45:273–297. doi: 10.1146/annurev-genet-110410-132430

Bozkurt B, Colvin M, Cook J, et al (2016) Current Diagnostic and Treatment Strategies for Specific Dilated Cardiomyopathies: A Scientific Statement from the American Heart Association. Circ 134:e579–e646. doi:10.1161/CIR.0000000000000455

Braunwald E (2017) Cardiomyopathies. Circ Res 121:711–721. doi: 10.1161/CIRCRESAHA.117.311812

Bravo-San Pedro JM, Kroemer G, Galluzzi L (2017) Autophagy and Mitophagy in Cardiovascular Disease. Circ Res 120:1812–1824. doi: 10.1161/CIRCRESAHA.117.311082

Breckwoldt K, Letuffe-Brenière D, Mannhardt I, et al (2017) Differentiation of cardiomyocytes and generation of human engineered heart tissue. Nat Protoc 12:1177–1197. doi: 10.1038/nprot.2017.033

Brenière-Letuffe D, Domke-Shibamiya A, Hansen A, et al (2018) Clonal dynamics studied in cultured induced pluripotent stem cells reveal major growth imbalances within a few weeks. Stem Cell Res Ther 9:. doi: 10.1186/s13287-018-0893-2

Brodehl A, Ebbinghaus H, Deutsch MA, et al (2019) Human Induced Pluripotent Stem-Cell-

Derived Cardiomyocytes as Models for Genetic Cardiomyopathies. Int J Mol Sci 20:. doi: 10.3390/ijms20184381

Byrne SM, Mali P, Church GM (2014) GENOME EDITING IN HUMAN STEM CELLS. Methods Enzymol 546:119–138. doi: 10.1016/B978-0-12-801185-0.00006-4

Caragnano A, Aleksova A, Bulfoni M, et al (2019) Autophagy and Inflammasome Activation in Dilated Cardiomyopathy. J Clin Med 8:1519. doi: 10.3390/jcm8101519

Carrier L, Bonne G, Bährend E, et al (1997) Organization and sequence of human cardiac myosin binding protein C gene (MYBPC3) and identification of mutations predicted to produce truncated proteins in familial hypertrophic cardiomyopathy. Circ Res 80:427–434. doi: 10.1161/01.res.0000435859.24609.b3

Carrier L, Mearini G, Stathopoulou K, Cuello F (2015) Cardiac myosin-binding protein C (MYBPC3) in cardiac pathophysiology. Gene 573:188–197. doi: 10.1016/j.gene.2015.09.008

Chi C, Leonard A, Knight WE, et al (2019) LAMP-2B regulates human cardiomyocyte function by mediating autophagosome–lysosome fusion. Proc Natl Acad Sci U S A 116:556–565. doi: 10.1073/pnas.1808618116

Cullup T, Kho AL, Dionisi-vici C, et al (2013) Recessive mutations in EPG5 cause Vici syndrome , a multisystem disorder with defective autophagy. Nat Genet 45:83–87. doi: 10.1038/ng.2497.

Dambrot C, Braam SR, Tertoolen LGJ, et al (2014) Serum supplemented culture medium masks hypertrophic phenotypes in human pluripotent stem cell derived cardiomyocytes. J Cell Mol Med 18:1509–1518. doi: 10.1111/jcmm.12356

Delbridge LMD, Mellor KM, Taylor DJ, Gottlieb RA (2017) Myocardial stress and autophagy: Mechanisms and potential therapies. Nat Rev Cardiol 14:412–425. doi: 10.1038/nrcardio.2017.35

Deter RL, De Duve C (1967) INFLUENCE OF GLUCAGON, AN INDUCER OF CELLULAR AUTOPHAGY, ON SOME PHYSICAL PROPERTIES OF RAT LIVER LYSOSOMES. J Cell Biol 33:437–449. doi: 10.1083/jcb.33.2.437

Dorsch LM, Schuldt M, Knežević D, et al (2019) Untying the knot: protein quality control in inherited cardiomyopathies. Pflugers Arch Eur J Physiol 471:795–806. doi: 10.1007/s00424-018-2194-0

Dunn TM, Grunfeld L, Kardon NB (2001) Trisomy 1 in a Clinically Recognized IVF Pregnancy. Am J Med Genet 99:152–153. doi: 10.1002/1096-

8628(2000)9999:999<00::aid-ajmg1130>3.0.co;2-p

Eschenhagen T (2010) Is ryanodine receptor phosphorylation key to the fight or flight response and heart failure ? J Clin Invest 120:4197–4203. doi: 10.1172/JCI45251

Eschenhagen T, Carrier L (2018) Cardiomyopathy phenotypes in human-induced pluripotent stem cell-derived cardiomyocytes—a systematic review. Pflügers Arch - Eur J Physiol 471:755–768. doi: 10.1007/s00424-018-2214-0

Eschenhagen T, Mummery C, Knollmann BC (2015) Modelling sarcomeric cardiomyopathies in the dish : from human heart samples to iPSC cardiomyocytes. Cardiovasc Res 105:424–438. doi: 10.1093/cvr/cvv017

Eskelinen EL (2006) Roles of LAMP-1 and LAMP-2 in lysosome biogenesis and autophagy. Mol Aspects Med 27:495–502. doi: 10.1016/j.mam.2006.08.005

Eskelinen EL, Saftig P (2009) Autophagy: A lysosomal degradation pathway with a central role in health and disease. Biochim Biophys Acta - Mol Cell Res 1793:664–673. doi: 10.1016/j.bbamcr.2008.07.014

Feng Y, He D, Yao Z, Klionsky DJ (2014) The machinery of macroautophagy. Cell Res 24:24–41. doi: 10.1038/cr.2013.168

Flashman E, Korkie L, Watkins H, et al (2008) Support for a trimeric collar of myosin binding protein C in cardiac and fast skeletal muscle , but not in slow skeletal muscle. FEBS Lett 582:434–438. doi: 10.1016/j.febslet.2008.01.004

Flashman E, Redwood C, Moolman-Smook J, Watkins H (2004) Cardiac Myosin Binding Protein C - Its Role in Physiology and Disease. Circ Res 94:1279–1289. doi: 10.1161/01.RES.0000127175.21818.C2

Fougerousse F, Delezoide A, Fiszman MY, et al (1998) Cardiac Myosin Binding Protein C Gene Is Specifically Expressed in Heart During Murine and Human Development. Circ Res 82:130–133. doi: 10.1161/01.RES.82.1.130

Garbern JC, Helman A, Sereda R, et al (2019) Inhibition of mTOR Signaling Enhances Maturation of Cardiomyocytes Derived from Human Induced Pluripotent Stem Cells via p53-Induced Quiescence. Circulation CIRCULATIONAHA.119.044205. doi: 10.1161/CIRCULATIONAHA.119.044205

Gautel M, Zuffardi O, Freiburg A, Labeit S (1995) Phosphorylation switches specific for the cardiac isoform of myosin binding protein-C: a modulator of cardiac contraction? EMBO J 14:1952–1960. doi: 10.1002/j.1460-2075.1995.tb07187.x

Geske JB, Ong KC, Siontis KC, et al (2017) Women with hypertrophic cardiomyopathy have worse survival. Eur Heart J 38:3434–3440. doi: 10.1093/eurheartj/ehx527

Ghosh R, Pattison JS (2018) Macroautophagy and Chaperone-Mediated Autophagy in Heart Failure: The Known and the Unknown. Oxid Med Cell Longev 2018:22 Pages. doi: 10.1155/2018/8602041

Giacalone JC, Sharma TP, Burnight ER, et al (2018) CRISPR-Cas9-Based Genome Editing of Human Induced Pluripotent Stem Cells. Curr Protoc Stem Cell Biol 44:5B.7.1-5B.7.22. doi: 10.1002/cpsc.46.

Goff ZD, Calkins H (2019) Sudden death related cardiomyopathies - Hypertrophic cardiomyopathy. Prog Cardiovasc Dis 62:212–216. doi: 10.1016/j.pcad.2019.04.001

Gore A, Li Z, Fung H-L, et al (2011) Somatic coding mutations in human induced pluripotent stem cells. Nature 471:63–67. doi: 10.1038/nature09805

Govindan S, Mcelligott A, Muthusamy S, et al (2012) Cardiac myosin binding protein-C is a potential diagnostic biomarker for myocardial infarction. J Mol Cell Cardiol 52:154–164. doi: 10.1016/j.yjmcc.2011.09.011.

Hailey DW, Kim PK, Satpute-Krishnan P, et al (2010) Mitochondria supply membranes for autophagosome biogenesis during starvation. Cell 141:656–667. doi: 10.1016/j.cell.2010.04.009.

Halliday BP, Gulati A, Ali A, et al (2018) Sex- and age-based differences in the natural history and outcome of dilated cardiomyopathy. Eur J Heart Fail 20:1392–1400. doi: 10.1002/ejhf.1216

Hanna JS, Shires P, Matile G (1997) Trisomy 1 in a Clinically Recognized Pregnancy. Am J Med Genet 68:98–98. doi: org/10.1002/(SICI)1096-8628(19970110)68:1<98::AID-AJMG20>3.0.CO;2-I

Hashem SI, Murphy AN, Divakaruni AS, et al (2017) Impaired mitophagy facilitates mitochondrial damage in Danon disease. J Mol Cell Cardiol 108:86–94. doi: 10.1016/j.yjmcc.2017.05.007

Hashem SI, Perry CN, Bauer M, et al (2015) Brief Report: Oxidative Stress Mediates Cardiomyocyte Apoptosis in a Human Model of Danon Disease and Heart Failure. Stem Cells 33:2343–2350. doi: 10.1002/stem.2015

Hayashi-Nishino M, Fujita N, Noda T, et al (2009) A subdomain of the endoplasmic reticulum forms a cradle for autophagosome formation. Nat Cell Biol 11:1433–1437. doi: 10.1038/ncb1991

Helms AS, Davis FM, Coleman D, et al (2014) Sarcomere Mutation-Specific Expression Patterns in Human Hypertrophic Cardiomyopathy. Circ Cardiovasc Genet 7:434–443. doi: 10.1161/CIRCGENETICS.113.000448

Herman DS, Lam L, Taylor MRG, et al (2012) Truncations of Titin Causing Dilated Cardiomyopathy. N Engl J Med 366:619–628. doi: 10.1056/NEJMoa1110186

Hershberger RE, Hedges DJ, Morales A (2013) Dilated cardiomyopathy: the complexity of a diverse genetic architecture. Nat Rev Cardiol 10:531–547. doi: 10.1038/nrcardio.2013.105

Hinson JT, Chopra A, Nafissi N, et al (2015) Titin Mutations in iPS cells Define Sarcomere Insufficiency as a Cause of Dilated Cardiomyopathy. Science (80-) 349:982–986. doi: 10.1126/science.aaa5458

Hockemeyer D, Wang H, Kiani S, et al (2011) Genetic engineering of human pluripotent cells using TALE nucleases. Nat Biotechnol 29:731–734. doi: 10.1038/nbt.1927

Huo J, Kamalakar A, Yang X, et al (2017) Evaluation of Batch Variations in Induced Pluripotent Stem Cell-Derived Human Cardiomyocytes from 2 Major Suppliers. Toxicol Sci 156:25–38. doi: 10.1093/toxsci/kfw235

Jahreiss L, Menzies FM, Rubinsztein DC (2008) The Itinerary of Autophagosomes: From Peripheral Formation to Kiss-and-Run fusion with Lysosomes. Traffic 9:574–587. doi: 10.1111/j.1600-0854.2008.00701.x

Kaebisch C, Schipper D, Babczyk P, Tobiasch E (2015) The role of purinergic receptors in stem cell differentiation. Comput Struct Biotechnol J 13:75–84. doi: 10.1016/j.csbj.2014.11.003

Karumbayaram S, Novitch B, Patterson M, et al (2009) Directed differentiation of human induced pluripotent stem cells generates active motor neurons. Stem Cells 27:806–811. doi: 10.1002/stem.31

Kim Y, Rim YA, Yi H, et al (2016) The Generation of Human Induced Pluripotent Stem Cells from Blood Cells: An Efficient Protocol Using Serial Plating of Reprogrammed Cells by Centrifugation. Stem Cells Int 2016:9. doi: 10.1155/2016/1329459

Kleinstiver BP, Pattanayak V, Prew MS, et al (2016) High-fidelity CRISPR-Cas9 nucleases with no detectable genome-wide off-target effects. Nature 529:490–495. doi: 10.1038/nature16526

Knaust AE (2017) Disease modelling of a phospholamban p . Arg14del mutation in hiPSC-derived cardiomyocytes

Korolchuk VI, Saiki S, Lichtenberg M, et al (2011) Lysosomal positioning coordinates cellular nutrient responses. Nat Cell Biol 13:453–462. doi: 10.1038/ncb2204

Krause J, Löser A, Lemoine MD, et al (2018) Rat atrial engineered heart tissue: a new in vitro model to study atrial biology. Basic Res Cardiol 113:1–14. doi: 10.1007/s00395-018-0701-2

Lange WJ De, Grimes AC, Hegge LF, et al (2013) E258K HCM-causing mutation in cardiac MyBP-C reduces contractile force and accelerates twitch kinetics by disrupting the cMyBP-C and myosin S2 interaction. J Gen Physiol 142:241–255. doi: 10.1085/jgp.201311018

Lawrence RE, Zoncu R (2019) The lysosome as a cellular centre for signalling, metabolism and quality control. Nat Cell Biol 21:133–142. doi: 10.1038/s41556-018-0244-7

Lemme M, Ulmer BM, Lemoine MD, et al (2018) Atrial-like Engineered Heart Tissue: An In Vitro Model of the Human Atrium. Stem Cell Reports 11:1378–1390. doi: 10.1016/j.stemcr.2018.10.008

Lewis YE, Moskovitz A, Mutlak M, et al (2018) Localization of transcripts, translation, and degradation for spatiotemporal sarcomere maintenance. J Mol Cell Cardiol 116:16–28. doi: 10.1016/j.yjmcc.2018.01.012

Löser A (2018) Epigenetic mechanisms of transcriptional regulation in cardiac hypertrophy using engineered heart tissue

Maejima Y, Isobe M, Sadoshima J (2017) Regulation of Autophagy by Beclin 1 in the Heart. J Mol Cell Cardiol 95:19–25. doi: 10.1016/j.yjmcc.2015.10.032

Marian A, Braunwald E (2017) Hypertrophic cardiomyopathy: Genetics, Pathogenesis, Clinical Manifestations, Diagnosis, and Therapy. Circ Res 121:749–770. doi: 10.1161/CIRCRESAHA.117.311059.

Maron BJ, Ommen SR, Semsarian C, et al (2014) Hypertrophic Cardiomyopathy: Present and Future, With Translation Into Contemporary Cardiovascular Medicine. J Am Coll Cardiol 64:83–99. doi: 10.1016/j.jacc.2014.05.003

Maron BJ, Towbin JA, Thiene G, et al (2006) Contemporary Definitions and Classification of the Cardiomyopathies: An American Heart Association Scientific Statement From the Council on Clinical Cardiology, Heart Failure and Transplantation Committee; Quality of Care and Outcomes Research and Functio. Circulation 113:1807–1816. doi: 10.1161/CIRCULATIONAHA.106.174287

Marston S, Copeland ON, Jacques A, et al (2009) Evidence From Human Myectomy

Samples That MYBPC3 Mutations Cause Hypertrophic Cardiomyopathy Through Haploinsufficiency*. Circ Res 105:219–222. doi: 10.1161/CIRCRESAHA.109.202440

McEwan DG, Dikic I (2011) The Three Musketeers of Autophagy : phosphorylation , ubiquitylation and acetylation. Trends Cell Biol 21:195–201. doi: 10.1016/j.tcb.2010.12.006.

McNally EM, Mestroni L (2017) Dilated Cardiomyopathy: Genetic Determinants and Mechanisms. Circ Res 121:731–748. doi: 10.1161/CIRCRESAHA.116.309396

Miller JC, Holmes MC, Wang J, et al (2007) An improved zinc-finger nuclease architecture for highly specific genome editing. Nat Biotechnol 25:778–785. doi: 10.1038/nbt1319

Moehle EA, Rock JM, Lee Y-L, et al (2007) Targeted gene addition into a specified location in the human genome using designed zinc finger nucleases. Proc Natl Acad Sci U S A 104:3055–3060. doi: 10.1073/pnas.0611478104

Mosqueira D, Lis-Slimak K, Denning C (2019a) High-Throughput Phenotyping Toolkit for Characterizing Cellular Models of Hypertrophic Cardiomyopathy In Vitro. Methods Protoc 2:. doi: 10.3390/mps2040083

Mosqueira D, Mannhardt I, Bhagwan JR, et al (2018) CRISPR/Cas9 editing in human pluripotent stem cell-cardiomyocytes highlights arrhythmias, hypocontractility, and energy depletion as potential therapeutic targets for hypertrophic cardiomyopathy. Eur Heart J 39:3879–3892. doi: 10.1093/eurheartj/ehy249

Mosqueira D, Smith JGW, Bhagwan JR, Denning C (2019b) Modeling Hypertrophic Cardiomyopathy: Mechanistic Insights and Pharmacological Intervention. Trends Mol Med 25:775–790. doi: 10.1016/j.molmed.2019.06.005

Muhammad E, Levitas A, Singh SR, et al (2015) PLEKHM2 mutation leads to abnormal localization of lysosomes, impaired autophagy flux and associates with recessive dilated cardiomyopathy and left ventricular noncompaction. Hum Mol Genet 24:7227–7240. doi: 10.1093/hmg/ddv423

Mummery CL, Zhang J, Ng ES, et al (2012) Differentiation of Human ES and iPS Cells to Cardiomyocytes: A Methods Overview. Circ Res 111:344–358. doi: 10.1161/CIRCRESAHA.110.227512

Musunuru K, Sheikh F, Gupta RM, et al (2018) Induced Pluripotent Stem Cells for Cardiovascular Disease Modeling and Precision Medicine: A Scientific Statement From the American Heart Association. Circ Genomic Precis Med 11:e000043. doi: 10.1161/HCG.0000000000000043

Nakamura S, Yoshimori T (2017) New insights into autophagosome–lysosome fusion. J Cell Sci 130:1209–1216. doi: 10.1242/jcs.196352

Närvä E, Autio R, Rahkonen N, et al (2010) High-resolution DNA analysis of human embryonic stem cell lines reveals culture-induced copy number changes and loss of heterozygosity. Nat Biotechnol 28:371–377. doi: 10.1038/nbt.1615

Nishino I, Fu J, Tanji K, et al (2000) Primary LAMP-2 deficiency causes X-linked vacuolar cardiomyopathy and myopathy (Danon disease). Nature 406:906–910. doi: 10.1038/35022604

Okamoto S, Amaishi Y, Maki I, et al (2019) Highly efficient genome editing for single-base substitutions using optimized ssODNs with Cas9-RNPs. Sci Rep 9:. doi: 10.1038/s41598-019-41121-4

Okumura T, Horie Y, Lai CY, et al (2019) Robust and highly efficient hiPSC generation from patient non-mobilized peripheral blood-derived CD34+ cells using the auto-erasable Sendai virus vector. Stem Cell Res Ther 10:. doi: 10.1186/s13287-019-1273-2

Olivotto I, Girolami F, Ackerman MJ, et al (2008) Myofilament Protein Gene Mutation Screening and Outcome of Patients With Hypertrophic Cardiomyopathy. Mayo Clin Proc 83:630–638. doi: 10.4065/83.6.630

Palma Medina LM, Becker A-K, Michalik S, et al (2019) Metabolic Cross-talk between Human Bronchial Epithelial Cells and Internalized Staphylococcus aureus as a Driver for Infection. Mol Cell Proteomics 18:892–908. doi: 10.1074/mcp.RA118.001138

Palpant NJ, Pabon L, Friedman CE, et al (2017) Generating high-purity cardiac and endothelial derivatives from patterned mesoderm using human pluripotent stem cells. Nat Protoc 12:15–31. doi: 10.1038/nprot.2016.153

Paquet D, Kwart D, Chen A, et al (2016) Efficient introduction of specific homozygous and heterozygous mutations using CRISPR/Cas9. Nature 533:125–129. doi: 10.1038/nature17664

Park JM, Jung CH, Seo M, et al (2016) The ULK1 complex mediates MTORC1 signaling to the autophagy initiation machinery via binding and phosphorylating ATG14. Autophagy 12:547–564. doi: 10.1080/15548627.2016.1140293

Park JM, Seo M, Jung CH, et al (2018) ULK1 phosphorylates Ser30 of BECN1 in association with ATG14 to stimulate autophagy induction. Autophagy 14:584–597. doi: 10.1080/15548627.2017.1422851

Phipson B, Lee S, Majewski IJ, et al (2016) ROBUST HYPERPARAMETER ESTIMATION

PROTECTS AGAINST HYPERVARIABLE GENES AND IMPROVES POWER TO DETECT DIFFERENTIAL EXPRESSION. Ann Appl Stat 10:946–963. doi: 10.1214/16-AOAS920.

Pohlmann L, Kröger I, Vignier N, et al (2007) Cardiac Myosin-Binding Protein C Is Required for Complete Relaxation in Intact Myocytes. Circ Res 101:928–938. doi: 10.1161/CIRCRESAHA.107.158774

Prondzynski M (2017) Modeling of hypertrophic cardiomyopathy and assessment of gene therapy in human iPSC-derived cardiomyocytes

Prondzynski M, Krämer E, Laufer SD, et al (2017) Evaluation of MYBPC3 trans -Splicing and Gene Replacement as Therapeutic Options in Human iPSC-Derived Cardiomyocytes. Mol Ther - Nucleic Acids 7:475–486. doi: 10.1016/j.omtn.2017.05.008

Prondzynski M, Lemoine MD, Zech ATL, et al (2019) Disease modeling of a mutation in a -actinin 2 guides clinical therapy in hypertrophic cardiomyopathy. EMBO Mol Med e11115:1–18. doi: 10.15252/emmm.201911115

Puertollano R (2014) mTOR and lysosome regulation. F1000Prime Rep 6:. doi: 10.12703/p6-52

Ran FA, Hsu PD, Wright J, et al (2013) Genome engineering using the CRISPR-Cas9 system. Nat Protoc 8:2281–2308. doi: 10.1038/nprot.2013.143

Ravikumar B, Moreau K, Jahreiss L, et al (2010) Plasma membrane contributes to the formation of pre- autophagosomal structures. Nat Cell Biol 12:747–757. doi: 10.1038/ncb2078.

Razzaque A, Gupta M, Osinska H, et al (2013) An Endogenously Produced Fragment of Cardiac Myosin Binding Protein C is Pathogenic and Can Lead to Heart Failure Abdur. Circ Res 113:553–61. doi: 10.1161/CIRCRESAHA.113.301225.

Russell RC, Tian Y, Yuan H, et al (2013) ULK1 induces autophagy by phosphorylating Beclin-1 and activating Vps34 lipid kinase. Nat Cell Biol 15:741–750. doi: 10.1038/ncb2757.

Sadayappan S, de Tombe PP (2014) Cardiac myosin binding protein-C as a central target of cardiac sarcomere signaling: a special mini-review series. Pflugers Arch Eur J Physiol 466:195–200. doi: 10.1007/s00424-013-1396-8

Sandri M, Robbins J (2014) Proteotoxicity: An Underappreciated Pathology in Cardiac Disease. J Mol Cell Cardiol 0:3–10. doi: 10.1016/j.yjmcc.2013.12.015

Sarikas A, Carrier L, Schenke C, et al (2005) Impairment of the ubiquitin-proteasome system by truncated cardiac myosin binding protein C mutants. Cardiovasc Res 66:33–44. doi: 10.1016/j.cardiores.2005.01.004

Schlaeger TM, Daheron L, Brickler TR, et al (2015) A comparison of non-integrating reprogramming methods. Nat Biotechnol 33:58–63. doi: 10.1038/nbt.3070

Schlossarek S, Englmann DR, Sultan KR, et al (2012) Defective proteolytic systems in Mybpc3-targeted mice with cardiac hypertrophy. Basic Res Cardiol 107:235. doi: 10.1007/s00395-011-0235-3

Schlossarek S, Mearini G, Carrier L (2011) Cardiac myosin-binding protein C in hypertrophic cardiomyopathy: Mechanisms and therapeutic opportunities. J Mol Cell Cardiol 50:613–620. doi: 10.1016/j.yjmcc.2011.01.014

Schultheiss H, Fairweather D, Caforio ALP, et al (2019) Dilated cardiomyopathy. Nat Rev Dis Prim 5:32. doi: 10.1038/s41572-019-0084-1

Schulze ML, Lemoine MD, Fischer AW, et al (2019) Dissecting hiPSC-CM pacemaker function in a cardiac organoid model. Biomaterials 206:133–145. doi: 10.1016/j.biomaterials.2019.03.023

Sciarretta S, Forte M, Frati G, Sadoshima J (2018) New Insights Into The Role of mTOR Signaling in the Cardiovascular System. Circ Res 122:489–505. doi: 10.1161/CIRCRESAHA.117.311147

Seeger T, Shrestha R, Lam CK, et al (2019) A Premature Termination Codon Mutation in MYBPC3 Causes Hypertrophic Cardiomyopathy via Chronic Activation of Nonsense-Mediated Decay. Circulation 139:799–811. doi: 10.1161/CIRCULATIONAHA.118.034624

Semsarian C, Ingles J, Maron MS, Maron BJ (2015) New Perspectives on the Prevalence of Hypertrophic Cardiomyopathy. J Am Coll Cardiol 65:1249–1254. doi: 10.1016/j.jacc.2015.01.019

Singh SR, Zech ATL, Geertz B, et al (2017) Activation of Autophagy Ameliorates Cardiomyopathy in Mybpc3-Targeted Knockin Mice. Circ Hear Fail 10:e004140. doi: 10.1161/CIRCHEARTFAILURE.117.004140

Smith C, Gore A, Yan W, et al (2014) Whole-Genome Sequencing Analysis Reveals High Specificity of CRISPR/Cas9 and TALEN-Based Genome Editing in Human iPSCs. Cell Stem Cell 15:12–13. doi: 10.1016/j.stem.2014.06.011

Smith JGW, Owen T, Bhagwan JR, et al (2018) Isogenic Pairs of hiPSC-CMs with

Hypertrophic Cardiomyopathy/LVNC-Associated ACTC1 E99K Mutation Unveil Differential Functional Deficits. Stem Cell Reports 11:1226–1243. doi: 10.1016/j.stemcr.2018.10.006

Smits AH, Ziebell F, Joberty G, et al (2019) Biological plasticity rescues target activity in CRISPR knock outs. Nat Methods 16:1087–1093. doi: 10.1038/s41592-019-0614-5

Song L, Su M, Wang S, et al (2014) MiR-451 is decreased in hypertrophic cardiomyopathy and regulates autophagy by targeting TSC1. J Cell Mol Med 18:2266–2274. doi: 10.1111/jcmm.12380

Squire JM, Luther PK, Knupp C (2003) Structural Evidence for the Interaction of C-protein (MyBP-C) with Actin and Sequence Identification of a Possible Actin-binding Domain. J Mol Biol 331:713–724. doi: 10.1016/S0022-2836(03)00781-2

Stepanenko AA, Dmitrenko V V. (2015) HEK293 in cell biology and cancer research: Phenotype, karyotype, tumorigenicity, and stress-induced genome-phenotype evolution. Gene 569:182–190. doi: 10.1016/j.gene.2015.05.065

Suomi T, Elo LL (2017) Enhanced differential expression statistics for data-independent acquisition proteomics. Sci Rep 7:1–8. doi: 10.1038/s41598-017-05949-y

Taapken SM, Nisler BS, Newton MA, et al (2011) Karotypic abnormalities in human induced pluripotent stem cells and embryonic stem cells. Nat Biotechnol 29:313–314. doi: 10.1038/nbt.1835

Takahashi K, Tanabe K, Ohnuki M, et al (2007) Induction of Pluripotent Stem Cells from Adult Human Fibroblasts by Defined Factors. Cell 131:861–872. doi: 10.1016/j.cell.2007.11.019

Takahashi K, Yamanaka S (2006) Induction of Pluripotent Stem Cells from Mouse Embryonic and Adult Fibroblast Cultures by Defined Factors. Cell 126:663–676. doi: 10.1016/j.cell.2006.07.024

Tannous P, Zhu H, Johnstone JL, et al (2008) Autophagy is an adaptive response in desmin-related cardiomyopathy. Proc Natl Acad Sci U S A 105:9745–9750. doi: 10.1073/pnas.0706802105

Thomson JA, Itskovitz-Eldor J, Shapiro SS, et al (1998) Embryonic Stem Cell Lines Derived from Human Blastocysts. Science (80-) 282:1145–1147. doi: 10.1126/science.282.5391.1145

Urnov FD, Miller JC, Lee Y-L, et al (2005) Highly efficient endogenous human gene correction using designed zinc-finger nucleases. Nature 435:646–651. doi:

10.1038/nature03556

van der Velden J, Stienen GJM (2019) CARDIAC DISORDERS AND PATHOPHYSIOLOGY OF SARCOMERIC PROTEINS. Physiol Rev 99:381–426. doi: 10.1152/physrev.00040.2017

van Dijk SJ, Dooijes D, dos Remedios C, et al (2009) Cardiac Myosin-Binding Protein C Mutations and Hypertrophic Cardiomyopathy - Haploinsufficiency, Deranged Phosphorylation, and Cardiomyocyte Dysfunction. Circulation 119:1473–1483. doi: 10.1161/CIRCULATIONAHA.108.838672

Veres A, Gosis BS, Ding Q, et al (2014) Low Incidence of Off-Target Mutations in Individual CRISPR-Cas9 and TALEN Targeted Human Stem Cell Clones Detected by Whole-Genome Sequencing. Cell Stem Cell 15:27–30. doi: 10.1016/j.stem.2014.04.020

Vignier N, Schlossarek S, Fraysse B, et al (2009) Nonsense-Mediated mRNA Decay and Ubiquitin–Proteasome System Regulate Cardiac Myosin-Binding Protein C Mutant Levels in Cardiomyopathic Mice. Circ Res 105:239–248. doi: 10.1161/CIRCRESAHA.109.201251

Yang X, Pabon L, Murry CE (2014) Engineering Adolescence: Maturation of Human Pluripotent Stem Cell-derived Cardiomyocytes. Circ Res 114:511–523. doi: 10.1161/CIRCRESAHA.114.300558

Yoshida S, Nakanishi C, Okada H, et al (2018) Characteristics of induced pluripotent stem cells from clinically divergent female monozygotic twins with Danon disease. J Mol Cell Cardiol 114:234–242. doi: 10.1016/j.yjmcc.2017.11.019

Zech ATL, Singh SR, Schlossarek S, Carrier L (2019) Autophagy in cardiomyopathies. Biochim Biophys Acta - Mol Cell Res. doi: 10.1016/J.BBAMCR.2019.01.013

9. Supplement

9.1. Supplementary figures and tables

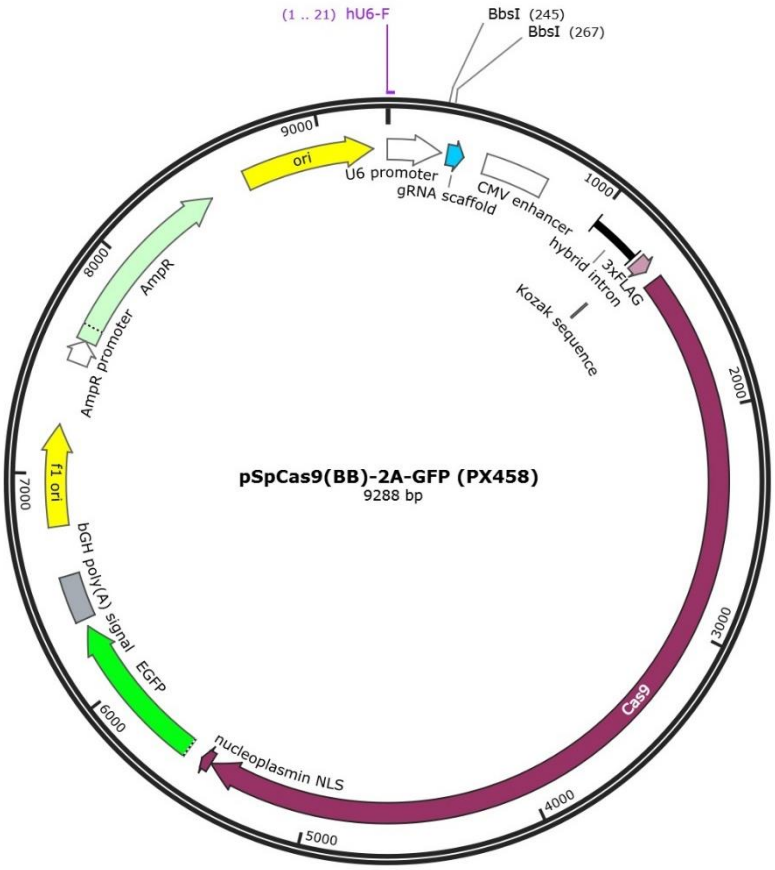

Figure S1: Map of pSpCas9(B)-2A-GFP plasmid. Cutting sites of BbsI and U6 Fwd primer (purple) are indicated.

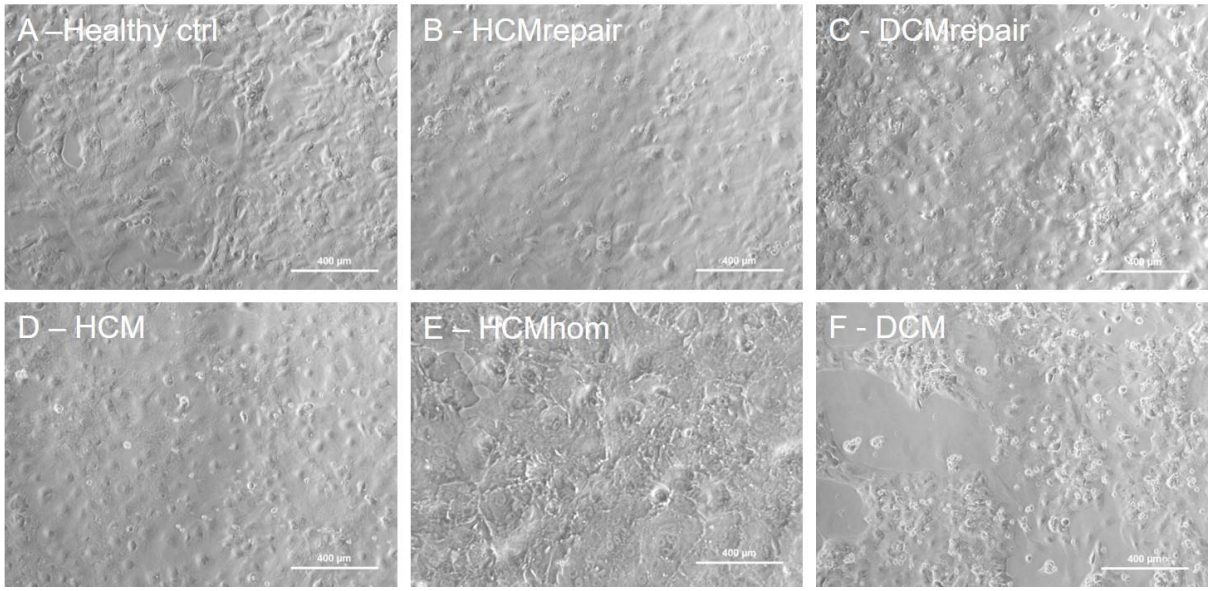

Figure S2: Phenotypic evaluation of the hiPSC-CMs of all investigated lines at day 7 of culture. To monitor the phenotype during the 30-day culture, all hiPSC-CM lines were subjected to light microscopic evaluation and pictures were taken (A – F). Scale bar = 400 µm. 10x magnification.

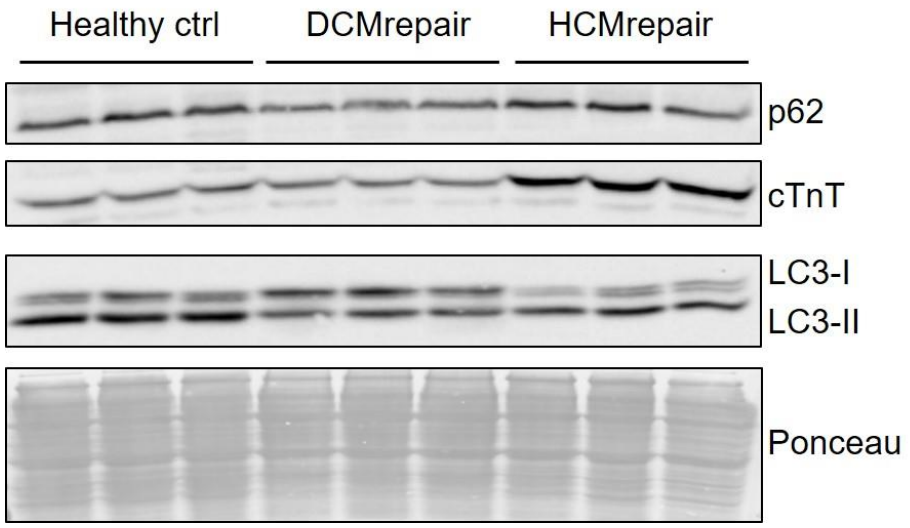

Figure S3: Representative immunoblot of healthy ctrl, HCMrepair and DCMrepair hiPSC-CMs to display the different genetic backgrounds. Thirty-day-old hiPSC-CMs were treated with DMSO (0.05%) and the main marker of the ALP evaluated by immunoblotting. Ponceau and cTnT was used as loading control.

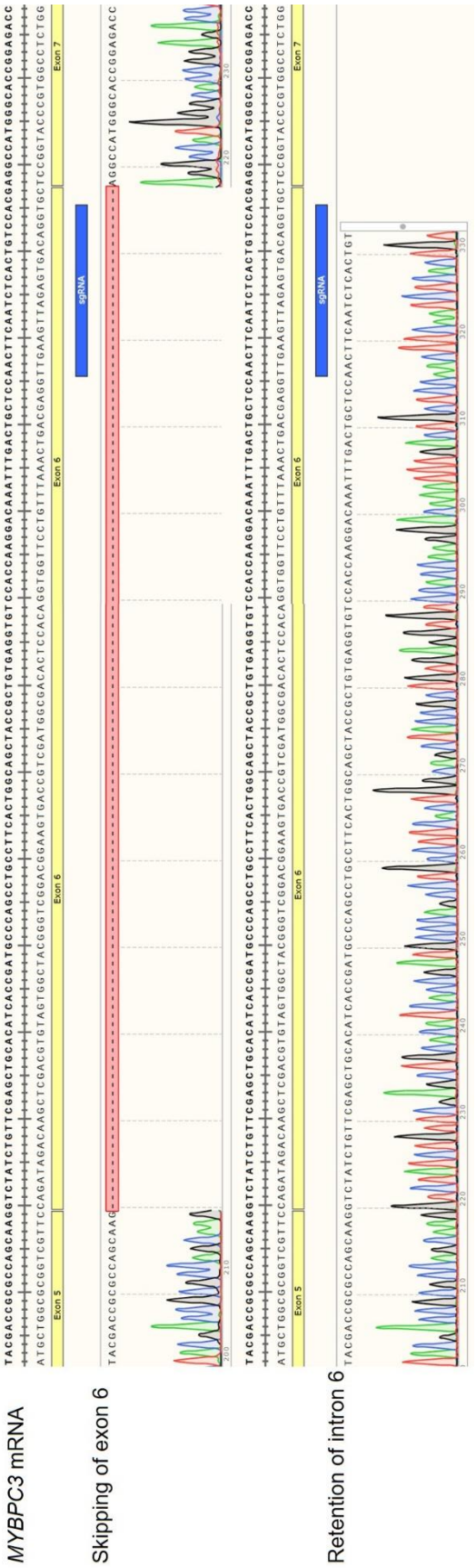

Figure S4: Analysis of sequencing of hom. clone#11 to evaluate its mRNA forms. For this clone skipping of exon 6 and retention of intron 6 was observed.

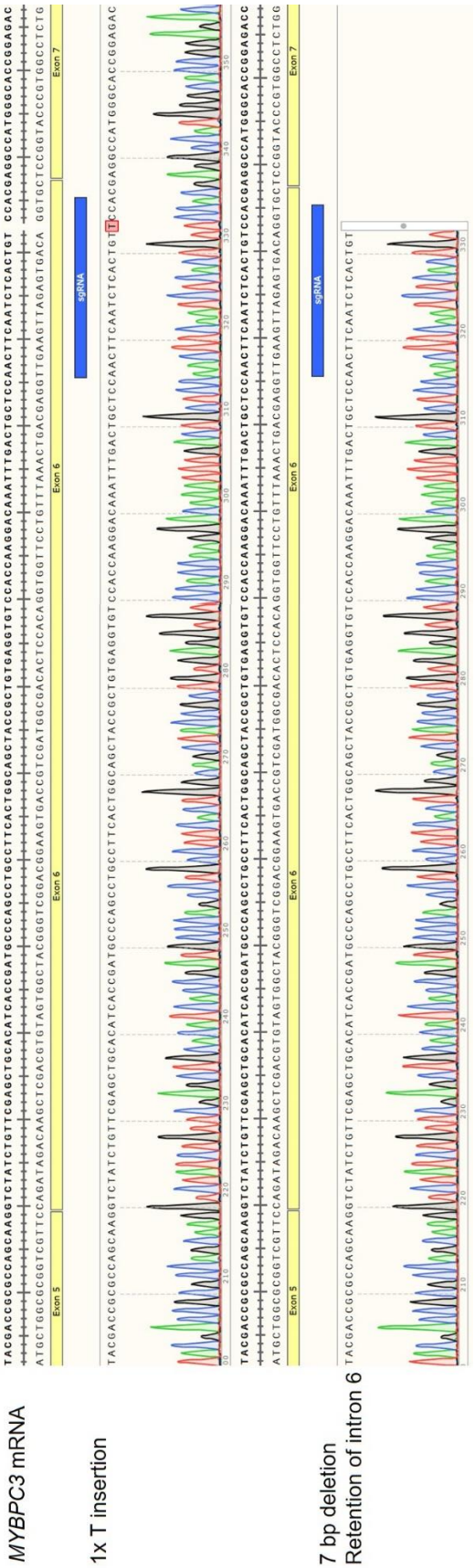

Figure S5: Analysis of sequencing of c.het. clone#14 to evaluate its mRNA forms. Sequencing revealed a T insertion and a 7-bp deletion along with the retention of intron 6.

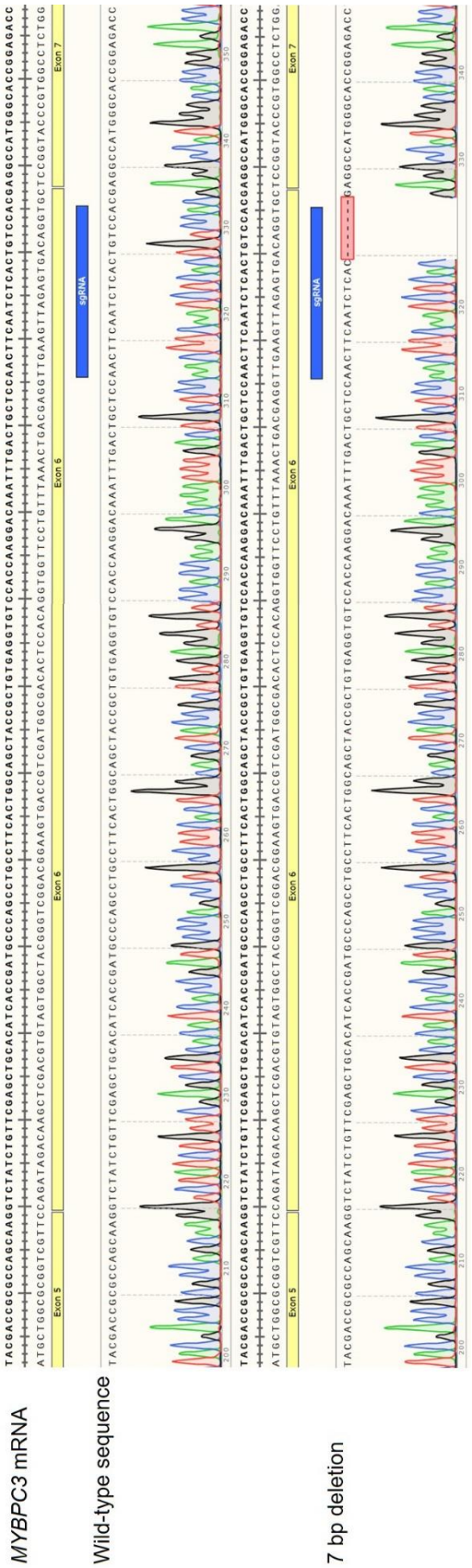

Figure S6: Analysis of sequencing of het. clone#15 to evaluate its mRNA forms. The wild-type sequence and a 7 bp deletion was detected for this clone.

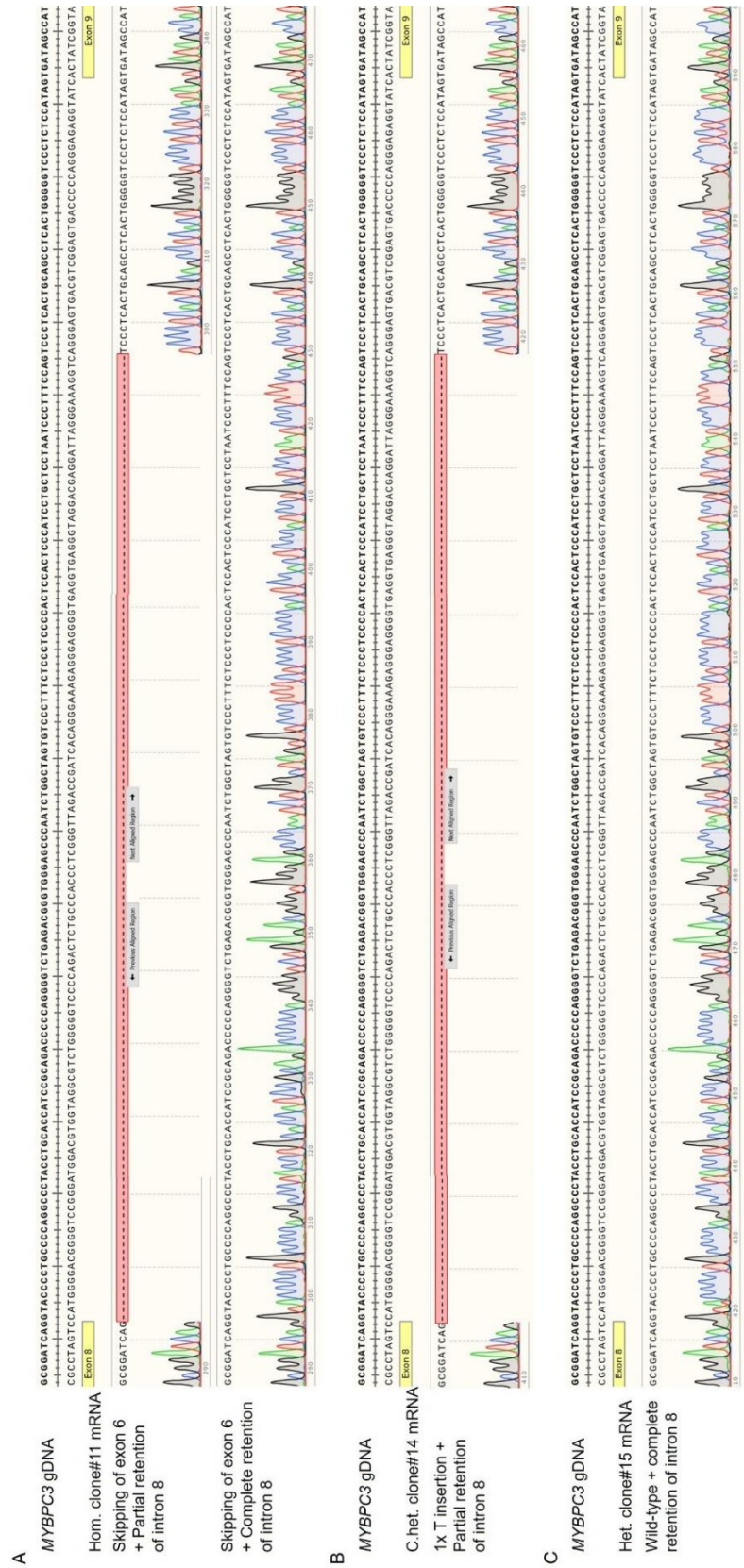

Figure S7: Overview of the alternative splicing of intron 8 for all CRISPR clones. The hom. clone#11 showed a partial and a complete retention of intron 8 (A), whereas the c.het. clone#14 only showed the partial retention (B) and the het. clone#15 the complete retention of intron 8 on its wild-type allele (C).

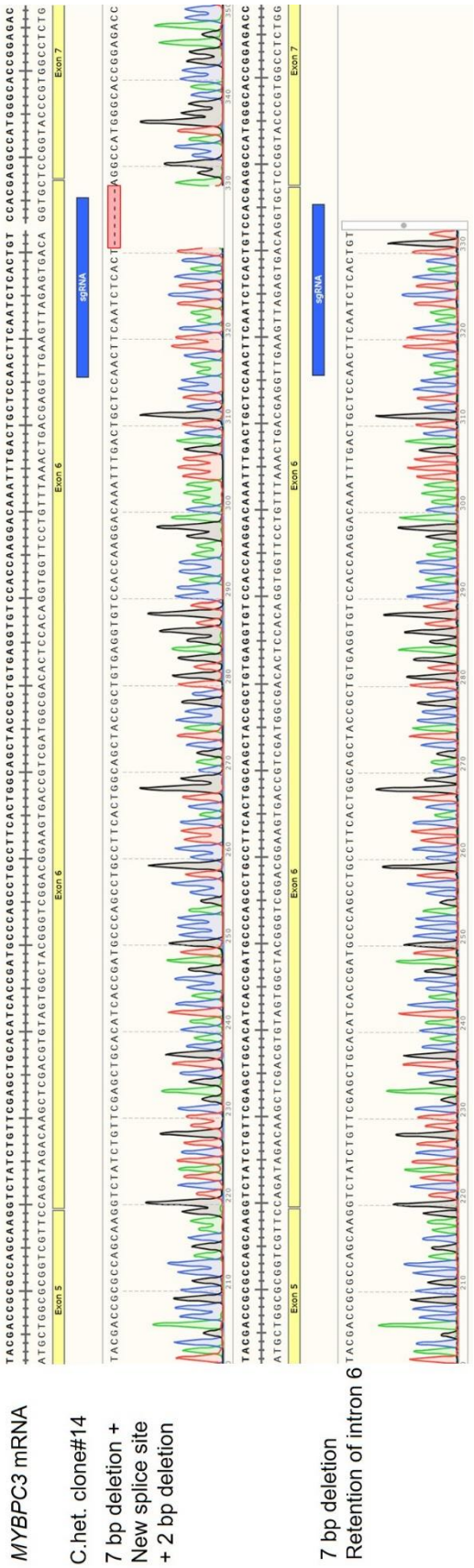

Figure S8: Formation of a cryptic donor splice site in c.het. clone#14. This new splice site led to the regular splicing of intron 6, but still a frameshift was induced and a PTC in exon 9 occurred. Without this new splice site, intron 6 would have been retained (see lower part).

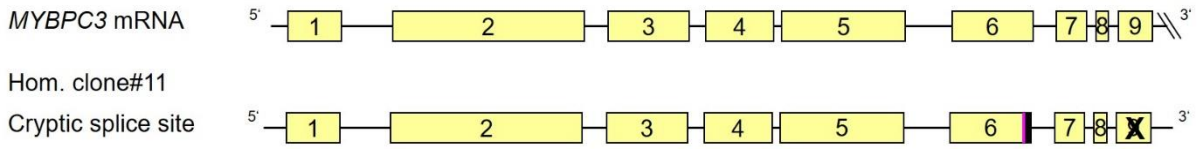

Figure S9: Putative cryptic splice site of the hom. clone#11. The cryptic splice enables the proper splicing of intron 6 but leads to a PTC in exon 9. Yellow = Exons. X = PTC. Black block = deletion. Pink line = 2 nucleotides deleted due to new splice site.

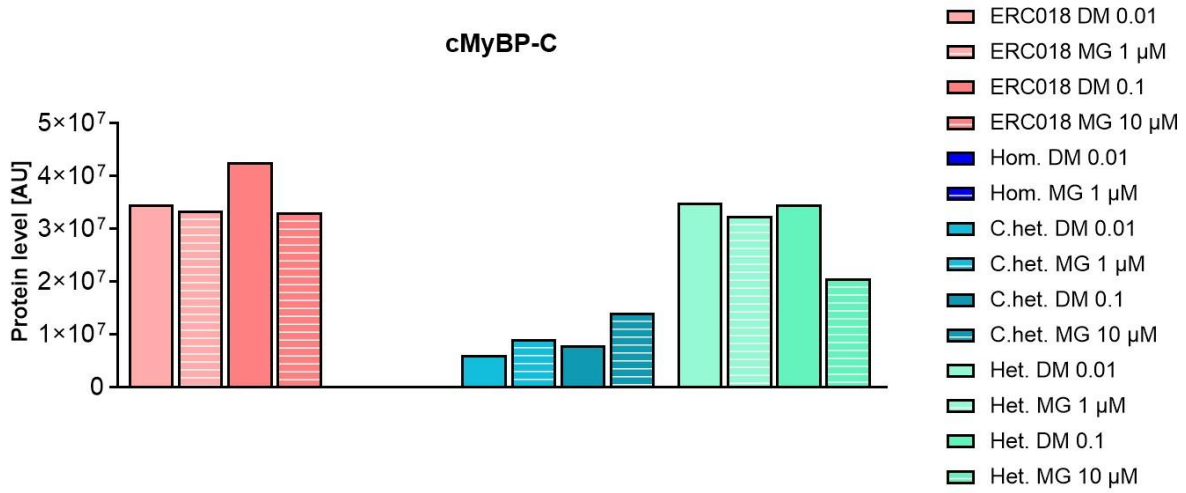

Figure S10: Quantification of cMyBP-C KO immunoblot. ERC018, hom. clone#11, c.het. clone#14 and het. clone#15 hiPSC-CMs were treated with 0.01% or 0.1% DMSO (DM) or 1 µM or 10 µM MG-132 (MG) for 24 h. For hom. clone#11 no signal for cMyBP-C was detected, whereas for c.het. clone#14 a weak signal for cMyBP-C was detected. Het. clone#15 showed a rather prominent for cMyBP-C that is comparable to the cMyBP-C signal of ERC018. n = 1 batch. Normalized to ponceau, expressed in arbitrary units (AU).

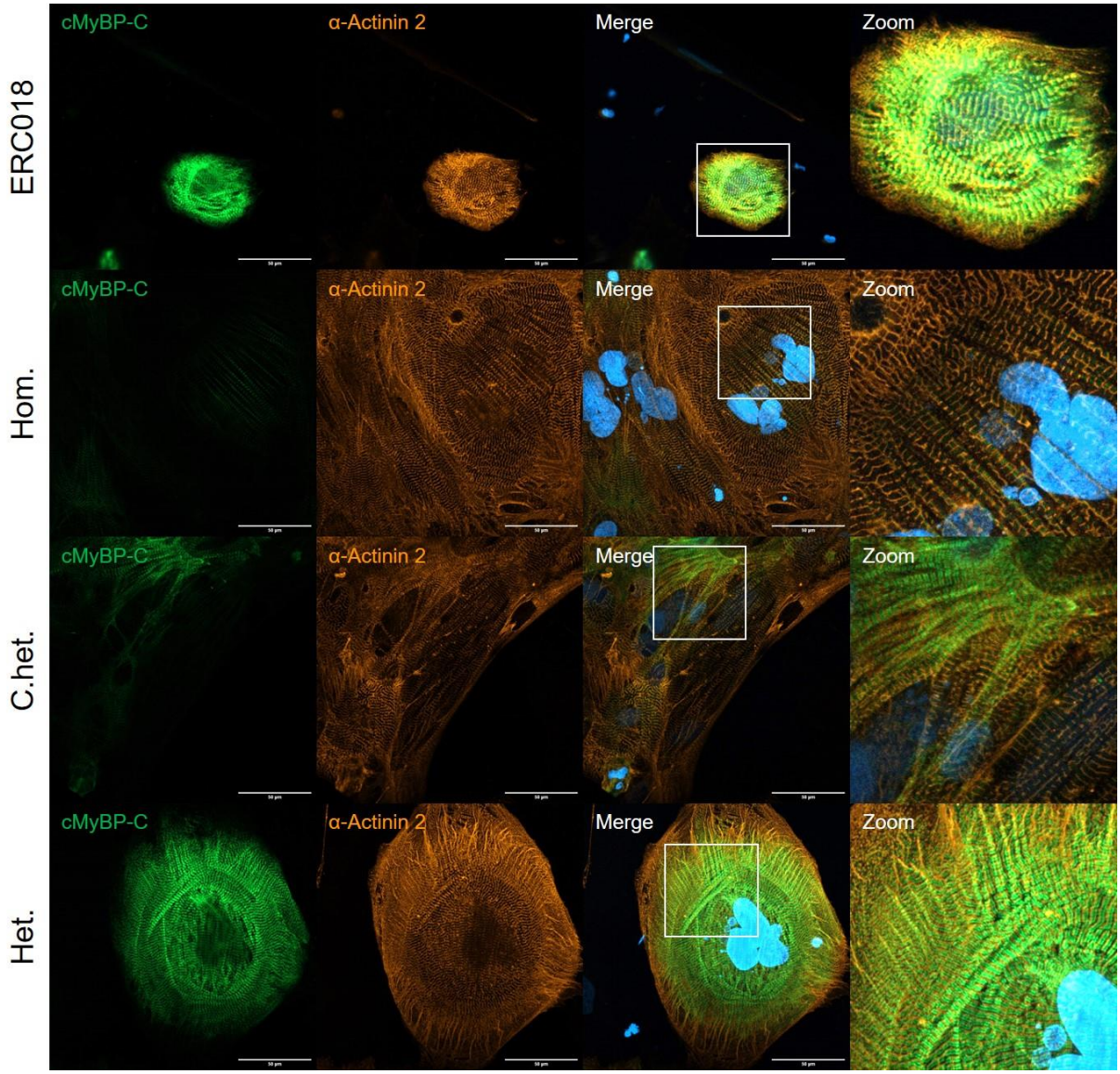

Figure S11*:* Evaluation of cMyBP-C with C0-C1 antibody in combination with α-actinin 2 in 30-day-old hiPSC-CMs by immunofluorescence. ERC018, hom. clone#11, c.het. clone#14 and het. clone#15 were stained for cMyBP-C (green), α-actinin 2 (orange) and Hoechst (blue), as the merged image, its zoom and the single channel images show. Striations were detectable for all clones with α-actinin 2 and for ERC018, the c.het. clone#14 and the het. clone#15 also with cMyBP-C. The hom. clone#11 solely showed a rather weak signal for cMyBP-C. Overall the morphology of the 30-day-old hiPSC-CMs is not as good as for the 7-day-old hiPSC-CMs. White box highlights the magnified area (zoom). Scale bar = 50 µm. 40x magnification.

9.2. List of abbreviations

A	
A	Area
AA	Amino acid
ABCF1	ATP binding cassette subfamily F member 1
ACE	Angiotensin-converting enzymes
ACTA2	Actin alpha 2, smooth muscle
ACTB	Actin beta
ACTC1	Cardiac muscle actin alpha 1
ACTN2**/ACTN2**	Alpha-Actinin 2
AGC	Automatic gain control
ALP	Autophagy-lysosomal pathway
AMPK	AMP-activated protein kinase
AP	Action potential
APS	Ammonium persulfate
ATG	Autophagy-related genes
ATP	Adenosine triphosphate/ATPase
ATP2A2	ATPase sarcoplasmic/endoplasmic reticulum Ca2+ transporting 2
AU	Arbitrary units
B	
Bafilo	Bafilomycin A_1
BF	Brightfield
Bp	Base pair
BCL2	BCL2 apoptosis regulator
Bcl-2	B-cell lymphoma 2
bFGF	Basic fibroblast growth factor
BMP4	Bone morphogenetic protein 4
BSA	Bovine serum albumin
BTS	N-Benzyl-p-Toluenesulfonamide
C	
Cas	CRISPR-associated
CASQ2	Calsequestrin 2
cDNA	Complementary DNA
C.het.	Compound heterozygous
CLTC	Clathrin heavy chain
CM	Cardiomyocyte

CMA	Chaperone-mediated autophagy
C-myc	Transcriptional regulator Myc-like
COL1A1	Collagen type I alpha 1 chain
COL3A1	Collagen type III alpha 1 chain
cMyBP-C	Cardiac myosin-binding protein C
CoM	Conditioned medium
CRISPR	Clustered regularly interspaced short palindromic repeats
crRNA	CRISPR RNA
CRT	Cardiac resynchronization therapy
CSQ	Calsequestrin
CTGF	Connective tissue growth factor
cTnC	Cardiac troponin C
cTnI	Cardiac troponin I
cTnT	Cardiac troponin T
D	
DCM	Dilated cardiomyopathy
DDA	Data dependent mode
ddH_2O	Distilled water
DEPTOR	DEP domain-containing mTOR-interacting protein
DIA	Data independent mode
Dim	Dimension
DMEM	Dulbecco's Modified Eagle Medium
DNMT3A	DNA methyltransferase 3A
DMSO	Dimethyl sulfoxide
DNA	Deoxyribonucleic acid
dNTP	Deoxy-nucleoside triphosphate
DSB	Double strand break
dsDNA	Double-stranded DNA
DTT	1,4-Dithiothreitol
E	
EB	Embryoid body
EDTA	Ethylenediaminetetraacetic acid
e.g.	Exempli gratia
***EPG5*/EPG5**	Ectopic P-granules autophagy protein 5 homolog
ER	Endoplasmic reticulum
ESC	Embryonic stem cell

et al.	Et alii
F	
FACS	Fluorescence-activated cell sorting
FC	Flow cytometry
FCS	Fetal calf serum
FHL2	Four and a half LIM domains 2
FIP200	Focal adhesion kinase family interacting protein of 200 kDa
FITC	Fluorescein isothiocyanate
FKBP12	FK506-binding protein of 12 kDa
FN1	Fibronectin 1
FOXO1	Forkhead box O1
FSC	Forward scatter
FTDA	bFGF, TGFβ1, dorsomorphin and activin A-based hiPSC culture medium
FWD	Forward
FYCO1	FYVE and coiled-coil domain autophagy adaptor 1
G	
GABARAP	γ-Aminobutyric acid receptor-associated protein
GAPDH	Glyceraldehyde 3-phosphate dehydrogenase
GATE-16	Golgi-associated ATPase enhancer of 16k Da
gDNA	Genomic DNA
GFP	Green fluorescent protein
GSK3β	Glycogen synthase kinase 3 beta
GTPase	Guanosine triphosphatase
H	
H	Height
HBSS	Hanks' Balanced Salt Solution
HCD	High energy collisional dissociation
HCM	Hypertrophic cardiomyopathy
HDAC6	Histone deacetylase 6
HDR	Homology-directed repair
Healthy ctrl	Healthy contrl
HEPES	4-(2-hydroxyethyl)-1-piperazineethanesulfonic acid
hESC	Human embryonic stem cell
Het.	Heterozygous
hiPSC	Human induced-pluripotent stem cell
hiPSC-CMs	Human induced-pluripotent stem cell derived cardiomyocytes

HK-II	Hexokinase-II
Hom.	Homozygous
HRM/iRT	Hyper Reaction Monitoring/indexed Retention Time
I	
ICa	Inward Ca^{2+} current
ICD	Implantable cardioverter-defibrillators
I.e.	Id est
IEPT	Institute of Experimental Pharmacology and Toxicology
IF	Immunofluorescence/Immunofluoreszenz
indel	Insertion-deletion
iPSC	Induced-pluripotent stem cell
J	
JNK	c-Jun N-terminal kinase
K	
kb	Kilobase
Klf4	Kruppel like factor 4
KO	Knockout
L	
LAMP1	Lysosome-associated membrane protein 1
LAMP2	Lysosome-associated membrane protein 2
Lamp-2	Lysosomal-associated membrane protein 2
LAMP-2	Lysosome-associated membrane protein-2
LAMP-2B	LAMP-2 isoform B
LC3	Microtubule-associated protein 1 light chain 3
LMM	Light meromyosin
LVNC	Left ventricular non-compaction
M	
M-motif	MyBP-C motif
MAP1LC3A	Microtubule associated protein 1 light chain 3 alpha
MAP1LC3B	Microtubule associated protein 1 light chain 3 beta
Mio.	Million
miRNA	microRNA
mLST8	Mammalian lethal with SEC13 protein 8
mRNA	Messenger RNA
MS	Mass spectrometric
mTOR	Mammalian/mechanistic target of rapamycin

MTOR	Mammalian/mechanistic target of rapamycin kinase
MYBPC1	Myosin binding protein C1
MYBPC2	Myosin binding protein C2
MYBPC3	Myosin binding protein C3
MYH6	Cardiac alpha-myosin heavy chain
MYH7	Beta-myosin heavy chain
N	
NaCl	Sodium chloride
***NBR1*/NBR1**	NBR1 autophagy cargo receptor/Neighbour of BRAC1
NCX	Sodium-calcium exchanger
NFKB1	Nuclear Factor Kappa B Subunit 1
NHEJ	Non-homologous end joining
NMD	Nonsense-mediated mRNA decay
NPPA	Natriuretic peptide A
NPPB	Natriuretic peptide B
O	
Oct4	Octamer binding transcription factor 4
ON	Overnight
OT_#1	Off-target 1
P	
p	Passage
PA	Proline-Alanine rich domain
PAGE	Polyacrylamide gel electrophoresis
PAM	Protospacer adjacent motif
PBS	Phosphate-buffered saline
PCA	Principal component analysis
PCR	Polymerase chain reaction
PE	Phosphatidylethanolamine
PGK1	Phosphoglycerate kinase 1
PI3K	Phosphatidylinositol 3-kinase
PI3K, class III	Phosphatidylinositol-3-phosphate kinase III
PKB	Protein kinase B
PLB/*PLN*/PLN	Phospholamban
PLEKHM2	Pleckstrin homology domain containing, family M member 2
POSTN	Periostin
PPP1R1A	Protein Phosphatase 1 Regulatory Inhibitor Subunit 1A

PRAS40	Proline-rich AKT substrate of 40 kDa
PTC	Premature termination codon
PVA	Polyvinyl alcohol
PVDF	Polyvinylidene fluoride
Q	
RT-qPCR	Real-time quantitative PCR
R	
Rapa	Rapamycin
RAPTOR	Regulatory-associated protein of mTOR
REV	Reverse
RHEB	Ras homolog enriched in brain
RNA	Ribonucleic acid
RPMI	Roswell Park Memorial Institute
RT	Room temperature
RT-PCR	Reverse Transcriptase-PCR
RyR	Ryanodine receptor
RYR2	Ryanodine receptor 2
S	
S100A4	S100 calcium binding protein A4
SDS	Sodium dodecyl sulphate
SEM	Standard error of the mean
SERCA	Sarcoplasmic reticulum Ca^{2+} ATPase
sgRNA	Single-guide RNA
SNARE	Soluble N-ethylmaleimide-sensitive-factor attachment receptor
SNP	Single Nucleotide Polymorphism
Sox2	Sex determining region Y -box 2
SR	Sarcoplasmic reticulum
SSC	Sideward scatter
SSEA3	Stage-specific Embryonic Antigen 3
ssODN	Single-stranded oligonucleotides
STAT1	Signal transducer and activator of transcription 1
STAT3	Signal transducer and activator of transcription 3
STX17	Syntaxin 17
SQSTM1	Sequestome 1
T	
TAE	Tris acetate EDTA

TALEN	Transcription activator-like effector nuclease
TBS	Tris-buffered saline
TBS-T	TBS-Tween
TFE3	Transcription factor binding to IGHM enhancer 3
***TFEB*/TFEB**	Transcription factor EB
TEMED	Tetramethylethylenediamine
TGFß	Transforming growth factor ß
tracrRNA	Trans-activating crRNA
Tris	Tris-(hydroxymethyl)-aminoethane
TSC1/2	Tuberous sclerosis protein 1 or 2
TTN	Titin
TUBB	Tubulin beta class I
U	
UKE	University Medical Center Hamburg Eppendorf
ULK1/2	Unc-51-like autophagy activating kinase 1/2
UPS	Ubiquitin-proteasome system
V	
VAMP8	Vesicle-associated membrane protein 8
V-ATPase	Vacuolar H^+-ATPase
VPS15	Vacuolar protein sorting 15
VPS34	Vacuolar protein sorting 34
vs.	Versus
W	
W	Width
WB	Western blot
WT	Wild-type
Y	
Y	Y-27632
Z	
ZFN	Zinc finger nucleases
ZKSCAN3	Zinc finger with KRAB and SCAN domains 3

9.3. Devices, materials & substances

9.3.1. Devices

4D-Nucleofector Core Unit and X Unit (Lonza)

ABI PRISM 7900HT Sequence Detection System (Applied Biosystems)

Analytic Scale Genius (Sartorius AG)

Cell culture incubator CB 220 (Binder)

Cell culture incubators S2020 1.8, HERAcell 240 & 150i (Thermo Fisher Scientific)

Cell culture incubators MCO-19M & MCO-20AIC (Sanyo)

Centrifuges 5415 R & 5810 R (Eppendorf)

Centrifuge Avanti JXN 26 (Beckmann Coulter)

Centrifuge J-6B (Beckmann Coulter)

Centrifuges Rotanta/RP & Universal 30 RF (Hettich)

ChemiDoc Touch Imaging System (Bio-Rad)

Confocal microscope (LSM800, Zeiss)

Cryopreservation system Asymptote EF600M (Grant Instruments)

Electrophoretic Transfer Cell Mini Trans-Blot cell (Bio-Rad)

FACSAriaTM IIIu (BD Biosciences)

FACS Canto II flow cytometer (BD Biosciences)

Gel electrophoresis cell Mini-PROTEAN 3 Cell (Bio-Rad)

Gel electrophoresis tank Sub-cell® GT (Bio-Rad)

Ice machine (Scotsman)

Magnetic stirring and heating plate IKA Combimag RET (Janke & Kunkel & Co KG)

Magnetic stirring plate Variomag / Cimarec Biosystem Direct (Thermo Fisher Scientific)

Magnetic stirring plate Variomag / Cimarec Biosystem 4 Direct (Thermo Fisher Scientific)

Microscope Axioskop 2 with AxioCam Color (Zeiss)

Microscope Axiovert 25 with ProgRes Speed XT core 5 camera (Jenoptik)

Microscope EVOS FL Cell Imaging System (Thermo Fisher Scientific)

Microwave (Sharp)

NanoDrop ND-1000 Spectrophotometer (Thermo Fisher Scientific)

nCounter SPRINT Profiler (NanoString Technologies)

Pipettes 10 / 100 / 1000 µL (Eppendorf)

Portable balance Scout Pro (Ohaus)

Power supply PowerPac Basic (Bio-Rad)

Precision Advanced Scale (Ohaus)

QExactive HFx mass spectrometer (Thermo Electron)

Qubit 3.0 Fluorometer (Thermo Fisher Scientific)

Safety workbench HeraSafe (Heraeus)

Safety workbench Safe 2020 (Thermo Fischer Scientific)

Thermal cycler Hybaid PCR Sprint (Thermo Fisher Scientific)

Thermal cycler vapo.protect (Eppendorf)

Thermomixer comfort (Eppendorf)

TissueLyser (QIAGEN)

TubeRoller (Benchmark)

Ultimate 3000 nano-LC system (Thermo Fisher Scientific)

Vortexer Vibrofix VF1 (Janke & Kunkel GmbH)

Water bath 25900 (Medax)

9.3.2. Software

Axio Vision Rel. 4.8.2 (Zeiss)

FACSDiva (BD Biosciences)

FlowJo 10 (BD Biosciences)

Image Lab Version 5.2.1 (Bio-Rad)

ImageJ 1.52n (Wayne Rasband)

nSolver Analysis Software 4.0 (NanoString Technologies)

Prism 8.3.0. (GraphPad)

ProgRes Capture Pro 2.8.8 (Jenoptik)

SDS 2.4.1 (Applied Biosystems)

SnapGene 5.0.1. (GSL Biotech LLC)

SpectronautTM Pulsar 13.4 (Biognosys AG)

ZEN 2.3 (Zeiss)

9.3.3. Materials

12-well plates (Nunc or Th. Geyer, 150628)

6-well plates (Nunc or Greiner, 657160)

96-well plate µClear black CELLSTAR (Greiner, 655090)

250 mL Vacuum Filtration "rapid"-Filtermax (TPP, 99250)

500 mL Vacuum Filtration "rapid"-Filtermax (TPP, 99500)

AlumaSeal 96 film (Sigma-Aldrich, Z721549-100EA)

Aspiration pipette 2 mL (Sarstedt, 86.1252.011)

Blotting paper Whatman 3MM (Schleicher & Schuell)

Cell culture flask T80 (Nunc, 178905)

Cell culture flask T75 (Sarstedt, 83.3911.002)

Cell culture flask T175 (Sarstedt, 2.502)

Cell culture plate 6 / 12 / 24-well (Nunc)

Cell scraper (Sarstedt, 83.1830)

Cell strainer 30 µm (Sysmex, 04-004-2326)

Cryovial CryoPure 1.6 mL (Sarstedt, 72.380)

Flow cytometry tubes (Sarstedt, 55.1579)

Mini-PROTEAN® Comb, 10-well, 1.0 mm, 44 µl (Bio-Rad, 1653359)

Mini-PROTEAN® Comb, 15-well, 1.0 mm, 44 µl (Bio-Rad, 1653360)

Mini-PROTEAN Short Plates (Bio-Rad, 1653308)

Mini-PROTEAN® Spacer Plates with 1.0 mm Integrated Spacers (Bio-Rad, 1653311)

Multiply®µStrip Pro mix colour (Sarstedt, 72.991.992)

Neubauer counting chamber (Karl-Hecht KG)

Nitrocellulose membrane (GE Healthcare, 10600003)

PCR tubes (Sarstedt)

Pipette tips (Sarstedt)

Pipette tips with Biosphere filter (10 µL / 100 µL / 1000 µL Sarstedt)

PVDF membrane (GE Healthcare, 10485289)

µPACTM micro-Chip (Pharmafluidics)

Qubit assay tubes (Thermo Fisher Scientific, Q32856)

Reaction tube graduated 15 mL (Sarstedt, 62.554.502)

Reaction tubes conical 15 / 50 mL (Sarstedt)

Reaction tubes Safe Lock 0.2 – 2 mL (Eppendorf)

Serological pipettes 1 / 2 / 5 / 10 / 25 / 50 mL (Sarstedt)

Spinner flasks 500 / 1000 mL (Integra Biosciences, 182101 / 182051)

Syringe filtration unit Filtropur S 0.2 µm (Sarstedt, 83.1826.001)

TissueLyser Steel Beads (QIAGEN, 69989)

9.3.4. Cell culture medium and serum

DMEM (Biochrom, F0415)

DMEM/F-12 without glutamine (Thermo Fisher Scientific, 21331-046)

Fetal calf serum (FCS; Biochrom, S0615)

Horse serum (Life Technologies, 26050088)

mTESR 1 (STEMCELL, 85870)

RPMI 1640 (Gibco, 21875)

9.3.5. Reagents

1,4-Dithiothreitol (DTT; Sigma-Aldrich, D9779)

1-Thioglycerol (Sigma-Aldrich, M6145)

2-Mercaptoethanol (Sigma-Aldrich, M6250)

2-Propanol (Merck Millipore, 107022)

6x DNA loading dye (Thermo Fisher Scientific, R0611)

Accutase Cell Dissociation Reagent (Sigma-Aldrich, A6964)

Acetic acid (Roth, HN65.1)

Acetonitrile (Pierce, Thermo Fisher, 51101)

Acrylamide/Bis 40% (29:1; Bio-Rad, 161-0146)

Activin A (R&D Systems, 338-AC)

Agarose (Invitrogen, 15510-027)

Ampicillin trihydrate (SERVA, 13397.01)

Ammoniumpersulfate (APS; Bio-Rad, 161-0700)

Aprotinin (Sigma-Aldrich, A1153)

Aqua ad injectabilia (Baxter S.A., 001428)

B27 Plus Insulin (Gibco, 17504-044)

BactoTM Agar (BD, 214010)

BactoTM Tryptone (BD, 211705)

BactoTM Yeast Extract (BD, 212750)

Bafilomycin A1 (Sigma-Aldrich, B1793)

bFGF (basic fibroblast growth factor; PeptroTech, 100-18B)

BMP4 (R&D Systems, 314-BP)

Bromphenol blue (Merck, 108122)

BSA (Sigma-Aldrich, A3059)

BTS (N-Benzyl-p-Toluenesulfonamide, TCI, B3082-25G)

Clarity Western ECL Substrate (Bio-Rad, 170-5061)

Collagenase II (Worthington, LS004176)

cOmplete, Mini, EDTA-free Protease Inhibitor (Roche, 04693159001)

DMSO (Dimethylsulfoxide; Sigma-Aldrich, D8418)

Dulbecco's Phosphate-Buffered Saline (PBS; Gibco 14040-133)

Dorsomorphin dihydrochloride (Tocris, 3093)

EDTA (Roth, 8043.2)

Ethanol, absolute (Chemsolute, 2246.1000)

Geltrex (Thermo Fisher Scientific, A1413302)

GeneRuler 1kb DNA ladder (Thermo Fisher Scientific, SM0313)

Gentle Cell Dissociation Reagent (STEMCELL, 07174)

Glycine (Roth, 3790.2)

Glycerol (Merck 1.04092)

HBSS (Thermo Fisher Scientific, 14175-053)

HEPES (Sigma-Aldrich, 9105.4)

Hoechst 33342 (Sigma-Aldrich, B2261-25MG)

Human recombinant insulin (Sigma-Aldrich, I9278)

Human serum albumin (Biological Industries, 05-720-1B)

Hydrochloric acid, 37% solution (Merck, 1.00317)

InSolution MG-132 (Carbobenzoxy-L-leucyl-L-leucyl-L-leucinal, Z-LLL-CHO; Merck Biosciences, 474791)

Iodoacetamide, BioUltra (Sigma Aldrich; I6125-100)

L-glutamine (Gibco, 25030-081)

Lipidmix (Sigma-Aldrich, L5146)

LysC (Promega, VA1170)

Matrigel Growth Factor Reduced Basement Membrane Matric (Corning, 354230)

Methanol (J.Baker, 8045)

Midori Green (Biozym, 617004)

N,N,N',N'-Tetramethylethylenediamine (TEMED, Bio-Rad, 161-0801)

Nitrogen, liquid (Cryotherm)

Non-essential amino acids (Gibco, 11140)

PageRuler Plus Prestained Protein Ladder (Thermo Fisher Scientific, 26619)

Penicillin/streptomycin (Gibco, 15140)

Phosphoascorbate (2-Phospho- L -ascorbic acid trisodium salt; Sigma-Aldrich, 49752)

Pluronic F127 (Sigma-Aldrich, P2443)

Polyvinyl alcohol (PVA; Sigma-Aldrich, P8136)

Ponceau S solution (Sigma-Aldrich, P7170)

Precision Plus Protein Dual Color (Bio-Rad, 161-0394)

Pursept (Schülke, 230125)

QIAshredder (QIAGEN, 79656)

Rapamycin (Sigma-Aldrich, R8781)

Restore PLUS Western Blot Stripping Buffer (Thermo Fisher Scientific, 46430)

Roti-Histofix 4% (Roth, P087.3)

Saponin (Merck, 558255)

Skim milk powder (Roth, T145.2)

S.O.C. medium (Thermo Fisher Scientific, 15544034)

Sodium azide (Sigma-Aldrich, 71290)

Sodium chloride (NaCl; JT Baker, 7647-14-5)

Sodium dodecyl sulphate (SDS pellets; Roth, CN30.3)

Sodium selenite (Sigma-Aldrich, S5261)

TGFß1 (Peprotech, 100-21C)

Thiourea (Sigma-Aldrich, T7875-500)

TOP10 chemically competent E. coli (Thermo Fisher Scientific, C404010)

Transferrin (Sigma-Aldrich, S5261)

Tris-hydrochloride (Roth, 9090.2)

Triton X-100 (Roth, 3051.3)

Trizma base (Sigma-Aldrich, T1503)

Trypan blue (Biochrom, L 6323)

Trypsin-EDTA 0.5% (Gibco, 15400054)

Trypsin Gold (Promega, V5111)

Tween 20 (Sigma-Aldrich, P1379)

UltraPure DTT (Sigma, 17-1318-02)

Urea (Merck, 1.08487.5000)

XAV 939 (Tocris, 3748)

Y-27632 (Biorbyt, orb154626)

ZipTip-µC18 tips (Merck Millipore, ZTC18S096)

9.3.6. Kits and enzymes

Table S1: Kits and enzymes.

Name	Company	Product code
AmpliTaq Gold (250 U) DNA polymerase	Thermo Fisher Scientific	4311806
CloneJET PCR Cloning Kit	Thermo Fisher Scientific	K1232
Coomassie Plus (Bradford) Assay Kit	Bio-Rad	500-0006
CytoTune™-iPS 1.0 Sendai Reprogramming Kit	Life Technologies	A16517
DNase	Sigma-Aldrich	D8764

DNeasy Blood & Tissue Kit	QIAGEN	69504
FastDigest BpiI/BbsI	Thermo Fisher Scientific	FD1014
HRM/iRT peptides	Biognosys AG	Ki-3002-1
Maxima SYBR Green/ROX qPCR Master Mix (2x)	Thermo Fisher Scientific	K0222
NucleoBond Xtra Maxi Kit	Macherey-Nagel	740414.50
NucleoSpin Plasmid Miniprep Kit	Macherey-Nagel	740588.250
P3 Primary Cell 4D-Nucleofector X Kit L	Lonza	V4XP-3024
Primary Cell Optimization 4D-Nucleofector X Kit	Lonza	V4XP-9096
PrimeSTAR HS DNA polymerase	Takara	R010A
QIAquick Gel Extraction Kit	QIAGEN	28706
QIAquick PCR Purification Kit	QIAGEN	28104
Qubit Protein Assay Kit	Thermo Fisher Scientific	Q33212
Qubit RNA BR Assay Kit	Thermo Fisher Scientific	Q10210
Qubit RNA HS Assay Kit	Thermo Fisher Scientific	Q32855
Ribonuclease H from E.coli (2U/ µL)	Thermo Fisher Scientific	18021014
RNeasy Mini Kit	QIAGEN	74106
Superscript III First Strand cDNA synthesis Kit	Thermo Fisher Scientific	18080-051
SV Total RNA Isolation System	Promega	Z3105
T4 Ligase	Thermo Fisher Scientific	EL0014

9.3.7. Composition of reagents, buffers & solutions

Table S2: List of the composition of the used reagents, buffers and solutions.

Reagent/ buffer/ solutions	**Composition**
10x annealing buffer	100 mM Tris-HCL, pH8 500 mM NaCl 10 mM EDTA in ddH_2O
Agar plates	15 g/L Bacto Agar, autoclaved and casted into TC dish 100
Activin A (157 µg/mL)	1 mg Activin A in 6.369 mL 4 mM HCl (sterile)
Aprotinin	33 mg/mL Aprotinin in aqua ad injectabilia 250 µL aliquots, stored at -20 °C for up to one year
bFGF (100 µg/mL)	1 mg bFGF

	0.1% BSA in PBS
Blocking solution	5% Milk powder or 5% BSA in ddH_2O
1x Blotting buffer I	400 mL 5x Blotting buffer 400 mL Methanol Fill up to 2 L with ddH*2*O
5x Blotting buffer I	29 g Trizma base (125 mM) 145 g Glycine (950 mM) in 2 L ddH_2O
BMP4 (50 µg/mL)	1 mg BMP4 in 20 ml 0.1% BSA 4mM HCl mix
BTS solution	30 mM BTS in DMSO 250 µL aliquots, stored at -20 °C for up to one year
Collagenase dissociation buffer	200 U/mL Collagenase II 1 mM HEPES 10 µM Y-27632 30 µM BTS in HBSS (-) calcium/magnesium
DNase solution	100 mg DNase II in 50 mL PBS 2 mL aliquots, stored at -20 °C for up to six months
EDTA	0.5 mM EDTA in PBS Stored at 4 °C
FACS buffer	5% (v/v) FCS 0.5% (w/v) Saponin 0.05% (v/v) Sodium azide in PBS
Freezing solution	90% FCS 10% DMSO
HEPES stock	1 M HEPES in 1xPBS (pH 7.4 adjusted with potassium hydroxide) Stored at 4 °C for up to one year

Kranias buffer	2 mL Tris (1.5 M, pH 8.8) 1 mL EDTA (0.5 M) 6 mL NaF (500mM) 15 mL SDS (20%) 10 mL Glycerol in 100 mL ddH_2O
Laemmli buffer (6x)	1.2 g SDS 6 mg Bromophenol blue 6 g Glycerol 1.2 mL of 0.5 M Tris (pH 6.8) 0.93 g DTT in ddH_2O
LB- medium	10 g Bacto Tryptone 5 g Basto Yeast Extract 10 g NaCl 1 L ddH_20, pH7.4
Permeabilization buffer (IF)	3% (w/v) Skim milk powder 0.1% (v/v) Triton X-100 in PBS
Phosphoascorbate (250 mM)	1 g Phosphoascorbate 12.4 mL PBS
Pluronic F-127 solution	1% (w/v) Pluronic F-127 in PBS Stored at 4 °C for up to one year.
50x Polyvinyl alcohol	20 g polyvinyl alcohol in 100 mL ddH_2O Stored at 4 °C for up to one year
10x SDS-PAGE electrophoresis buffer	30.2 g Trizma base (250 mM) 10 g SDS (1%) or 50 mL of 20% SDS sol. 144 g Glycine (1.92 M) in 1 L ddH_2O
Separation gel SDS-PAGE (12%)	3 mL Acrylamide/Bis 40% 2.5 mL Tris pH 8.8 (1.5 M) 100 µL SDS (10% solution) 100 µL APS (10% solution) 4 µL TEMED 4.3 mL ddH_2O

Stacking gel SDS-PAGE	1.28 mL Acrylamide/Bis 40% 2.5 mL Tris (0.5 M, pH 6.8) 100 µL SDS (10% solution) 100 µL APS (10% solution) 10 µL TEMED 6.03 mL ddH_2O
50x TAE-buffer (for agarose gel electrophoresis)	242 g Trizma base 37.2 g Titriplex III (EDTA) 57.1 mL concentrated acetic acid 1 L ddH_2O (pH 8.5)
10xTBS	121.1 g Trizma base (1 M) 87.66 g NaCl (1.5 M) in ddH_2O (pH 7.5, adjusted with 37% HCL)
TBS-T	100 mL TBS 900 mL ddH_2O 1 mL Tween20 (0.1%)
TGFß1 (20 µg/mL)	100 µg TGFß1 in 0.1% HSA-solution
Transferrin-selenite solution	100 mg Transferrin dissolved in 2 mL sodium selenite (382 µM) Stored at -80 °C for up to six months
0.5 M Tris (pH 6.8)	60.6 g Trizma base in 1 L ddH_2O
1.5 M Tris (pH 8.8)	181.7 g Trizma base in 1 L ddH_2O
XAV 939 (10 mM)	50 mg XAV 939 in 14.3 mL DMSO

9.3.8. Antibodies

Table S3: Primary antibodies used for flow cytometry (FC), western blot (WB) and immunofluorescence (IF) microscopy.

Antibody	Species	Application and dilution	Company (product code)
α-Actinin 2, clone EA 53	Mouse	WB: 1:20,000; IF: 1:800	Sigma (A7811)
α-Actinin 2	Rabbit	WB: 1:10,000; IF: 1:800	Sigma (SAB2108642)
α-CSQ	Rabbit	WB: 1:5000	Dianova (ABR-01164)
α-cMyBP-C C0-01	Rabbit	WB: 1:10,000	Gautel
α-cMyBP-C F-1	Mouse	WB: 1:2000; IF: 1:200	Santa Cruz (sc-137181)
α-Titin Z1	Rabbit	IF: 1:200	Labeit
α-cTnT (clone13-11)	Mouse	WB: 1:5000; IF: 1:100	Abcam (ab10218)
α-cTnT (clone 1C11)	Mouse	WB: 1:5000; IF: 1:100	Abcam (ab8295)
α-cTnT FITC	Recombinant human IgG1	FC: 1:10	Miltenyi Biotec (130-106-687
α-LAMP-2 H4B4	Mouse	IF: 1:50	DHSB (H4B4-s)
α-LAMP-2	Rat	WB: 1:2000(tissue) / 1:5000 (hiPSC-CMs	Abcam (ab13524)
α-LC3	Rabbit	WB: 1:1000 in 5% BSA	Novus Biological (NB100-2331)
α-LC3	Rabbit	WB: 1:1000 in 5%BSA	Cell Signaling (2775)
α-p62	Mouse	WB: 1:2000	BD (610832)
α-p62	Rabbit	IF: 1:200	Sigma P0067
PE-Rat IgM, κ Isotype control	Mouse	FC: 1:50	BD (553943)
α-pS6	Rabbit	WB: 1:2000	Cell Signaling (2215)
REA Control (I)-FITC	Isotype control IgG1	FC: 1:10	Miltenyi Biotec, 130-104-611
α-S6	Rabbit	WB: 1:5000	Cell Signaling (2217)
α-SSEA3 PE	Rat	FC: 1:5	BD (560237)
α-Ubiquitin	Mouse	WB: 1:50 000	Biomol (BML-PW 8810)

Table S4: Secondary antibodies used for WB and IF.

Antibody	Dilution	Company (product code)
Alexa Fluor 488 goat anti-mouse IgG	IF: 1:800	Life Technologies (A11029)
Alexa Fluor 488 goat anti-rabbit IgG	IF: 1:800	Life Technologies (A11034)
Alexa Fluor 546 goat anti-rabbit IgG	IF: 1:800	Life Technologies (A11035)
Alexa Fluor 546 rabbit anti-mouse IgG	IF: 1:800	Life Technologies (A11030)
Anti-mouse IgG peroxidase-conjugated	WB: 10 000	Sigma Aldrich (A9044)
Anti-mouse IgG Pox peroxidase-conjugated	WB: 10 000	Dianova (515-035-003)
Anti-rabbit IgG peroxidase-conjugated	WB: 10 000	Sigma Aldrich (A0545)
Anti-rabbit IgG Pox peroxidase-conjugated	WB: 10 000	Dianova (111-035-045)
Anti-rat IgG peroxidase-conjugated	WB: 10 000	Dianova (112-035-003)

9.3.9. Primer lists & NanoString Expression CodeSet

Table S5: Primer pairs for sequencing, PCR and RT-qPCR.

Target	Sequence [5'-3']	Tm [°C]	Product size [bp]
GAPDH exon 5 - 6	Fwd: ATGTTCGTCATGGGTGTGAA Rev: TGAGTCCTTCCACGATACCA	59.8 59.1	136
LMNA exon 4	Fwd: TGAGACCAAGCGCCGTCA Rev: GGCATTGTCCAGCTTGGCA	65.3 65.6	175
MYBPC3 exon 1 - 2	Fwd: GCCAGTCTCAGCTTTTAGCAA Rev: CAGGCCGTACTTGTTGCTG	59.8 60.5	151
MYBPC3 exon 26	Fwd: CCCAGCCCTTCATGCCTAT Rev: CCTCTGGGCAGTACTCCAC	62.3 58.2	153
MYBPC3 exon 6	Fwd: CCTCCATGCACACAGGTCTA Rev: ATCTCACCTTCCCAGCCTTT	59.10 59.02	515
MYBPC3 exon 4 - 9	Fwd: TCAAGCTCAGCAGCTCTCAA Rev: TCCAGAATCCCAGTGTCCTC	59.32 58.43	473
OT_#1	Fwd: AAGAGTGGGTCACAGAGACTG Rev: AGTCCTACACATCATTGCTGCT	59.03 59.76	548
OT_#2	Fwd: GGGTGGTAGGAGCATCTTCAG Rev: GGATACTGCTGGAGCTTATGGG	59.86 60.29	725
OT_#3	Fwd: GGAGCTTTCTGTGCTGATCCA Rev: TCTAGCAGTTCTAAGGCTGGC	60.34 59.52	535
OT_#4	Fwd: AGCCTGTGAATCATCTGGGC Rev: AGTAGGTAGAGGGCATGGGG	60.11 60.10	771

OT_#5	Fwd: TTCCTACGGAGAGACTGAGGG Rev: AGGGGCATGTCTGCATTTTC	60.06 58.81	588
OT_#6	Fwd: CGATAGGGGTAATGGTGCCC Rev: CCAATCCACATGGCCCTTCT	59.96 60.03	531
OT_#7	Fwd: TGGCCTATTTAGATCCTTGGCA Rev: TCCCCAGGCCAAGAAAGAAT	59.22 58.92	761
OT_#8	Fwd: CCCTAGGCCTTCAGACAACC Rev: GAGCTTCTACAGCGCCAGAT	59.75 59.90	679
OT_#9	Fwd: CTTATGCTCTCGGGGAGTGG Rev: TGGGGGTTCAGAAGCTTATTT	59.61 57.17	718
OT_#10	Fwd: CTGGGGACAGCATTATCGCA Rev: TAAACCGGGGCCTCTTTTGT	60.18 59.52	577
U6 Fwd promoter	Fwd: GAGGGCCTATTTCCCATGATT	58	-

The here used NanoString Expression CodeSet are build-up of the human basic TagSet and the autophagy extension TagSet (Table S6).

Table S6: Listing of applied NanoString Expression CodeSet.

Housekeeping	**Human basic TagSet**		**Autophagy extension TagSet**	
ABCF1	*ACTA2*	*MYH6*	*BAG3*	*MAP1LC3B*
ACTB	*ACTN2*	*MYH7*	*BECN1*	*MTOR*
CLTC	*ATP2A2*	*NFKB1*	*CHMP2B*	*NBR1*
GAPDH	*BAX*	*NPPA*	*EPG5*	*NRG1*
PGK1	*BCL2*	*NPPB*	*FOXO1*	*SQSTM1*
TUBB	*CASQ2*	*PLN*	*FYCO1*	*STAT1*
	COL1A1	*POSTN*	*LAMP1*	*STAT3*
	COL3A1	*PPP1R1A*	*LAMP2*	*TFEB*
	CTGF	*RYR2*		
	FHL2	*S100A4*		
	FN1			

9.4. Security information

All of the performed experiments were conducted in certified security standard S1 and S2 laboratories and complied to the obligatory safety standards. Thus, the here used buffers, chemicals and solutions were handled and disposed according to their security data sheets in the appropriate containers, whereby cell culture utilities and contaminated material was

autoclaved before disposal. In case of a putative contamination of a surface with genetically modified organism, cleaning with 70% ethanol was performed.

Table S7: H- and P- statements for all used chemicals.

Chemical	Company	H-statement	P-statement
1,4-Dithiothreitol (DTT)	Applichem	H: 302, 315, 319, 412	P: 264, 270, 273, 280, 337+313, 501
1-Thioglycerol	Sigma-Aldrich	H: 302, 311, 315, 319, 335	P: 261, 264, 280, 301+312+330, 302+352+312, 333+313
2-Mercaptoethanol	Sigma-Aldrich	H: 301+331, 310, 315, 317, 318, 373, 410	P: 270, 280, 302+352, 330, 304+340, 305+351+338, 310
2-Propanol	Merck Millipore	H: 225, 319, 336	P: 210, 261, 305+351+338
Acetic acid	Roth	H: 226, 290, 314	P: 210, 280, 301+330+331, 305+351+338, 308+310
Acetonitrile	Pierce, Thermo Fisher	H: 225, 311, 302+332, 319	P: 210, 280
Acyrlamide/bis solution 40% (29:1)	Bio-Rad	H: 302, 312, 315, 317, 319, 340, 350, 361, 372	P: 260, 280, 281, 305+351+338, 405, 501
Ammonium persulfate (APS)	Bio-Rad	H: 272, 302, 315, 317, 319, 334, 335	P: 210, 221, 285, 305+351+338, 405, 501
Ampicillin trihydrate	SERVA	H: 317, 334	P: 280, 285, 302+352, 304+340, 333+313, 342+311
BTS	TCI	H: 301	P: 264, 270, 301+310, 321, 330, 405, 501
Collagenase II	Worthington	H: 334	P: 261, 284, 304+340, 342+311
cOmplete, Mini, EDTA-free Protease Inhibitor	Roche	H: 315, 319	P: 264, 280, 302+352, 332+313, 337+313, 362+364

Ethylenediamine tetraacetic acid (EDTA)	Roth	H: 319	P: 305+351+338
Ethanol, absolute	Chemsolute	H: 225, 319	P: 210, 240, 305+351+338, 403+233
Hoechst 33342	Sigma-Aldrich	H: 302, 315, 335, 341	P: 280, 301+312+333
Hydrochloric acid, 37% solution	Merck	H: 290, 314, 335	P: 280, 301+330+331, 305+351+338, 308+310
Iodoacetamide, BioUltra	Sigma-Aldrich	H: 301, 317, 334	P: 261, 280, 301+310, 342+311
Lipidmix	Sigma-Aldrich	H: 225, 319	P: 210, 280, 305+351+338, 337+313, 403+235
Methanol	J T Baker	H: 225, 301, 331, 311, 370	P: 210, 233, 280, 302+352
Midori Green	Biozym	-	P: 261, 280
N,N,N´,N´-Tetramethylethylenediamine (TEMED)	Bio-Rad	H: 225, 302, 314, 332	P: 210, 233, 280, 301+330+331, 305+351+338, 308, 310
Nitrogen, liquid	Cryotherm	H: 281	P: 282, 336+315, 403
Penicillin/streptomycin	Gibco	H: 315, 317, 334, 335	P: 280, 261, 264, 284, 271, 302+352, 304+340, 333+313
Ponceau S	Sigma	H: 315, 319, 335	P: 261, 305+351+338
Pursept	Schülke	H: 226, 319	P: 210, 280, 305+351+338, 337+313, 403+235
Restore PLUS Western Blot Stripping Buffer	Thermo Fisher Scientific	H: 290	P: 234, 390
Roti-Histofix 4%	Roth	H: 302, 317, 341, 350	P: 261, 280, 302+352,308+313
Saponin	Sigma	H: 319, 335	P: 261, 305+351+338
Sodium azide	Merck	H: 300, 400, 410	P: 273, 309, 310
Sodium dodecyl sulphate (SDS)	Roth	H: 228, 302+332, 315, 318, 335, 412	P: 210, 261, 280, 302+352, 305+351+338, 312

Sodium selenite	Sigma-Aldrich	H: 300+330, 315, 317, 319, 411	P: 273, 280, 301+310+330, 302+352, 304+340+310, 305+351+338
Thiourea	Sigma-Aldrich	H: 302, 351, 361d, 411	P: 201, 273, 301+312+330, 308+313
Tris-HCl	Roth	H: 315, 319, 335	P: 280, 302+352, 305+351+338
Triton X-100	Roth	H: 302, 318, 411	P: 273, 280, 305+351+338
Trypan blue	Gibco	H: 350	P: 201-308+313
Trypsin Gold	Promega	H: 315, 319, 334, 335	P: 264, 280, 284, 305+351+338, 312
UltraPure DTT	Sigma-Aldrich	H: 302, 315, 319, 412	P: 264, 270, 273, 280, 337+313, 501
Y-27632	Biorbyt	H: 302, 312, 332	P: 280

9.4.1. EU-GHS Hazard (H) statements

Table S8: List of EU-GHS H-statements.

H-statement	**H-phrase**
H225	Highly flammable liquid and vapour.
H226	Flammable liquid and vapour.
H228	Flammable solid.
H272	May intensify fire; oxidizer.
H281	Contains refrigerated gas; may cause cryogenic burns or injury.
H290	May be corrosive to metals.
H300	Fatal if swallowed.
H300 + H330	Fatal if swallowed or if inhaled.
H301	Toxic if swallowed.
H301 + H331	Toxic if swallowed or if inhaled.
H302	Harmful if swallowed.
H302 + H332	Harmful if swallowed or if inhaled.
H310	Fatal in contact with skin.
H311	Toxic in contact with skin.

H312	Harmful in contact with skin.
H314	Causes severe skin burns and eye damage.
H315	Causes skin irritation.
H317	May cause an allergic skin reaction.
H318	Causes serious eye damage.
H319	Causes serious eye irritation.
H334	May cause allergy or asthma symptoms or breathing difficulties if inhaled.
H335	May cause respiratory irritation.
H336	May cause drowsiness or dizziness.
H340	May cause genetic defects.
H341	Suspected of causing genetic defects.
H350	May cause cancer.
H351	Suspected of causing cancer.
H361/H361d	Suspected of damaging fertility or the unborn child.
H370	Causes damage to organs.
H371	May cause damage to organs.
H372	Causes damage to organs through prolonged or repeated exposure.
H373	May cause damage to organs through prolonged or repeated exposure.
H400	Very toxic to aquatic life.
H410	Very toxic to aquatic life with long lasting effects.
H411	Toxic to aquatic life with long lasting effects.
H412	Harmful to aquatic life with long lasting effects.

9.4.2. EU-GHS Precaution (P) statements

Table S9: List of EU-GHS P-statements.

P-statement	**P-phrase**
P201	Obtain special instructions before use.
P210	Keep away from heat, hot surfaces, sparks, open flames and other ignition sources. No smoking.
P233	Keep container tightly closed.
P234	Keep only in original packaging.
P240	Ground and bond container and receiving equipment.
P260	Do not breathe dust/fume/gas/mist/vapors/spray.
P261	Avoid breathing dust/fume/gas/mist/vapors/spray.
P264	Wash … thoroughly after handling.

P270	Do not eat, drink or smoke when using this product.
P271	Use only outdoors or in a well-ventilated area.
P273	Avoid release to the environment.
P280	Wear protective gloves/protective clothing/eye protection/face protection.
P281	Use personal protective equipment as required.
P282	Wear cold insulating gloves and either face shield or eye protection.
P284	[In case of inadequate ventilation] wear respiratory protection.
P285	In case of inadequate ventilation wear respiratory protection.
P301 + P310	IF SWALLOWED: Immediately call a POISON CENTRE/doctor/…
P301 + P312 + P330	IF SWALLOWED: Call a POISON CENTER or doctor/physician if you feel unwell. Rinse mouth.
P301 + P330 + P331	IF SWALLOWED: Rinse mouth. Do NOT induce vomiting.
P302 + P352	IF ON SKIN: Wash with plenty of water/…
P302 + P352 + P312	IF ON SKIN: Wash with plenty of soap and water. Call a POISON CENTER or doctor/physician if you feel unwell.
P304 + P340	IF INHALED: Remove person to fresh air and keep comfortable for breathing.
P304 + P340 + P310	IF INHALED: Remove person to fresh air and keep comfortable for breathing. Immediately call a POISON CENTER/doctor.
P305 + P351 + P338	IF IN EYES: Rinse cautiously with water for several minutes. Remove contact lenses, if present and easy to do. Continue rinsing.
P308	IF exposed or concerned:
P308 + P310	IF exposed or concerned: Immediately call a POISON CENTRE/doctor/…
P308 + P313	IF exposed or concerned: Get medical advice/attention.
P309	IF exposed or if you feel unwell:
P310	Immediately call a POISON CENTRE/doctor/…
P312	Call a POISON CENTRE/doctor/… if you feel unwell.
P321	Specific treatment (see … on this label).
P330	Rinse mouth.
P332 + P313	If skin irritation occurs: Get medical advice/attention.
P333 + P313	If skin irritation or rash occurs: Get medical advice/attention.

P336 + P315	Thaw frosted parts with lukewarm water. Do not rub affected area. Get immediate medical advice/attention.
P337 + P313	If eye irritation persists: Get medical advice/attention.
P342 + P311	If experiencing respiratory symptoms: Call a POISON CENTRE/doctor/…
P362 + P364	Take off contaminated clothing and wash it before reuse.
P390	Absorb spillage to prevent material damage.
P403	Store in a well-ventilated place.
P403 + P233	Store in a well-ventilated place. Keep container tightly closed.
P405	Store locked up.
P501	Dispose of contents/container to …

9.5. Publications & congress participations

9.5.1. Publications

Prondzynski, M, Lemoine, MD, Zech, ATL, Horvath, A, Di Mauro, V, Koivumäki, JT, Kresin, N, Busch, J, Krause, T, Krämer, E, Schlossarek, S, Spohn, M, Friedrich, F, Münch, J, Laufer, S, Redwood, C, Volk, AE, Hansen, A, Mearini, G, Catalucci, D, Meyer, C, Christ, T, Patten, M, Eschenhagen, T & Carrier, L. (2019) Disease modeling of a mutation in α-actinin 2 guides clinical therapy in hypertrophic cardiomyopathy. EMBO Mol Med. e11115: 1-18.

Zech ATL*, Singh SR*, Schlossarek S, Carrier L. (2019) Autophagy in cardiomyopathies. Biochim Biophys Acta – Mol Cell Res 1-14.

Lemme M, Ulmer BM, Lemoine MD, Zech ATL, Flenner F, Ravens U, Reichenspurner H, Rol-Garcia M, Smith G, Hansen A, Christ T & Eschenhagen T. (2018) Atrial-like Engineered Heart Tissue: An In Vitro Model of the Human Atrium. Stem Cell Rep 11:1378-1390.

Singh SR, Zech ATL, Geertz B, Reischmann-Düsener S, Osinska H, Prondzynski M, Krämer E, Meng Q, Redwood C, Van der Velden J, Robbins J, Schlossarek S, Carrier L. (2017) Activation of Autophagy Amerliorates Cardiomyopathy in Mybpc3-Targeted Knockin Mice. Circ Hear Fail 10.

Harder L, .Eschenburg G, Zech A, Kriebitzsch, Otto B, Streichert T, Behlich AS, Dierck K, Klingler B, Hansen A, Stanulla M, Zimmermann M, Kremmer E, Stocking C, Horstmann MA. (2013) Aberrant ZNF423 impedes B cell differentiation and is linked to adverse outcome of ETV6-RUNX1 negative B precursor acute lymphoblastic leukemia. J Exp Med 210:2289-2304.

9.5.2. Participations at congresses

"Cardiac Regulatory Mechanisms"– Gordon Research Conference, 3rd – 8th of June 2018, New London, NH USA; poster presentation "Common autophagy alteration but specific lysosomal dysfunction in human hypertrophic and dilated cardiomyopathies".

"Cardiac Regulatory Mechanisms"– Gordon Research Seminar, 2nd – 3rd of June 2018, New London, NH USA; selected oral abstract and poster presentation "Common autophagy alteration but specific lysosomal dysfunction in human hypertrophic and dilated cardiomyopathies".

34th Annual Meeting of the European Section of the ISHR, 24th – 27th of July 2017, Hamburg, Germany; selected oral abstract and poster presentation "Evaluation of the autophagy-lysosomal pathway in cardiac tissue and hiPSC-derived cardiomyocytes from patients with inherited cardiomyopathies", awarded with a poster prize.

NCCR retreat, 3rd – 4th of February 2017, Tremsbüttel, Germany; poster presentation "Alteration of the autophagy-lysosomal pathway in hypertrophic and dilated cardiomyopathy".

Heart Failure Winter Research Meeting, 25th – 28th of January 2017, Les Diablerets, Switzerland; poster presentation "Alteration of the autophagy-lysosomal pathway in hypertrophic and dilated cardiomyopathy".

10. Acknowledgement

First of all, I would like to thank Prof. Dr. Lucie Carrier, who not only gave me the opportunity to perform my PhD in her lab but also always encouraged me to perform experiments and to participate in conferences to exchange ideas with other scientists. Furthermore, she always challenged my findings and scientific ideas, although this meant to argue a lot with me. Nonetheless, she trusted my skills and gut and let me do my thing in the lab.

I would also like to thank Prof. Dr. Thomas Eschenhagen for giving me the opportunity to do my PhD at his Institute and for his great, challenging scientific feedback during meetings.

Further, I would also like to thank Prof. Dr. Elke Oetjen very much for reviewing this thesis.

Another big thank you is addressed to the AG Carrier, including Dr. Sonia Singh, Dr. Frederik Flenner, Dr. Giulia Mearini, Lisa Krämer and Niels Pietsch, but also former students, such as Anna Rinas, Neele Warnecke, Alexander Tourounoglou and many more.

A special thank you goes to Dr. Saskia Schlossarek, who had to put up with a lot to help me finalize this thesis, while being supportive and reassuring. I do owe her a lot of chocolate. However, also Josefine Busch largely contributed to this thesis by supporting me 100% in the lab during pregnancy and as a friend. Furthermore, Silke Reischmann-Düsener helped me to finish all the experiments.

One of the biggest thank you goes to my triple Ms – Maks, Marta and Mirja -, who helped me to finish my PhD by supporting me 100% in the lab, especially during pregnancy. Each of them supported me in their own way, scientifically and personally, and even though we are not working any longer in one place, they are an important part of my life that I do not want to miss.

Further, I want to thank the people that supported me during CRISPR, such as Sandra Laufer, Christiane Neuber, Anika E Knaust. Alexandra Madsen and Maks Prondzynski. Moreover, a big thank goes to the member of our hiPSC-CM working group that helped me to successfully differentiate, especially Thomas Schulze, Birgit Klampe, Aya Shibamiya and Marina Reinsch. I also want to say thank you to Lotta Behrens and Malte Loos who supported me in the last weeks with food and company, and Alexandra Madsen for proofreading this thesis.

I also want to thank my friends that supported me in the last four years. A special thank you goes to Bianca Dawson that greatly supported me mentally in the last weeks and year.

Finally, the biggest thank you is addressed to my family that always supported me in every manner you can think of. Especially in the last year, my parents and my siblings, helped me to finalize this thesis that otherwise wouldn’t have been possible. Particularly, my fiancé Philip Goldhahn and my son Emil Goldhahn, helped and motivated me every day to do the best I can.

11. Declaration of academic honesty – Eidesstattliche Erklärung

I hereby declare that my thesis was written independently by myself and further I did not use any other sources or aids other than those indicated. The submitted written form of the thesis complies with the one on the electronic storage medium. This thesis was not handed in any other form for another examination procedure.

Hamburg, 13.12.2019 

„Hiermit versichere ich Eides statt, die vorliegende Dissertation selbst verfasst und keine anderen als die angegebenen Hilfsmittel benutzt zu haben. Die eingereichte schriftliche Fassung entspricht der auf dem elektronischen Speichermedium. Ich versichere, dass diese Dissertation nicht in einem früheren Promotionsverfahren eingereicht wurde.“

Hamburg, den 13.12.2019